Distribution Agreement

Signature:

Youngsun Kim	Date

Structures and Functions of Peptide-metal Co-assemblies

By

Youngsun Kim

Doctor of Philosophy

Chemistry

David G. Lynn, Ph.D.

Advisor

Laura Finzi, Ph.D.

Committee Member

Vincent Conticello, Ph.D.

Committee Member

Accepted:

Kimberly Jacob Arriola, Ph.D., MPH

Dean of the James T. Laney School of Graduate Studies

Date

Structures and Functions of Peptide-metal Co-assemblies

By

Youngsun Kim

B.Sc., Kwangwoon University, South Korea, 2014
M.Sc., Kwangwoon University, South Korea, 2016

Advisor: David G. Lynn, Ph.D.

An abstract of
a dissertation submitted to the Faculty of the
James T. Laney School of Graduate Studies of Emory University
in partial fulfillment of the requirements for the degree
of Doctor of Philosophy
in Chemistry

2022

Abstract

Structures and Functions of Peptide-metal Co-assemblies

By Youngsun Kim

Amyloid-beta (Aβ) peptide is a hallmark of Alzheimer's disease in forming toxic aggregates or fibers. A hydrophobic sequence of Aβ, LVFFA, is a nucleating core sequence for forming assemblies. Short peptides with this core sequence assemble well-ordered supramolecules with cross-beta sheet secondary structures in nano- fibers, ribbons, or tubes morphologies. Incorporating transition metal ions allows for development of functions of the well-ordered peptide assemblies. In the nucleation steps of peptide assembly, in which metastable structures exist, adding transition metal ions template the assembly of peptide-metal co-assemblies. H-HHQALVFFA-NH_2, (K16A), and H-HHQALFFAL-NH_2, (K16AL), sequences with the N-terminal histidine residues were utilized for peptide-metal co-assemblies. We found that peptide assemblies with and without metal ions have morphological, optical, and structural differences. Through structural studies, K16A-Cu(II) co-assemblies' detailed information such as assembly structures and copper complex structures were characterized. Electrochemical properties and applications were also tested, and high reduction potentials (~700 mV) were measured. To modify surface and morphology of the K16A-Cu co-assemblies, K16AL with C-terminal leucine was synthesized. Compared to K16A, K16AL assembly series have different morphologies and because of high hydrophobicity, K16AL self- and co-assemblies with metals shows faster rates of forming assemblies in aqueous solution, by CD and TEM analyses. We also demonstrate that co-assemblies of the peptides and lead(II) ions also form well-ordered structures. The assemblies were tested in DMF solvent systems for applications requiring organic solvents. Among the K16A self- and co-assemblies with metals in DMF solvent systems, K16A-PbI_2 co-assemblies in DMF with 20% water shows well-organized fiber structures and distinct UV/Vis absorption range from lead ion arrays. As a proof-of-concept of K16A and K16AL can remove heavy metals from contaminated water. Copper ions were well isolated by both K16A and K16AL, while high concentrations of lead ions were measured after the treatments. Construction of a model for nanotubes of a peptide assembly with Cryo-EM was performed to get detailed structures and isotope-edited infrared (IE-IR) study identified defects in strand conformational fidelity in beta-sheets.

Structures and Functions of Peptide-metal Co-assemblies

By

Youngsun Kim

B.Sc., Kwangwoon University, South Korea, 2014
M.Sc., Kwangwoon University, South Korea, 2016

Advisor: David G. Lynn, Ph.D.

A dissertation submitted to the Faculty of the
James T. Laney School of Graduate Studies of Emory University
in partial fulfillment of the requirements for the degree
of Doctor of Philosophy
in Chemistry

2022

Acknowledgements

I really appreciate people around me for being my teachers, mentors, friends, and family. Although I cannot express what I really want to say to thank with my English, I hope it can be well delivered to you. I especially thank Dr. David Lynn, my PI, for his patience and guidance. His teaching for chemistry and science from big pictures to details made me a better scientist. I could learn not only chemistries but also lessons for life from him. I am really glad that I met you in my history of chemistry and life.

I also thank my committee members, Dr. Laura Finzi and Dr. Vincent Conticello. Their careful advice, suggestions, and questions for my annual presentations really help to understand how I can propose and present my ideas. I could always feel their encouragement from my second-year qualifying exam to my defense presentation.

To Anthony and Christella, I am pretty sure that I could not survive in this Ph.D. program if I did not have you guys as friends, and family. When I was suffering with my English, chemistry, and mental health, your supports made me alive (Well, you actually saved my life when I cut my leg). Your existence is significantly critical for my life. Dr. Anthony Sementilli, your mentoring actually saved and towed me from nightmares of graduate school to reality where I can survive. Thank you so much for your teaching and help, and support even after you graduated. Christella, my sister, thank you for your cares. You and I spent a lot of difficult time inside and outside of science. Although I could not give many helps to you, you helped and encouraged me a lot. It was you who took me out of the lab and apartment and let me experience US and spend time with people.

To my previous and current lab mates, Drs. Noel Li, Chen Liang, Olga Taran, and Ming-Chein Hsiesh, your legacy handing down for Lynn lab came into my steady fundamentals. Thank you for your teaching when I was a baby in the lab. Alexis, it was impressive that you learn organic synthesis skills so quickly and I feel glad that you successfully developed the synthesis of C-terminal aldehyde. Good luck for your rest of Ph.D. journey! I also would like to appreciate all friends in Lynn lab members, Mandy, Lucy, Chad, Seth, Nicolas, JP, Regina, Griffin, Alexis^2, George, Ethan, Alfonso and Yihoon. It was delightful to interact with you. Specially thanks to Yihoon who is continuing and keeping the peptide-metal blood. I am glad you enjoy the chemistry research and thank you for your huge help.

To my friends, David, Sara, Torie, Yasha, Bo, Yannick, and Sheng! Thank you so much for being my friend. You filled my graduate life with memorable moments. Because of the pandemic and as we became higher year students, we could not enjoy our times together in the ends though, I am still recalling the moments when we had dinners and played basketball/volleyball/board games.

Lastly, I would like to express my deepest appreciation to my family in Korea. My parent, (Yeontae Kim/ Youngsook Lee) and brother (Yehyeong Kim), thank you so much for your endless support.

Table of Contents

Chapter 3.

Chapter 4.

Chapter 1.

Introduction: Emerging functions of peptide self-assemblies and control of its structures

1.1 Self-assemblies in biology

Self-assemblies with molecular recognition are playing significant roles in extended biology such as antigen-antibody, lipids in membranes, DNA duplexes, and amyloidogenic diseases[1]. Molecular recognition results from noncovalent interactions such as hydrophobic interactions, charge-charge interactions, π-π interactions, hydrogen bonding interactions, and metal-ligand interaction. DNA (Deoxyribonucleic acid) base pairs from by hydrogen bonding and the pairs are stabilized by pi-pi stacking in the DNA duplex (Fig. 1-1)[2]. Membrane lipids have hydrophilic head groups and hydrophobic tails,

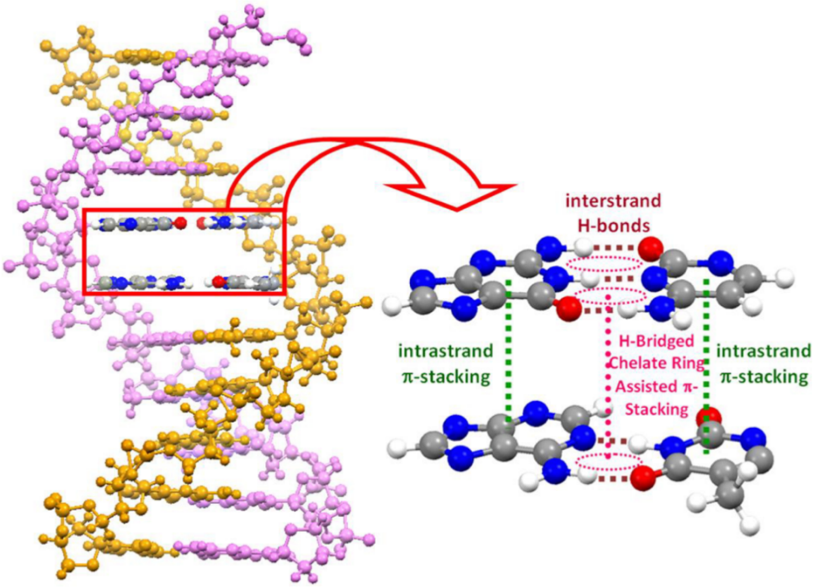

Figure 1-1. Non-covalent interactions, H-bonding, and pi-pi stacking, in DNA duplex. (reprinted from ref. 1)

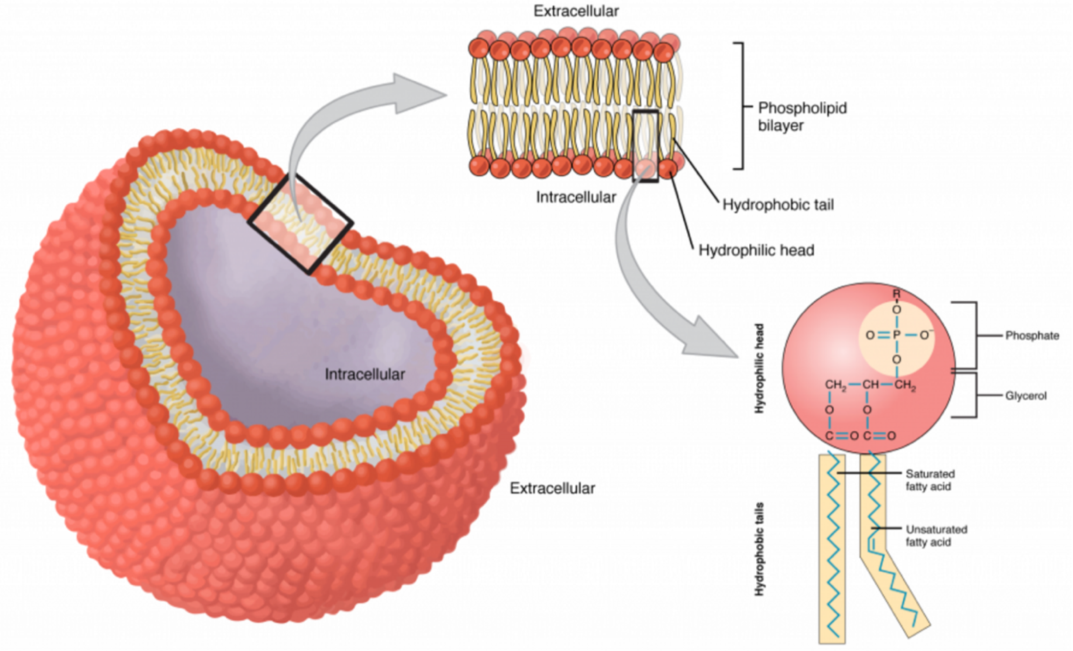

Figure 1-2. Phospholipid Bilayer.
https://open.oregonstate.education/aandp/chapter/3-1-the-cell-membrane/

so that the aqueous environment forces them to bilayer cell membrane (Fig. 1-2). Amyloid filaments have cross-beta secondary structure which consists of a combination of noncovalent interactions (Fig. 1-3)[3]. In the cross-beta structure, hydrogen bonding between peptide strands are colinear with growing fiber axis, and the laminations of beta sheets made by interactions of amino acid side chains. This high propensity for forming fibers or aggregations in brains results in amyloidogenic diseases such as Alzheimer's and Parkinson's diseases. Therefore, these examples of storing/propagating genetic information, keeping shapes/forms of biological components related to diseases, understanding supramolecular chemistry of the assemblies with noncovalent interactions is significant. In this dissertation, studies of structures and properties of peptide assemblies are focused on having a better understands of the assemblies and developing in functions by using the well-ordered structures and behaviors.

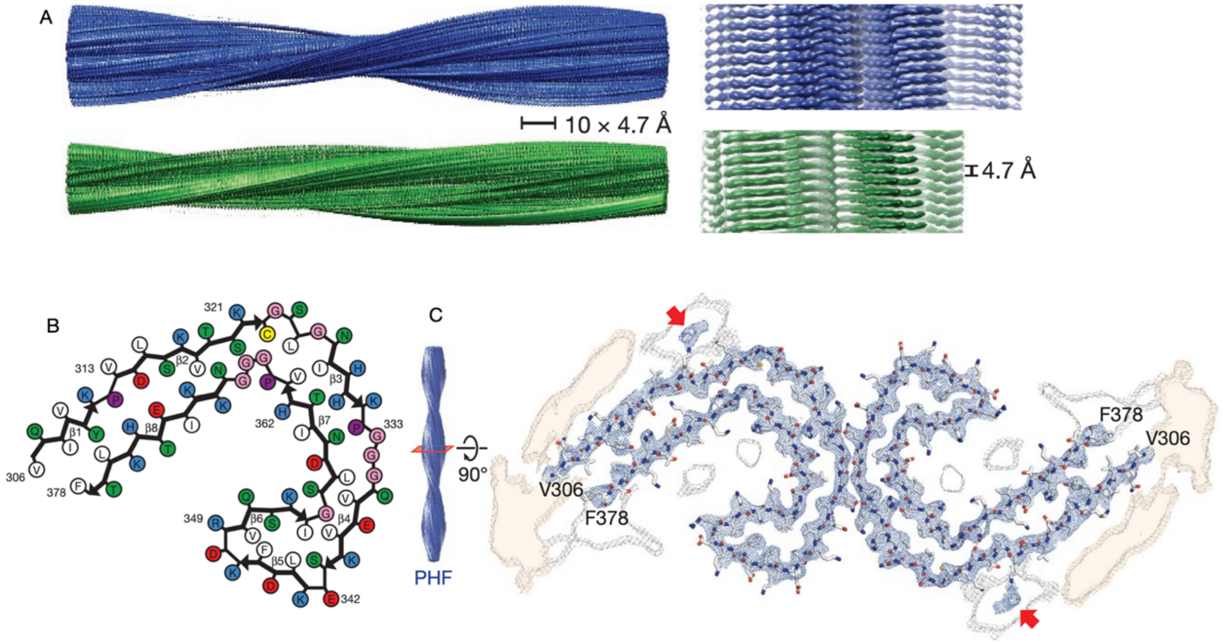

Figure 1-3 Tau filaments from Alzheimer's brain. A structure of the filaments. B a strand with amino acid labels. C. Cross-section of the filament. (reprinted from ref. 3)

1.2 Structures of peptide self-assemblies

The studies of amyloid beta peptides[4-5] related to the amyloidogenic diseases have focused on nucleation mechanisms and the assembled structures. From full sequences of amyloid beta 42 to short motifs assembled peptides can have alpha helix or beta sheet secondary structures with their hydrogen bonding interactions between the peptide backbones. Furthermore, with the secondary structure, they form ordered structures with

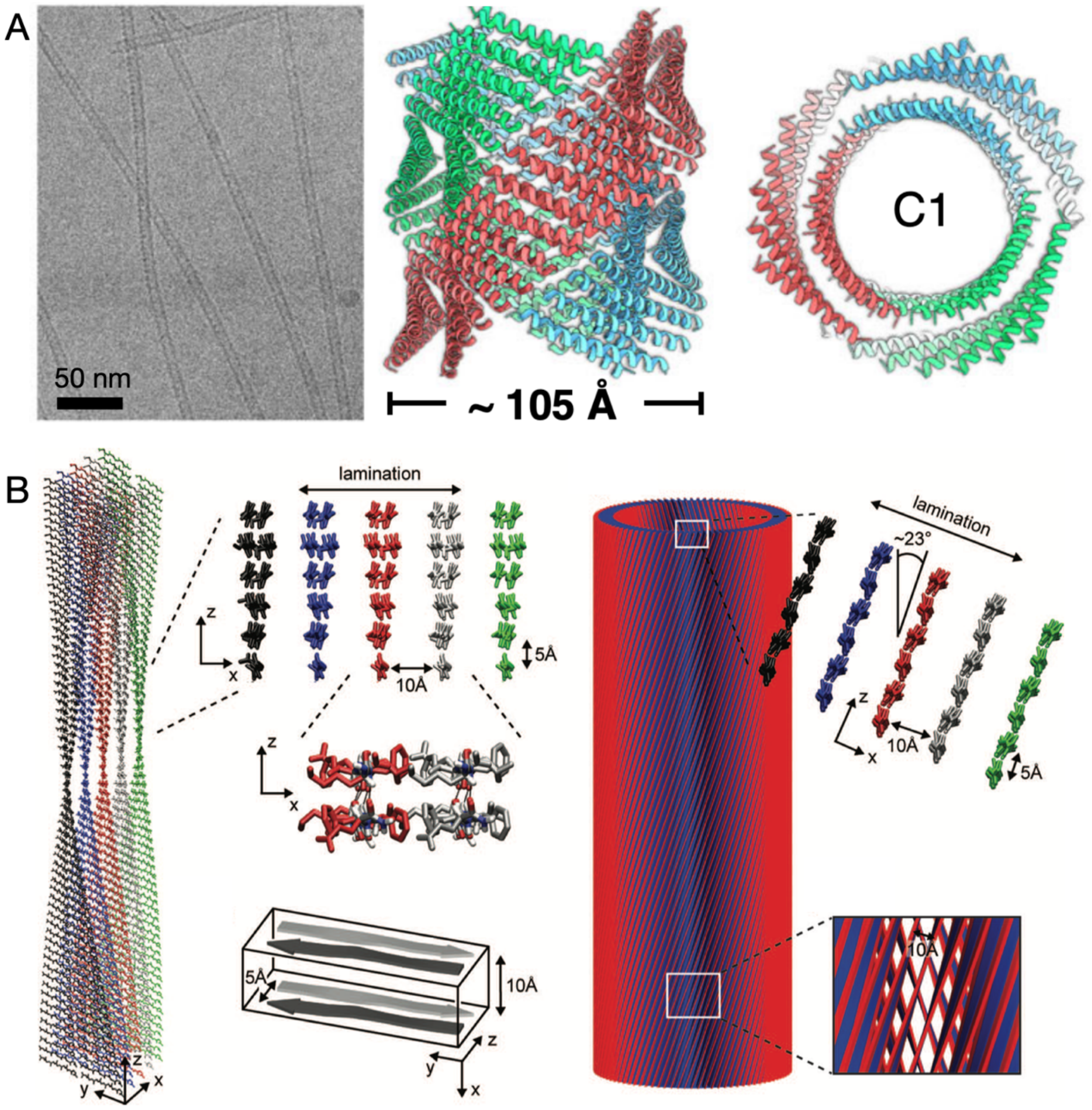

Figure 1-4. The well-ordered structures of peptide assemblies with alpha-helix (A) and cross-beta sheet (B) secondary structure. (reprinted from ref. 6 and 7)

nanoscale morphologies such as nanotubes[6-7], fibers[7], ribbons, and sheets (Fig. 1-4). For nanostructures with alpha helix, due to the interactions of charge or hydrophobic interactions at interfaces, assembly structures as in figure 1-4A[7]. The hydrogen bonding and sequence residues' side chain interactions of the cross-beta secondary structures result in long range supramolecules making nanofibers or nanotubes (Fig. 1-4B).

Especially when the laminations have high curvature, they form nanoribbons or nanotubes.

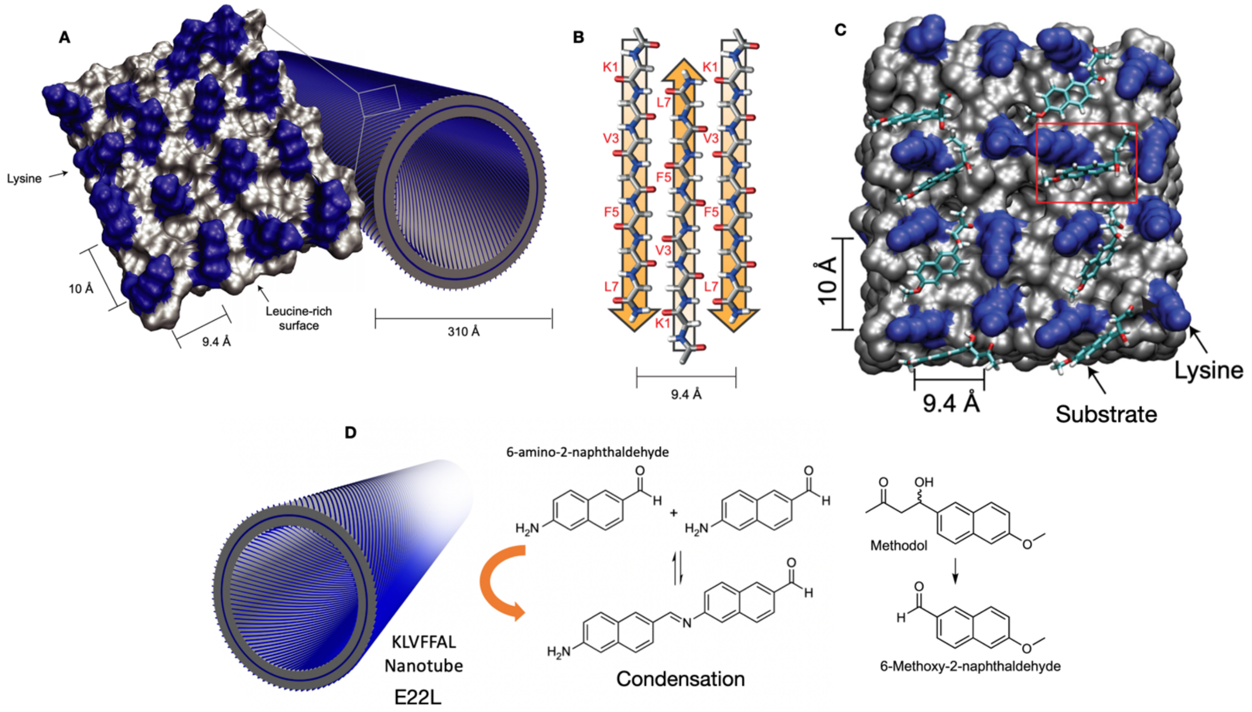

Figure 1-5. (A) A model of E22L nanotube and surface. (B) E22L sequence's anti-parallel out-of-register strand conformation. (C) A surface model with small hydrophobic molecules bound on the surface. (D) the condensation and retro-aldol reactions catalyzed by E22L nanotubes. (Ref 8)

1.3 Functions and applications of peptide self-assemblies

Because of the well-ordered structures of the peptide self-assemblies, functions arise such as enzymatic catalytic reactivities[8], piezoelectricity[9], and electronic properties[10-11]. Omosun and co-workers predicted and confirmed enzymatic catalytic reactivities of peptide self-assembly nanotubes (Fig. 1-5)[8]. The Ac-KLVFFAL-NH_2 (E22L) sequence forms nanotubes with the surface where lysine residues are exposed from hydrophobic surface (Fig. 1-5A) consists of leucine residues because of anti-parallel out-

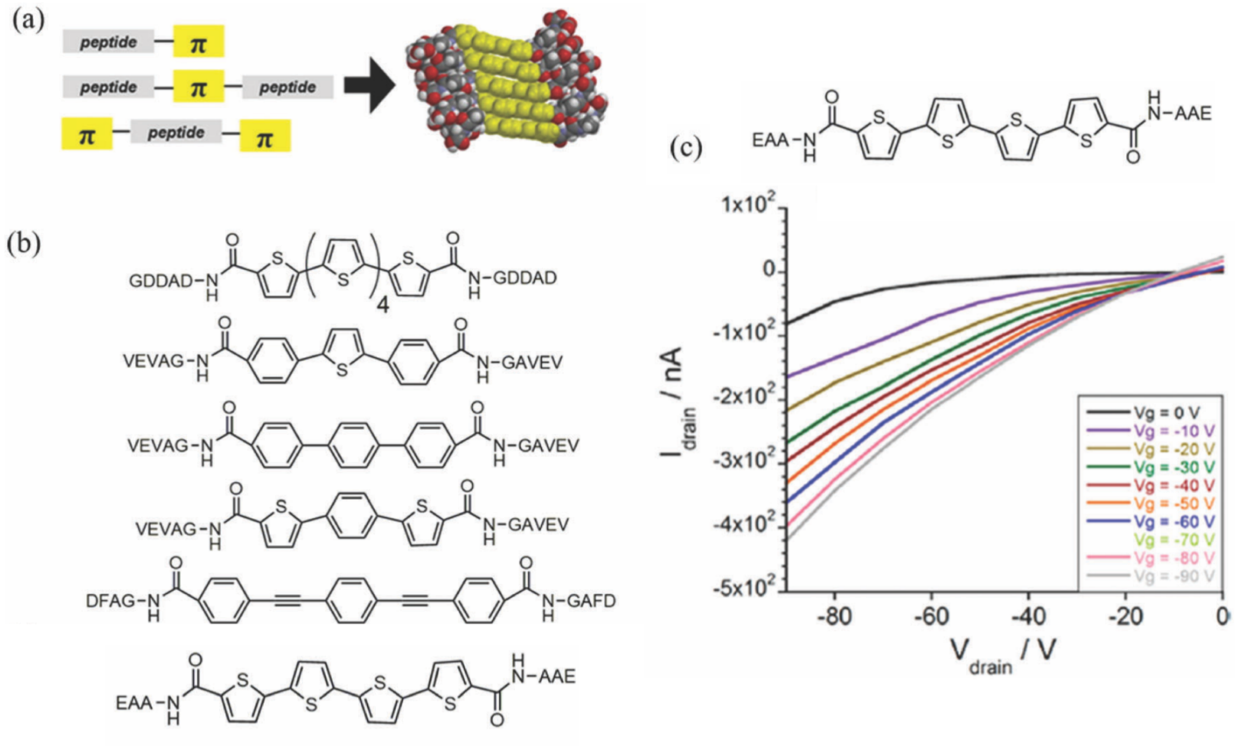

Figure 1-6. The structures of the FF based short peptides and its assembled supramolecular model, and piezoelectricity. (Ref. 11)

of-register strand conformation of the E22L assemblies (Fig. 1-5B). The researchers tested condensation and retro-aldol reactions with small hydrophobic molecules that can be bound on the hydrophobic surface (Fig. 1-5C) and found that the reactions are catalyzed by the E22L nanotubes (Fig. 1-5D). Due to the researcher's hypothesis that catalytic reactivities originate from covalent catalysis of lysine side chains. The reactivity was tested with N-terminal histidine to give greater reactivities, N-terminal lysine residues were replaced with histidine, and the nanotubes with N-terminal histidine have higher reactivities. Bera and co-workers found piezoelectricity of peptide assemblies which are diphenylalanine (Phe-Phe) based short peptides (Fig. 1-7)[9]. The hierarchically well-organized peptide assemblies can have electromechanical properties because of the supramolecular polarization. Mechanical forces changing the polarity of the material

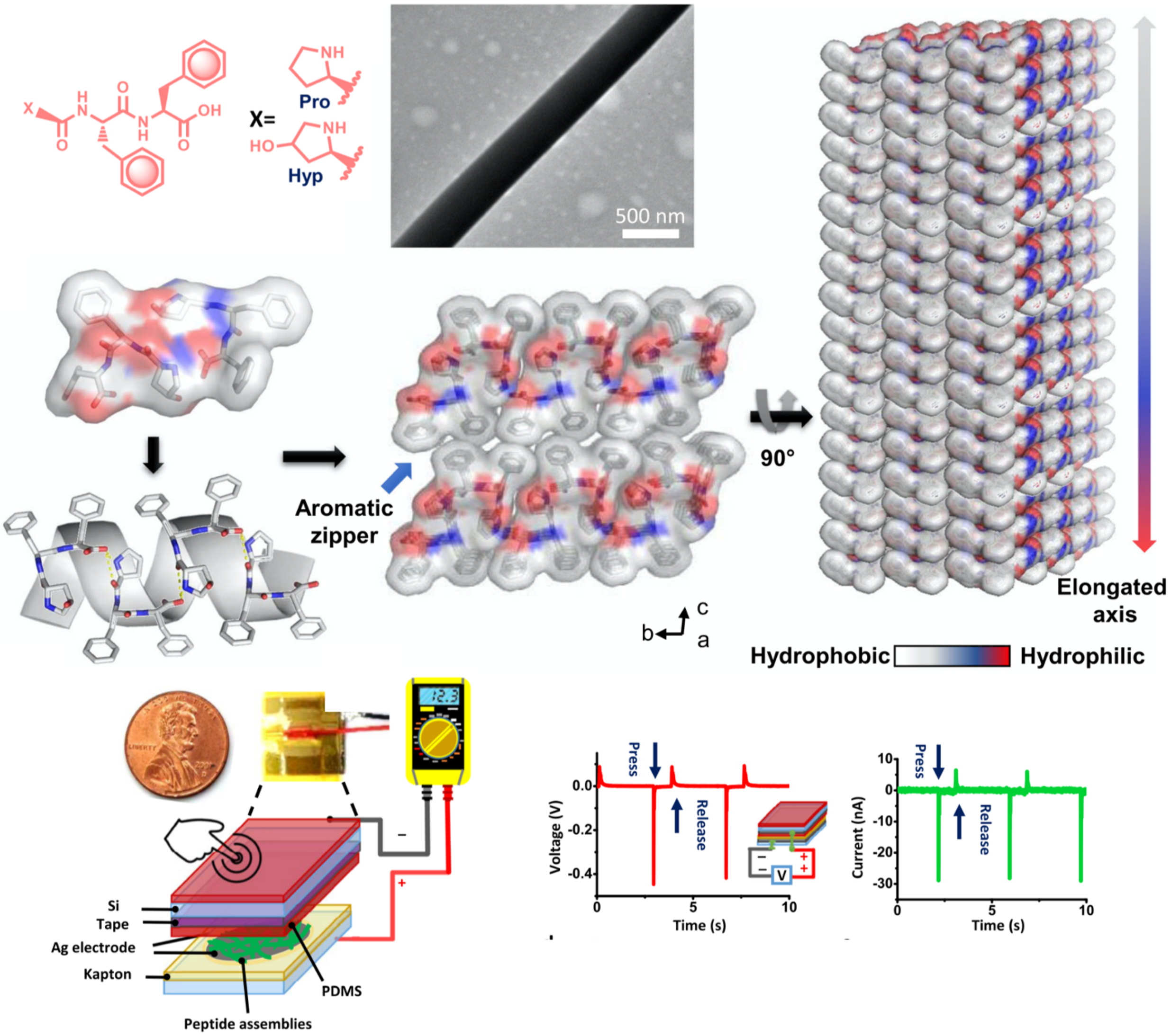

Figure 1-7. (a)Schematic of pi-conjugated peptide assemblies. (b) Different pi-conjugated groups incorporated in pi-conjugated peptides (c) Output curve of the OFET with EAA-4T-AAR peptide. (Ref. 9)

causes the piezoelectricity. The assembled structures have collagen-like helical structures, so the hydrogen bonds can be aligned. Furthermore, each helical structures can be ordered with aromatic packing interactions, called aromatic zippers, giving directional supramolecular polarity. Using this supramolecular polarity and changes of it by mechanical force, the researchers demonstrated electromechanical properties (Fig. 1-7). Moreover, Besar and co-workers designed pi-conjugated peptide assemblies for

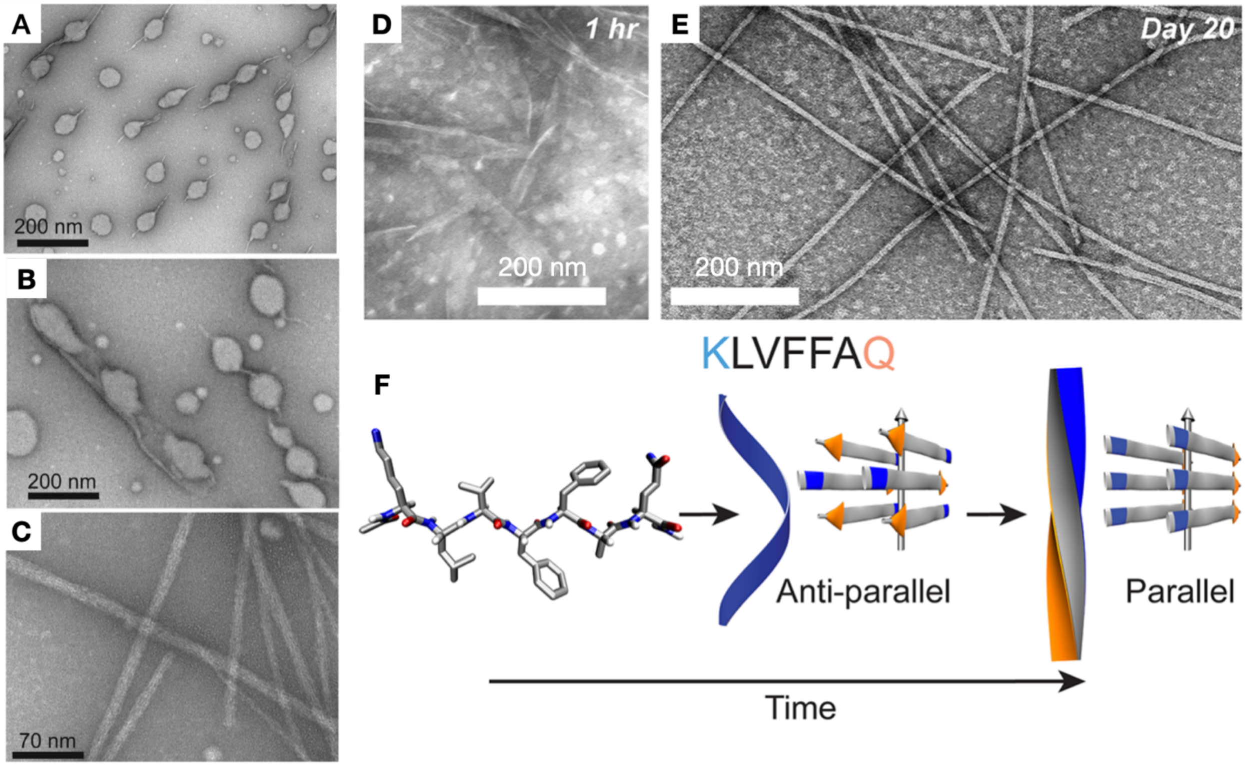

Figure 1-8. The particle phase (A), liquid-solid phase (B), and matured morphology (C) of KLVFFAE assemblies in Neutral pH at 37 degrees Celsius. Ribbon morphology with anti-parallel (D), and fiber morphology (E) of KLVFFAQ assemblies. (Ref. 21)

bioelectronics[11]. The pi-conjugated peptides have beta sheet secondary structure because the peptide sequences have propensity to form beta sheet structures so, the pi-conjugated components are well organized and exciton-coupled. Because of this couplings, the pi-conjugated peptide assembly materials can have semiconductivity that can be used for organic electronics such as organic field-effect transistors (OFETs) (Fig. 1-6). The Tovar group reported the OFETs with pi-conjugated peptides also tested resonance-energy-transfer (RET) and electron-transfer between different pi-conjugated components in the pi-conjugated assemblies, and demonstrated photovoltaic and organic electronic applications[12]. These examples the use of well-ordered hierarchical structures of peptide assembly materials for applications where the control of structure is significant to develop the applicable functions.

1.4 Control of peptide assembly structures

Since functions of peptide assemblies result from the ordered structure, control of assembly morphology is important. Many approaches to control the structures of peptide assembly materials have been reported using modifications of sequences, temperature, pH[13], external fields[14-15], solvents[16-17], and templates[18]. Peptide self-assemblies proceeds via two-step nucleation including a monomer rich biomolecular condensate step with pre-order peptide nucleation, and a liquid-solid transition step where the peptide assembly

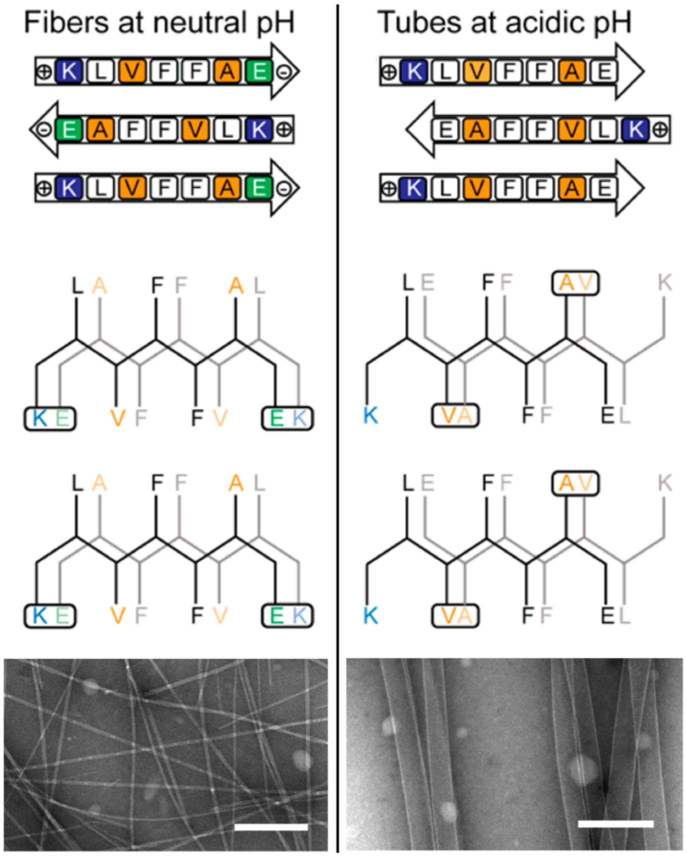

Figure 1-9 Structures and morphologies of KLVFFAE assemblies in neutral and acidic pH condition. Scale bar = 200 nm. (Ref. 22)

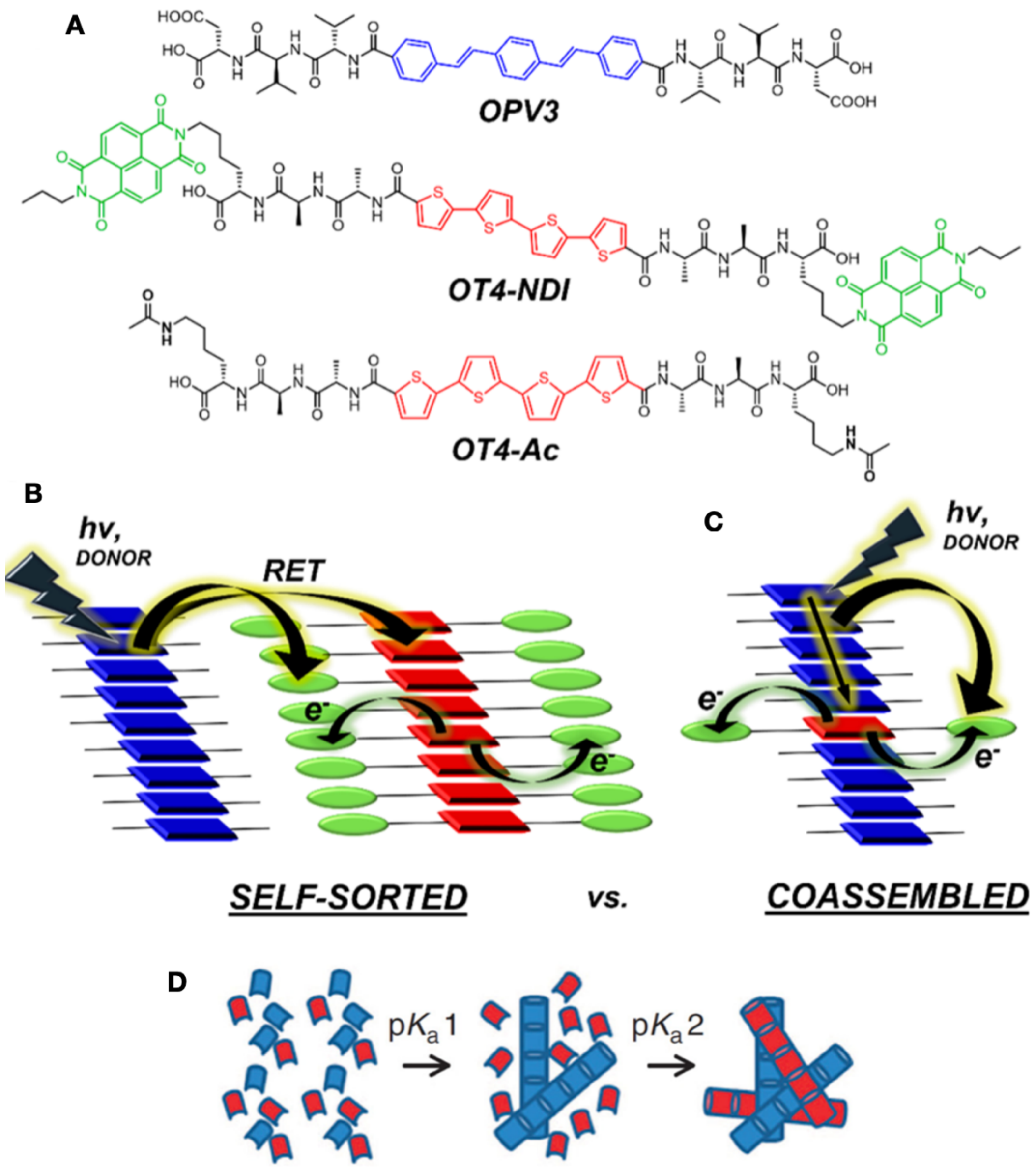

Figure 1-10. A pi-conjugated peptides. B and C diagrams of self-sorted and co-assembled assembly systems indicating different electron/energy transfer. D. self-sorting mechanism with different acidification steps (Ref. 12)

structures are propagating into nanoscale supramolecules (Fig 1-8A, B, and C)[19-20]. The pre-order nucleation can have metastable structures which converge into more stable ordered structures propagating as solid states of nano-fibers, tubes, or sheets. Therefore, controlling the metastable phase provide the key to control of the final structures. In addition, structural changes in the propagation steps are observed (Fig 1-8D, E, and F)[21],

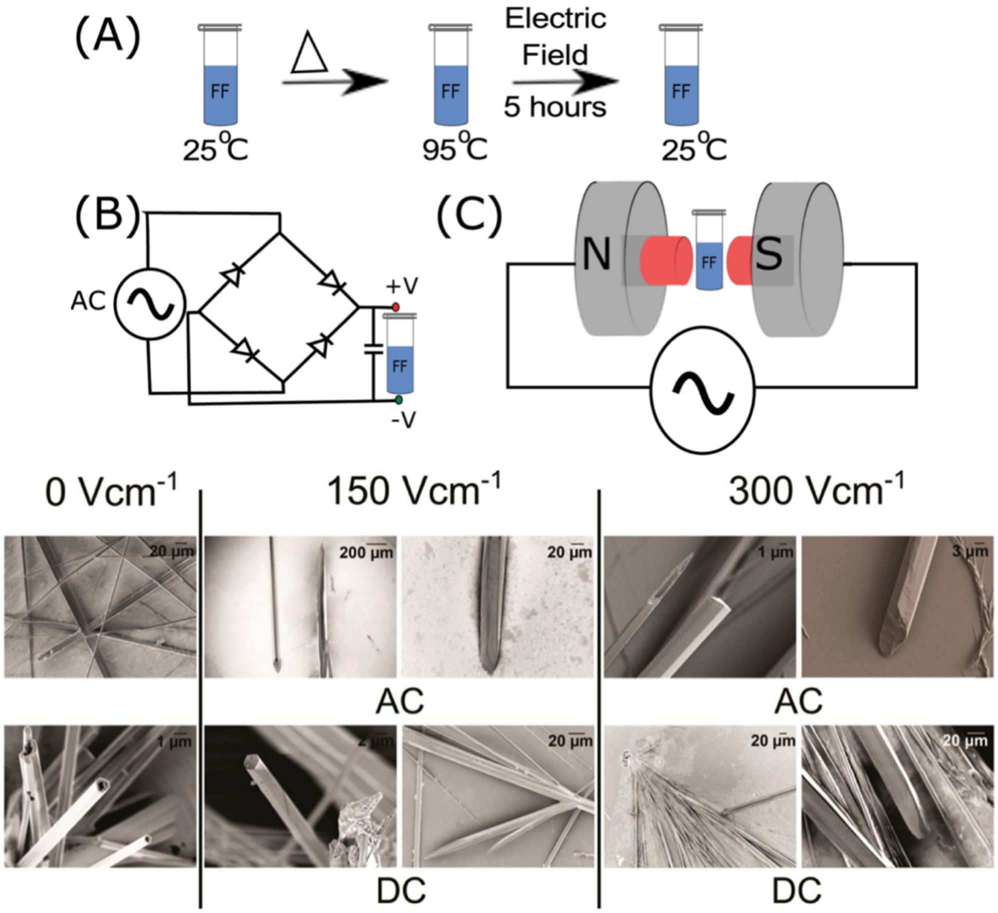

Figure 1-11. (a, b) Photographs of FF dissolved in acetonitrile solvent at 90°C and FF assemblies formed at 25°C. (c) SEM image of the FF nanowires formed in acetonitrile solvent. (d, e) Photographs of FF dissolved in acetonitrile-water solution (95:5 v/v) at 90°C and FF assemblies formed at 25°C. (f) SEM image of the FF nanowires formed in acetonitrile-water solution (95:5 v/v). (g) structure differences of FF in water and methanol. (reprinted from Ref. 16 and 17)

which indicate that there are other options to control the structures and morphologies after or during the assemblies are mature in the solid phase.

Control of pH can modify assemblies' structures and morphologies. For example, KLVFFAE sequence can have two different structures and morphologies in different pH environments (Fig. 1-9)[7, 22]. The assemblies at neutral pH form fibers, and tubes in acidic conditions, respectively. The differences result from different strand conformations that can have significant impacts on packing of strands and laminations. At neutral pH, the N-

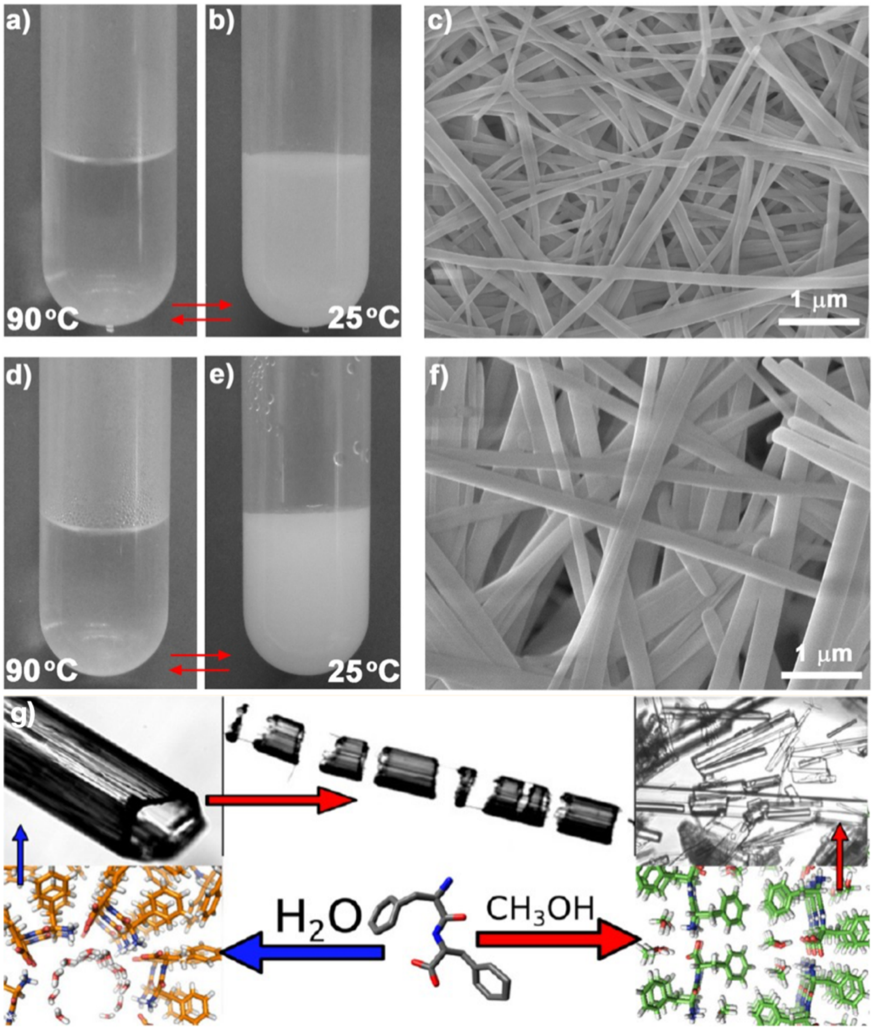

Figure 1-12. Schematic representation of experimental setup. (A) Dissolved peptide was allowed to cool down from 95 °C to room temperature while incubating in the presence of electric field. (B) Electric field set up and (C) magnetic field setup. (reprinted from Ref. 14)

terminal lysine residue protonated, and the C-terminal glutamic acids are deprotonated, and the charge-charge interactions favor in-register strand alignments (Fig. 1-9). However, in acidic condition, the glutamic acids do not have negative charges because of the acidic condition and only the lysine residues have positive charges, resulting in less stabilization when they have in-register strands. The out-of-register strand alignment was created by the facial complementary between valine and alanine, and di-phenylalanine's interactions. Mehta et. al. established the strand conformations regulated in nucleation and propagate of the macroscale morphologies[7].

Moreover, pH can be also useful to control the kinetics which involve fidelity of assemblies[12-13]. pH has significant impacts on the peptide assemblies modifying charge states of amino acid residues[22]. Charge-charge interactions between peptide strands by pH changes can change the kinetics of assembly form the assemblies[12-13]. For another Ardona et. al. constructed work, pi-conjugated peptides with aspartic acid on the both ends of peptides to control the kinetics and fidelity of the assemblies (Fig. 1-10A)[12]. The peptides are deprotonated in basic condition, having negatively charged residues that repel each other and prohibit assembly. Acidification removes the negative charges on the aspartic acid and C-terminus, allowing assembly. Modulating the rate of acidification can control both kinetics and fidelity. For example, when the rate of acidification is high, the different peptides form co-assemblies, when the rate is low, the peptides self-assembly (Fig. 1-10B and C). By using the pH controls, the researchers made two different assembly

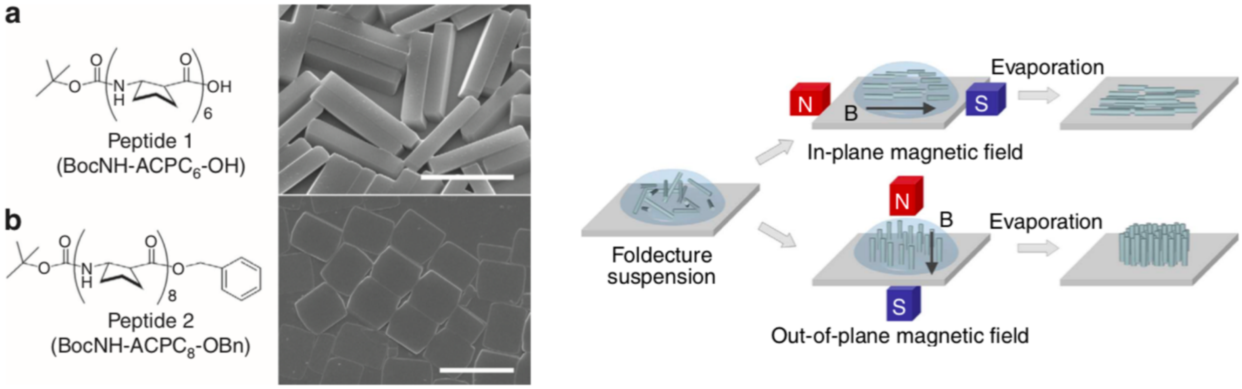

Figure 1-13. b-Peptide duilding blocks and scanning electron microscopy (SEM) images of corres ponding foldectures. (a) Peptide 1 (BocNH-ACPC6-OH) (b) Peptide 2 (BocNHACPC8-OBn). Scale bars, 5 µm. Boc, tert-butyloxycarbonyl. (c) Alignment of foldectures by static magnetic field. Schematic diagram of experimental process for alignment of foldectures under static magnetic field. (reprinted from Ref. 24)

systems with the same kinds of peptide strands. Moreover, when different acidification steps with different pK_a values are used, the self-sorting can be more efficient (Fig. 1-10D)[13]. If peptide species have different acid groups with different pK_a, adjusting the pH of the solvent can control the assemblies allowing one peptide species to be assembled while the other peptides do not form assemblies.

Solvents also have effects on the assemblies' structures and morphologies. Polarities, pKa, and hydrogen bonding ability of the solvents are factors which can modify peptide self-assemblies. Many studies have now been conducted to control and to understand the relationships between solvents and structures, morphologies, and properties of diphenylalanine self-assemblies (Fig. 1-11)[16-17].

Other studies have used external fields to modify structures and morphologies of peptide assemblies. Ramakrishnan et. al. studied electric and magnetic fields on peptide assemblies[14, 23]. They investigated the morphological changes of diphenylalanine self-assemblies by introducing electric and magnetic fields in the annealing step (Fig. 1-12)[14]. While the magnetic field did not have a significant effect on assembly, electric fields impacted both the kinetics and morphology. They also tested external field effects on the self-assemblies of the core sequence of amyloid peptide, KLVFFAE[23]. This research showed that electric field inhibits self-assembly. Amyloid beta 42 sequence was also affected by electric and magnetic fields. They hypothesized that the fields stabilized alpha helix rather than beta sheets. In addition, magnetic fields showed high impacts on assemblies which have high total dipole[15, 24]. Hill and co-workers showed strong magnetic fields arranged diphenylalanine peptide assembly nanotubes into the magnetic field direction[15]. Kwon and co-workers synthesized beta-peptide foldamers which have alpha helical secondary structures and form assemblies with rod morphologies[24]. They confirmed the movement of peptide foldamers in the direction of the magnetic field (Fig. 1-13). The effect of aromatic groups and amide groups is calculated by computational methods, demonstrating that aromatic groups' influence is significant.

Furthermore, introducing of template for peptide self-assemblies or co-assemblies also have been investigated[18]. Using the electrostatic interactions between nucleic acids and peptides, or utilizing metal binding properties of amino acids, which is described in Chapter 3.

1.5 Conclusion

In summary, like enzymes' highly efficient reactivities with high selectivity can be achieved with protein folding, understanding the fundamental non-covalent interactions of intern peptide assembly can control the functions. Fidelity/homogeneity of the supramolecular structures then become critical. Although small defects can cause serious impacts on the properties of materials, The next chapter will handle this topic and show how to identify and quantify defects on peptide self-assemblies.

1.6 References

1. Hardy, J.; Selkoe, D. J., The Amyloid Hypothesis of Alzheimer's Disease: Progress and Problems on the Road to Therapeutics. *Science* **2002,** *297* (5580), 353-356.

2. Karabıyık, H.; Sevinçek, R.; Karabıyık, H., π-Cooperativity effect on the base stacking interactions in DNA: is there a novel stabilization factor coupled with base pairing H-bonds? *Physical Chemistry Chemical Physics* **2014,** *16* (29), 15527-15538.
3. Fitzpatrick, A. W. P.; Falcon, B.; He, S.; Murzin, A. G.; Murshudov, G.; Garringer, H. J.; Crowther, R. A.; Ghetti, B.; Goedert, M.; Scheres, S. H. W., Cryo-EM structures of tau filaments from Alzheimer's disease. *Nature* **2017,** *547* (7662), 185-190.
4. Findeis, M. A., The role of amyloid β peptide 42 in Alzheimer's disease. *Pharmacology & Therapeutics* **2007,** *116* (2), 266-286.
5. Cohen, S. I. A.; Linse, S.; Luheshi, L. M.; Hellstrand, E.; White, D. A.; Rajah, L.; Otzen, D. E.; Vendruscolo, M.; Dobson, C. M.; Knowles, T. P. J., Proliferation of amyloid-β42 aggregates occurs through a secondary nucleation mechanism. *Proceedings of the National Academy of Sciences* **2013,** *110* (24), 9758-9763.
6. Wang, F.; Gnewou, O.; Modlin, C.; Beltran, L. C.; Xu, C.; Su, Z.; Juneja, P.; Grigoryan, G.; Egelman, E. H.; Conticello, V. P., Structural analysis of cross α-helical nanotubes provides insight into the designability of filamentous peptide nanomaterials. *Nature Communications* **2021,** *12* (1), 407.
7. Mehta, A. K.; Lu, K.; Childers, W. S.; Liang, Y.; Dublin, S. N.; Dong, J.; Snyder, J. P.; Pingali, S. V.; Thiyagarajan, P.; Lynn, D. G., Facial Symmetry in Protein Self-Assembly. *Journal of the American Chemical Society* **2008,** *130* (30), 9829-9835.
8. Omosun, T. O.; Hsieh, M.-C.; Childers, W. S.; Das, D.; Mehta, A. K.; Anthony, N. R.; Pan, T.; Grover, M. A.; Berland, K. M.; Lynn, D. G., Catalytic diversity in self-propagating peptide assemblies. *Nature Chemistry* **2017,** *9* (8), 805-809.

9. Bera, S.; Guerin, S.; Yuan, H.; O'Donnell, J.; Reynolds, N. P.; Maraba, O.; Ji, W.; Shimon, L. J. W.; Cazade, P.-A.; Tofail, S. A. M.; Thompson, D.; Yang, R.; Gazit, E., Molecular engineering of piezoelectricity in collagen-mimicking peptide assemblies. *Nature Communications* **2021,** *12* (1), 2634.

10. Panda, S. S.; Katz, H. E.; Tovar, J. D., Solid-state electrical applications of protein and peptide based nanomaterials. *Chemical Society Reviews* **2018,** *47* (10), 3640-3658.

11. Besar, K.; Ardoña, H. A. M.; Tovar, J. D.; Katz, H. E., Demonstration of Hole Transport and Voltage Equilibration in Self-Assembled π-Conjugated Peptide Nanostructures Using Field-Effect Transistor Architectures. *ACS Nano* **2015,** *9* (12), 12401-12409.

12. Ardoña, H. A. M.; Draper, E. R.; Citossi, F.; Wallace, M.; Serpell, L. C.; Adams, D. J.; Tovar, J. D., Kinetically Controlled Coassembly of Multichromophoric Peptide Hydrogelators and the Impacts on Energy Transport. *Journal of the American Chemical Society* **2017,** *139* (25), 8685-8692.

13. Morris, K. L.; Chen, L.; Raeburn, J.; Sellick, O. R.; Cotanda, P.; Paul, A.; Griffiths, P. C.; King, S. M.; O'Reilly, R. K.; Serpell, L. C.; Adams, D. J., Chemically programmed self-sorting of gelator networks. *Nature Communications* **2013,** *4* (1), 1480.

14. Pandey, G.; Saikia, J.; Sasidharan, S.; Joshi, D. C.; Thota, S.; Nemade, H. B.; Chaudhary, N.; Ramakrishnan, V., Modulation of Peptide Based Nano-Assemblies with Electric and Magnetic Fields. *Scientific Reports* **2017,** *7* (1), 2726.

15. A. Hill, R. J.; Sedman, V. L.; Allen, S.; Williams, P.; Paoli, M.; Adler-Abramovich, L.; Gazit, E.; Eaves, L.; Tendler, S. J. B., Alignment of Aromatic Peptide Tubes in Strong Magnetic Fields. *Advanced Materials* **2007,** *19* (24), 4474-4479.

16. Huang, R.; Wang, Y.; Qi, W.; Su, R.; He, Z., Temperature-induced reversible self-assembly of diphenylalanine peptide and the structural transition from organogel to crystalline nanowires. *Nanoscale Research Letters* **2014,** *9* (1), 653.

17. Mason, T. O.; Chirgadze, D. Y.; Levin, A.; Adler-Abramovich, L.; Gazit, E.; Knowles, T. P. J.; Buell, A. K., Expanding the Solvent Chemical Space for Self-Assembly of Dipeptide Nanostructures. *ACS Nano* **2014,** *8* (2), 1243-1253.

18. Rha, A. K.; Das, D.; Taran, O.; Ke, Y.; Mehta, A. K.; Lynn, D. G., Electrostatic Complementarity Drives Amyloid/Nucleic Acid Co-Assembly. *Angewandte Chemie International Edition* **2020,** *59* (1), 358-363.

19. Rengifo, R. F.; Sementilli, A.; Kim, Y.; Liang, C.; Li, N. X. A.; Mehta, A. K.; Lynn, D. G., Liquid-Like Phases Preorder Peptides for Supramolecular Assembly. *ChemSystemsChem* **2020,** *2* (6), e2000007.

20. Childers, W. S.; Anthony, N. R.; Mehta, A. K.; Berland, K. M.; Lynn, D. G., Phase Networks of Cross-β Peptide Assemblies. *Langmuir* **2012,** *28* (15), 6386-6395.

21. Liang, C.; Ni, R.; Smith, J. E.; Childers, W. S.; Mehta, A. K.; Lynn, D. G., Kinetic intermediates in amyloid assembly. *J Am Chem Soc* **2014,** *136* (43), 15146-9.

22. Hsieh, M.-C.; Liang, C.; Mehta, A. K.; Lynn, D. G.; Grover, M. A., Multistep Conformation Selection in Amyloid Assembly. *Journal of the American Chemical Society* **2017,** *139* (47), 17007-17010.

23. Saikia, J.; Pandey, G.; Sasidharan, S.; Antony, F.; Nemade, H. B.; Kumar, S.; Chaudhary, N.; Ramakrishnan, V., Electric Field Disruption of Amyloid Aggregation: Potential Noninvasive Therapy for Alzheimer's Disease. *ACS Chemical Neuroscience* **2019,** *10* (5), 2250-2262.

24. Kwon, S.; Kim, B. J.; Lim, H.-K.; Kang, K.; Yoo, S. H.; Gong, J.; Yoon, E.; Lee, J.; Choi, I. S.; Kim, H.; Lee, H.-S., Magnetotactic molecular architectures from self-assembly of β-peptide foldamers. *Nature Communications* **2015,** *6* (1), 8747.

Chapter 2.

Structural studies of peptide self-assemblies with cryo-EM and IE-IR

2.1-1 Introduction - cryo-EM for reconstruction of E22L peptide assembly

As mentioned in the previous chapter, functions of peptide assemblies are from its structures which are highly hierarchically ordered. Therefore, analysis and characterizations of macromolecular structures are important to design and development of desired structures and functions. Many methods and analytical techniques are used such as circular dichroism (CD), infra-red (IR), electron microscopies (EMs), diffractions with electron/X-ray beams, and other X-ray techniques. In order to get structural

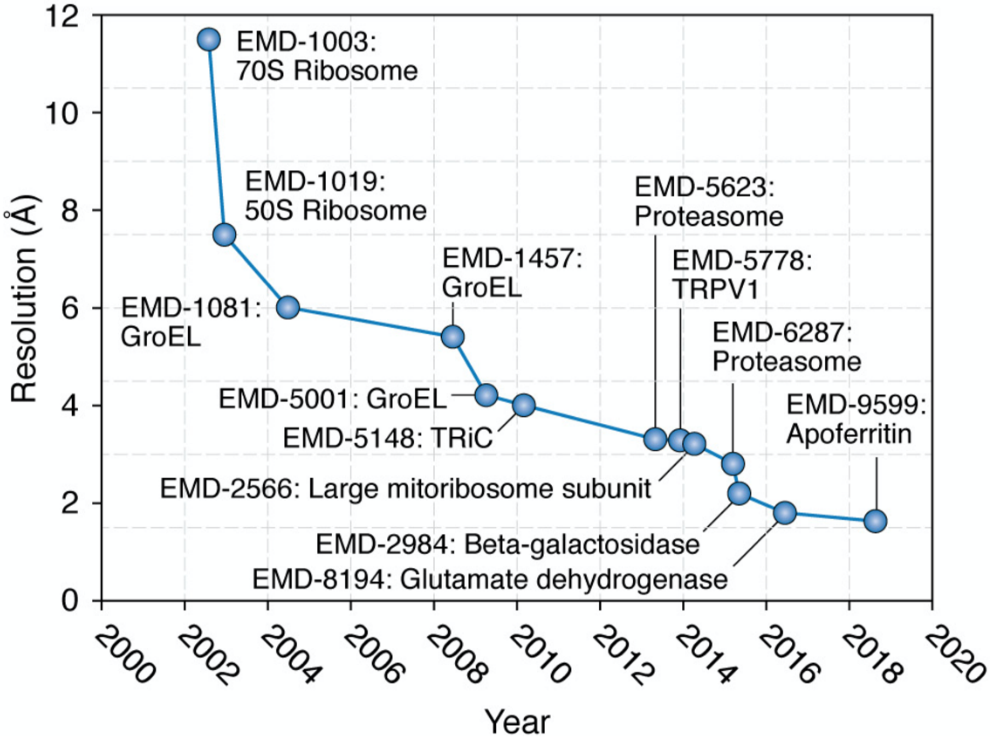

Figure 2-1. Highest resolutions for non-icosahedral specimens by year. (Ref. 7)

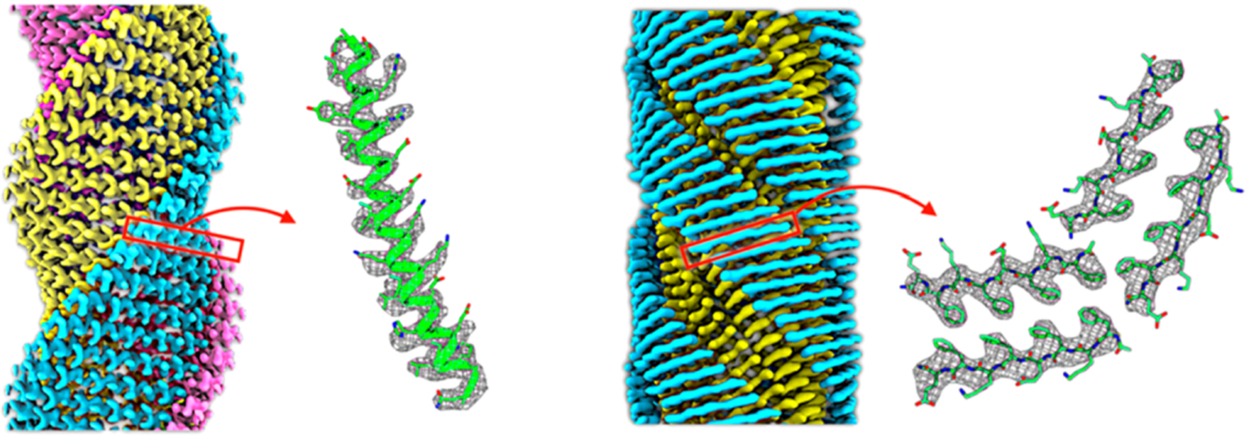

Cross-α nanotube (36-31-3 peptide, ~3.8 Å)

Cross-β nanotube (KFE8, ~3.5 Å)

Figure 2-2. a) Cryo-EM reconstruction of a cross-α nanotube at 3.8 Å resolution. The α-helices form stacks, and the three stacks forming the tube are each shown in a different color. The density from a single subunit is shown on the right as a gray mesh, and a ribbon diagram of the atomic model has been fit into this density. (b) Cryo-EM reconstruction of a cross-β nanotube at 3.5 Å resolution. Ref[1-2].

information with high resolutions, X-ray crystallography is commonly used for biomaterials such as proteins, and viruses[3-5]. However, since X-ray crystallography requires fine crystals of target materials, this technique is not available for peptide assemblies that cannot form fine crystals[6-7]. As an alternative and a new method for high resolution data, cryogenic electron microscopy (cryo-EM) techniques have been developed and used[6-7]. Because the samples are preserved at near native condition in a thin ice film that is amorphous in grids, it is beneficial and powerful for structural studies. Cryo-EM has been rapidly developed and reached under 3 Å resolutions (Fig. 2-1)[7].

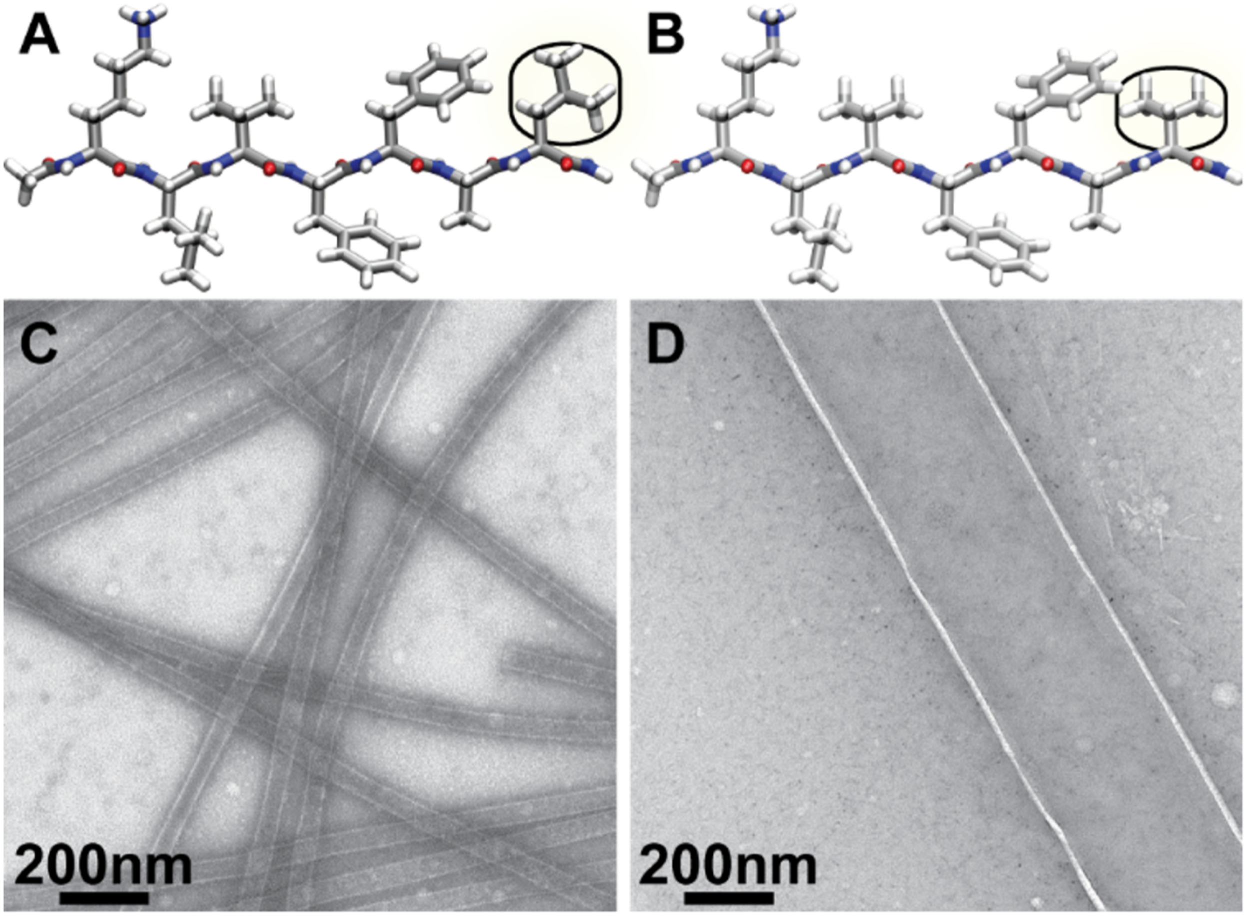

Figure 2-3. Structures of (A) Ac-KLVFFAL-NH2 (E22L) and (B) Ac-KLVFFAV-NH2 (E22V) peptides and the corresponding TEM micrographs of each peptide assembled (1.3mM) in 40% acetonitrile containing 0.1% TFA, (C) Ac-KLVFFAL-NH2 (E22L) and (D) Ac-KLVFFAV-NH2 (E22V).

That high resolutions allow amino acid residues' position and conformations to be defined (Fig. 2-2)[1-2],. For example, only one carbon chain (a methylene) difference on the C-terminal residues in Ac-KLVFFAL-NH2 (E22L), and Ac-KLVFFAV-NH2 (E22V) makes huge morphological and spectroscopical differences (Fig 2-3). Both E22L and E22V form nanotubes but they have different diameters: E22L's diameter is ~38 nm and E22V has ~279 nm diameter. In addition to this, they show nearly opposite cotton effect signatures (Fig 2-4). E22L shows left-hand twisted beta sheet structure, and E22V has right-hand

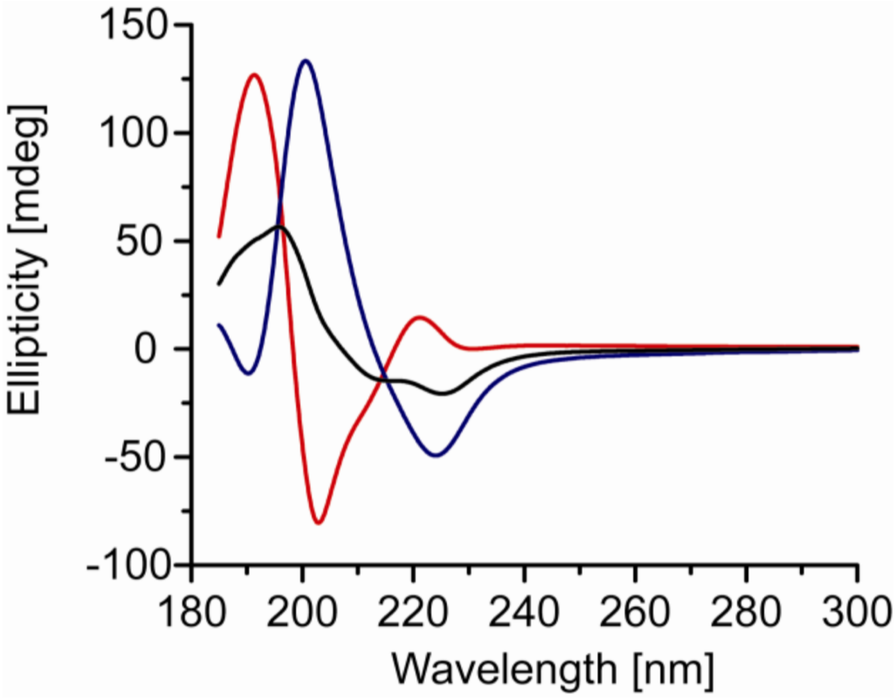

Figure 2-4. CD spectra of E22L (blue), E22V (Red), and 1:1 mixture of E22L and E22V (black)

twisted beta sheets[8]. Why and how these two different sequences form significantly different nanotubes remain unknown, because conventional methods like CD, IR, and diffractions cannot provide details of side chains conformations and X-ray crystallography is not available. Therefore, cryo-EM, that can give high resolution information data and reconstructed models is explained this chapter, a reconstructed model, which has not reached a final outcome, is shown and detailed procedures are explained for next junior lab members.

2.1-2 Results and Discussio

2.1-2.1 Optimization of sample vitrification and a model of E22L nanotubes

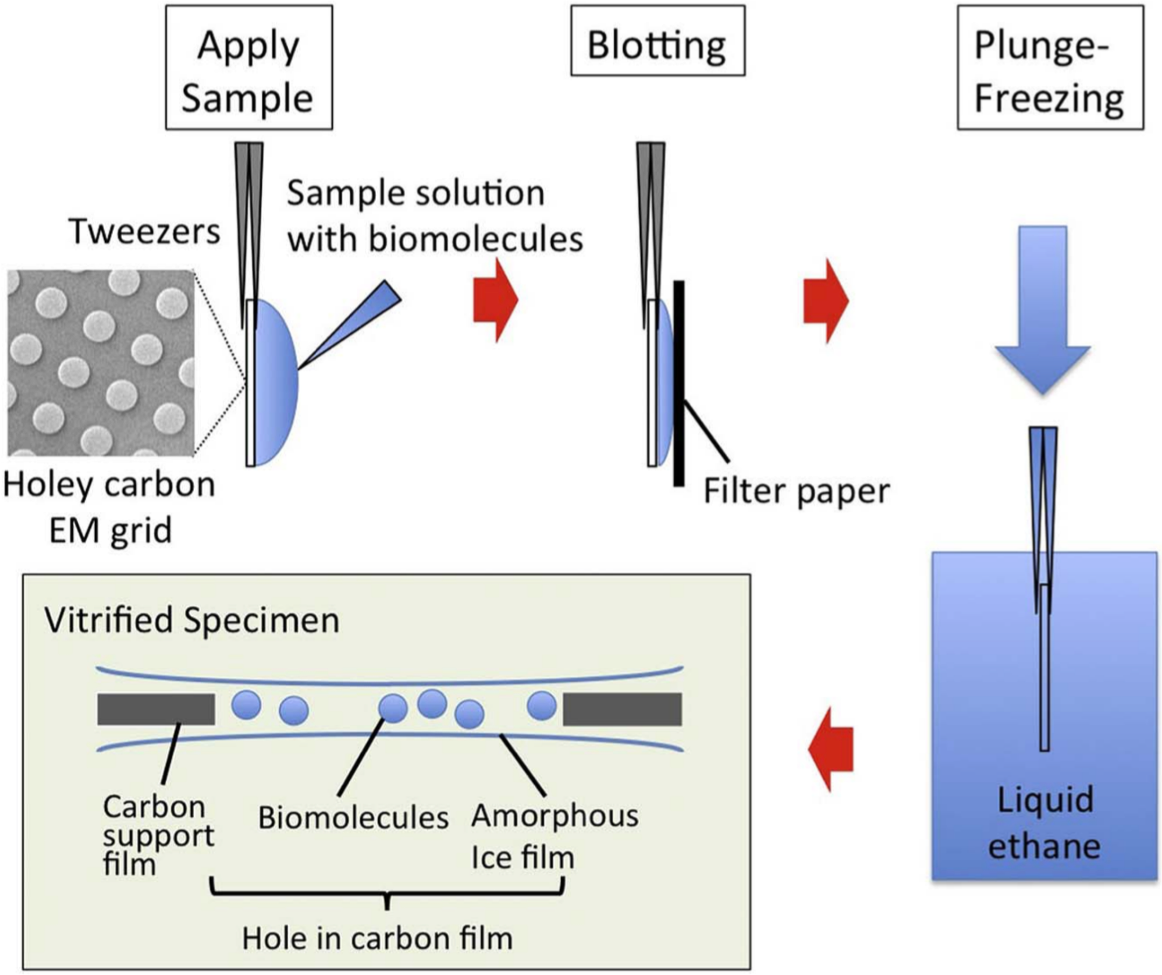

Figure 2-4. A sample preparation by plunge-freezing. Aqueous sample solution is applied onto glow-discharged (hydrophilic) holey carbon film supported by EM grid. Excess solution is removed with filter paper from one or both sides. Blotted grid is rapidly plunged into a cryogen precooled at liquid nitrogen temperature. Biomolecules embedded in thin amorphous ice film are observed in cryo-electron microscope. Ref[6]

In order to take images with cryo-EM, vitrification of the sample in holey carbon grids is required[6], because ice crystal formation can damage the samples and interrupt imaging with electron beams. The vitrification includes very fast freezing of samples with

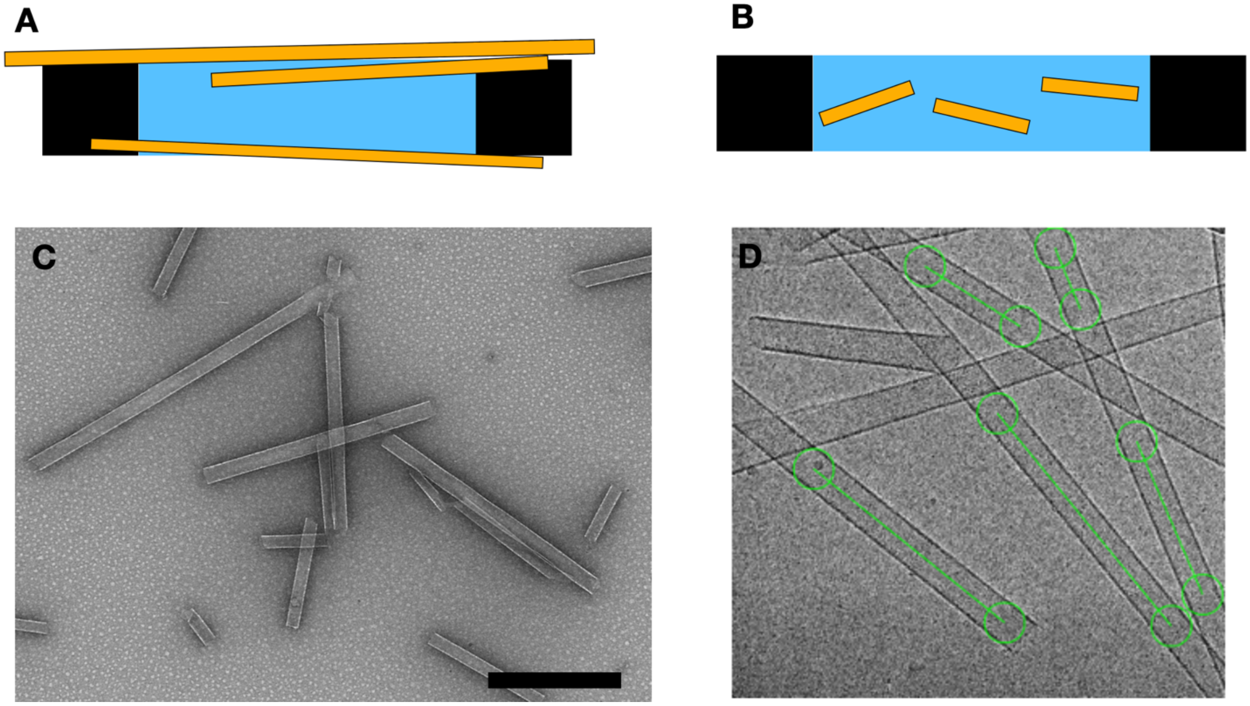

Figure 2-5. A possible case of vitrificated sample without shortening (A) and with shortening (B). Yellow: peptide assemblies, Black: carbon supports of grids, and Blue: ice film. (C) a TEM image of shortened nanotubes. The scale bar is 500 nm. (D) manually picked nanotubes for image processing.

liquid ethane and liquid nitrogen, so it minimizes forming ice crystals. The vitrified samples should be within the amorphous ice in holes (Fig 2-4), but E22L nanotubes are long enough to be out of the ice film (Fig 2-5A). Therefore, shortening of the nanotubes were conducted with sonication to fit the ice film. The E22L nanotubes were formulated with 2 mM peptide in 40% of acetonitrile and 0.1% of TFA in water with pH 2 for about 2 weeks. The 100 uL of matured assembly solution was transferred to a 1.5 mL centrifuge tube and sonicated (probe sonication) for one second with lowest intensity. The sonicated solution was centrifuged at 4000 RPM for 10 minutes at 4 °C and the supernatant (98 uL) was removed to discard fragmented assemblies, aggregations, or immatured assemblies. Right before vitrification 2 uL of residues was resuspended with 98 uL of pure water. A

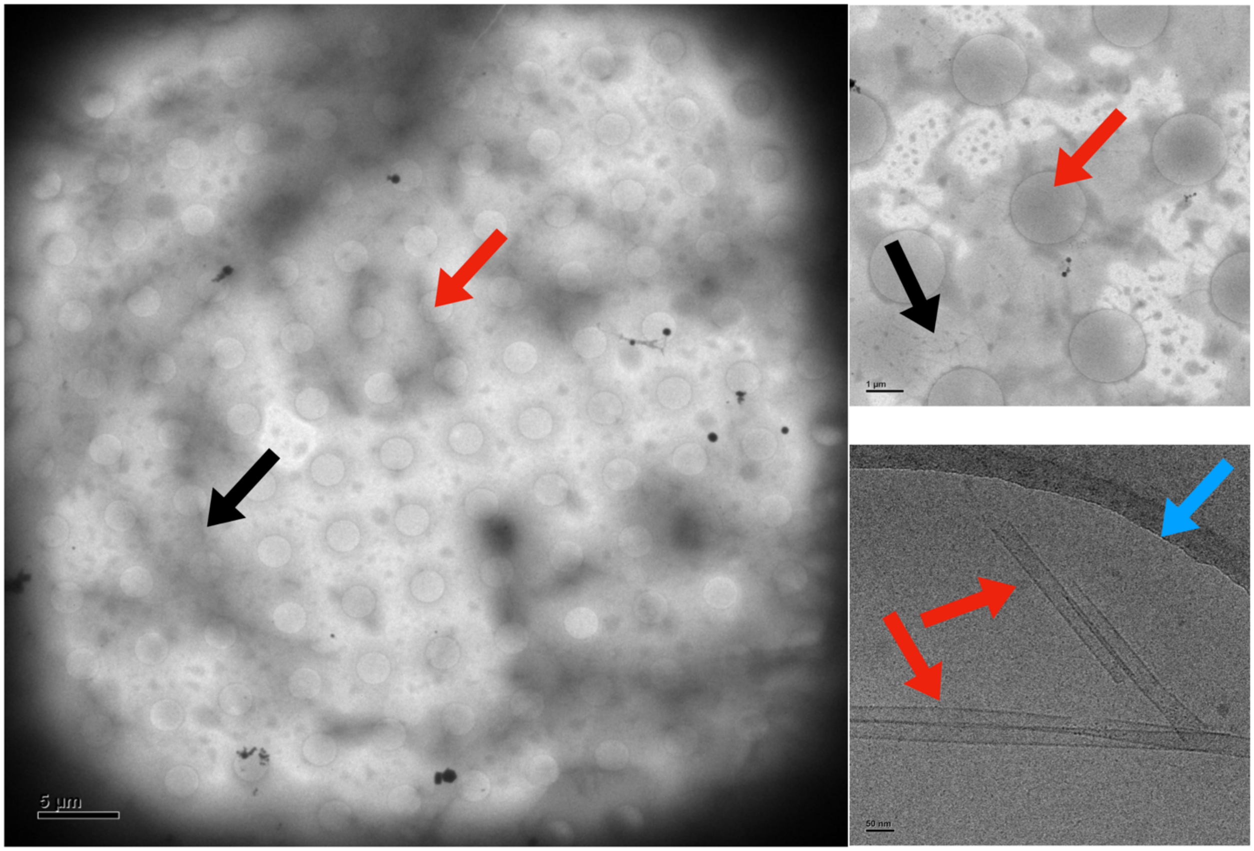

Figure 2-6. EM images of vitrificated samples on grids. Black arrows indicate nanotubes out of the holes, red arrows indicate nanotubes in holes, and blue arrow shows a boundary between a hole and carbon support.

TEM image of shortened E22L nanotubes is shown in figure 2-5C. In the vitrification steps, 3 uL of the resuspended assembly solution was spotted on a grid and blotted for 1.5 seconds with -10 force. Before it was used, the grids were negatively glow discharged. After sample preparation with vitrification, EM images were taken to check the ice quality and the existence of nanotubes in holes. Through the screening, the factors such as sonication intensity, centrifuge intensity, blotting time, and force were optimized. The nanotubes were found in relatively thick ice film which is depicted in gray area in figure 2-6. Although many nanotubes are preset on the carbon support of the grid rather than in the holes, some of the nanotubes in the hole are found. The images were processed by

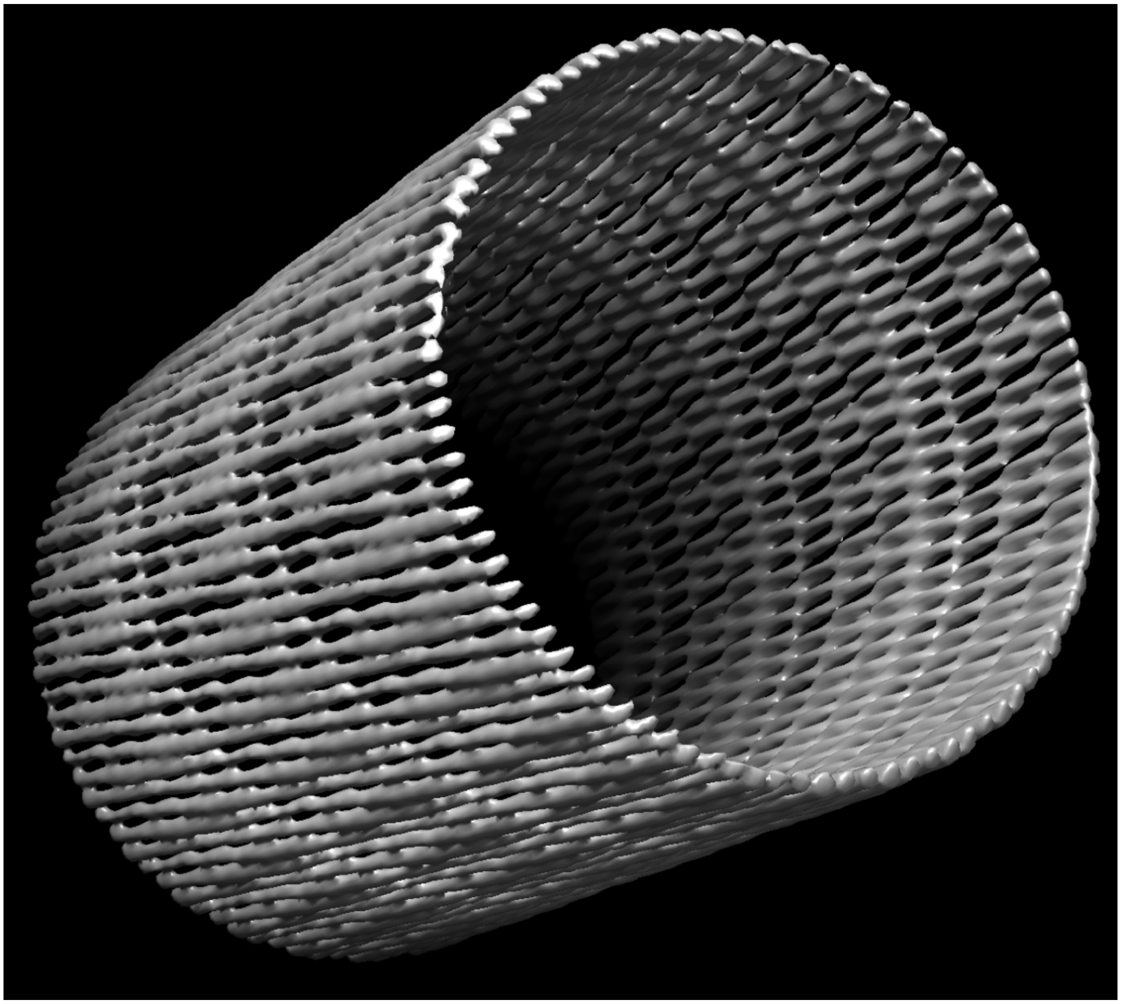

Figure 2-7. A model of E22L nanotube processed by Relion with cryo-EM images. Resolution is 5.29 Å.

Relion, the program for reconstruction of models from cryo-EM images. Within the process, fine nanotubes that are not overlapping each other are collected (Fig. 2-5D). The series of processing steps gave a primary model with 5.29 Å resolution was reconstructed (Fig. 2-7). Although a final model with high resolution could not be reconstructed in my period, the primary model shows the beta sheet lamination patterns which have 10 Å gaps (to compare, see figure 1-4B). The final desired resolution is less than 3 Å, so that the specific positions of amino acid residues can be specified to reveal what makes the difference between E22L and E22V.

2.2-1 Introduction - IR studies of peptide assemblies for detection of defects.

(Collaborated with Samuel Ban-Seok Jeong, Chen Liang, Brian Dyer, and David G Lynn, Departments of Chemistry and Biology, Emory University,)

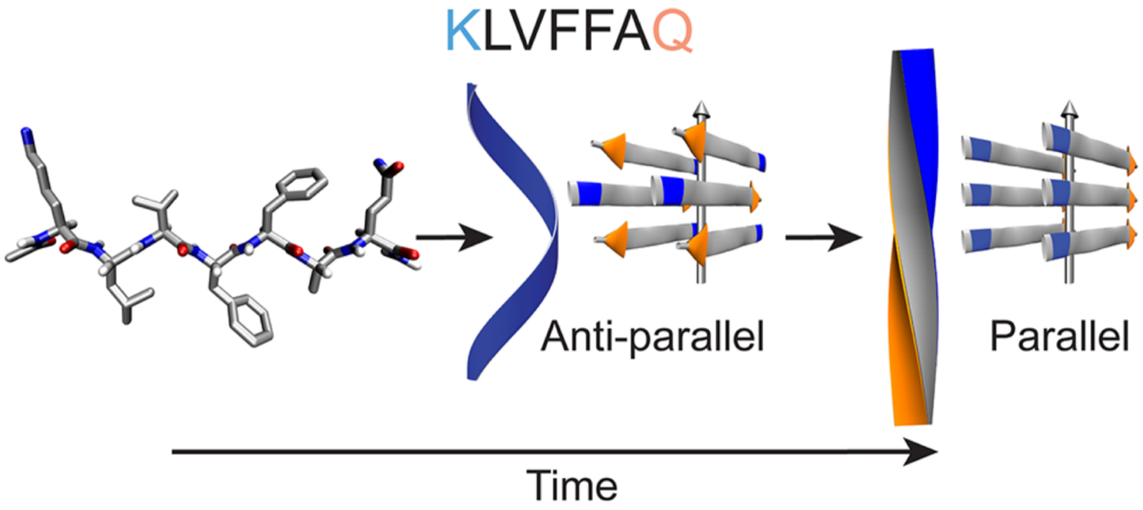

Figure 2-8. Model for the progressive transitions observed for E22Q. Paracrystalline forms emerge under these conditions as ribbons with antiparallel out-of-register β-strands. A subsequent transition to fibers is observed with parallel in-register strands. In cartoons, blue represents lysine residues, and orange represents glutamine residues. (Ref. 15)

Defects in materials have significant impacts on functions of the materials. Defects are frequently found in semiconductors with dopants which are intentionally added to give pathway where electrons/holes travel. Spider silk fibers also have heterogeneous paracrystallinity to generate flexibility[9-10]. Defects, however, are generally not preferred and they can result in cause critical flaw or material failes[10-11]. Although controls of defects have been studied[12-13], characterizing or detecting defects is limited because most spectroscopic analyses averaged the overall material. Defects or heterogeneity of peptide assembly systems also have been reported[13-14] and in this study, we report detection of defects in assembly strand conformations.

IR simulations have been developed with density functional theory (DFT) calculations and transition dipole coupling (TDC). Isotope edited infrared spectroscopy (IE-IR) allows for structural information of peptide assemblies with site-specific vibrational mode[15-19], inter-strand long-range coupling in beta-sheets[20-21], registry alignment[22], and strand directionality[23-25] to be assigned. However, taken together, these methods allows for empirical validation of beta sheet assemblies.

Ac-KLVFFAQ-NH_2 (E22Q), which consists of a hydrophobic core, LVFFA, and hydrogen bonding C-terminal glutamine residue assemble via 2-step nucleation via biomolecular condensation with secondary liquid-solid nucleation forming nanoribbons with out-of-register anti-parallel strand conformation (Fig. 2-8)[15, 26]. The assembly has third transition to nanofibers with in-register parallel strand conformation. The transitions and structures are confirmed by extensive studies with IE-IR, ssNMR, XRD, and CD analysis[15, 26]. Using the advantages of E22L where anti-parallel, and parallel strand alignments are observed in the same simple sequence, simulations of vibrational excitons couple were used to identify conformational defects in the different paracrystalline forms.

2.2-2 Results and discussion

2.2-2.1 IE-IRs of E22L and IR-simulation with transition dipole coupling

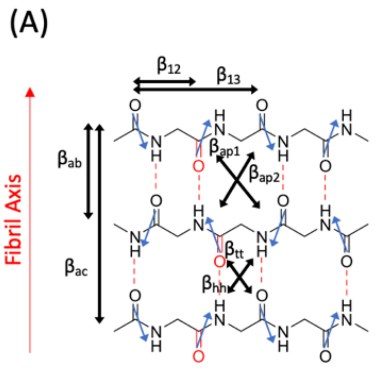

(B)

β (cm^{-1})	Even	Odd
β_{12}^{*}	3.2 (-2.5)	3.2 (-2.5)
β_{13}	2.1	2.1
β_{ab}	-11.8	-12.3
β_{ac}	-1.4	-1.4
β_{ap1}	-5.0	-3.1
β_{ap2}	1.0	1.1
β_{hh}	3.1	3.3
B_{tt}	5.7	7.0

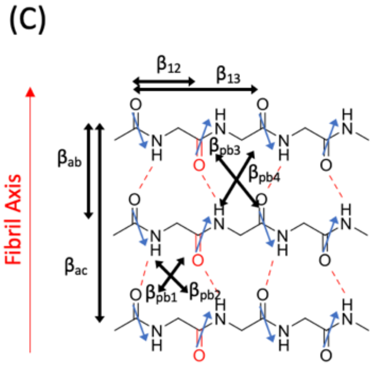

(D)

β (cm^{-1})	
β_{12}^{*}	3.2 (-2.5)
β_{13}	2.1
β_{ab}	-11.2
β_{ac}	-1.4
β_{pb1}	0.2
β_{pb2}	2.2
β_{pb3}	0.1
β_{pb4}	2.2

Figure 2-9. (A) Structure and transition dipoles of perfectly ordered anti-parallel β-sheet. (B) The main coupling constants, β, for an anti-parallel β-sheet either formed from even number or odd number of amide bonds in a β-strand when in-register configuration is assumed. (In out-of-register configuration, this is switched) (C) Structure and transition dipoles of perfectly ordered parallel β-sheet. (D) The main coupling constants, β, for an parallel β-sheet.

Infrared mode simulations and transition dipole coupling were calculated in collaborated with Dr. Samuel Ban-Seok Jeong with open-source MATLAB program employed the coupled oscillator spectrum simulator (COSMOSS). The Ramachandran angles for the simulations were set at φ = –119° and ψ = 113° and hydrogen bond angle (C=O---H) of ~150°, as the idealized beta-sheet structure[27-28]. Transition dipole coupling

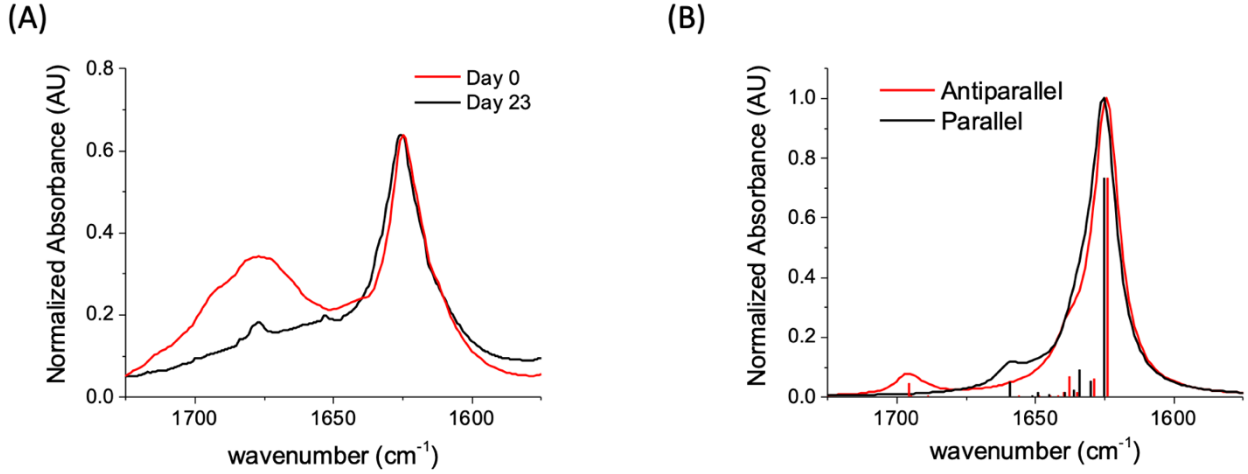

Figure 2-10. ATR FT-IR of Aβ(16-22)E22Q assembled at acidic pH (0.1% TFA) in 20% CH$_3$CN. (A) In day 0, anti-parallel β-sheet structure grows first. Then, it slowly makes a transition to parallel β-sheet structure results in the spectrum of pure parallel β-sheet in day 23. (B) The simulated spectra of non-labeled Aβ(16-22)E22Q peptide in antiparallel or parallel β-sheet structure. Each vibrational mode was depicted as a bar graph.

constants of amide bonds in anti-parallel and parallel conformations were assigned by previous research including TCD modeling and Jansen maps (Fig. 2-9)[29-31]. The couplings directed perpendicular to the direction of the beta-strands shows strong coupled modes and large coupling constants while other coupling modes, including lateral and diagonal couplings. The simulation results are validated by experimental IR spectra analysis of E22L peptide assembly with a single ^{13}C enrichment at each of the L17, V18, F19, F20, and A21 amino acid position for isotope edited analysis.

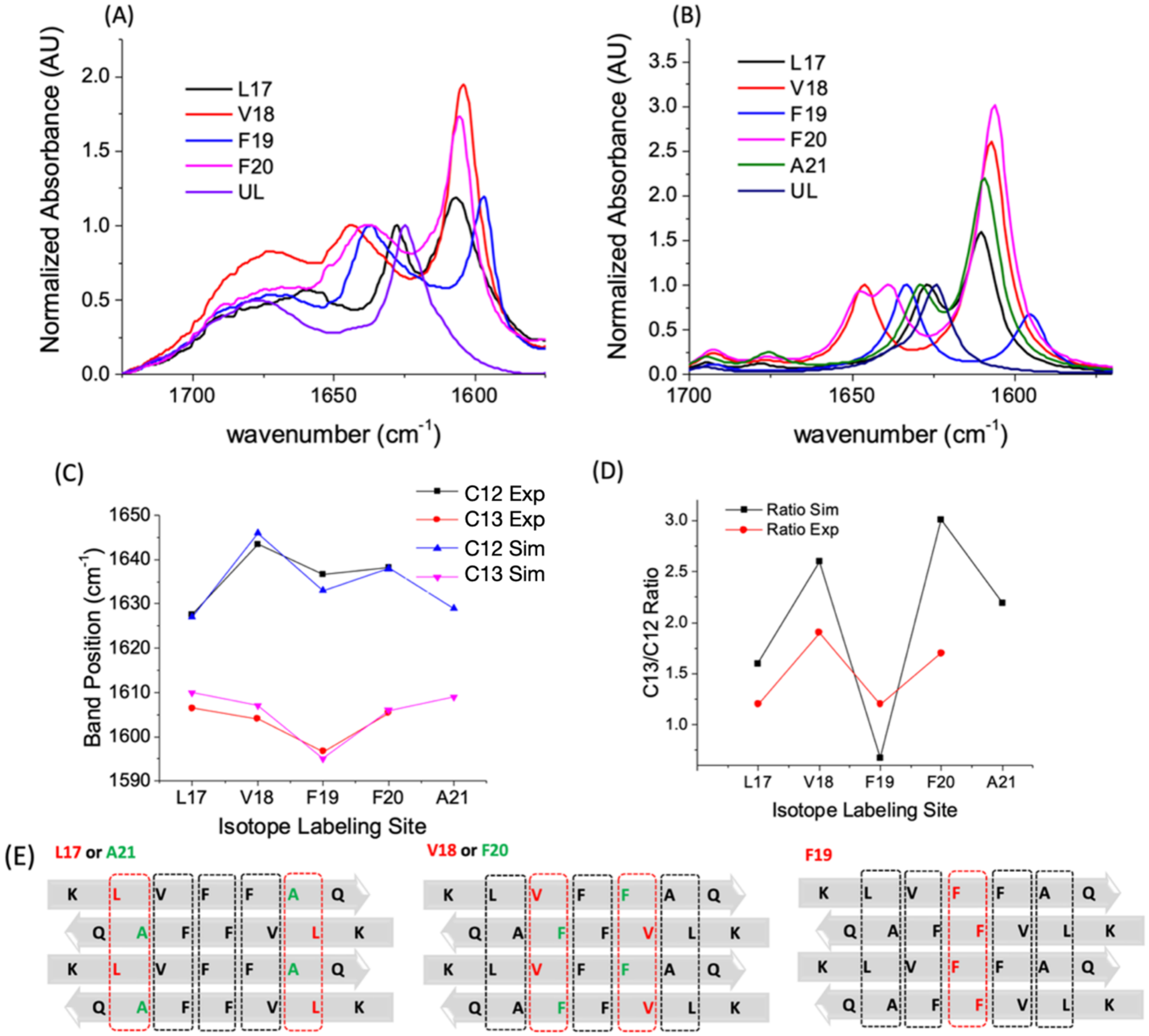

Figure 2-11. IE-IR spectrum of Aβ(16-22)E22Q assembled as anti-parallel out-of-register b-sheets. The amide region of each IR spectra are shown with isotope enrichment in the backbone carbonyl of the indicated amino acid. (A) spectra normalized to the ^{12}C band (B) simulated spectra normalized to the ^{12}C band. (C) The comparison between experimental and simulated ^{12}C main band and ^{13}C isotopic band position, and (D) intensity ratio between 13C band maxima and ^{12}C band maxima in various positions of ^{13}C isotope labeling. (E) The proximity of the transition dipoles in anti-parallel β-sheet labeled by ^{13}C amides in various position. Amino acids in black are ^{12}C amides, while the colored amido acids, with red and green, are ^{13}C amides.

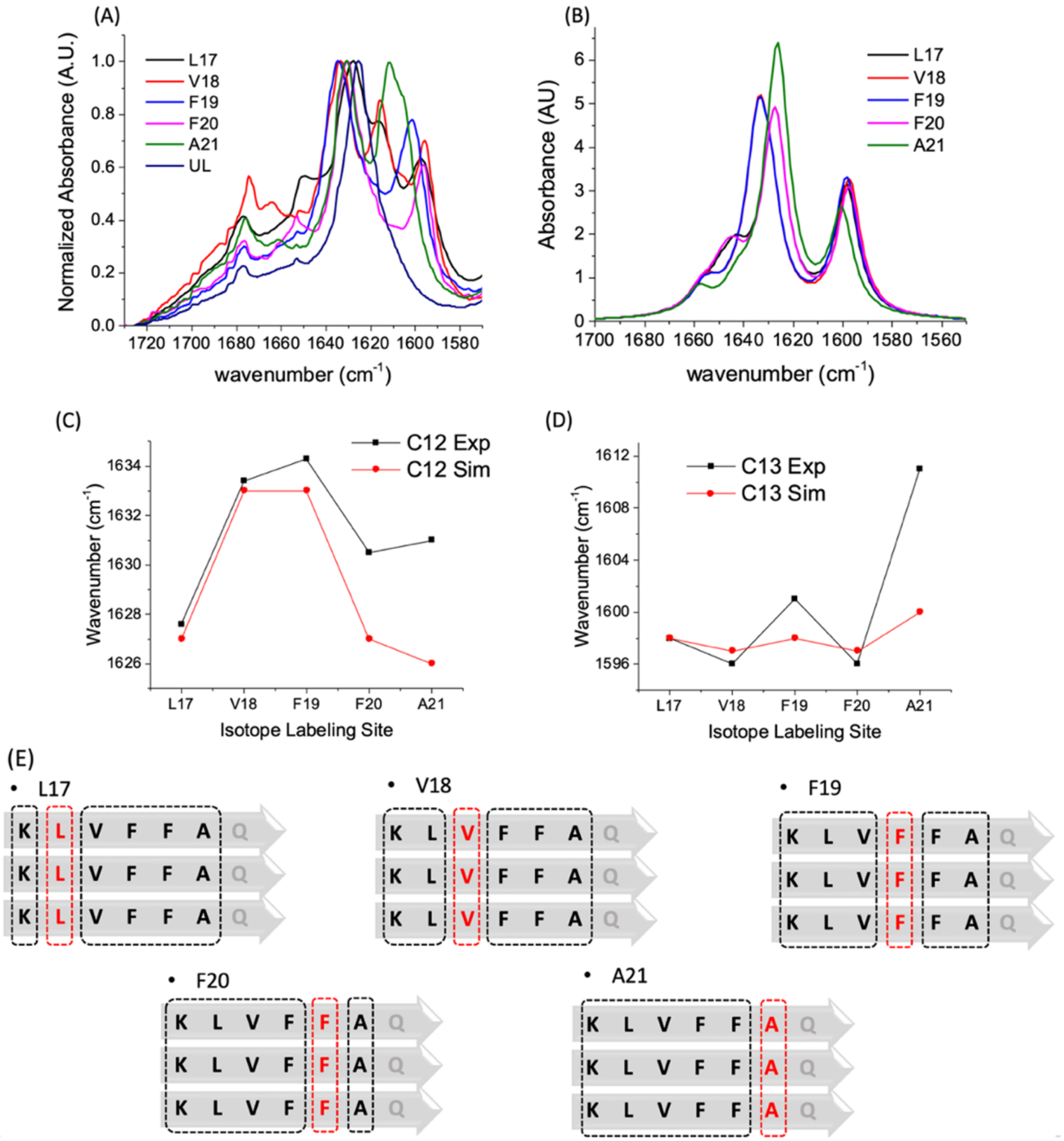

Figure 2-12. IE-IR spectrum of Aβ(16-22)E22Q assembled as parallel in-register β-sheets. The amide region of each IR spectra are shown with isotope enrichment in the backbone carbonyl of the indicated amino acid. (A) spectra normalized to the ^{12}C band (B) simulated spectra normalized to the ^{12}C band. (C) The comparison between experimental and simulated ^{12}C main band position, and (D) and ^{13}C isotopic band position. The geometry of transition dipole couplings in parallel β-sheet labeled by ^{13}C amide in various position.

Without isotope labeling, the IR spectra of anti-parallel and parallel conformation of E22L assemblies show similar main bands position at 1624 cm^{-1} for anti-parallel and 1626 cm^{-1} for parallel (Fig 2-10A). The strong main bands indicate exciton delocalization along the E22L fiber backbones which is hydrogen bonding directions. IR simulations of the anti-parallel and parallel of beta sheets also present the main bands at around 1625 cm^{-1} with strong intensities. The small peaks in the simulation are from lateral couplings of hydrogen bonded amides which are parallel to the peptide strands. However, these modes have weak intensities, so it is often hard to observe because of baseline noise, or other modes such as the sidechains' modes. For instance, the peak at 1676 cm^{-1} is from glutamine's sidechain mode that is strong enough to cover the lateral modes.

The isotope labels in different positions of the peptide backbone (^{13}C=O) changes the vibrational network, showing frequency shifts and intensities of the bands of amide couplings with ^{13}C and ^{12}C. The IR spectra of E22L assembly and simulations of anti-parallel beta sheet shows well matched trends of band positions (Fig. 2-11A, B and C). The peptide assembly with ^{13}C labeling at F19 position shows most red shifted 13C band because as described in figure 2-11E it has best aligned ^{13}C carbonyls with maximized vibrational exciton delocalization, while other peptide assemblies with different ^{13}C positions have alternative carbonyls with ^{13}C and ^{12}C. In addition to this, the F19 isotopomer's aligned ^{13}C carbonyls are coupled with neighbor ^{12}C amides, having more red-shifted band. The other isotomers' linear chains of alternating ^{13}C and 12C carbonyls have ~ 1612 cm-1 bands, but the alternative amides of V18 and F20 are sandwiched by ^{12}C amides so V18 and F20 have more red-shifted main bands than L17 and A21 isotopomers that have only one side lateral coupling with 12C amides. 12C main bands also show the

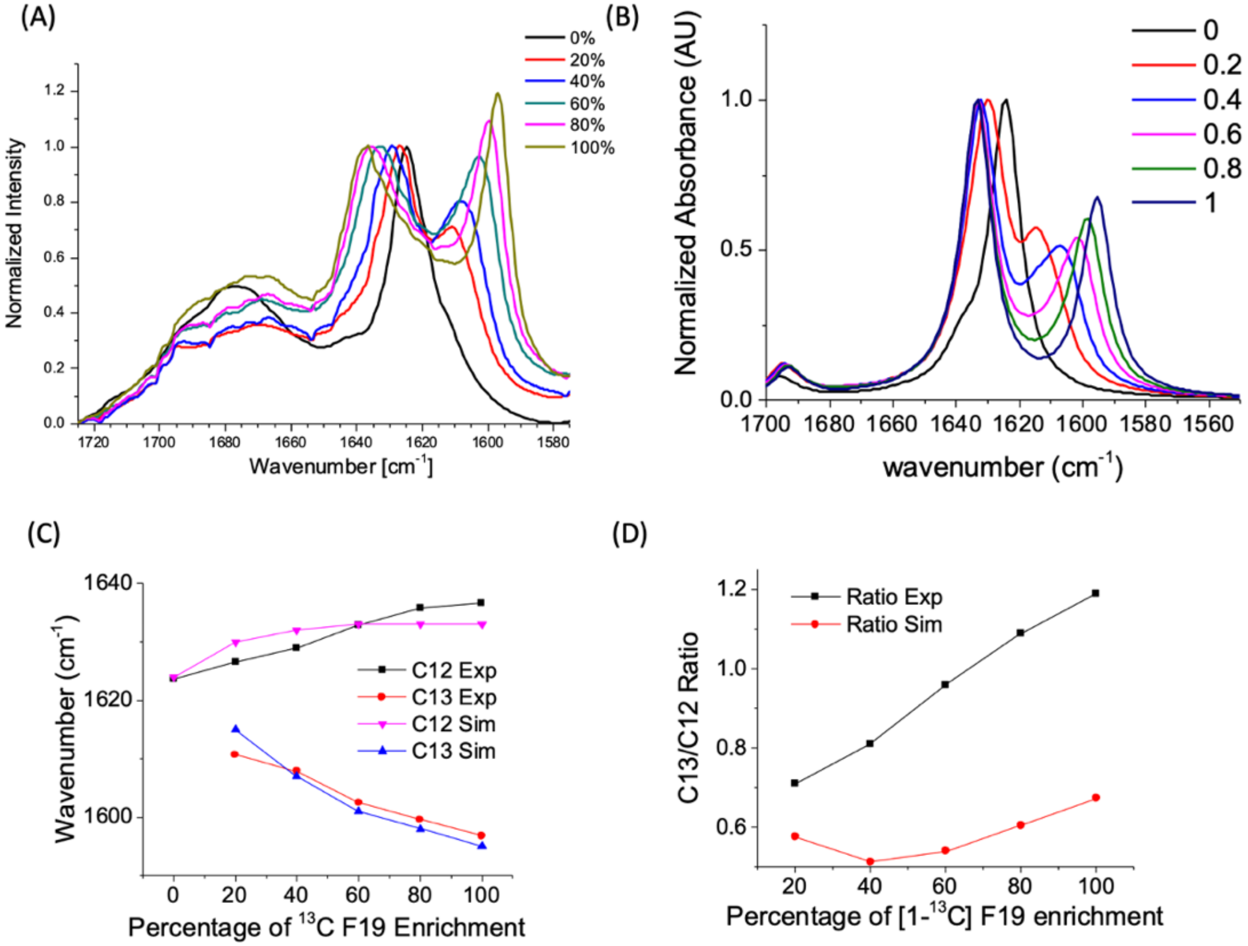

Figure 2-13. F19 Isotope-dilution IR spectrum of Aβ(16-22)E22Q assembled as anti-parallel out-of-register β-sheets. The amide region of each IR spectra is shown with the percentage of isotope enrichment at F19 carbonyl. (A) spectra normalized to the ^{12}C band (B) simulated spectra not normalized. (C) The comparison between experimental and simulated ^{12}C main band and ^{13}C isotopic band position, and (D) intensity ratio between ^{13}C band maxima and ^{12}C band maxima as a function of ^{13}C enrichment at F19 residue.

impact of lateral couplings on peak position shifts. L17 and A21 isotopomers which have the widest ^{12}C amide track (three-residue track) shows most red-shifted ^{12}C bands because of the lateral exciton delocalization while V18 and F20 isotopomers present the most blue-shifted ^{12}C bands compared to the case of L17 & A21, and F19 isotopomer with two-residue ^{12}C tracks.

The in-register parallel beta sheet's experimental spectra and simulations also shows similar trend about the lateral couplings. Like the parallel beta sheets' coupling

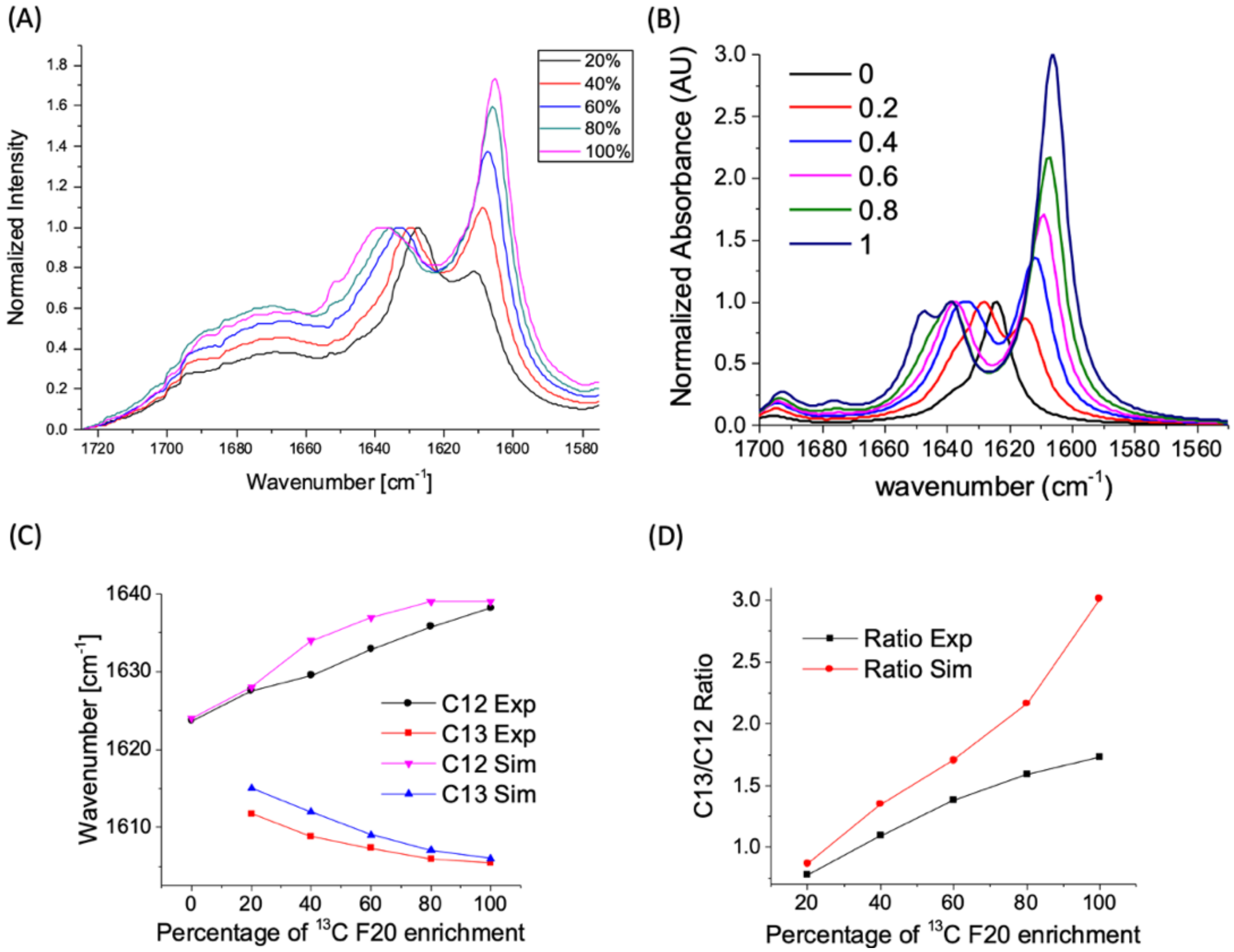

Figure 2-14. F20 Isotope-dilution IR spectrum of Aβ(16-22)E22Q assembled as anti-parallel out-of-register β-sheets. The amide region of each IR spectra are shown with the percentage of isotope enrichment at F20 carbonyl. (A) spectra normalized to the ^{12}C band (B) simulated spectra not normalized. (C) The comparison between experimental and simulated ^{12}C main band and 13C isotopic band position, and (D) intensity ratio between ^{13}C band maxima and ^{12}C band maxima as a function of ^{13}C enrichment at F20 residue.

constant of linear couplings along the fibril axis is slightly less than anti-parallel's constant, overall shifts of the ^{13}C and ^{12}C main bands are less red shifted (Fig. 2-12). Since all isotopomers has linear couplings of ^{13}C amides, the difference between isotopomers is minimized except for A21's case. For the bands of ^{12}C carbonyls, the isotopomers with wider lateral coupling (L17, F20, and A21) have more red-shifted ^{12}C bands, while V18 and F19 isotopomers shows relatively blue shifted ^{12}C bands due to disrupted lateral couplings

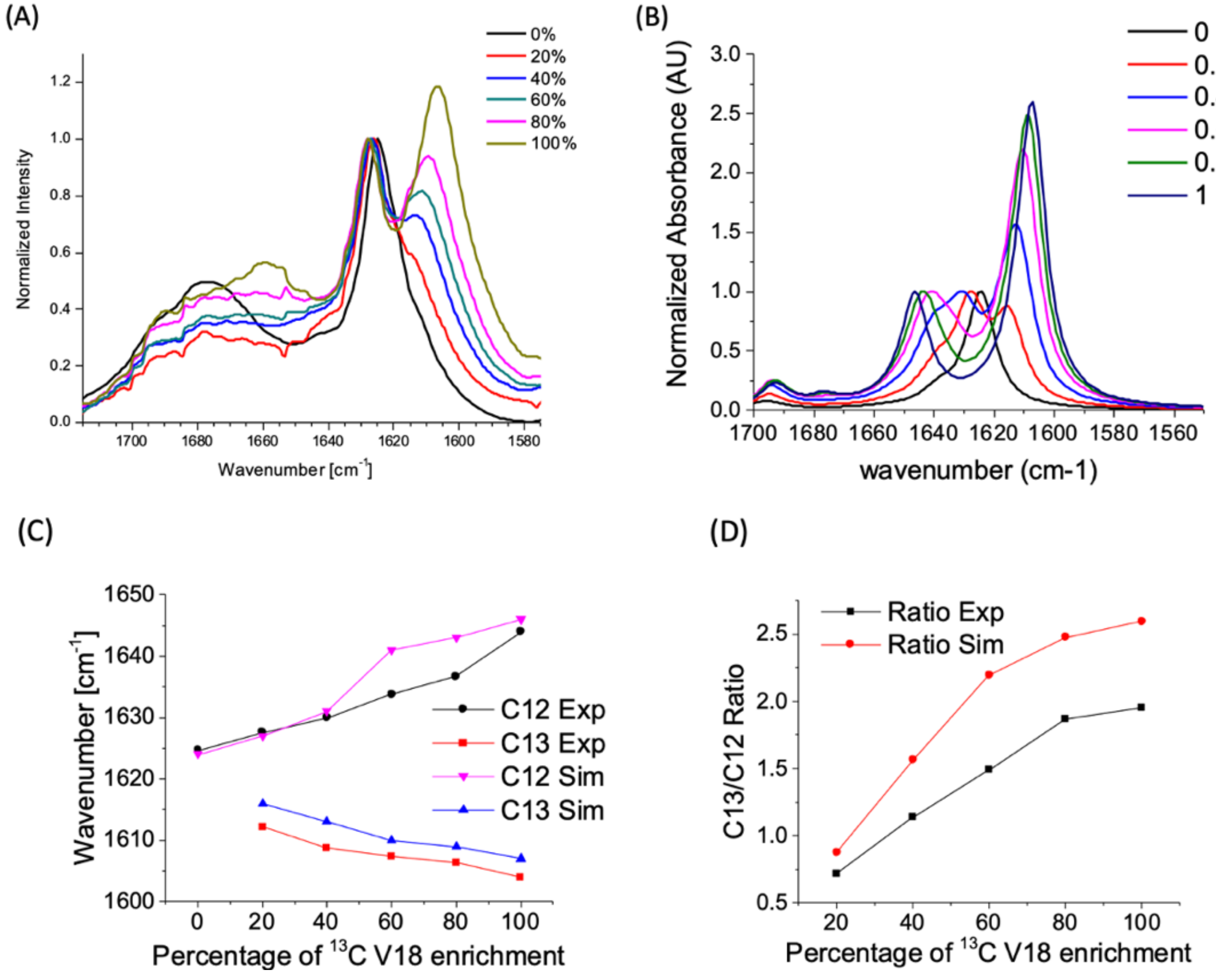

Figure 2-15. V18 Isotope-dilution IR spectrum of Aβ(16-22)E22Q assembled as anti-parallel out-of-register β-sheets. The amide region of each IR spectra are shown with the percentage of isotope enrichment at V18 carbonyl. (A) spectra normalized to the ^{12}C band (B) simulated spectra not normalized. (C) The comparison between experimental and simulated ^{12}C main band and ^{13}C isotopic band position, and (D) intensity ratio between ^{13}C band maxima and ^{12}C band maxima as a function of ^{13}C enrichment at V18 residue.

of two- and three-residue tracks. In the A21's case, only one-sided lateral coupling and different environment of the edge of the sheet can be the cause. Furthermore, there are huge differences between empirical data and simulations in L17, and V18. Additional bands between the ^{12}C and ^{13}C bands was shown in figure 2-12A, which can be considered as defects, and this will be further explained next experiments.

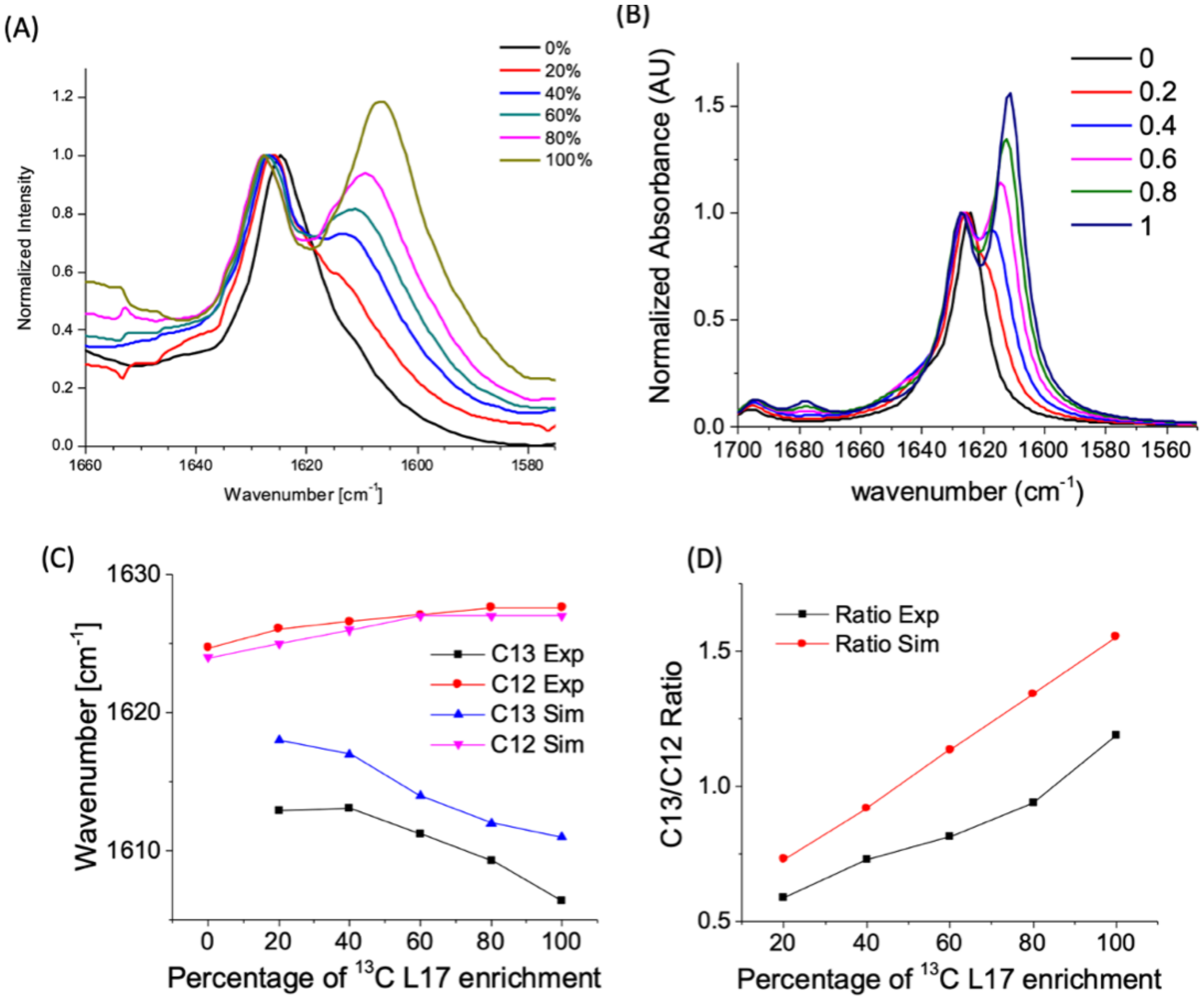

Figure 2-16. L17 Isotope-dilution IR spectrum of Aβ(16-22)E22Q assembled as anti-parallel out-of-register β-sheets. The amide region of each IR spectra are shown with the percentage of isotope enrichment at L17 carbonyl. (A) spectra normalized to the ^{12}C band (B) simulated spectra normalized to the ^{12}C band. (C) The comparison between experimental and simulated ^{12}C main band and ^{13}C isotopic band position, and (D) intensity ratio between ^{13}C band maxima and ^{12}C band maxima as a function of ^{13}C enrichment at L17 residue.

Titrating the E22Q assemblies with ^{13}C site-specifically isotope labeled peptides from 0 to 100% can give estimations of the magnitude of linear coupling of amides along the fibril axis in beta sheets. Because the introducing of isotope can disrupt the delocalization of vibrational excitons, as the ratio of ^{13}C site-specifically isotope labeled peptides increase, the isotope bands will be red-shifted and the ^{12}C bands will be blue-

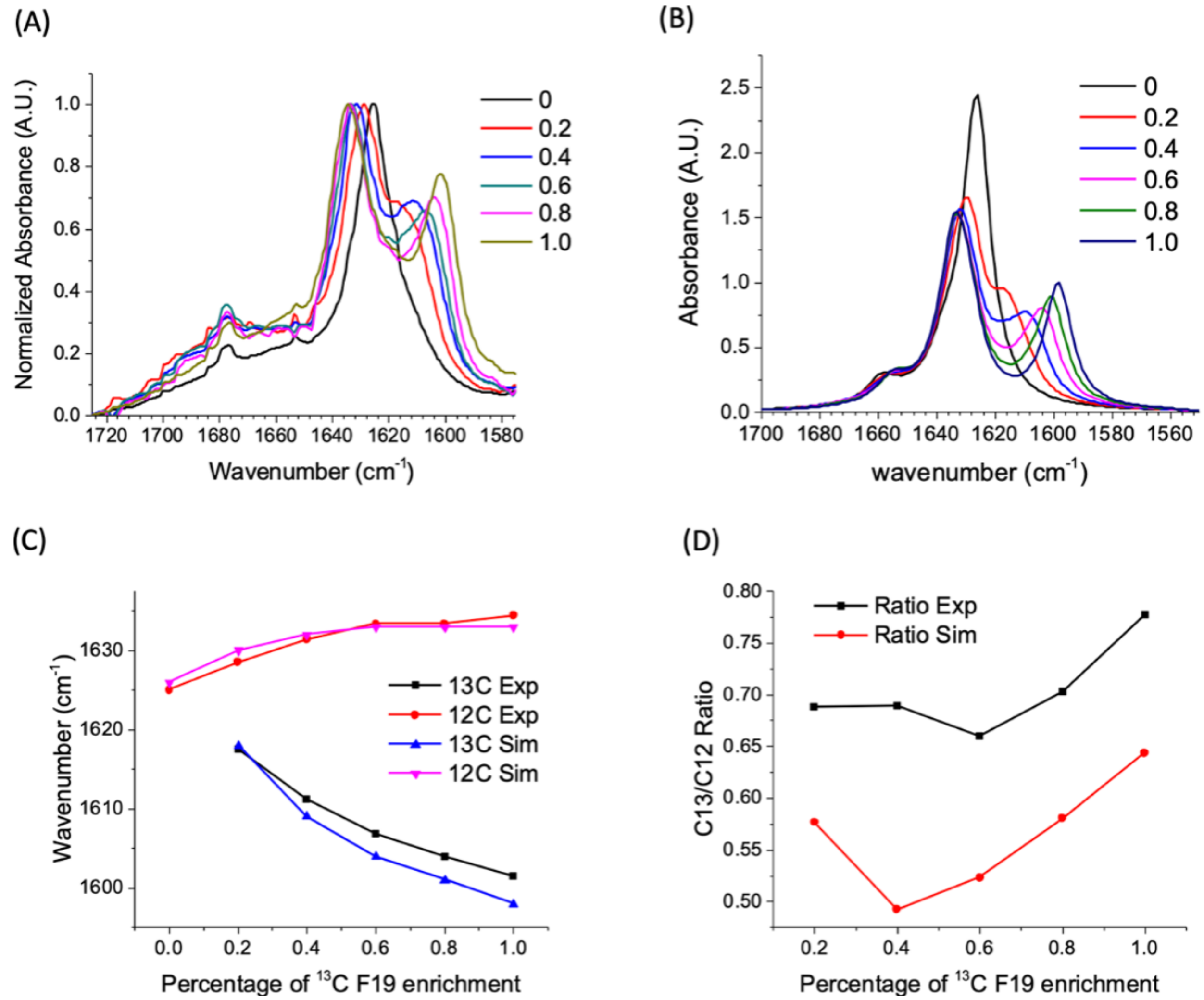

Figure 2-17. F19 Isotope-dilution IR spectrum of Aβ(16-22)E22Q assembled as parallel in-register β-sheets. The amide region of each IR spectra are shown with the percentage of isotope enrichment at F19 carbonyl. (A) spectra normalized to the ^{12}C band (B) simulated spectra. (C) The comparison between experimental and simulated ^{12}C main band and ^{13}C isotopic band position, and (D) intensity ratio between ^{13}C band maxima and ^{12}C band maxima as a function of 13C enrichment at F19 residue.

shifted. Since the F19 peptide assembly with anti-parallel conformation showed linear coupling of ^{13}C amides (Fig 2-11E), the influence of the titration is clearly shown (Fig. 2-13). Simulated frequency shifts of ^{13}C and ^{12}C amide bands are also well matched. Although the experimental bands of F20, V18, L17 peptide assemblies are slightly more red-shifted than simulations, overall trends are well projected (Fig. 2-14, 2-15, and 2-16).

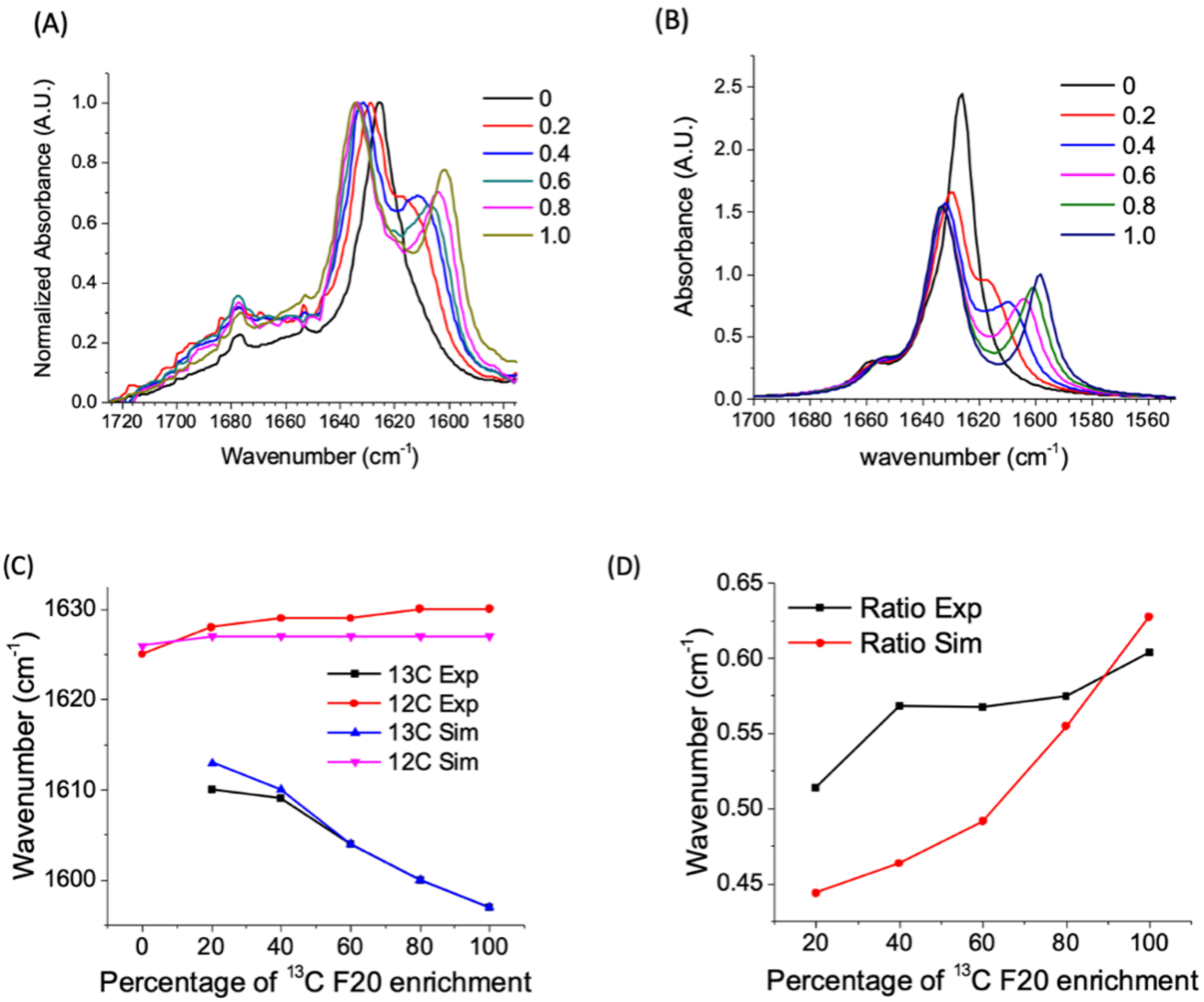

Figure 2-18. F20 Isotope-dilution IR spectrum of Aβ(16-22)E22Q assembled as parallel in-register β-sheets. The amide region of each IR spectra are shown with the percentage of isotope enrichment at F20 carbonyl. (A) spectra normalized to the ^{12}C band (B) simulated spectra. (C) The comparison between experimental and simulated ^{12}C main band and ^{13}C isotopic band position, and (D) intensity ratio between ^{13}C band maxima and ^{12}C band maxima as a function of ^{13}C enrichment at F20 residue.

All anti-parallel conformation of peptide assemblies with titrated isotope labeled peptides shows the expected results of red-shifted 12C bands in lower ratio of 13C isotopomers due to the lateral couplings.

The in-register parallel conformations from the 3rd transition with ^{13}C site-specifically isotope labeled peptides from 0 to 100% were also analyzed. F19 and F20

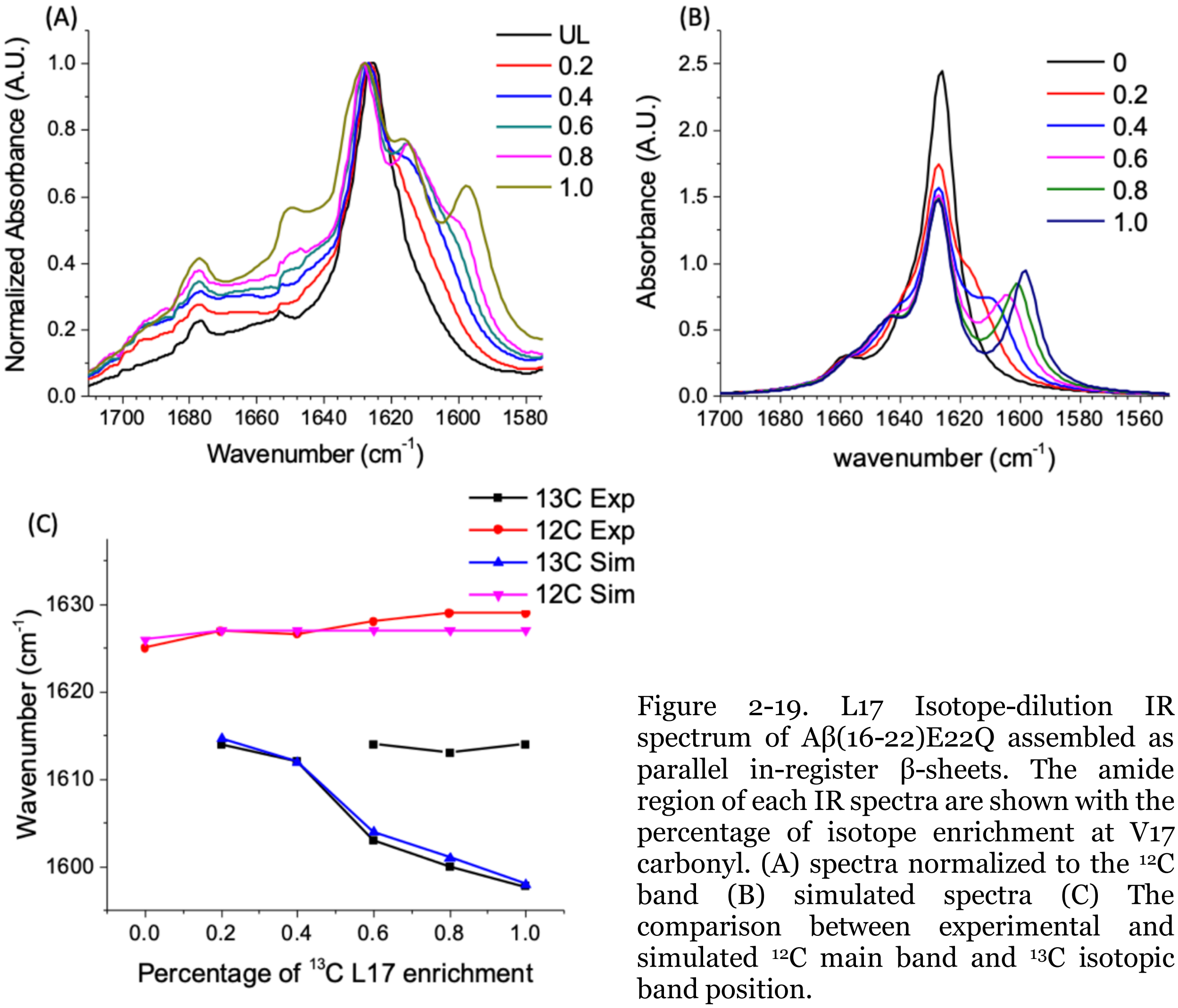

Figure 2-19. L17 Isotope-dilution IR spectrum of Aβ(16-22)E22Q assembled as parallel in-register β-sheets. The amide region of each IR spectra are shown with the percentage of isotope enrichment at V17 carbonyl. (A) spectra normalized to the ^{12}C band (B) simulated spectra (C) The comparison between experimental and simulated ^{12}C main band and ^{13}C isotopic band position.

assemblies show clear shifting bands matched with simulations (Fig 2-17 and 2-18). For example, F19 assemblies shows shifting isotope bands from 1618 cm^{-1} to 1602 cm^{-1} and ^{12}C bands from 1634 cm^{-1} to 1625 cm^{-1} as the isotope enriched peptide's ratio increase, and it shows good agreement with the simulated data. However, the anti-parallel peptide assemblies with ^{13}C at L17, V18, and A21 positions shows complicated features. As shown in the figure 2-12A, L17 peptide assembly with titrated ^{13}C peptide shows an additional band between ^{12}C and ^{13}C bands which are well matched with the simulated data (Fig 2-

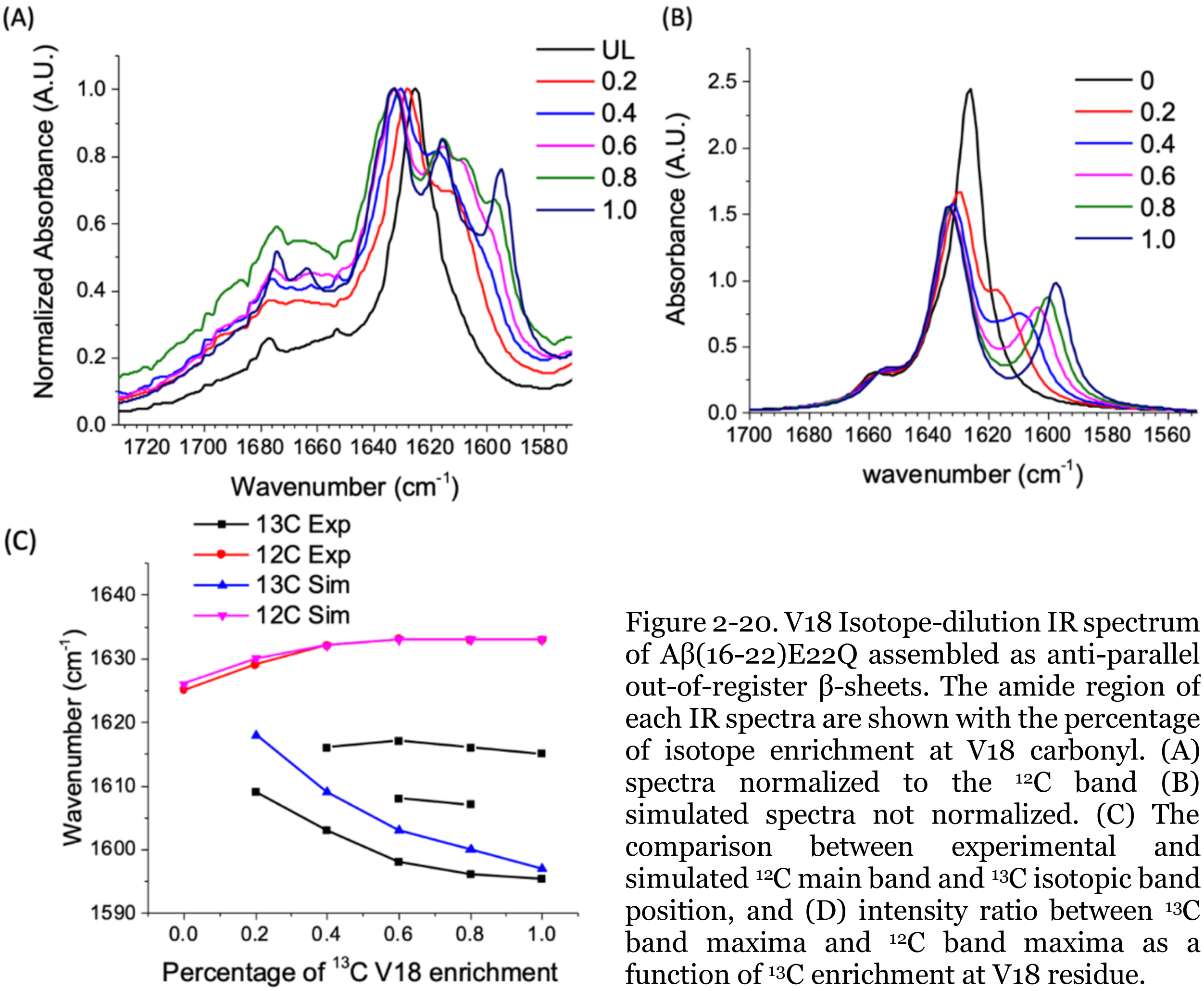

Figure 2-20. V18 Isotope-dilution IR spectrum of Aβ(16-22)E22Q assembled as anti-parallel out-of-register β-sheets. The amide region of each IR spectra are shown with the percentage of isotope enrichment at V18 carbonyl. (A) spectra normalized to the ^{12}C band (B) simulated spectra not normalized. (C) The comparison between experimental and simulated ^{12}C main band and ^{13}C isotopic band position, and (D) intensity ratio between ^{13}C band maxima and ^{12}C band maxima as a function of ^{13}C enrichment at V18 residue.

19). While the ^{12}C and ^{13}C bands are shifting as the ratio of ^{13}C peptides increase, the additional band is not shifting, staying at 1613~1614 cm-1 which is similar with the ^{13}C band of 20% isotope-label peptide ratio sample (Fig. 2-19). Note again that in the 20% sample, ^{13}C amide are isolated and coupled only ^{12}C carbonyls. Furthermore, the 100% sample, which has linear coupling of ^{13}C amide due to the in-register parallel strand conformation, also shows the additional band. The V18 assemblies after the transition to parallel conformation even present one or two additional bands between ^{13}C and ^{12}C bands (Fig. 2-20). One additional band located at 1615 ~ 1617 cm^{-1} which is a similar with

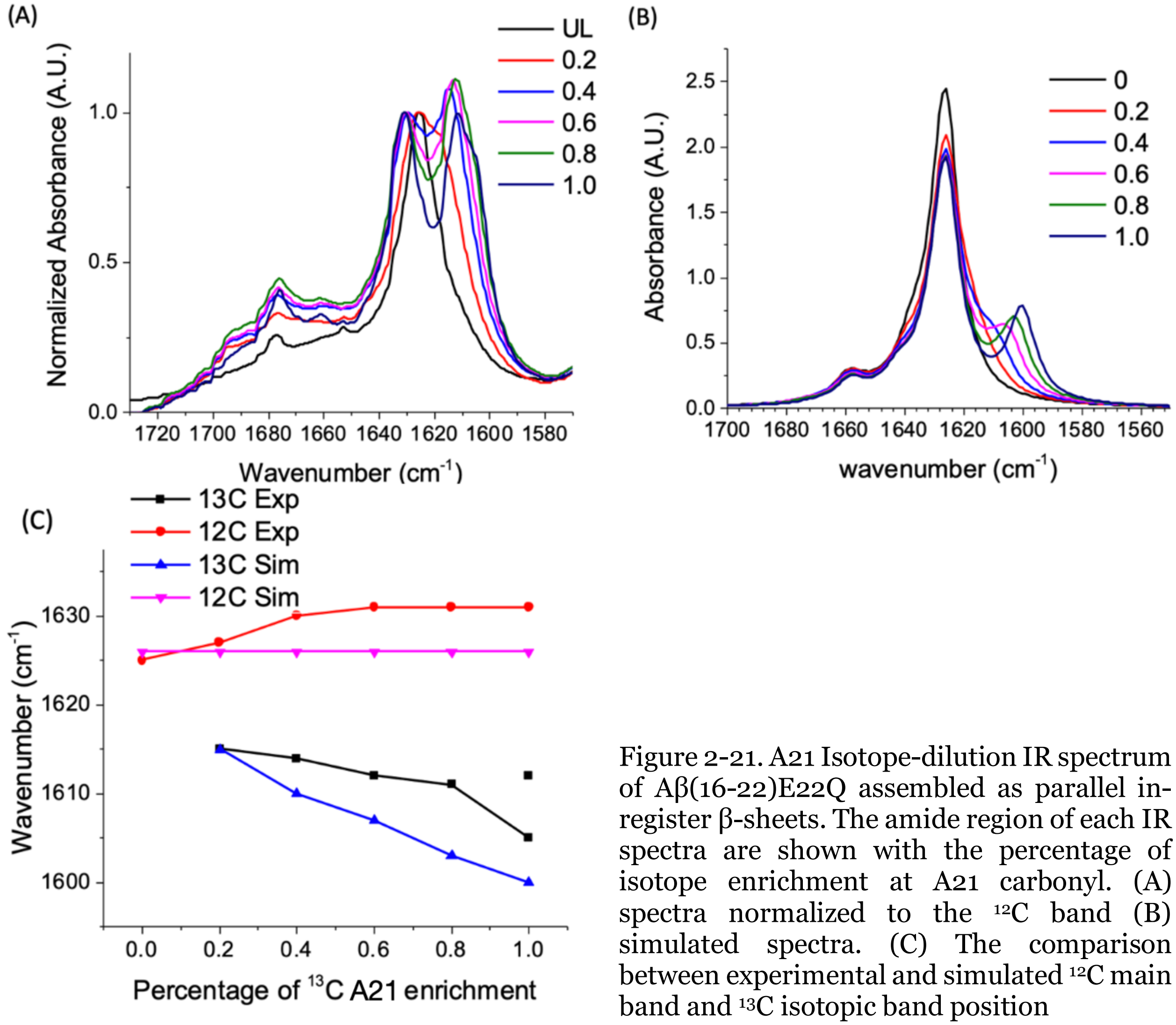

Figure 2-21. A21 Isotope-dilution IR spectrum of Aβ(16-22)E22Q assembled as parallel in-register β-sheets. The amide region of each IR spectra are shown with the percentage of isotope enrichment at A21 carbonyl. (A) spectra normalized to the ^{12}C band (B) simulated spectra. (C) The comparison between experimental and simulated ^{12}C main band and ^{13}C isotopic band position

the additional band in the L17 assembly case (Fig. 2-20). The other additional band have 1607 ~ 1608 cm^{-1}, lower wavenumber, in 60% and 80% enrichment assembly samples. Because the A21 isotopomer has ^{13}C amide at the end of the sheet, it shows distinctive features (Fig. 2-21). It also shows additional bands which is overlapped with ^{13}C bands. The ^{13}C amide band of 100% enrichment sample are more blue shifted than other isotopomers, which can be resulted from small coupling constant. The unusual small coupling constant can be caused by twisted dihedral angle by adjacent phenylalanine side-

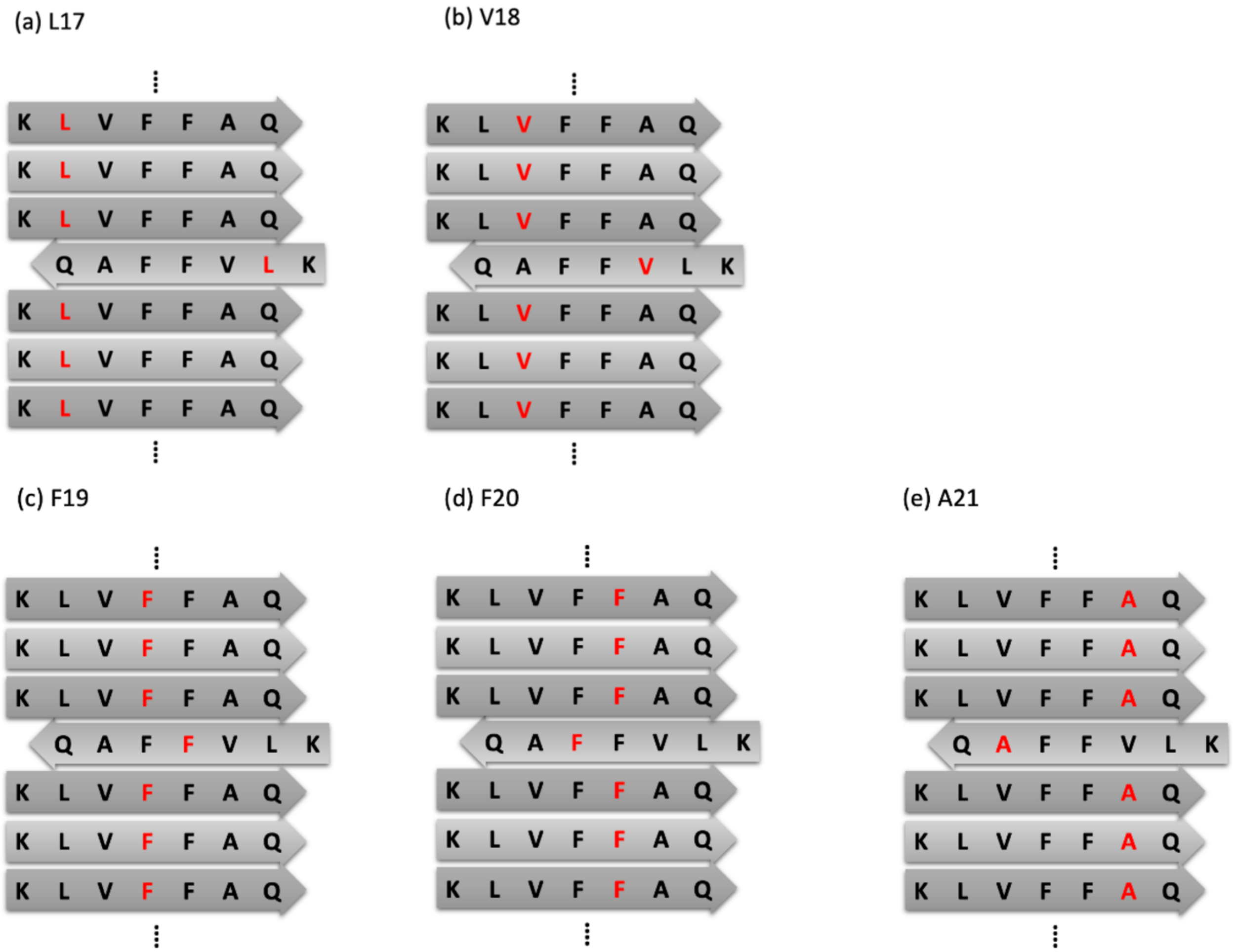

Figure 2-22. The proposed structure of an anti-parallel defect in parallel β-sheet of E22Q labeled by ^{13}C amide in various position.

chain interaction, sheet stacking or solvent exposure[25]. Also, because ^{13}C amide is on the C-terminal position, the dihedral angle can be quite different from other positions.

The cases of L17 and V18 isotopomers with parallel in-register are not common, and to investigate this phenomenon, several possibilities were simulated. Because the additional bands can be oriented from noon-idealized beta sheet structures, such as twisted, bent, or disordered, TCD simulations with twisted beta sheets were tested. Other bands were found but, these bands are positioned at higher wavenumbers than ^{12}C main bands. There are examples of multiple bands in parallel beta sheets: two different structures of $^{13}C{=}^{18}O$ A25 isotope labeled human islet amyloid peptide reported by Zanni and coworkers[19], ^{13}C F20 labeled Ab(10-35) that forms two different fiber structures[32], and multiple structures of amyloid beta aggregation core, KLVFFA[33]. However, if the additional bands of E22Q are from different structures, the shifting should have linear changes as the relative concentrations of isotope labeled peptide increase, which suggests that the additional bands are not originated from the different population of beta sheet structures. To satisfy the phenomenon, we suggest that existence of anti-parallel defect in parallel assembly like figure 2-22. When F19 and F20 samples even have defects, ^{13}C amides are still coupled diagonally, which explains why they do not have the additional bands. On the other hands, L17, V18, and A21 cases show distinct isolated ^{13}C amides coupled with ^{12}C amides that can consistently occur from 20% - 100% of isotope labeled peptide ratio samples. This can explain the additional bands without significant shifting through the different ratios.

2-3 Conclusion

This study shows TDC models characterizing vibrational exciton couplings in the beta sheets of E22L peptides which have both out-of-register anti-parallel and in-register parallel strand conformations. Using this benefit of different conformations in the same peptide minimizing sequence difference, linear chain of vibrational exciton couplings along the fibril axis and lateral couplings are considered, and the correlations of IE-IR spectra and the structures of beta sheet with both out-of-register anti-parallel and in-register parallel strand conformations are analyzed. The analyses with comparing the simulated data and experimental spectra give insight into defects which can be resulted from the transition of strand conformations. With the distinct ^{13}C and ^{12}C couplings showing features in spectra, the IE-IR analyses shows advantages of detecting subtle defects that can be ignored by averaging with major features in other analytical methods. However, it is not clear whether the defect of anti-parallel in parallel beta sheets is from kinetical or thermodynamical selection. Considering that the anti-parallel conformation is selected in the initial biomolecular condensation and parallel configuration, which is formed the third transition, is probably thermodynamically preferred, the defect can be kinetically trapped.

2.4 Materials and Methods

Peptide Synthesis and Purification

The nucleating core of the Dutch mutant of the Ab peptide, Ac-^{16}KLVFFA^{22}Q-NH$_2$ (E22Q) was synthesized via standard Fmoc-based solid-phase chemistry with Fmoc rink-amide polystyrene resin (Anaspec, Inc.) on Liberty CEM Microwave Automated Peptide Synthesizer (Matthews, NC, USA). Microwave assisted Fmoc deprotection was completed using 20% piperidine in dimethylformamide at 45-55°C for 180 sec and washed by 3 times with dimethylformamide. Each amino acid coupling step was performed using 0.1M Fmoc protected amino acid and activated with 0.1 M 2-(1H-benzotriazole-1-yl)-1,1,3,3-tetramethyluronium hexafluorophosphate (HBTU), and 0.2 M N,N–diisopropyl-ethylamine (DIEA) in DMF. Coupling temperatures using microwave were maintained between 75-82°C for 330 sec, then rinsed with three aliquots of dimethylformamide. Final acetylation of the N-terminus was achieved by addition 20% acetic anhydride in dimethylformamide. Resin was filtered and washed with dichloromethane and dried in a vacuum desiccator.

Peptides were cleaved from dried resin by addition of cleavage cocktail (90 vol% TFA, 5 vol% thioanisole, 3 vol% ethanedithiol and 2 vol% anisole) for 4 hr at room temperature and the resulting filtrate was added drop wise to cold diethylether, centrifuged and extracted in diethylether three more times.

Peptides were purified by reverse-phase HPLC (Waters Delta 600) using a Waters Atlantis C-18 preparative column (19 x 250 mm) and employing a linear gradient at 20 mL/min starting at 20% acetonitrile and ending with 55% acetonitrile over 35 min. After removing acetonitrile in rotavap, the peptide fractions were frozen and lyophilized to yield a peptide powder that was stored at 4°C in a vacuum desiccator. Product mass was confirmed by MALDI-TOF on a Voyager-DETM STR Biospectrometry Workstation using α-cyano-4-hydroxycinnamic acid (CHCA) as matrix.

Attenuated Total Reflectance Fourier Transform Infrared (AT-FTIR):

Aliquots (10 μL) of peptide solution were dried as thin films on a Pike GladiATR (Madison, WI, USA) ATR diamond crystal. FT-IR spectra were acquired using a Jasco FT-IR 4100 (Easton, MD, USA) at room temperature and averaging 500 to 800 scans with 2 cm^{-1} resolution, using either an MCT or TGS detector, 5mm aperture and a scanning speed of 4mm/sec. Spectra were processed with zero-filling and a cosine apodization function. Further ATR correction was performed with incidence angle, ϕ, of 45°, ATR crystal refractive index, n_1, of 2.4, sample refractive index, n_2, of 1.5[34] and single reflection to minimize the spectral distortion from wavelength dependent penetration depth change and refractive dispersion caused by sample absorption.

IR Simulation of Ideal β-sheet structure

IR spectra of ideal β-sheet, of which Ramachandran angles were φ = −119° and ψ = 113°, were simulated by using an open-source MATLAB program, coupled oscillator spectrum simulator (COSMOSS).[35] In our IR simulation, following the basic setting of COSMOSS program, the transition dipole of local amide is tilted by 27.5 degrees from the vector of carbonyl CO bond of amide and the its center was located at

$$\mathbf{r} = \boldsymbol{r}_C + 0.665 \cdot \boldsymbol{r}_{CO} + 0.256 \cdot \boldsymbol{r}_{CN}$$

, where $\boldsymbol{r}_C$ is the location of carbonyl carbon, $\boldsymbol{r}_{CO}$ is the unit vector of carbonyl CO bond, and $\boldsymbol{r}_{CN}$ is that of CN bond of amide.[36] To construct an excitonic Hamiltonian matrix, diagonal elements, which are the local mode oscillation frequency of unlabeled and ^{13}C labeled backbone carbonyl, were set to 1668 cm^{-1} and 1628 cm^{-1}, respectively,[37] since ^{13}C labeling causes a shift of 40 cm^{-1}. And all corresponding coupling constants between transition dipoles of amides are computed from the atomic resolution structure and used as off-diagonal elements while local amide frequency as diagonal elements. In pure TDC model, short range couplings are underestimated, and the through-bond couplings, such as mechanical couplings, are neglected. Hence, the coupling between the nearest-neighbors on the same strand is corrected by a Jansen map based on their dihedral angles.[38] The resulting Hamiltonian matrix was numerically diagonalized to compute eigenvalues (energy of normal modes) and their correspondent eigenvectors. Frequency and intensity of each mode were obtained from the eigenvalues and their corresponding total transition dipole strength, $|\mu|^2$, and the stick graph was convoluted with Lorentzian lineshape (FWHM 11 cm^{-1}). Isotope-dilution experiment was simulated by sampling 36 idealized β-strands of 5 residues (including only residue in ordered structure)

8 residues (including N- acetyl protecting group) either in parallel in-register or anti-parallel out-of-register form which were labeled a specific residue in randomly selected strands to shift the local mode frequency down by 40 cm^{-1}. To sample all possible combinations, 300 independent sampling were performed, and the resulting stick graphs were pooled and convoluted (Lorentzian, FWHM 11 cm^{-1}), generating a spectrum.

2-5 References

1. Wang, F.; Gnewou, O.; Solemanifar, A.; Conticello, V. P.; Egelman, E. H., Cryo-EM of Helical Polymers. *Chemical Reviews* **2022**.
2. Wang, F.; Gnewou, O.; Modlin, C.; Beltran, L. C.; Xu, C.; Su, Z.; Juneja, P.; Grigoryan, G.; Egelman, E. H.; Conticello, V. P., Structural analysis of cross α-helical nanotubes provides insight into the designability of filamentous peptide nanomaterials. *Nature Communications* **2021,** *12* (1), 407.
3. Ryu, W.-S., Chapter 2 - Virus Structure. In *Molecular Virology of Human Pathogenic Viruses*, Ryu, W.-S., Ed. Academic Press: Boston, 2017; pp 21-29.
4. Rhodes, G., Chapter 3 - Protein Crystals. In *Crystallography Made Crystal Clear (Third Edition)*, Rhodes, G., Ed. Academic Press: Burlington, 2006; pp 31-47.
5. Nachiappan, M.; Guru Raj Rao, R.; Richard, M.; Prabhu, D.; Rajamanikandan, S.; Chitra, J. P.; Jeyakanthan, J., Chapter 6 - 3D Structural Determination of Macromolecules Using X-ray Crystallography Methods. In *Molecular Docking for Computer-Aided Drug Design*, Coumar, M. S., Ed. Academic Press: 2021; pp 119-140.

6. Murata, K.; Wolf, M., Cryo-electron microscopy for structural analysis of dynamic biological macromolecules. *Biochimica et Biophysica Acta (BBA) - General Subjects* **2018,** *1862* (2), 324-334.
7. Lyumkis, D., Challenges and opportunities in cryo-EM single-particle analysis. *J Biol Chem* **2019,** *294* (13), 5181-5197.
8. Micsonai, A.; Wien, F.; Kernya, L.; Lee, Y.-H.; Goto, Y.; Réfrégiers, M.; Kardos, J., Accurate secondary structure prediction and fold recognition for circular dichroism spectroscopy. *Proceedings of the National Academy of Sciences* **2015,** *112* (24), E3095-E3103.
9. Malay Ali, D.; Suzuki, T.; Katashima, T.; Kono, N.; Arakawa, K.; Numata, K., Spider silk self-assembly via modular liquid-liquid phase separation and nanofibrillation. *Science Advances* *6* (45), eabb6030.
10. McCluskey, M. D.; Janotti, A., Defects in Semiconductors. *Journal of Applied Physics* **2020,** *127* (19), 190401.
11. Ball, J. M.; Petrozza, A., Defects in perovskite-halides and their effects in solar cells. *Nature Energy* **2016,** *1* (11), 16149.
12. Zhan, G.; Cai, Z.-F.; Strutyński, K.; Yu, L.; Herrmann, N.; Martínez-Abadía, M.; Melle-Franco, M.; Mateo-Alonso, A.; Feyter, S. D., Observing polymerization in 2D dynamic covalent polymers. *Nature* **2022,** *603* (7903), 835-840.
13. Zhang, F.-C.; Zhang, F.; Su, H.-N.; Li, H.; Zhang, Y.; Hu, J., Mechanical Manipulation Assisted Self-Assembly To Achieve Defect Repair and Guided Epitaxial Growth of Individual Peptide Nanofilaments. *ACS Nano* **2010,** *4* (10), 5791-5796.

14. Li, S.; Mehta, A. K.; Sidorov, A. N.; Orlando, T. M.; Jiang, Z.; Anthony, N. R.; Lynn, D. G., Design of Asymmetric Peptide Bilayer Membranes. *Journal of the American Chemical Society* **2016,** *138* (10), 3579-3586.

15. Liang, C.; Ni, R.; Smith, J. E.; Childers, W. S.; Mehta, A. K.; Lynn, D. G., Kinetic intermediates in amyloid assembly. *J Am Chem Soc* **2014,** *136* (43), 15146-9.

16. Hsieh, M.-C.; Liang, C.; Mehta, A. K.; Lynn, D. G.; Grover, M. A., Multistep Conformation Selection in Amyloid Assembly. *Journal of the American Chemical Society* **2017,** *139* (47), 17007-17010.

17. Smith, J. E.; Liang, C.; Tseng, M.; Li, N.; Li, S.; Mowles, A. K.; Mehta, A. K.; Lynn, D. G., Defining the Dynamic Conformational Networks of Cross-β Peptide Assembly. *Israel Journal of Chemistry* **2015,** *55* (6-7), 763-769.

18. Maj, M.; Lomont, J. P.; Rich, K. L.; Alperstein, A. M.; Zanni, M. T., Site-specific detection of protein secondary structure using 2D IR dihedral indexing: a proposed assembly mechanism of oligomeric hIAPP. *Chemical Science* **2018,** *9* (2), 463-474.

19. Shim, S. H.; Gupta, R.; Ling, Y. L.; Strasfeld, D. B.; Raleigh, D. P.; Zanni, M. T., Two-dimensional IR spectroscopy and isotope labeling defines the pathway of amyloid formation with residue-specific resolution. *Proc Natl Acad Sci U S A* **2009,** *106* (16), 6614-9.

20. Moran, S. D.; Zanni, M. T., How to Get Insight into Amyloid Structure and Formation from Infrared Spectroscopy. *The Journal of Physical Chemistry Letters* **2014,** *5* (11), 1984-1993.

21. Strasfeld, D. B.; Ling, Y. L.; Gupta, R.; Raleigh, D. P.; Zanni, M. T., Strategies for Extracting Structural Information from 2D IR Spectroscopy of Amyloid: Application to Islet Amyloid Polypeptide. *The Journal of Physical Chemistry B* **2009,** *113* (47), 15679-15691.

22. Petty, S. A.; Decatur, S. M., Intersheet rearrangement of polypeptides during nucleation of β-sheet aggregates. *Proceedings of the National Academy of Sciences of the United States of America* **2005,** *102* (40), 14272-14277.
23. Paul, C.; Wang, J.; Wimley, W. C.; Hochstrasser, R. M.; Axelsen, P. H., Vibrational Coupling, Isotopic Editing, and β-Sheet Structure in a Membrane-Bound Polypeptide. *Journal of the American Chemical Society* **2004,** *126* (18), 5843-5850.
24. Shanmugam, G.; Polavarapu, P. L., Isotope-assisted vibrational circular dichroism investigations of amyloid β peptide fragment, Aβ(16-22). *J Struct Biol* **2011,** *176* (2), 212-9.
25. Shanmugam, G.; Polavarapu, P. L., Site-specific structure of Aβ(25-35) peptide: isotope-assisted vibrational circular dichroism study. *Biochimica et Biophysica Acta* **2013,** *1834* (1), 308-316.
26. Liang, C.; Hsieh, M. C.; Li, N. X.; Lynn, D. G., Conformational evolution of polymorphic amyloid assemblies. *Curr Opin Struct Biol* **2018,** *51*, 135-140.
27. Baker, E. N.; Hubbard, R. E., Hydrogen bonding in globular proteins. *Prog Biophys Mol Biol* **1984,** *44* (2), 97-179.
28. Kortemme, T.; Morozov, A. V.; Baker, D., An orientation-dependent hydrogen bonding potential improves prediction of specificity and structure for proteins and protein-protein complexes. *J Mol Biol* **2003,** *326* (4), 1239-59.
29. Kim, Y. S.; Liu, L.; Axelsen, P. H.; Hochstrasser, R. M., Two-dimensional infrared spectra of isotopically diluted amyloid fibrils from Aβ40. *Proceedings of the National Academy of Sciences* **2008,** *105* (22), 7720.

30. Cheatum, C. M.; Tokmakoff, A.; Knoester, J., Signatures of beta-sheet secondary structures in linear and two-dimensional infrared spectroscopy. *J Chem Phys* **2004,** *120* (17), 8201-15.

31. Jansen, T. l. C.; Dijkstra, A. G.; Watson, T. M.; Hirst, J. D.; Knoester, J., Erratum: "Modeling the amide I bands of small peptides" [J. Chem. Phys. 125, 044312 (2006)]. *The Journal of Chemical Physics* **2012,** *136* (20), 209901.

32. Paul, C.; Axelsen, P. H., beta Sheet structure in amyloid beta fibrils and vibrational dipolar coupling. *J Am Chem Soc* **2005,** *127* (16), 5754-5.

33. Colletier, J. P.; Laganowsky, A.; Landau, M.; Zhao, M.; Soriaga, A. B.; Goldschmidt, L.; Flot, D.; Cascio, D.; Sawaya, M. R.; Eisenberg, D., Molecular basis for amyloid-beta polymorphism. *Proc Natl Acad Sci U S A* **2011,** *108* (41), 16938-43.

34. Benesch, J.; Askendal, A.; Tengvall, P., The determination of thickness and surface mass density of mesothick immunoprecipitate layers by null ellipsometry and protein 125iodine labeling. *J Colloid Interface Sci* **2002,** *249* (1), 84-90.

35. Ho, J.-J., Coupled OScillator MOdel Spectrum Simulator.

36. Ding, B.; Laaser, J. E.; Liu, Y.; Wang, P.; Zanni, M. T.; Chen, Z., Site-Specific Orientation of an α-Helical Peptide Ovispirin-1 from Isotope-Labeled SFG Spectroscopy. *The Journal of Physical Chemistry B* **2013,** *117* (47), 14625-14634.

37. Lomont, J. P.; Rich, K. L.; Maj, M.; Ho, J.-J.; Ostrander, J. S.; Zanni, M. T., Spectroscopic Signature for Stable β-Amyloid Fibrils versus β-Sheet-Rich Oligomers. *The Journal of Physical Chemistry B* **2017,** *122* (1), 144-153.

38. la Cour Jansen, T.; Dijkstra, A. G.; Watson, T. M.; Hirst, J. D.; Knoester, J., Modeling the amide I bands of small peptides. *The Journal of Chemical Physics* **2006,** *125* (4), 044312.

Chapter 3.

Copper arrays in peptide-metal co-assemblies

(Collaborated with Anthony Sementilli[†], Rolando F. Rengifo[†], Wei Li[*], Andrew M. Stewart[*], Katie L. Stewart[*], Umar Twahir[*], Youngsun Kim[†], Jipeng Yue[†], Anil K. Mehta[†], Jason Shearer[◆‡], Kurt Warncke[*‡], David G. Lynn[†‡§], Departments of Chemistry[†], Biology[§], and Physics[*], Emory University, Atlanta, GA / Department of Chemistry[◆], Trinity University, San Antonio, TX)

3.1 Introduction

Peptide assemblies are processed via two-step nucleation with liquid-liquid phase separation and liquid-solid phase transition[1-3]. When peptides accumulate into peptide-

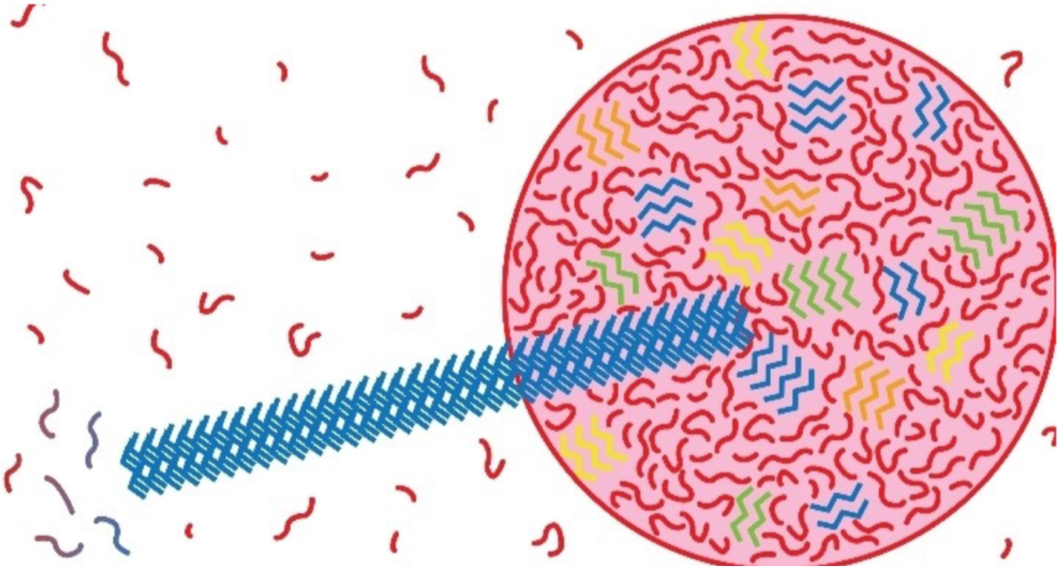

Figure 3-1. Proposed model for 2-step amyloid nucleation. Peptide strands (red lines) collapse into solute-rich particle phases. Within the particles, strands sample distinct β-sheets (orange, yellow, green, blue lines). Liquid-solid phase transition occurs through sheet lamination in the particle, propagating the selected structure (blue).

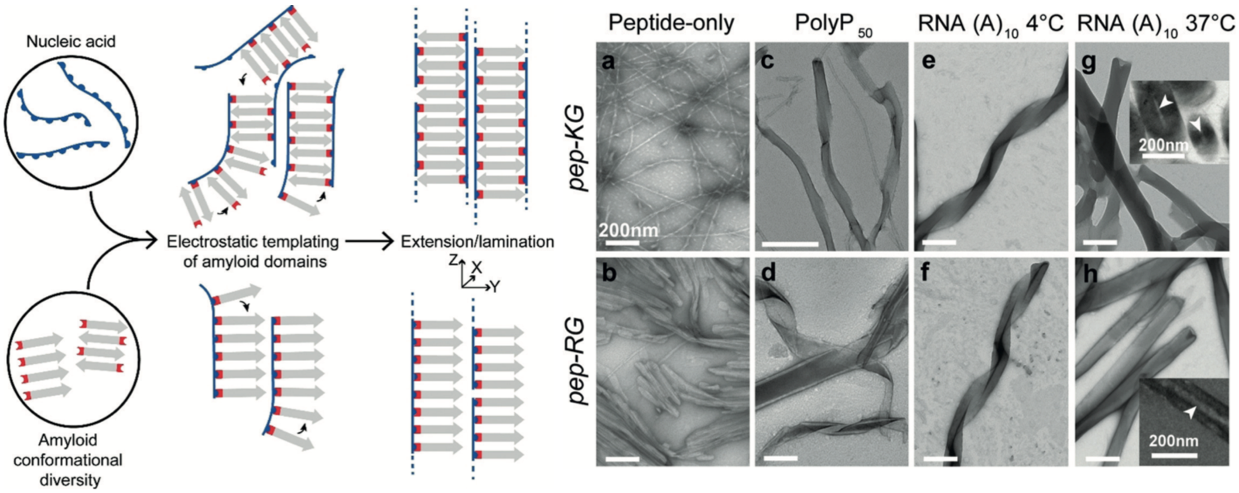

Figure 3-2. Proposed templating of peptides by nucleic acids. Positively charged peptides form cationic phases capable of complementary electrostatic interactions with nucleic acid polyanions (Left). RNA/Peptide co-assembly. (a,b) TEM images of pep-KG and pep-RG self-assemblies. (c,d) $PolyP_{50}$ -templated assembly of pep-KG and pep-RG. e,f) RNA (A_{10})-templated assembly of pep-KG and pep-RG at 4 °C. (g,h) At 37 °C, the ribbons fuse to form thick-walled nanotubes; TEM insets show nanotube cross-sections. Pep-KG refers to Ac-KLVIIAG-NH_2 and pep-RG to Ac-RLVIIAG-NH_2. White arrowheads indicate hollow nanotube interior. Scale bars are 200 nm. (Ref. 7)

rich particle phase, the liquid-like particle includes metastable structures (Fig. 3-1). Then, in the liquid-solid transition, a selected structure is propagating making nanostructure morphologies. As introduced the first chapter, modifications of factors, such as pH, temperature, fields, and solvents, can have significant impacts on the selection. This property of changeable metastable/selected structures resembles intrinsically disordered proteins (IDPs) that adapt to environment or adapt with binding partners, forming different conformations and functions[6]. The IDP-like adaptability of peptide assembly can allow itself to have other structures and functions.

Introducing templates to peptide assemblies have great impacts on the structures and morphologies. There are studies attempting to select/modify the metastable/selected structure by introducing templates that can charge-complementary interaction or form complex with amino acid residues[7-8]. Rha and co-workers reported peptide co-assemblies with RNA templates (Fig. 3-2)[7]. RNA's polyanionic phosphates play as templates for positive charged lysine or arginine of the peptides, resulting different structures and morphologies from the peptide self-assemblies without the templates. The peptide self-assemblies in absence of RNA form beta sheet structure with parallel strand conformation, but when it forms co-assemblies with RNA, anti-parallel strand conformation is dominant, which suggests that propagated assembly nano structures from the liquid-like particles modified by the template's effects. Moreover, it causes different nano-scale morphologies, from fibers/bundled short fibers of the peptide self-assemblies to laminated ribbons/tubes (Fig 3-2).

Here, utilizing changeable/adaptable structures of peptide assemblies via two-step nucleation, and metal binding property of certain amino acids, new co-assembled structures including metal arrays was attempted to design new functions such as redox reactions.

3.2 Results and discussion

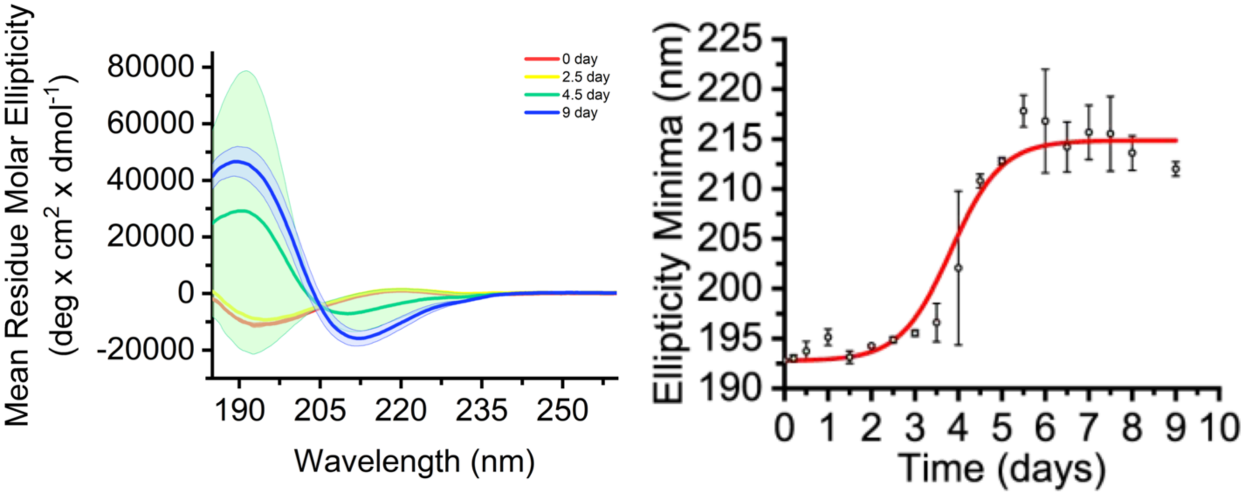

Figure 3-3. Representative CD spectra of select timepoints (left), and circular dichroism minimum as a function of time for K16A.Time-dependent CD showing a red shift of λ_{min} ellipticity of a 1 mM K16A solution at 25°C

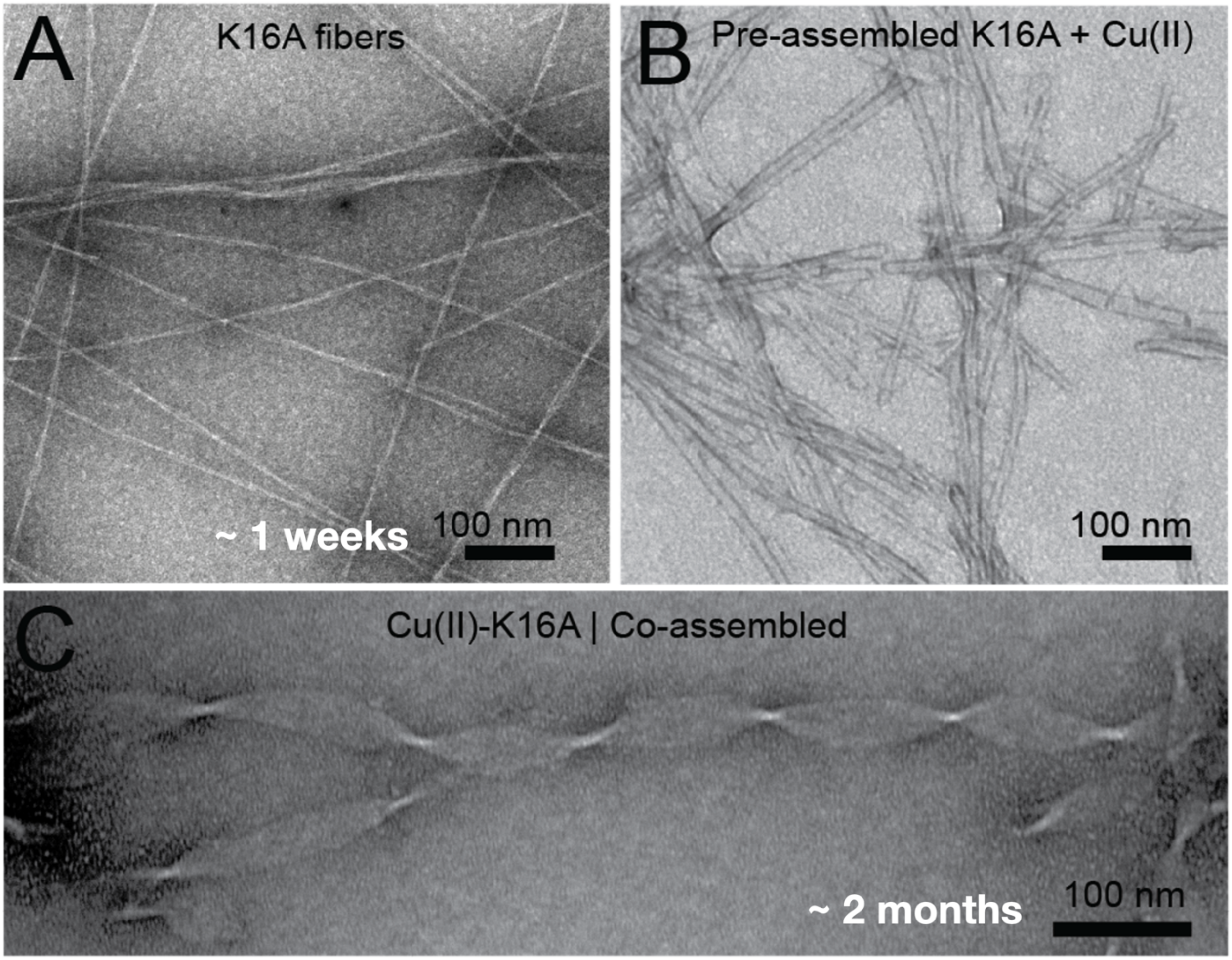

Figure 3-4. Negative stained TEM images of (A) K16A peptide self-assemblies without any copper ions, (B) Pre-assembled K16A and Cu(II) mixture, and (C) K16A and Cu(II) co-assemblies. 2 mM K16A, 2 mM CuCl2, and 25 mM MES pH 5.6.

3.2.1 kinetics and morphologies of K16A-Cu(II)/Cu(I) co-assemblies

Histidine, an amino acid with a thiazole ring, is well known for one of the representative metal binding residues, used in histidine-rich metal binding proteins[9-11]. To use amyloidogenic cross-beta structures and the metal binding properties, H-HHQALVFFA-NH_2 (K16A) is designed. K16A is a congener of the core sequence of amyloid beta 42 peptide with a mutation of lysine to alanine to avoid any complicated

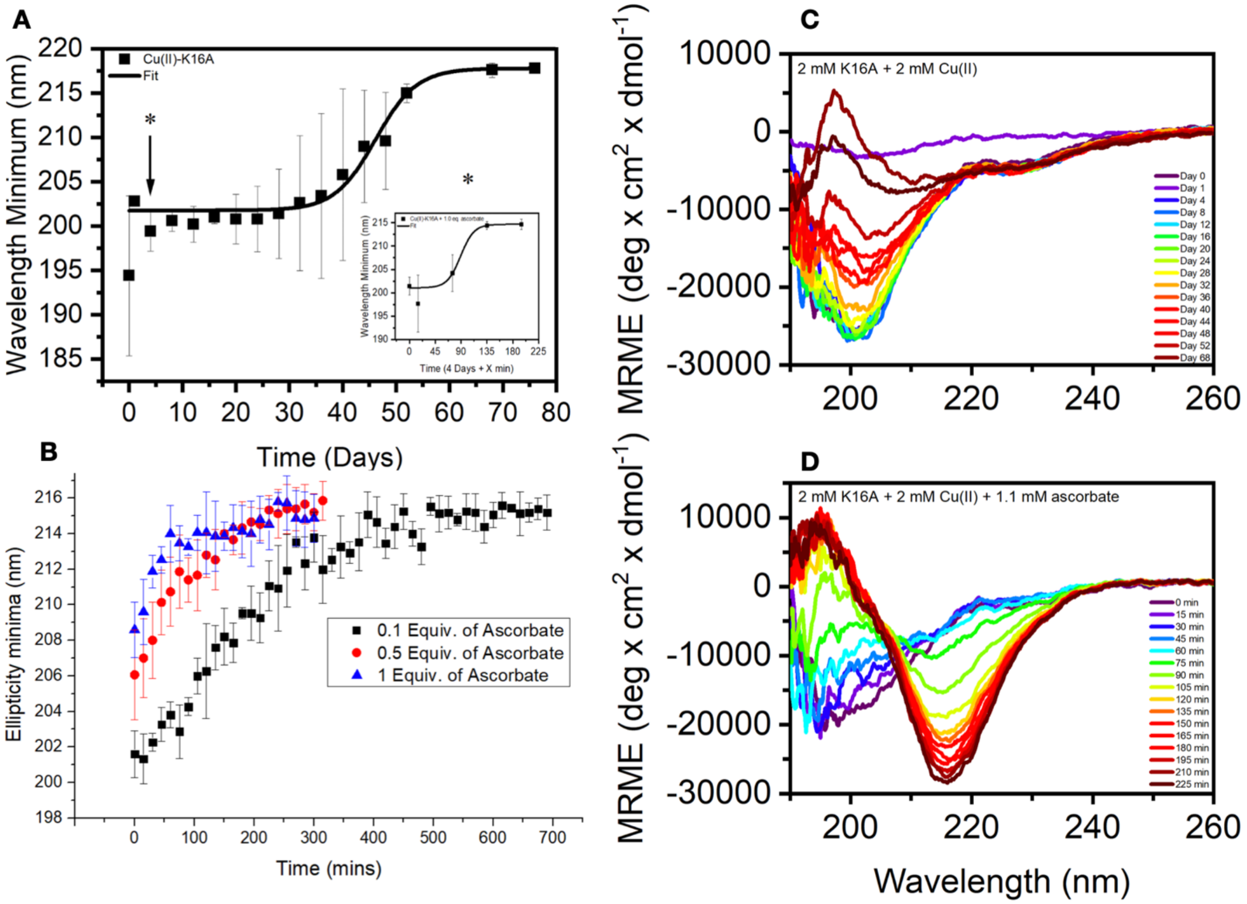

Figure 3-5. Circular dichroism minimum as a function of time for Cu(II)-K16A (A) and Cu(I)-K16A with titrated ascorbate concentrations (B) . Asterisks in panel A indicate an experiment where a Cu(II)-K16A aliquot was titrated with 1.0 eq ascorbate at day 4 (inset). Circular dichroism spectra of representative Cu(II)-K16A (C) and Cu(I)-K16A (D).

situation between metals and lysine. The N-terminal Histidine-dyad can make the histidine-rich environment for the metal binding in liquid-like particle phase or even in just a peptide strand. I and my co-workers already published K16A's peptide self-assemblies showing that it is following the two-step nucleation as well as the various metastable structure in liquid-like particles[1]. The assembly also has beta sheet secondary structure taking about 1 week to be matured (Fig. 3-3) with fiber morphologies (Fig 3-4A). CD spectra of matured K16A assembly shows the typical beta sheet features with maximum at around 193 nm (pi→pi*) and minimum at around 215 nm (n→pi*) and indicates the transition to beta sheets at 3.8±0.17 days.

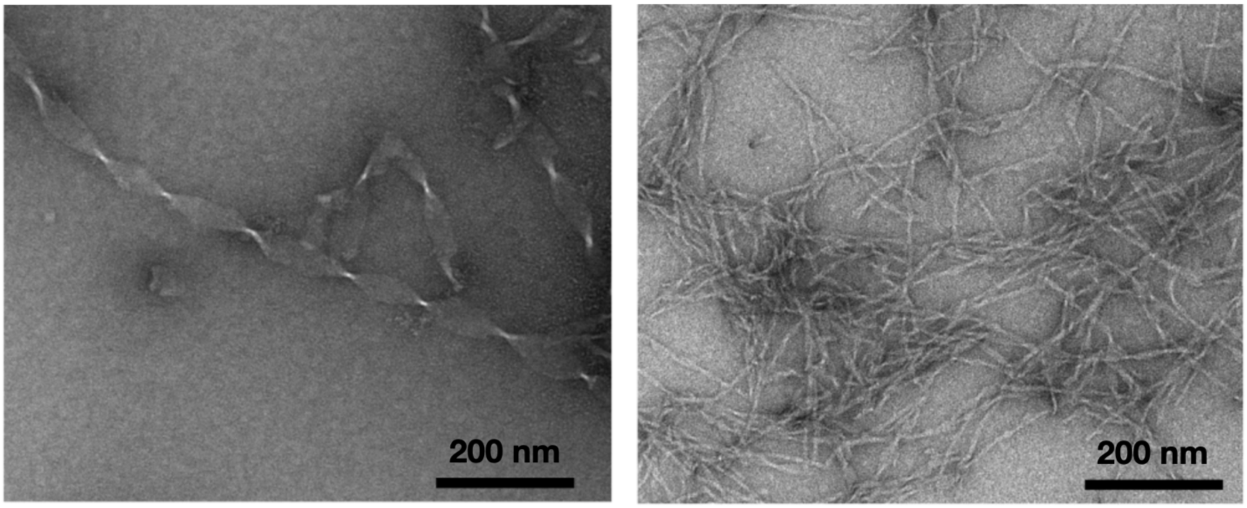

Figure 3-6. TEM images of the representative K16A-Cu(II) co-assembly (Left), and K16A-Cu(I) co-assembly. The samples prepared with 2 mM K16A peptide, 2 mM $CuCl_2$, and 25 mM MES (pH 5.6) and the Cu(I) co-assembly sample has 1 mM sodium ascorbate additionally to reduce Cu(II) to Cu(I).

K16A co-assemblies with copper ions (I/II) was designed because Cu(II) is one of the abundant metal ions in amyloid beta rich plagues[12-15]. Figure 3-4 B and C present that the mixture of pre-assembled K16A fiber and Cu(II) has bundled fiber morphology while the K16A-Cu(II) co-assembly has twisted ribbons. To clarify, The pre-assembled mixture was prepared by adding Cu(II) ions after the K16A peptide forms fiber, and the co-assembled samples made by adding K16A peptide and Cu(II) ion both into solution at the same time. Both have 2 mM K16A peptide, and 25 mM MES (pH 5.6) concentration, and Cu(II) samples have 2 mM $CuCl_2$ additionally. In addition to the morphological difference between K16A peptide self-assembly and K16A-Cu(II) co-assembly, there is a difference of the rate of forming assemblies. While the co-assembly takes more than 2 months to be matured (Fig. 3-5A and C), the K16A self-assembly takes only 1 weeks (Fig 3-3). K16A-

Cu(II) co-assembly also has beta sheet secondary structure features in CD spectra with transition at 46.1±2 days.

Based on the oxidation state of copper ions, the co-assemblies have huge differences in the rate of forming assembly and morphologies. As shown in the CD spectra in Figure 3-5, the K16A-Cu(II) co-assembly takes more than 2 months to be mature, but the K16A-Cu(I) co-assemblies take at least 4 hours to have fine fiber morphologies (Fig. 3-6). K16A-Cu(I) co-assemblies was prepared with sodium ascorbate, the reductant for Cu(II), which was added in the assembly solution with K16A and $CuCl_2$ at the same time.

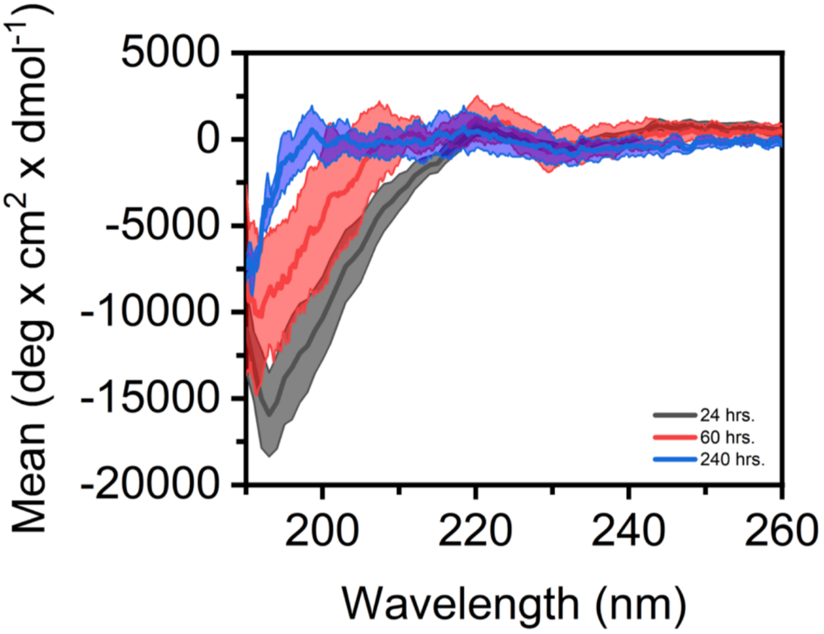

Figure 3-7. Representative circular dichroism spectrum of 2 mM K16A + 2 mM ascorbate at 24 (black), 60 (red) and 240 (blue) hrs. Error bars denote signal average distribution taken in triplicate

As a control, a co-assembly of K16A peptide and sodium ascorbate, the reductant for Cu(II), was tested. CD spectra of the control sample indicates that sodium ascorbate is not showing significant impact on the increased assembly rate, because even after 10-day

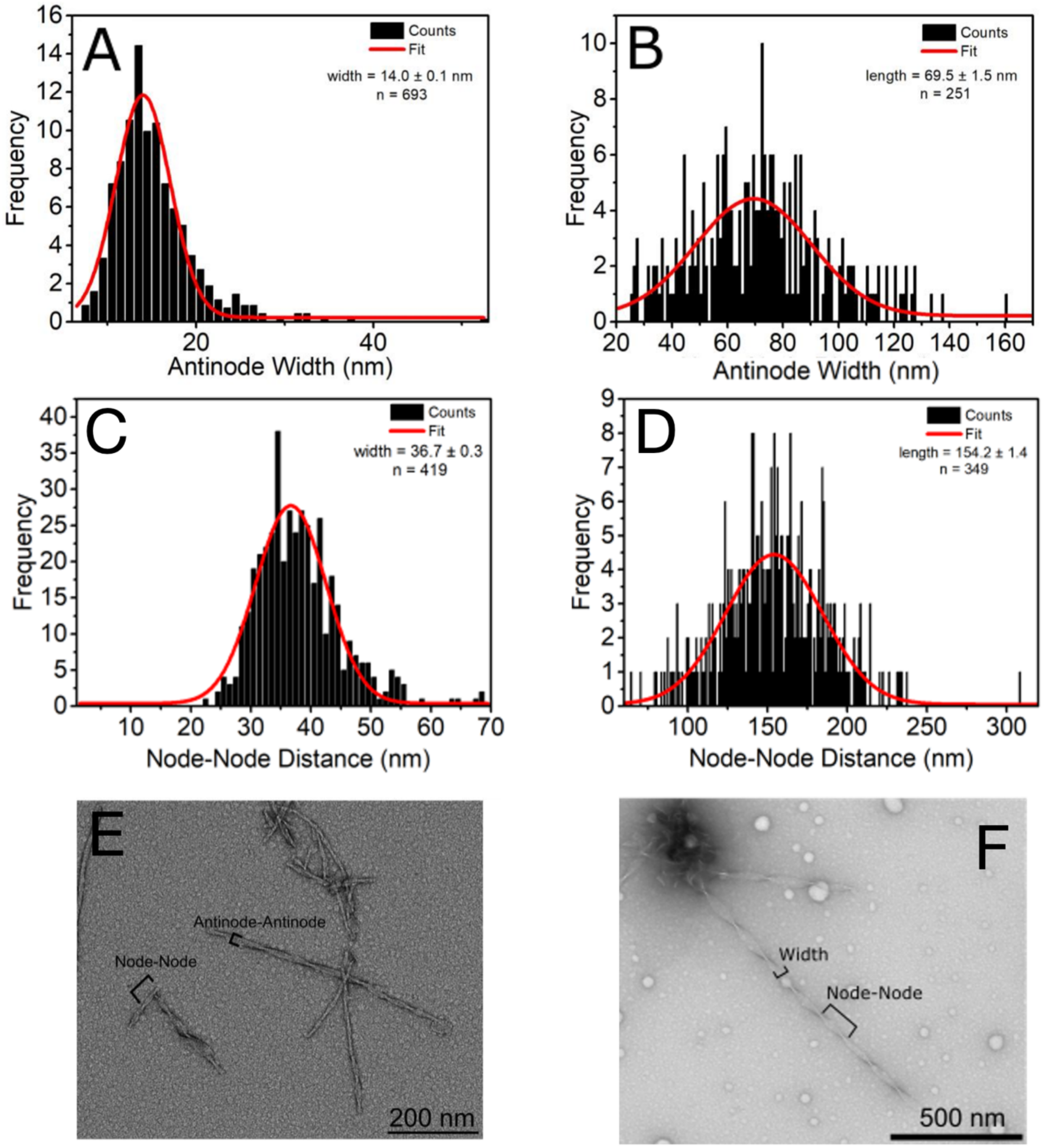

Figure 3-8. TEM statistics on Cu(I)-K16A co-assembly's widths(A) and internode distances (B), and Cu(II)-K16A co-assembly's widths(C) and internode distances (D), and Representative TEM displaying sample measurements of Cu(I) co-assembly (E), and Cu(I) co-assembly (F).

time point the control sample did not show the transition from random coil to beta sheet secondary structure.

Indeed, the acceleration of forming assemblies was observed when the ascorbate was added in the sample of K16A and Cu(II) at 4 day time point (Fig 3-5A, inset).

Moreover, with lower equivalent of ascorbate concentration, the co-assemblies showed rapid formation of the nanofibers (Fig 3-6B). Considering that the Cu(II) co-assemblies have much longer time of liquid-like particle phase, and the Cu(I) co-assemblies show short particle phase, Cu(I) ions quickly form thermodynamically favorable structure at the particle phase making nanofibers with the selected structure, while Cu(II) ions kinetically capture structures that are unfavorable for liquid-solid phase transition or even destabilize the primary nucleation.

TEM analysis indicates clear difference of detailed morphologies between the Cu(I) co-assembly and Cu(II) co-assembly (Fig. 3-8). The Cu(I) co-assembly has 14.0±0.1 nm width at antinode and the Cu(II) sample has 36.7±0.3 nm width. For node to node distance, the Cu(I) and Cu(II) co-assemblies show 69.6±1.5 nm and 154.2±1.4 nm. Overall, the Cu(I) co-assembly has narrower width and shorter repeating of the twisted ribbons than the Cu(II) co-assembly, which is well reflected in X-ray power diffraction (XRD) data

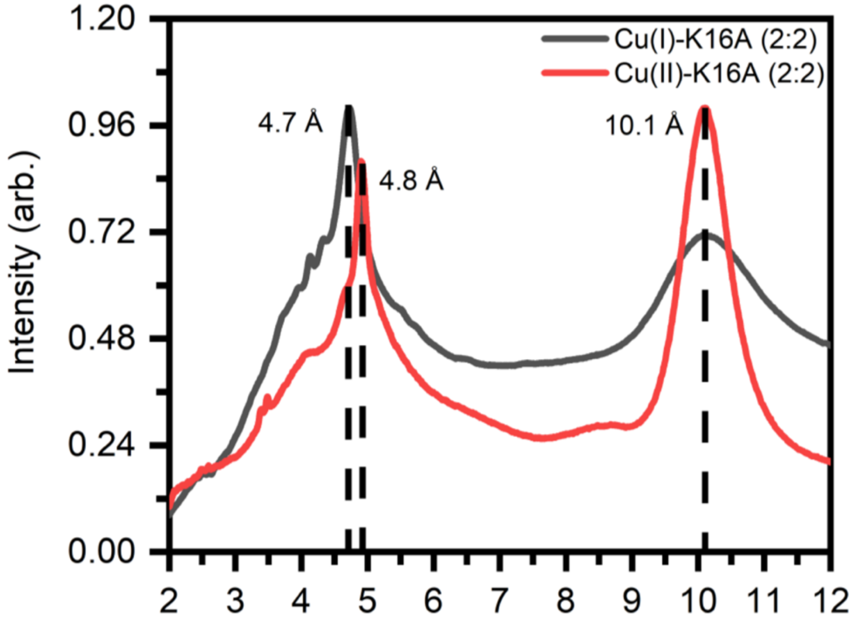

Figure 3-9. pXRD diffraction patterns of cu(I)- and Cu(II)-K16A co-assemblies.

(Fig. 3-9). The XRD shows the typical d-spacing for amyloid; hydrogen bonding between beta sheet strands at 4.7 Å for the Cu(I) co-assembly and 4.8 Å for the Cu(II) sample, and also the d-spacing of the laminations of beta sheets at 10.1Å. The higher intensity of the hydrogen bonding reflection than that of the lamination d-spacing in the K16A-Cu(I) co-assembly indicates that it is growing the fiber propagating direction, the hydrogen bonding axis. Whereas, the Cu(II) co-assembly presents higher intensity of d-spacing the

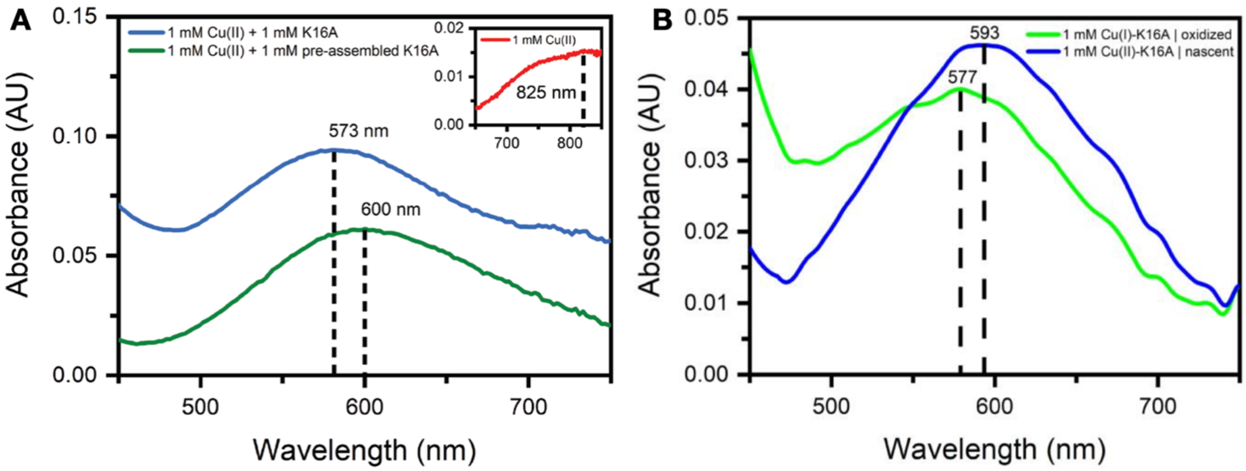

Theoretical Ligand Composition	**Estimated λ_{max} (± 10 nm)**
$(Im)_2(H_2O)_2$	692
$(Im)(ammino)(H_2O)_2$	681
$(ammino)_2(H_2O)_2$	670
$(Im)_3(H_2O)$	634
$(Im)_3(ammino)$	625
$(Im)_2(ammino)_2$	570
$(Im)_2(hydroxo/alkoxido)_2$	617
$(Im)(ammino)(hydroxo/alkoxido)_2$	603
$(ammino)_2(hydroxo/alkoxido)_2$	595

Sample	**Experimental λ_{max}**
Cu(II)-K16A, co-assembled	573
Cu(II)-K16A, pre-assembled	600
Cu(II)-K16A, nascent	593
Cu(I)-K16A, co-assembled (oxidized)	577

Figure 3-10. UV/Vis spectra of K16A-Cu(II) co-assembly (A, blue), pre-assembled K16A-Cu(II) (A, green), K16A-Cu(II) particle (B, blue), and oxidized K16A-Cu(I) co-assembly (B, green). The table shows predicted λmax values of ligand compositions of Cu(II) complexes, calculated based on Ref. 4.

laminations while it still shows similar intensity of H-bonding d-spacing, which is well matched with the wider width of the nanostructures in the TEM images.

3.2.2 Structure studies of the K16A-Cu(II) co-assembly

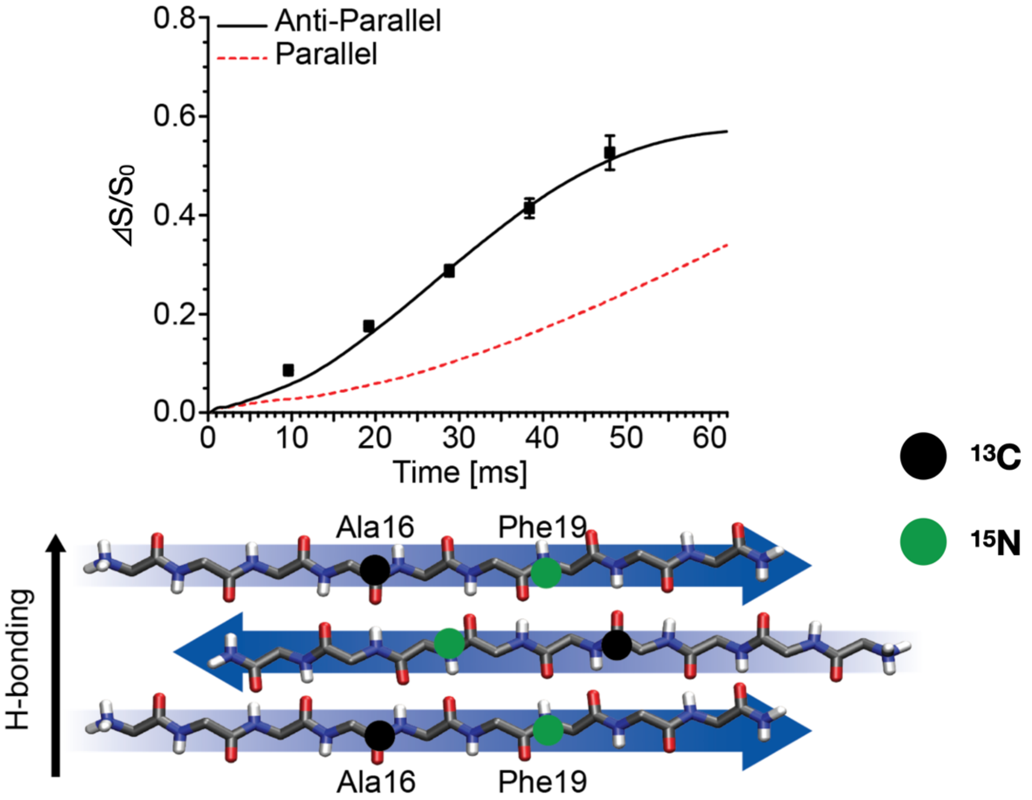

Figure 3-11. REDOR data for HHQ[1-^{13}C]A^{16}LV[^{15}N]F^{19}FA-NH$_2$ + Cu(II) (Cu(II)-K16A) ribbons fit to a REDOR dephasing curve for antiparallel, doubly out-of-register model (black) as well as an parallel in-register model (red dashed). A doubly out-of-register arrangement maximizes access to the histidine sidechains (top). Cartoon of the doubly out-of-register β-sheet with enrichment designations for [1-^{13}C]A^{16} (black) and [^{15}N]F^{19} (green). Sidechains hidden for clarity.

UV/Vis spectra analysis shows strong blue-shifted absorption of Cu(II) complexes in the co-assemblies relative to hexaaquacopper with maximum absorption at 573 nm for K16A-Cu(II) co-assembly, and 600 nm for pre-assembled K16A-Cu(II) (Fig 3-10A). It can

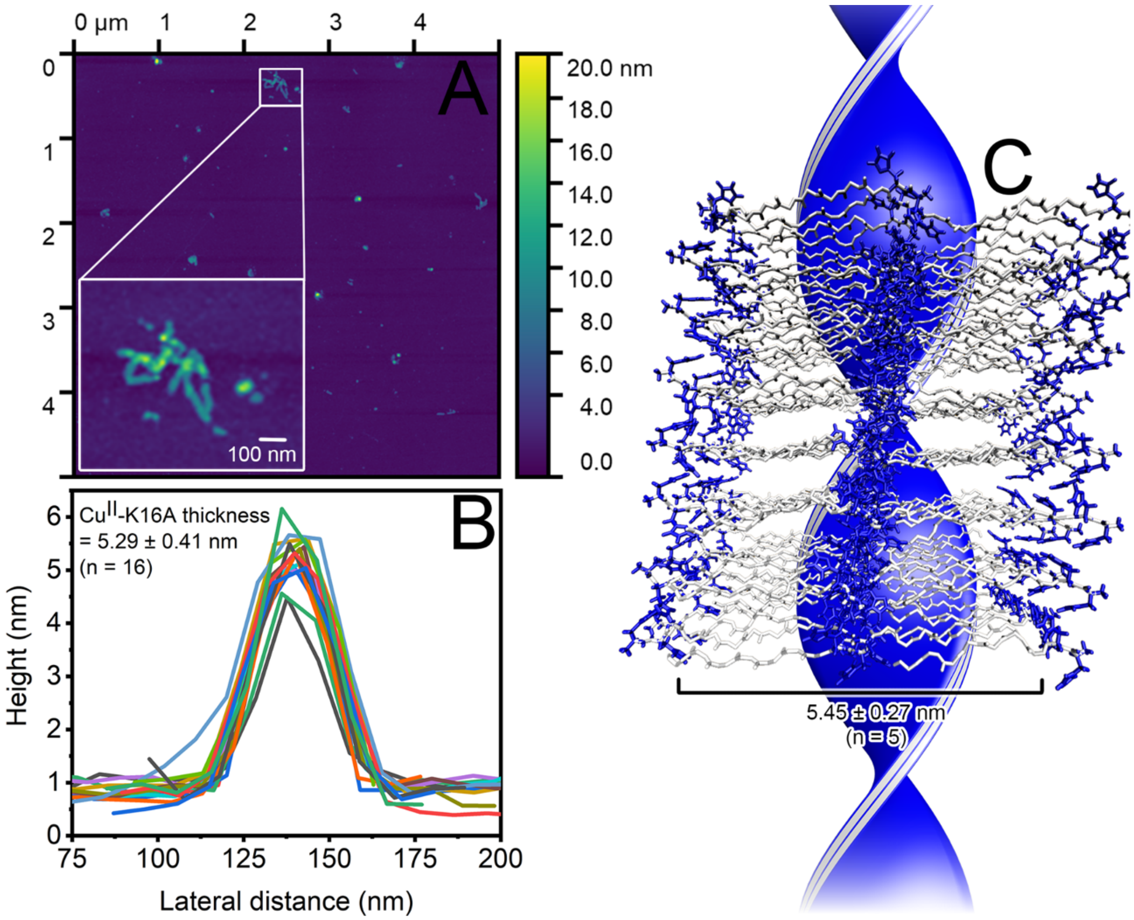

Figure 3-12. Representative Cu(II)-K16A's atomic force micrograph (A) with measurement profiles (B). Simulated structural model of K16A self-assembly's bilayer lattice constructed with experimentally defined d-spacings and strand registry (C).

mean the co-assembly has different structure of the copper complexes from the pre-assembled sample which probably has copper ions on the surface or between the bundled fibers. According to the Prenesti's report[4], that (Im)$_2$(ammino)$_2$ coordination for 573 nm absorption, and (Im)(ammino)(hydroxo)$_2$ coordination for 600 nm can be predicted (Fig 3-10) and this result is consistent with the differences of copper ions inside of the co-assembly and outside of the fibers. The copper complex, which has 600 nm maximum absorption, outside of the fiber will have hydroxy ligands due to it is exposed to the solvent, water. However, the Cu(II) co-assembly at the particle phase has different maximum absorption at 593 nm (Fig 3-10B). The prediction by the ligand-spectrum correlation can be matched (Im)(Ammino)$(hydroxo)_2$ or $(Ammino)_2(hydroxo)_2$, which also means the particles' copper ions are interacted with water molecules in the liquid-like condensates. The consistent λ_{max} of oxidized K16A-Cu(I) co-assembly, which has Cu(II) made by oxidation of Cu(I) causing no morphological changes, with the matured K16A-Cu(II) co-assembly indicates that the oxidation state changes do not cause overall structural shifts. The redox chemistry of the co-assembly will be more elucidated in next 3.2.3 section.

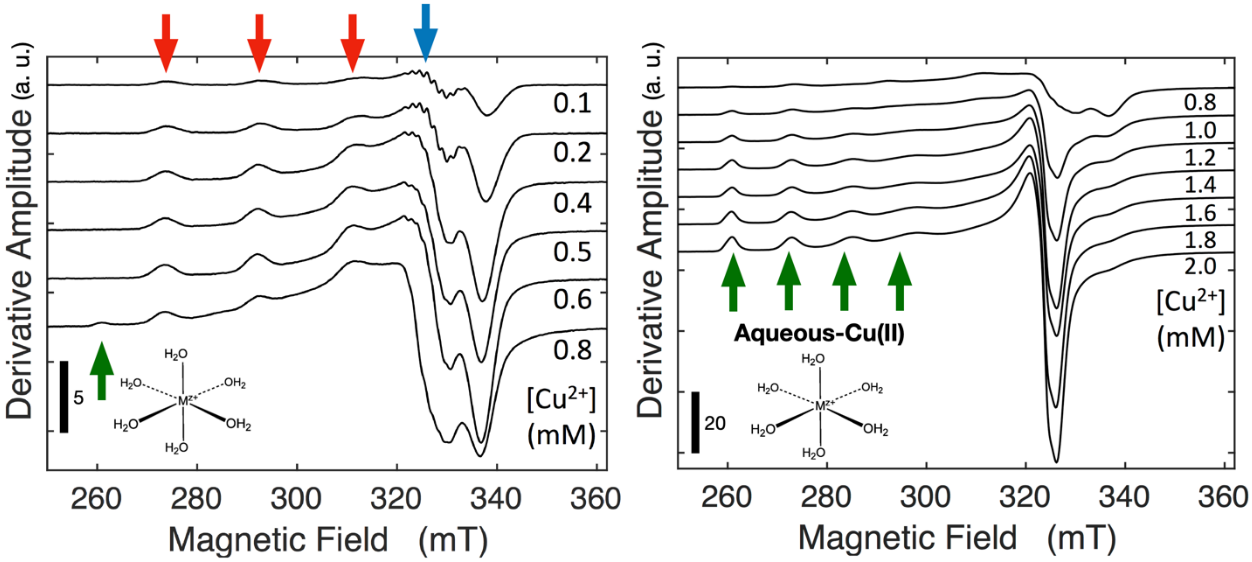

Figure 3-13. EPR spectra of K16A-Cu(II) co-assemblies with different Cu(II) concentration (0.1 mM - 2.0 mM). All samples have the same 1.0 mM concentration of K16A. Red and blue allows indicate hydperfine and superhyperfine features of Cu(II)-histidine, interaction, respectively. Green arrows present aquo-Cu(II) (inset) features.

In order to define the strand conformation of the co-assembly, 13C-15N rotational-echo double-resonance (REDOR) NMR analyses with isotope labeled K16A was conducted, which shows anti-parallel and doubly out-of-register strand conformation with beta sheet strands (Fig. 3-11). Atomic force microscopy (AFM) analysis shows that the K16A-Cu(II) co-assembly has 5.29±0.41 nm thickness which is higher than the K16A self-assembly's AFM result, 3.49±0.25 nm[1]. The simulated expected bilayer thickness, 6.4 nm is slightly higher than the measured thickness (Fig. 3-12B). This is because the fibers on the AFM grid were dried, so the overhanging end of strands of the doubly out-of-register are collapsed making slightly less height. The calculation of the bilayers without overhanging residues indicates the thickness is 5.45±0.27 nm which is consistent with the measured result (Fig 3-12).

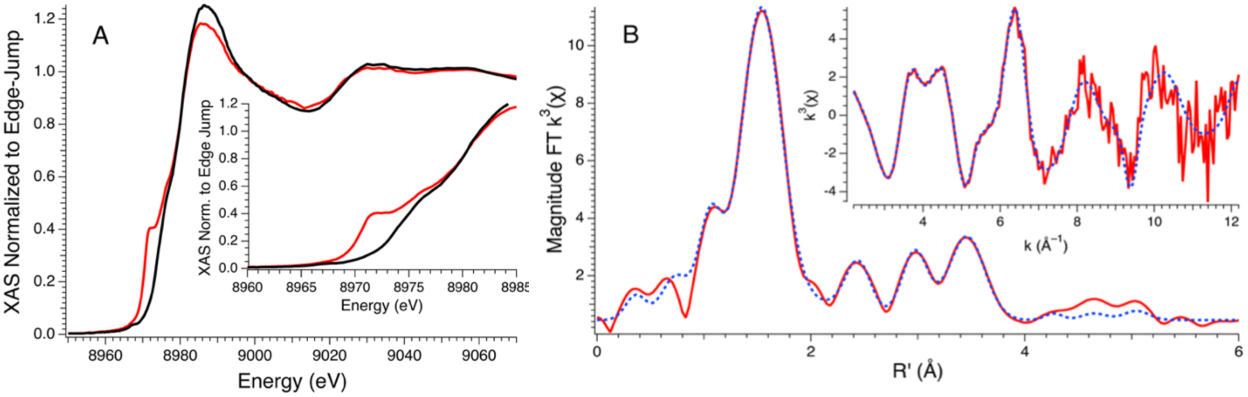

Figure 3-14. (A) XANES region of the Cu K-edge X-ray absorption spectrum for oxidized (black) and reduced (red) Cu-K16A assemblies with magnified (inset) pre-edge features. (B) k^3 -weighted EXAFS spectrum of Cu(II)-K16A (solid red) with reported bis-His fit (dashed blue) with k^3 -weighted magnitude Fourier transform of the EXAFS (inset). bis-His fit: E_o =8984.3 eV Shell #1 Cu-O: n = 2 (restrained), r = 1.988(3) Å, σ^2 = 0.0041(2) Å^2 ; Shell #2 Cu-imidazole: n = 1 (restrained) r = 2.022(4) Å, σ^2 = 0.0028(3) Å^2 , θ = 4(1)°, φ = 133(16)°; Shell #3 Cu-imidazole: n = 1 (restrained) r = 2.057(4) Å, σ^2 = 0.0019(4) Å^2 , θ = 8(5)°, φ = 135(11)°;ε^2 = 0.81. For definition of angles in fits, refer to Shearer and Soh[5].

Electron paramagnetic resonance (EPR) analysis showed that four hyperfine features (one of four is overlapped with superhyperfine features) which are result from the interaction between an unpaired electron of Cu(II) and copper's nuclei with spin, I=3/2 (Fig 3-13, Red allows). The superhyperfine features show the characteristic splitting of coordination between an unpaired electron of Cu(II) and ^{14}N (I=1) ligands which are from the histidine residues of K16A. The EPR analysis also presents spectra of 1 mM K16A peptide co-assembly with titrated Cu(II) from 0.1 mM to 2.0 mM. As the concentration of Cu(II) increase, the vibronic features of superhyperfine are getting less-resolved and aquo-Cu(II) features are getting higher which is described green arrows in figure 3-13, which means that copper bindings site of K16A are saturated and exceed copper ions form aquo-Cu(II) (Fig. 3-13, inset). Considering that the first aquo-Cu(II) was shown in the sample with 0.8 mM of Cu(II), the saturation is made with around 1:0.8 ratio of K16A:Cu(II).

K-edge X-ray absorption spectroscopy analysis was performed for the more information of coordination of copper in the co-assembly. As the sample with low copper concentration showed the fine vibronic features, samples for the X-ray absorption spectroscopy were prepared with co-assemblies of 6 mM of K16A and 1.2 mM of Cu(II) (0.2 eq.). A weak pre-edge feature at 8972.5(1) eV for a nominal Cu(1s ->3d) transition, and an additional shoulder in the edge at 8978.1(5) eV which is corresponding to the Cu(1s->4p) transition were shown in the X-ray absorption near edge structure (XANES) region, which indicates four-coordinate square-planar Cu(II) (Fig. 3-14, A, Black)[16-17]. The spectrum in extended X-ray absorption fine structure (EXAFS) region is also supporting the four ligands' coordination for a Cu(II) complex (Fig. 3-14, B). Electron spin echo envelope modulation (ESEEM) spectroscopy was also used to get more details of the

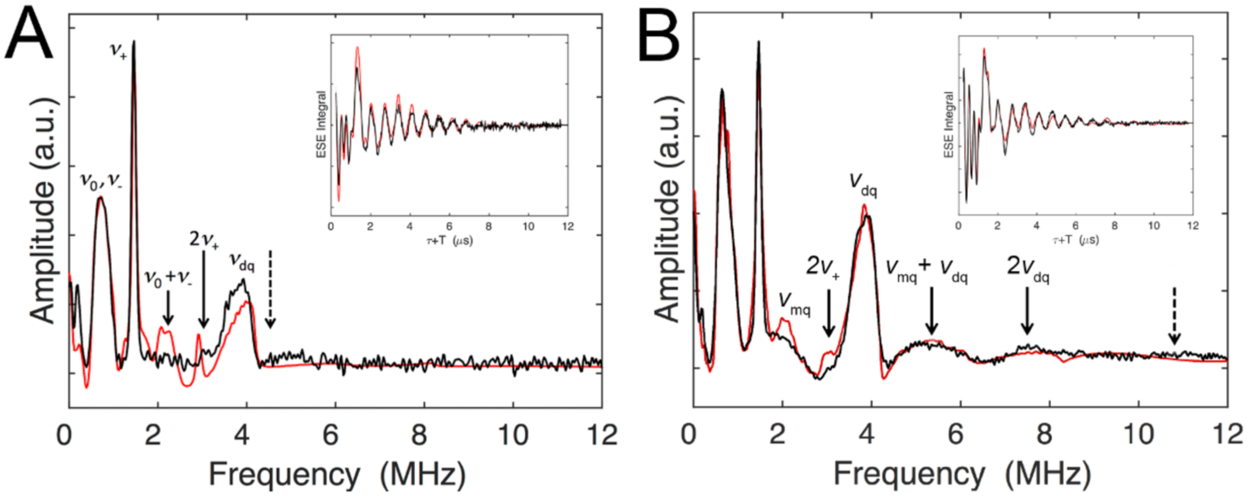

Figure 3-15. ESEEM frequency spectra (black lines) for dephasing times, τ, of 160 ns (A) and 310 ns (B) with respective free induction decay (FIDs) (insets) and fits (red lines). Features arising from 14 N nqi and superhyperfine coupling with the unpaired electron spin on the Cu(II) are described in the text and indicated by solid arrows.

coordination of Cu(II) complex in the K16A-Cu(II) co-assembly (Fig 3-15). Superhyperfine coupling of the unpaired electron spin of Cu(II) with ^{14}N nuclear spin of the remote nitrogen in each coordinating histidine was investigated by three-pulse ESEEM spectroscopy[18-19]. To enhance features that are from the ^{14}N nuclear quadrupole interaction (nqi) and ^{14}N superhyperfine combination features, pulse sequence delay times, τ = 160 ns and 310 ns respectively, were chosen, minimizing the ^{1}H Larmor signal. The nqi frequencies ν_0, ν_-, ν_+, and $2\nu_+$, which indicate the remote ^{14}N and two histidine ligands of a Cu(II) complex (Fig 3-15A). By fitting (Fig 3-15, red lines), two major coordination of Cu(II) complexes in the co-assembly, mono and bis-His in about 4:1 ratio respectively, were considered. In the ESEEM frequency spectra for 310 ns dephasing time

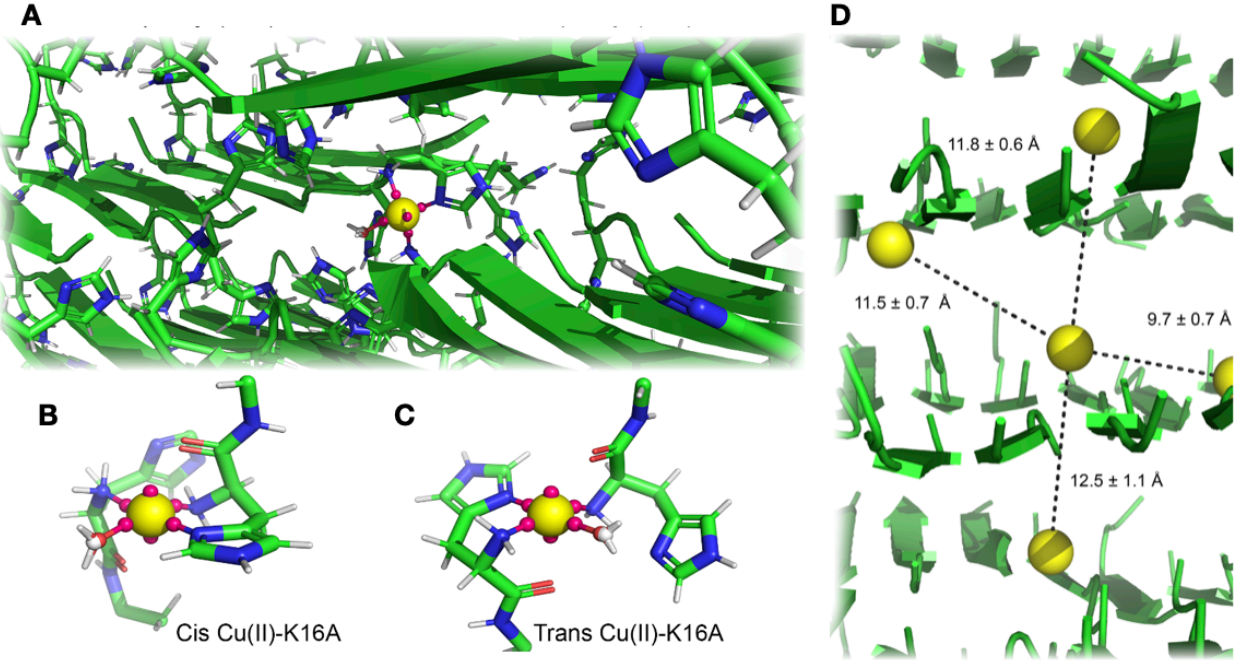

Figure 3-16. Simulated mono-His Cu(II)-K16A assembly with ESEEM and XAFS restraints as a single site featuring a dummy copper atom (yellow sphere) with six ligand-localizing dummy charges (pink spheres). Non-histidine sidechains are hidden for clarity (A). Plausible, time-averaged coordination spheres extracted from separate simulations featuring cis (B) and trans (C)-positioned N-termini ligands consistent with the spectroscopic data. Simulated Cu(II)-K16A lattice with five DCUs in adjacent laminates and strands with Cu(II)- Cu(II) distances shown. Sidechains are hidden for clarity (D).

shows the double quantum feature with self- and mono-quantum combination lines ($2\nu_{\mathrm{dq}}$, and $\nu_{\mathrm{mq}} + \nu_{\mathrm{dq}}$) which indicate the orientation of the two coordinating imidazole rings of histidine[20-22]. ESEEM simulations lead to Euler angles of [-50°, -94°, -100°] ± 10° which by the two histidine ligands are rotated[23].

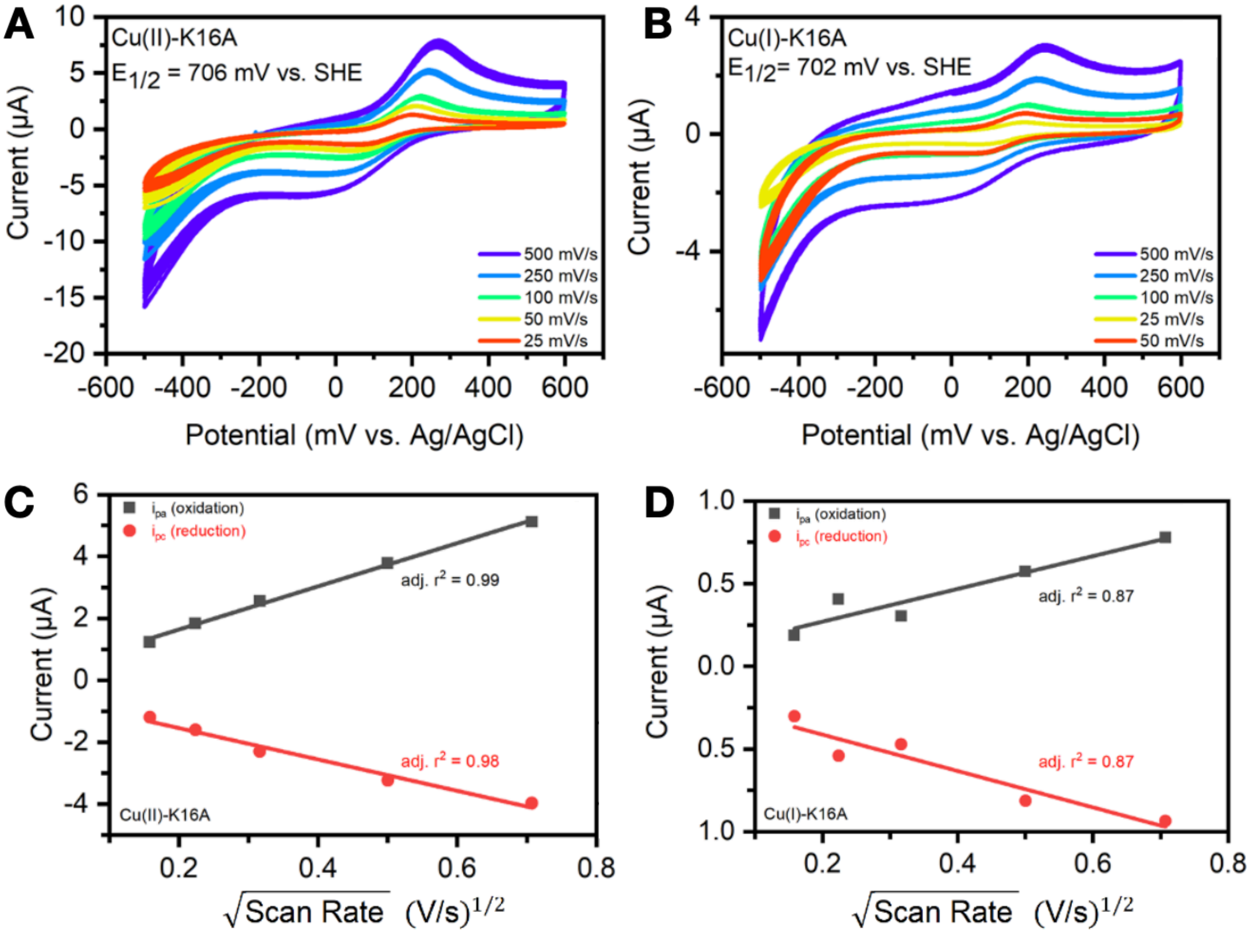

Figure 3-17. Cyclic voltammograms of K16A-Cu(II) (**A**) and K16A-Cu(I) (**B**). Anodic (black) and cathodic (red) currents as a function of square root of V/s (C, D) for Cu(II)- and Cu(I)-K16A respectively.

With the spectroscopic and structural data such as ssNMR, UV/Vis, ESEEMs, XAFS, and XRD, Simulated models were reconstructed by Dr. Anthony sementilli who was a co-worker and former graduate student in my lab. The mono-His Cu(II) complex with *cis* and *trans* forms, and bis-*cis*-His structure were modeled and showed consistency with the spectroscopic and structural data (Fig 3-16A, B, and C). Moreover, the simulation

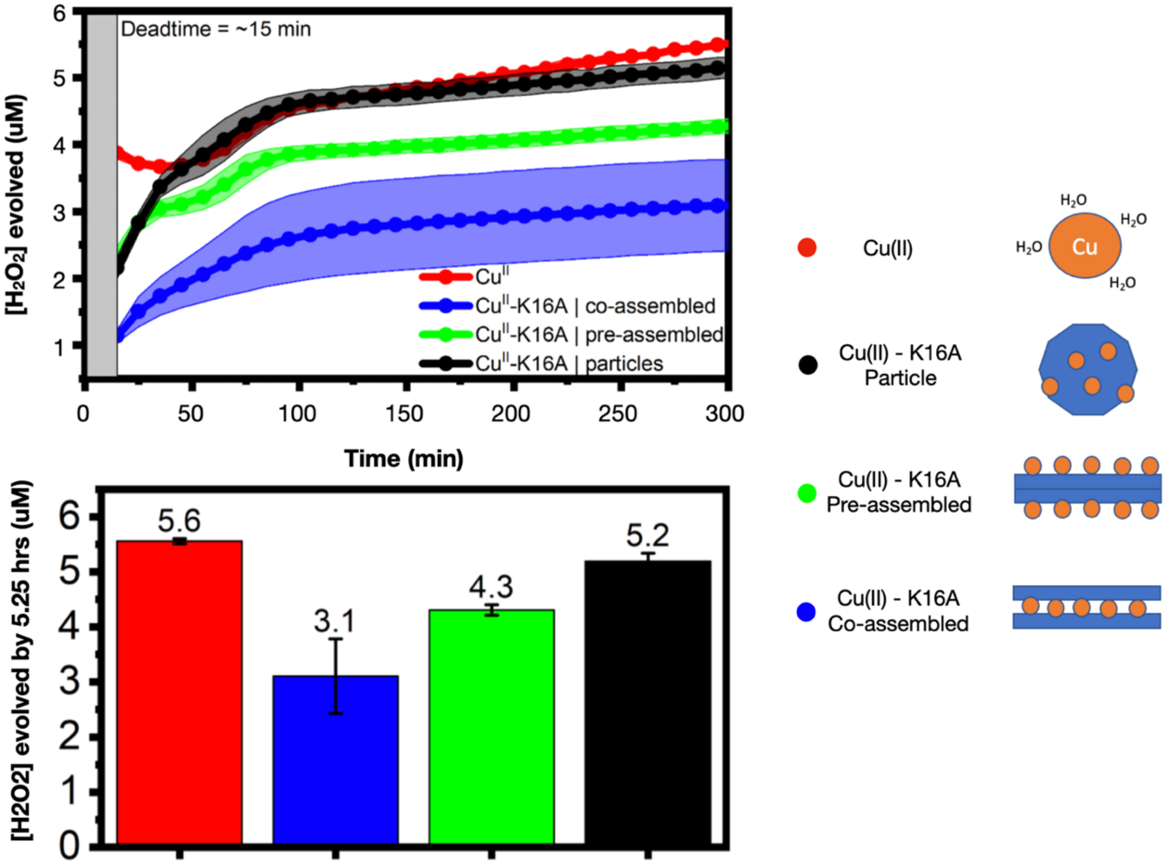

Figure 3-18. (Top) H_2O_2 production reported as resorufin fluorescence via an Amplex Red Assay across only Cu(II), particulate (unassembled), pre-, and co-K16A-Cu(II) preparations (Right). (Bottom) Cumulative H_2O_2 evolution across measured samples by the final timepoint. All samples were diluted to a final concentration of 0.1 mM K16A peptide and 0.08 mM Cu(II) via sample preparation.

with multi copper units shows average distances between Cu(II) ions within 9.7-12.5 Å (Fig 3-16D), which is consistent with the EPR data that does not have spin-spin interaction between unpaired electrons of adjacent Cu(II) ions within 7 Å[24]. Since similar or longer distances are found in electron transport chain proteins, the simulation results suggest the possibility of electron transfer between the copper metals in the co-assemblies with high reduction potentials which can be applied for redox chemistry[25-29].

3.2.3 Catalytic reactivities of K16A-Cu(II)/Cu(I) co-assemblies

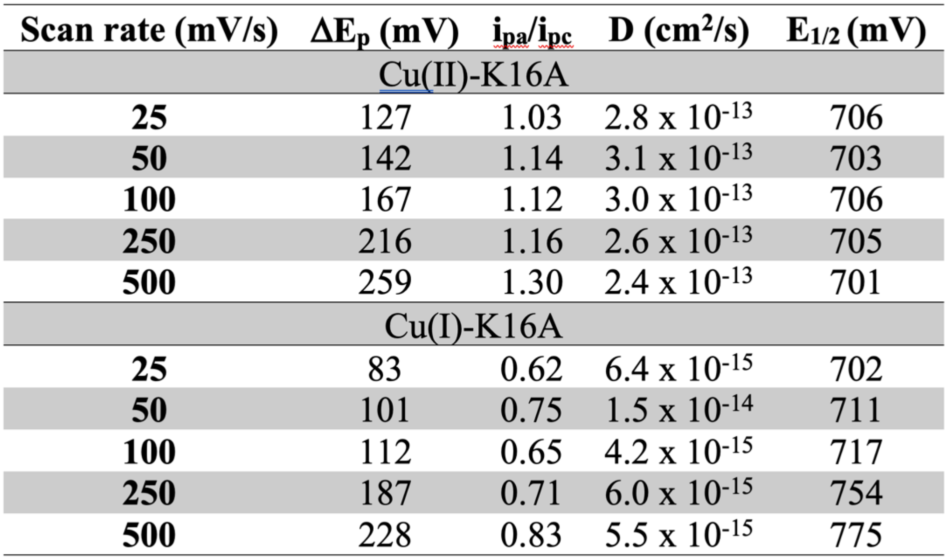

Scan rate (mV/s)	ΔE_p (mV)	i_{pa}/i_{pc}	D (cm^2/s)	$E_{1/2}$ (mV)
Cu(II)-K16A				
25	127	1.03	2.8×10^{-13}	706
50	142	1.14	3.1×10^{-13}	703
100	167	1.12	3.0×10^{-13}	706
250	216	1.16	2.6×10^{-13}	705
500	259	1.30	2.4×10^{-13}	701
Cu(I)-K16A				
25	83	0.62	6.4×10^{-15}	702
50	101	0.75	1.5×10^{-14}	711
100	112	0.65	4.2×10^{-15}	717
250	187	0.71	6.0×10^{-15}	754
500	228	0.83	5.5×10^{-15}	775

Table 3-1. Summary of electrochemical data derived from Cu(II)- and Cu(I)-K16A.

To test the redox properties that were expected from the previous chapter, cyclic voltammetry (CV) was used to measure electrochemical properties of the K16A-Cu co-assemblies. Samples prepared with 2 mM K16A, 1.6 mM $CuCl_2$, 25 mM MES, and 0.8 mM sodium ascorbate (for the Cu(I) co-assembly), and the final concentrations for the CV have 1 mM K16A, 0.8 mM $CuCl_2$, 25 mM MES, and 200 mM KCl. The cyclic voltammograms for Cu(II) and Cu(I) co-assemblies show reversible curves with different scan rates and $E_{1/2}$ of 706 mV and 702 mV, respectively (Fig. 3-17A, and B). These reduction potentials are much higher than mononuclear copper proteins by over two-fold[30] and also similar with laccases' reduction potentials ranging from 400 mV to 800 mV[31]. In addition, the plots of both co-assemblies with peak-currents as a function of square root of the scan rate are linear, which means electro chemical quasi-reversibility. The calculated diffusion constants from Randles-Sevcik equation, modified for quasi-reversible systems at room temperature (Eq. 1), shows slow diffusion rate ranging 10^{-13} - 10^{-15} cm^2/s (Table 3-1).

$$i^{quasi} = 2.62\ X\ 10^5 FAcn^{\frac{3}{2}}\sqrt{Dv} \qquad (Eq. 1)$$

i^{quasi} = forward voltammetric current (A), F = Faraday's Constant (96,485 C/mol), A = electrode area (0.071 cm^2), c = concentration (0.0008 M), n = number of electrons (1), v = scan rate, and D = diffusion coefficient (cm^2/s)[32].

The slow-diffusion rate with linear Cottrell-like relationships has been reported in bulky materials such as metalloporphyrin metal organic frameworks (MOFs)[33-34], and ferroocene- or Ru-(bpy)$_3$-embedded polymers[35-36] which show charge-hopping between metal centers. Based on these cases, K16A-copper co-assemblies broad and queasy-reversibility can be from multiple heterogeneous electron hopping between coppers in the copper arrays inside of the bilayers. Evolution of reactive oxygen species by redox chemistry of Cu-amyloid beta complexes have been reported[37-42]. To test redox chemical properties of the Cu(II) co-assemblies, Hydrogen peroxide evolution experiments with Amplex Red Assay kit were performed. The assay works with hydrogen peroxidase that converts amplex red to resorufin by using hydrogen peroxide which is reduced by Cu(I). The converted resorufin molecules are red fluorescent, so measuring the fluorescence can detect the concentration of hydrogen peroxide evolved by copper's redox chemistry. Four different samples, Cu(II) without peptides, particles of K16A-Cu(II) co-assembly, pre-

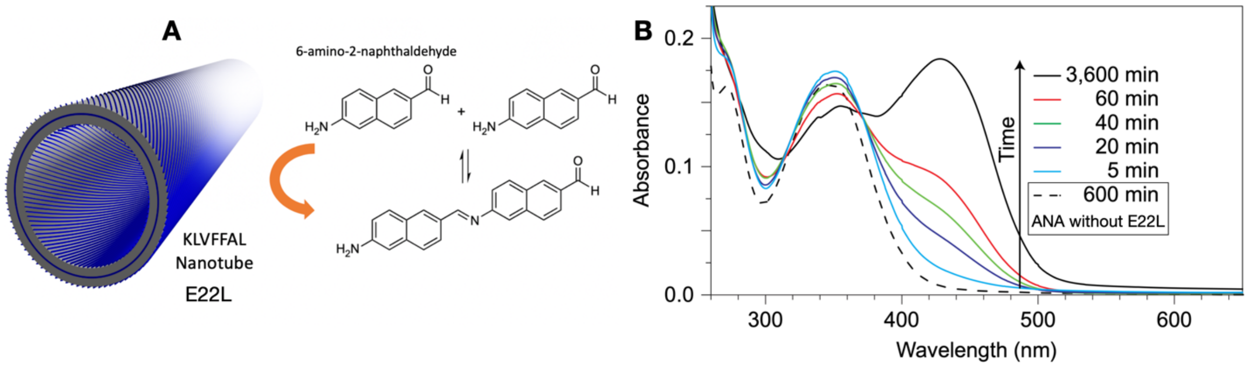

Figure 3-19. Condensation reaction of 6-amino-2-naphthaldehyde catalyzed by E22L nanotubes (A), and UV/Vis spectra of the reactions.

assembled K16A and Cu(II) mixture, and K16A-Cu(II) co-assembly, were prepared. The higher reactivities of the samples of Cu(II) only and the particles than the co-assemblies were expected because of the limitation of accessibility of copper ions in the co-assemblies which have been reported[37]. The results show the expected relative reactivities (Fig. 3-18). Although the reaction site is still unknown, the reactivity of coppers in the co-assemblies was found. The co-assembly samples has the lowest reactivity, and the buffered Cu(II) and the particles have the higher reactivities according to the results. Pre-assembly sample also has relatively less reactivity than the two samples, which can interpret that the copper ions are buried in the between bundled fibers (Fig. 3-4B).

To develop and further test the redox chemical properties of K16A-Cu co-assemblies, experiments for redox catalytic reactivity of the co-assembly were designed. Previously enzyme-like catalytic activities of peptide self-assemblies such as a condensation reactions catalyzed by E22L peptide self-assembly nanotubes (Fig. 3-19)[43]. As described in Figure 1-5 in Chapter 1, anti-parallel out-of-register strand conformation

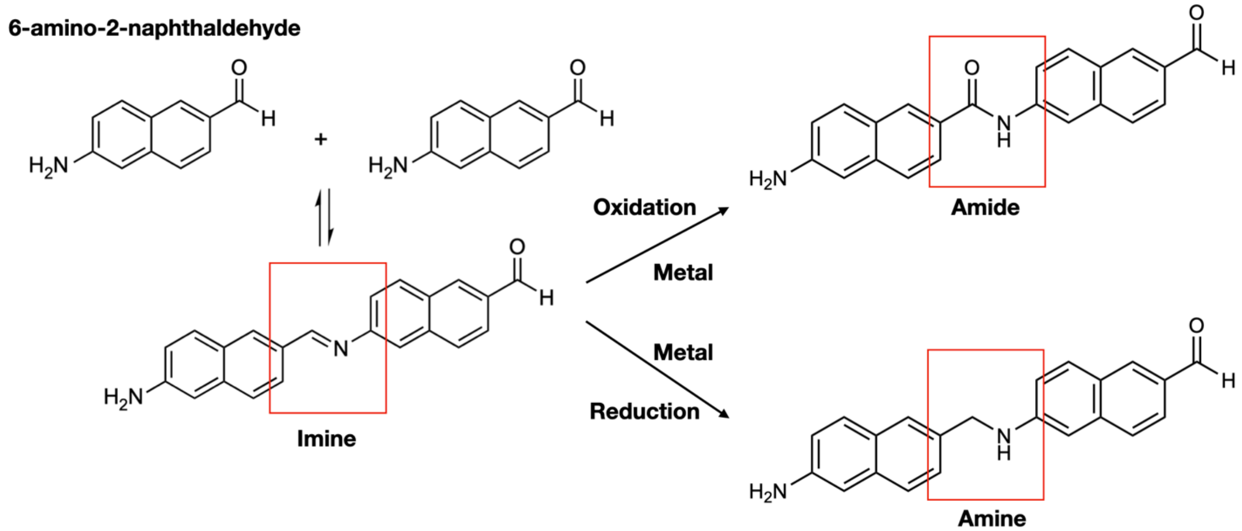

Figure 3-20. Reaction scheme of K16A-Cu co-assemblies' redox chemistry with imine bond from the condensation.

of E22L forms exposed lysine from hydrophobic surface which consists of leucine on C-terminal. Small hydrophobic molecules can be bound to the surface and catalyzed by the lysine's acid-base catalytic properties. Also, N-terminal histidine's better catalytic activity was also reported from the research. In addition to the enzyme-like catalytic activity, introducing redox properties of the peptide-metal co-assemblies can suggest metalloenzyme-like catalytic redox chemistry. The experiments for redox catalytic reactivity of the co-assembly were designed as described in figure 3-20. Using the redox chemistry, K16A-Cu co-assemblies can oxidize or reduce the imine bond from the condensation reaction, making amide or amine, respectively. The new oxidized/reduced bonds are not reversible by hydrolysis, so longer polymers can be catalyzed. Moreover, the amide formation can suggest a new way to synthesize peptides or proteins that is not used in biology. Based on the reported data of anti-parallel out-of-register strand conformation of the K16A-Cu co-assembly (Fig. 3-11) and the better catalytic activity of histidine[43], the hypothesized conditions for enzyme-like catalytic activities are satisfied.

The catalytic activities of the K16A assembly series for the condensation with 6-amino-2-naphthaldehyde (ANA) was tested. When ANA molecules are oligomerized

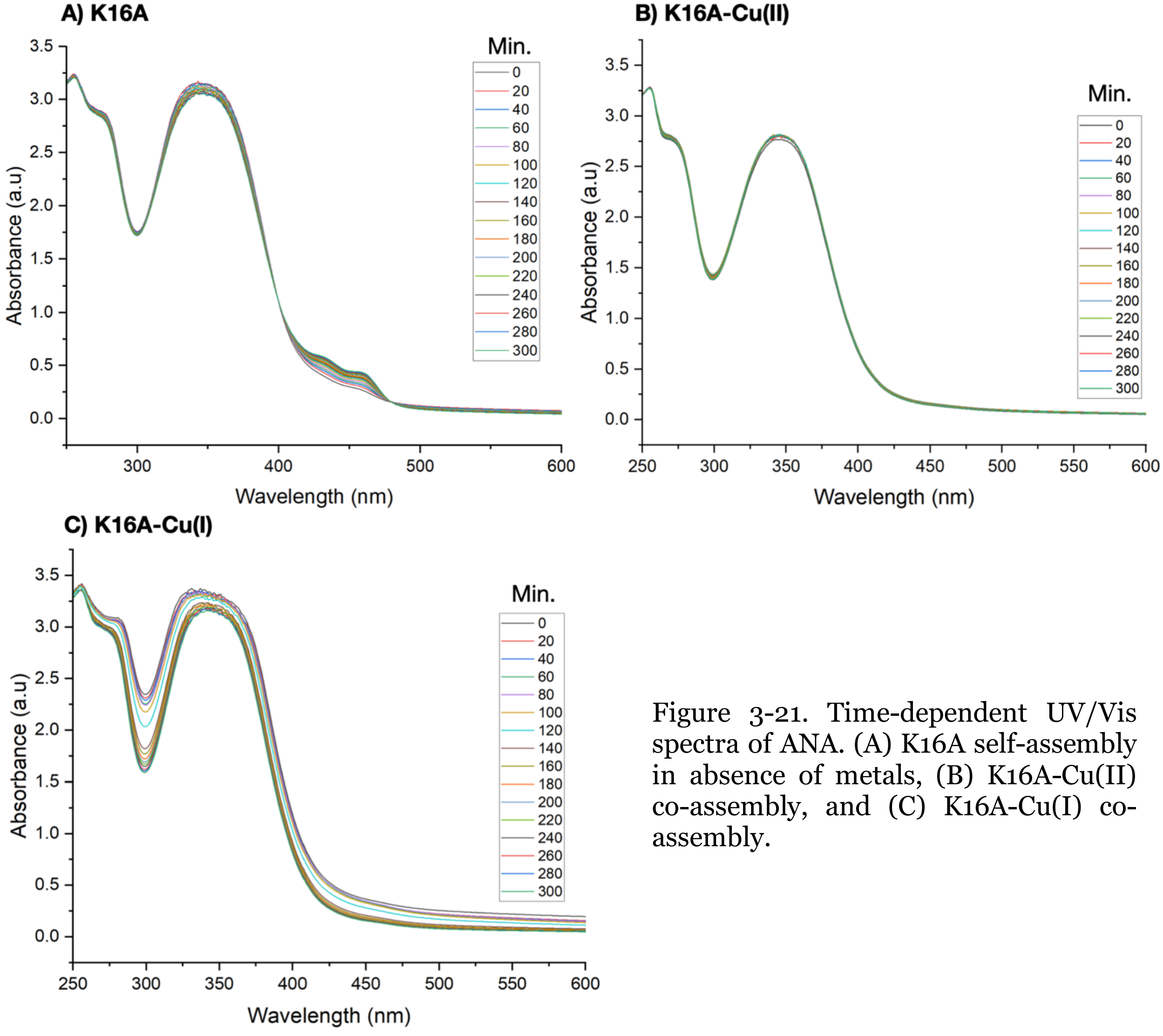

Figure 3-21. Time-dependent UV/Vis spectra of ANA. (A) K16A self-assembly in absence of metals, (B) K16A-Cu(II) co-assembly, and (C) K16A-Cu(I) co-assembly.

forming imine by the catalytic activity, the longer pi-conjugation between naphthalene through the imine makes the oligomers absorb red-shifted wavelength, so that the oligomerization can be detected by UV/Vis spectroscopy (Fig. 3-19/20). 0.5 mM ANA was prepared with K16A self- or co-assemblies (with 0.3 mM CuCl2 and 0.15 mM Ascorbate if necessary) for UV/Vis spectroscopy. K16A self-assembly shows much less intensities of red-shifted peaks than E22L, which means less catalytic activity of K16A self-assembly. In addition, two different red-shifted peaks at 430 nm and 460 nm were found in the UV/Vis spectra that can be cis and trans forms of dimerized ANA, or dimers and trimers of the substrates. However, K16A-Cu(II)/(I) co-assemblies did not show the red-shifted peak while the monomer of ANA peaks has high intensities. Even though K16A self-assembly has catalytic activity, it is not enough high like E22L.

3.2.4 K16AL and K16AL-Cu(II)/Cu(I) Co-assemblies and its catalytic reactivities

I hypothesized that the low/no catalytic activities of the K16A assembly series can be a result from low hydrophobicity of the surface of the nanomaterials. The C-terminal alanine of K16A cannot make enough hydrophobicity on the surface to bind the small hydrophobic molecules, because again, the C-terminal residues are important when the peptides form the surface with anti-parallel out-of-register conformation (Fig. 1-5). In order to increase the hydrophobicity of the surface, leucine was introduced on the C-terminal of the K16A sequence, making H-HHQALVFFAL-NH_2 (K16AL). In addition to the hydrophobicity of surface, C-terminal modifications have a significant impact on morphologies of the peptide assemblies. Based on Lynn lab experience, assemblies of peptides with C-terminal leucine or valine form nanotubes that have more surface area like E22L. Morphological changes from nanofibers to nanotubes or nanoribbons at least with larger surface were also expected as well as with more hydrophobicity.

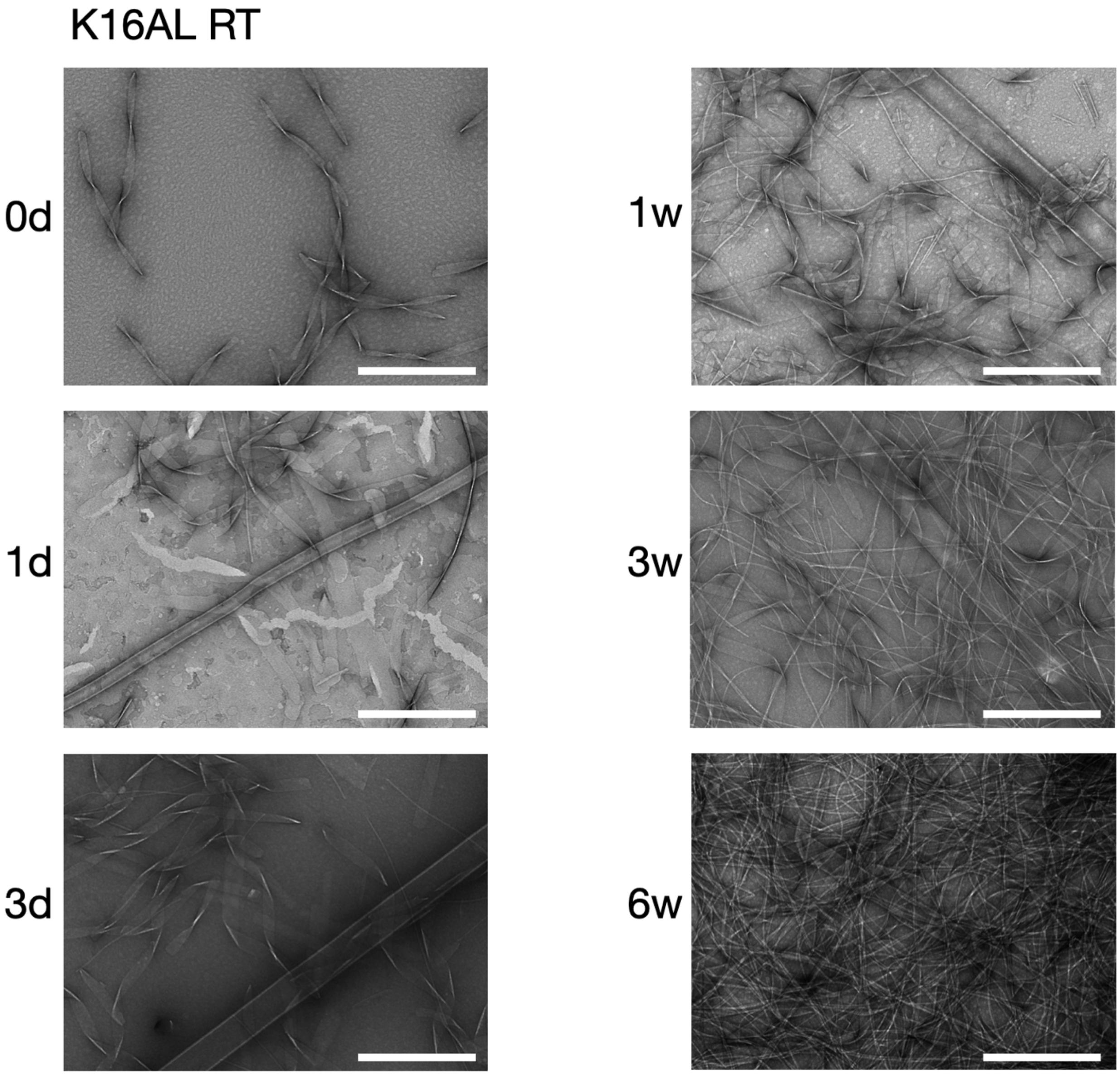

Figure 3-22. Representative TEM images of K16AL self-assembly at room temperature at different time points. Scale bars are 500nm.

K16AL peptides were synthesized and tested for assembly properties such as morphologies and kinetics. Unlike K16A, K16AL forms nanostructures at the initial time point, and it precipitated when 2 mM concentration of K16AL used. This is probably resulted from higher hydrophobicity of the K16AL sequence that accelerates hydrophobic interaction between peptide strands since the solvent is hydrophilic. This phenomenon

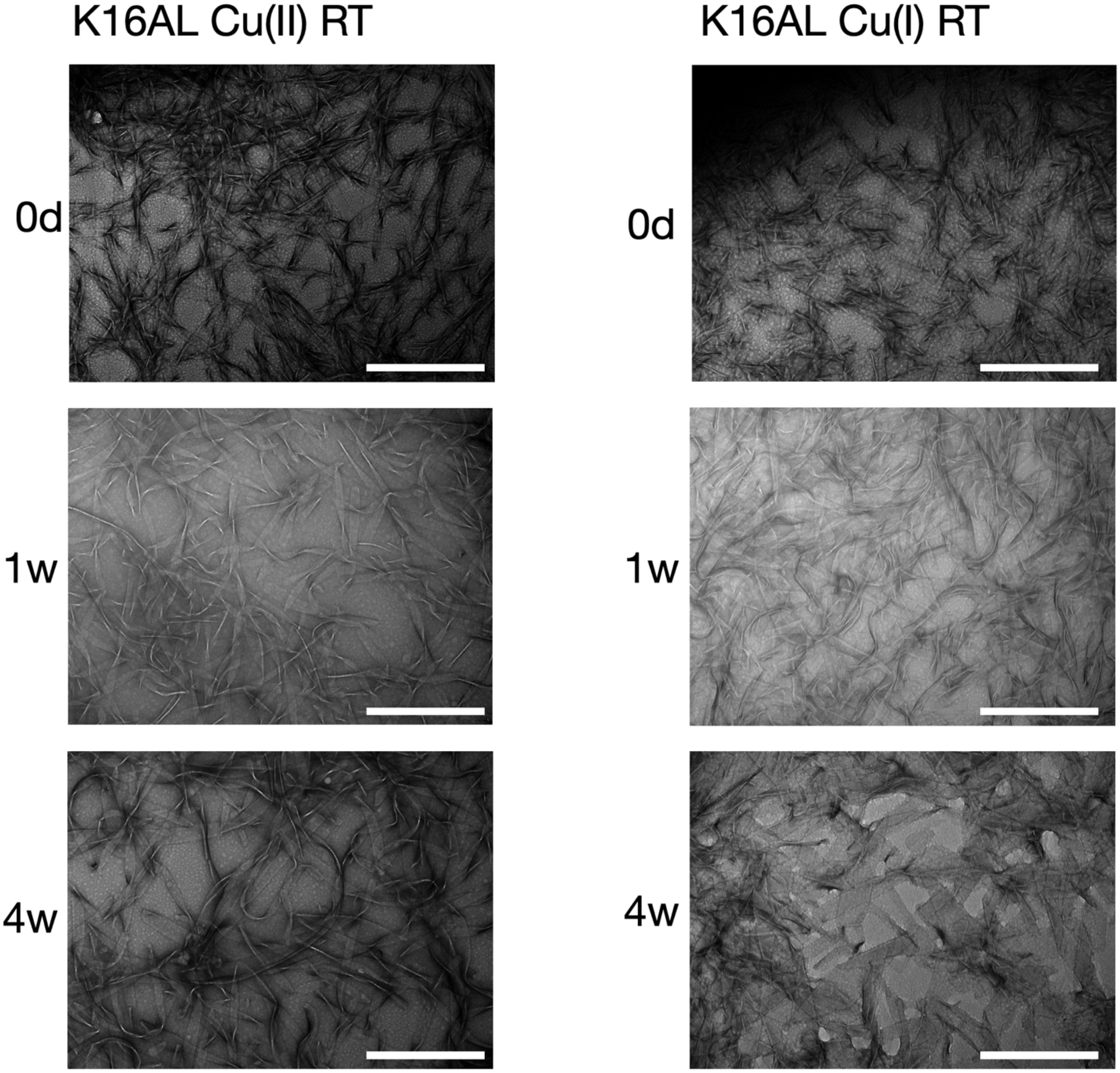

Figure 3-23. Representative TEM images of K16AL-Cu(II) and -Cu(I) assemblies, left and right respectively, at room temperature at different time points. Scale bars are 500nm.

was shown in all K16AL assembly series. Thus, the assemblies were prepared with 0.5 mM K16AL peptides. K16AL peptide assembly in absence copper ions at room temperature forms twisted nanoribbons at the initial time point (Fig. 3-22). However, as time goes by,

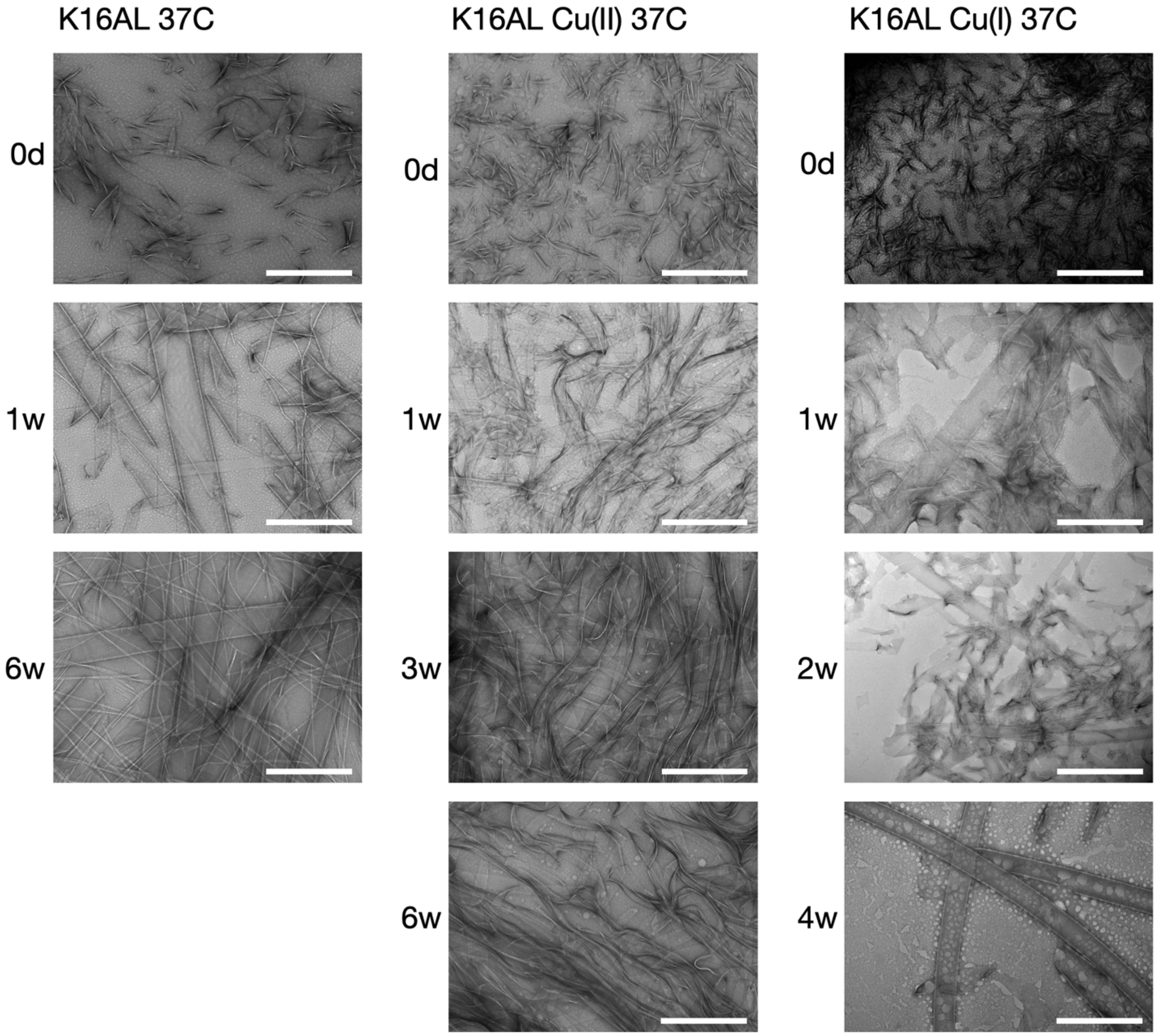

Figure 3-24. Representative TEM images of K16AL assembly series, K16AL (left), K16AL-Cu(II) (middle) and K16AL-Cu(I) right respectively, at 37°C at different time points. Scale bars are 500nm.

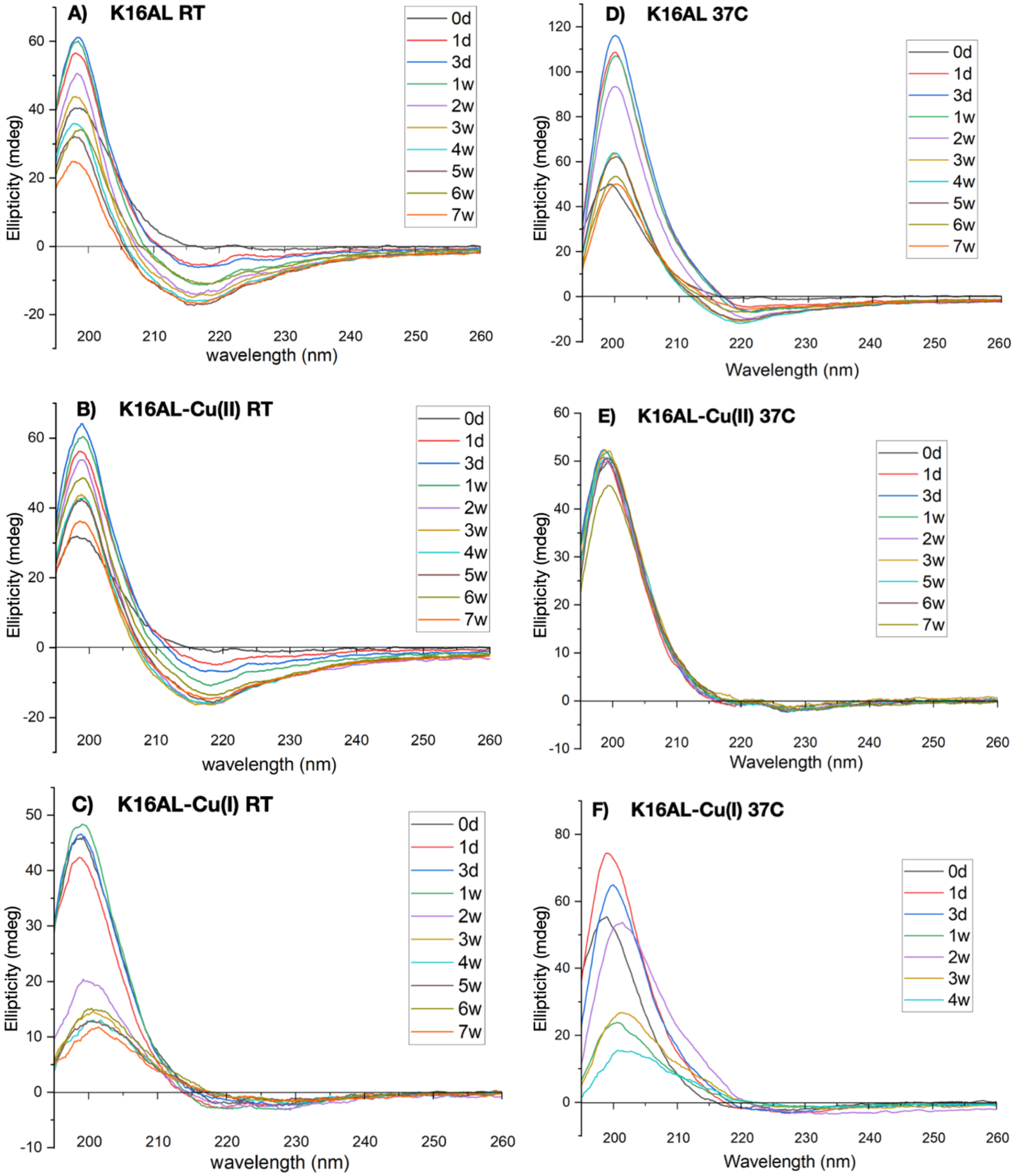

Figure 3-25. Time-dependent CD spectra of the K16AL assembly series at RT and 37°C. A) K16AL at RT, B) K16AL-Cu(II) at RT, C) K16AL-Cu(I) at RT, D) K16AL at 37°C, E) K16AL-Cu(II) at 37°C, and F) K16AL-Cu(I) at 37°C

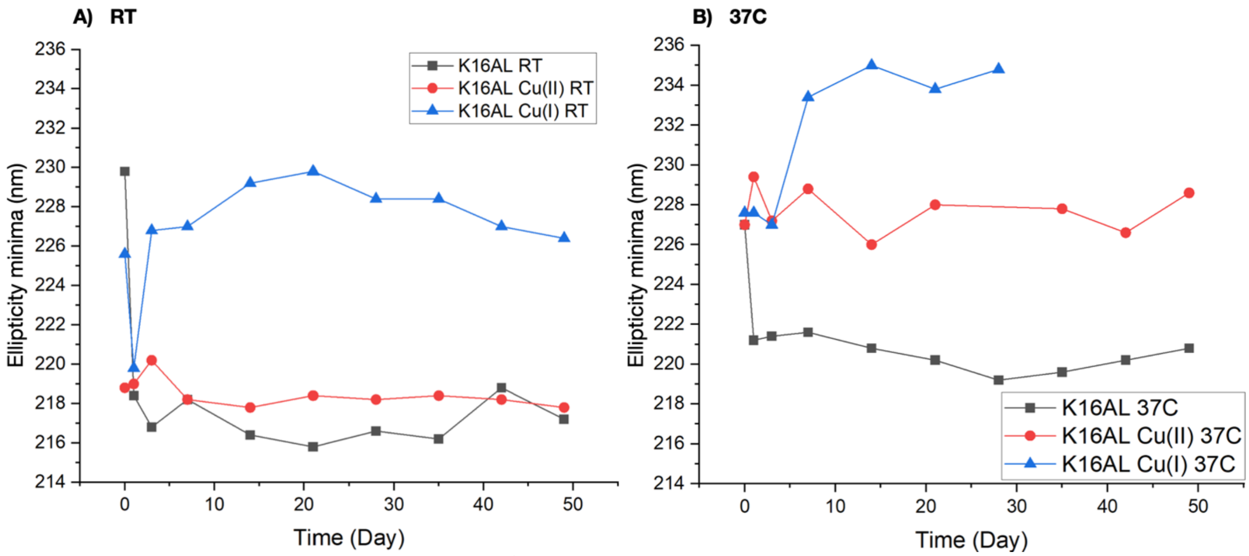

Figure 3-26. Ellipticity minima of the K16AL assembly series at RT (A) and 37°C (B).

the assembly solution showed morphological changes with heterogeneous morphologies of tubes, ribbons, and fibers. Eventually, only many fibers and few tubes were remained. Considering the final morphologies, thermodynamically favorable morphologies are fibers and ribbons. K16AL-Copper co-assemblies also forms twisted-nanoribbons from the beginning, but Cu(II) co-assembly has longer flat ribbons while Cu(I) forms much wider ribbons which looks like making nanotubes (Fig. 3-23). Previous research showed that higher temperature helps forming nanotubes from ribbons[7], thus K16AL assemblies in 37°C were tested. Although K16AL self-assembly without copper ions still has heterogeneous morphologies with fibers and tubes when it is matured, the TEM images show more tubes compared to the room temperature sample (Fig. 3-24).

To quantify the morphological changes, CD analyses were also conducted (Fig. 3-25, 26, and 27). CD spectra also show that both K16AL self-assemblies at RT and 37°C have the features of beta-sheet secondary structure (Fig. 3-25A and B). However, they

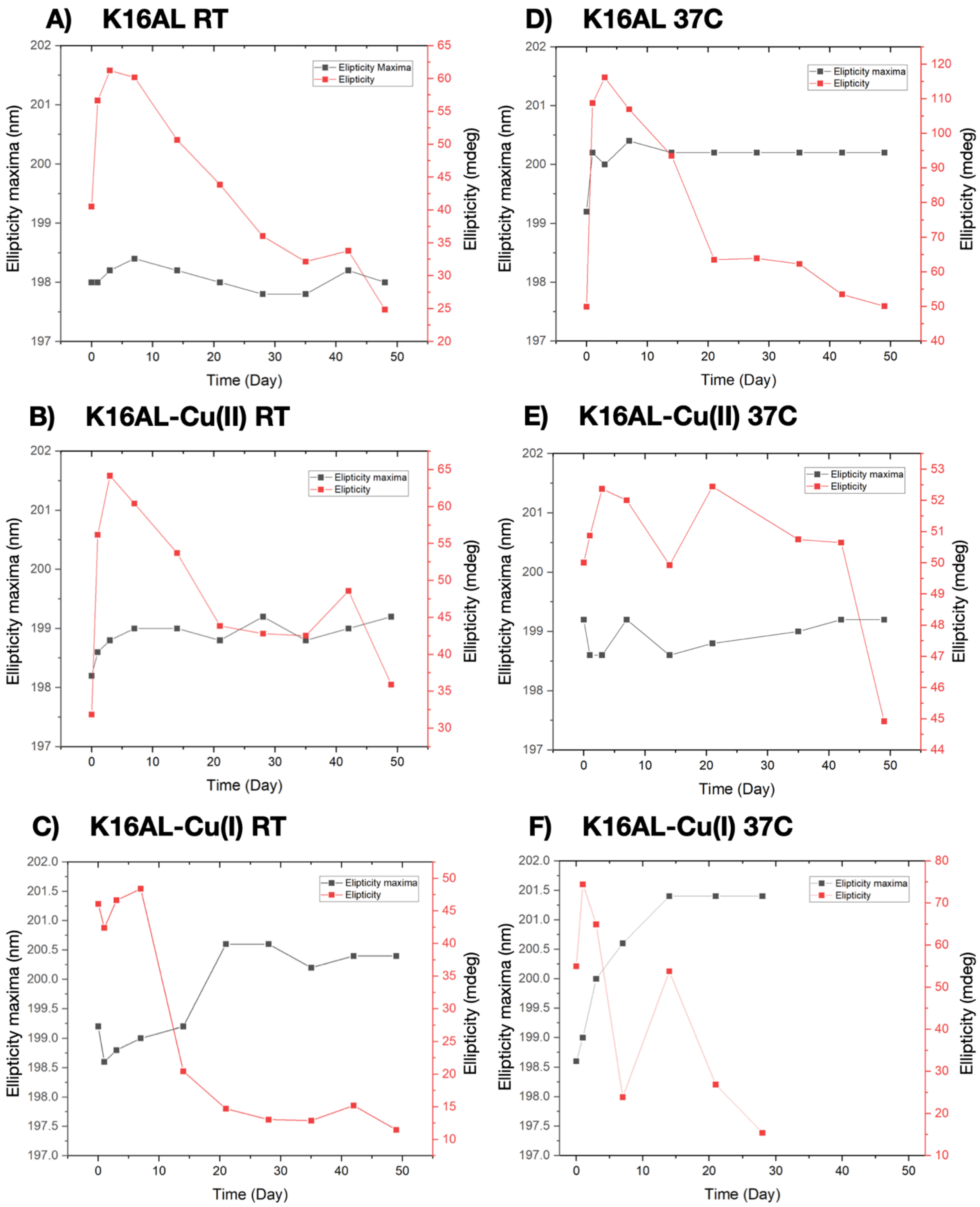

Figure 3-27. Ellipticity maxima and its ellipticities of the K16AL assembly series at RT and 37°C. A) K16AL at RT, B) K16AL-Cu(II) at RT, C) K16AL-Cu(I) at RT, D) K16AL at 37°C, E) K16AL-Cu(II) at 37°C, and F) K16AL-Cu(I) at 37°C. Note that the ellipticity maxima (black) have same scale but ellipticities (Red) have different scale in the graphs.

have different ellipticity maxima and minima; 198 nm/218 nm of maximum/minimum at RT, and slightly red-shifted 200 nm/220 nm of maximum/minimum at 37°C (Fig 3-26A and B, 3-27A and B). Even though the differences are not extensive, the reason why it is elucidated is that other K16AL-Cu co-assemblies have morphological and spectroscopical differences between K16AL assemblies and between K16A and K16AL. K16AL-Cu(II) co-assemblies at RT and 37°C have similar flat ribbon morphologies based on the TEM images (Fig. 3-23 and 3-24), but the TEM images indicates that sample at 37 °C have the flat ribbons while the sample at RT has twisted features. CD spectra present that the co-assembly at 37°C have steady spectra from the beginning with constant ellipticity minima at 228 nm which is red-shifted from typical anti-parallel conformation's minima (217 nm)[44-46], but the sample at RT has ellipticity changes of the minima at 217 nm. Both Cu(I) co-assemblies at 37°C and RT have further red-shifted ellipticity minima compared to the other assemblies and have significant changes of ellipticity maxima and its ellipticity (Fig 3-27 C and F; note that the ellipticity scale is varied). When we compare between K16AL-Cu(I) at 37°C and RT, nanotube morphology is found at the sample 37°C, while the RT sample have wide nanoribbons. Moreover, The Cu(I) co-assembly at 37°C has more red-shifted ellipticity minima and maxima than the co-assembly at RT. Since peptide assemblies follow two-step nucleation, CD-spectra usually show changes from random coil to secondary structures like alpha helix or beta sheet like the cases of K16A assembly series in the figure 3-5. Thus, the ellipticity minima moved from 200 nm to 217 nm indicating random coil and beta sheet (or alpha helix with two minima at 205 nm and 220 nm). However, the K16AL assembly series form nanostructures at the beginning and show huge features that do not indicate random coil (Fig. 3-25). This can be interpreted as evidence that K16AL assemblies have significant rapid nucleation steps because of the strong hydrophobicity and its interactions. Furthermore, unusual ellipticity maxima at round 198 nm behavior was found. Due to the transition from random coil to secondary structure, the ellipticity maxima usually increase as peptides form assembly structure, but the K16AL assemblies have decreasing the maxima's ellipticity in all samples, and further red-shifting in Cu(I) co-assemblies at 37°C and RT. These changes can be caused by transitions of twisting angles of beta-sheets that include, in this case, negative exciton chirality to positive exciton chirality, by transitions of strand conformations from anti-

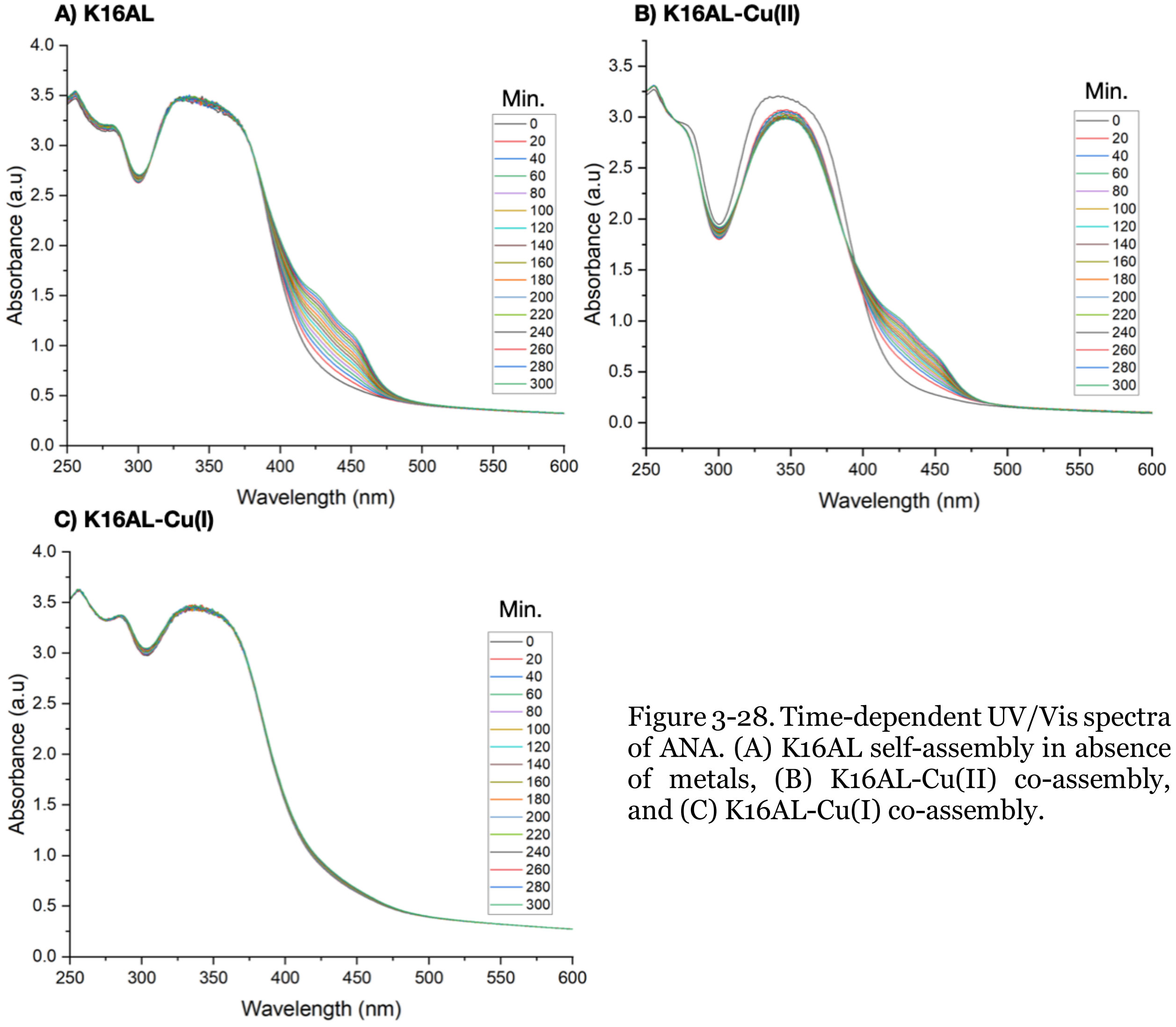

Figure 3-28. Time-dependent UV/Vis spectra of ANA. (A) K16AL self-assembly in absence of metals, (B) K16AL-Cu(II) co-assembly, and (C) K16AL-Cu(I) co-assembly.

parallel to parallel, or even by transitions of secondary structures from alpha helixes to beta sheets[44-47]. Since the high propensity of the hydrophobic core, LVFFA, from amyloid beta 42 peptide sequence to form beta-sheet secondary structure, the K16AL's cases can be from one of or both first two transitions. Kinetically captured structures of the K16A series at the initial time point of assemblies undergo transitions to have thermodynamically favorable structure. These thermodynamical transitions probably cause more extensive changes of the assemblies at 37°C. Although further structural studies should be performed to reveal detailed structures and make more supportive relationship with CD spectra, it can be expected that K16AL-Cu(I) co-assemblies at 37°C with significant red-shifting and extensive decreases in ellipticities of maxima may have nanotube morphologies with parallel strand conformations. This also can support that the K16AL self-assembly at 37°C has slightly red-shifted ellipticity minima because it has much more nanotubes, which may have parallel strand conformation, than the self-assembly at RT.

The catalytic activity for ANA condensation was investigated with the new K16AL assembly series. The samples were prepared with 0.5 mM K16AL (0.5 mM Cu(II) or Cu(I)) with 0.5 mM ANA. The catalytic activity was measured by UV/Vis spectroscopy with different time points. As shown in figure 3-28A and B, the K16AL self-assembly and K16AL-Cu(II) co-assembly have red-shifted peaks which indicate oligomerization of ANA monomers. Both peptide only samples, K16A and K16AL, have the reactivity but K16AL shows higher intensity of the red-shifted peaks, and unlike K16A-Cu(II), K16AL-Cu(II) have the red-shifted peaks, which were probably resulted from more hydrophobic surface because of the C-terminal leucine. However, Cu(I) has no activity, which is consistent with the parallel hypothesis that cannot make hydrophobic grooves, which can bind and catalyze hydrophobic substrates, on the surface.

3.3 Conclusion

In order to study behavior of peptide-metal co-assemblies and its structures which result in functions, K16A-copper co-assemblies were designed, synthesized and characterized. Between K16A self-assembly, and K16A-Cu(II)/Cu(I) co-assemblies, morphological and kinetical differences were found. K16A self-assembly takes 1~2 weeks to be matured while K16A-Cu(II) takes more than 2 months, and K16A-Cu(I) needs only 2~4 hours. Also, K16A-Cu(II) co-assembly has wider twisted ribbons than Cu(I) co-assembly. Structural studies reveal that the K16A assembly series has beta-sheet secondary structures. Further studies of K16A-Cu(II) indicates bilayer of beta sheet strands, coordination of Cu(II) complex in the co-assemblies (four-coordinate square-planar, mono and bis-His) and distance between copper ions. Through CV and Amplex red assay experiments, we found redox chemical activities of Cu(II) co-assemblies with high reduction potentials and reversibility. Even though catalytic activity of K16A self-assembly for the condensation reaction of ANA was found, it showed low activity and Cu(II) and Cu(I) co-assemblies even did not show the activities. The low hydrophobicity of C-terminal alanine was considered as the reason of low/no activities. To improve the hydrophobicity of the surface of nanostructures, leucine residue was introduced on the C-terminal of K16AL, having HHQALVFFAL sequence called K16AL. K16AL assembly series present distinct assembly kinetics and morphologies from K16A assembly series. Although further studies are needed, K16AL-Cu(I) co-assembly at 37°C forms nanotube structures with probably parallel strand conformation. As a result, K16AL-Cu(I) co-assembly did not have the catalytic activity while K16AL self- and K16AL-Cu(II) co-assemblies showed catalytic activities. Overall catalytic activities of K16A and K16AL assemblies are low, which can be resulted from the two histidine residues passivation effects on the surface, not allowing the small hydrophobic molecules to be bound on the surface. Therefore, sequences with one N-terminal histidine can be tried to prove the hypothesis and improve the catalytic activity.

3.4 Materials and methods

Synthesis and purification of peptides

Peptides were synthesized on a CEM Corporation microwave peptide synthesizer (Matthews, NC, USA) using standard Fmoc chemistry. The solid support for peptide synthesis was an Fmoc rink-amide resin (AnaSpec, Inc., Fremont, CA, USA) with a typical substitution range of 0.4-0.6 meq./g. Resin was pre-swollen in minimal dimethylformamide (DMF) for 15 min. Microwave assisted Fmoc deprotection was completed using 20% piperidine in DMF at 45-55°C for 180 sec followed by three DMF flushes. Each coupling step was performed using 0.1 M Fmoc-protected amino acid and activated with 0.1 M 2-(1H-Benzotriazole-1-yl)-1,1,3,3-tetramethyluronium hexafluorophosphate (HBTU) and 0.2 M N,N-diisopropylethylamine (DIEA) in DMF. Microwave coupling temperatures were maintained within 75-82 °C for 300 s then rinsed with DMF 3x. Histidines were doubly coupled at 50 °C with 11 W power instead of 8 W. After cleavage with trifluoroacetic acid/thioanisole/EDT/anisole, 95/5/3/2 v/v/v/v, crude peptide was extracted 3x in -20 ^{o}C ether and vacuum desiccated.

Peptides were purified using a Waters HPLC with a XSELECT™ CSH™ Prep C18 column (Waters, Milford, MA, USA) with a reverse-phase gradient of H_2O/MeCN. All solvents contain 0.1% TFA. Gradient method was optimized to allow for a minimum of 10 min before sample peak elution and a minimum of 5 min after peak collection before column re-equilibration. Gradient ramp rate = 1%/min. Fraction quality was assessed by MALDI-TOF on an Applied Biosystem 4700 Proteomics analyzer with a 355 nm ND:Yag laser operating at 200 Hz (Foster City, CA, USA). The matrix used to facilitate analyte desorption was α-cyano-4-hydroxycinnamic. (HHQALVFFA-NH_2, 1068.228 ($M+H^+$). Confirmed product fractions were concentrated in vacuo before lyophilizing in a FreeZone Plus 12 Liter Cascade, Labconco, freeze dryer system (Kansas City, MO, USA). Lyophilized peptides were stored at room temperature inside a vacuum desiccator.

Peptide Assembly

peptide assemblies and buffers were prepared using ASTM Type II metal-free water (EMD Chemicals Inc., Gibbstown, NJ, USA) with 25 mM MES, pH 5.6.

<u>Peptide fibrils</u>: K16A/K16AL peptide was dissolved at 2x the desired concentration in metal-free water and vortexed for 5 sec. This 2x peptide stock was diluted to full volume with 50 mM MES buffer, pH 5.6, accompanying another vortex period.

<u>Pre-assembled K16A-Cu(II) fibrils:</u> Mature K16A fibrils were titrated with a small volume of 100 mM $CuCl_2$ solution to the desired metal equivalent.

Co-assembled Cu(II)-peptide in aqueous solvent: a 2x peptide stock was prepared as described previously, except with the 100 mM metal stock addition occurring directly after diluting to 1x with 50 mM MES, along with a third vortex period. Note, the volume of water used to prepare the 2x stock was reduced to accommodate the final addition of metal stock.

Visible Absorbance Spectroscopy

Scatter-free absorbance spectra of peptide-metal assemblies were measured with an RSM 1000 at Olis, Inc. (Bogart, GA). Samples were diluted 2x with buffer to a final volume of 3.2 mL in a 9 mL DeSa Suspension Presentation Cavity. Spectra were collected with an 850-400 nm grating, 2.25 nm data interval, and a 180 nm/min scan rate.

Cyclic Voltammetry

Cyclic voltammetry was performed at room temperature using a WaveDriver potentiostat (Pine Research Instrumentation, Durham, NC, USA). Experiments used a standard three-electrode arrangement and a microvolume cell. Electrodes used were a 1 M Ag/AgCl reference electrode (0.228 V vs SHE), a Pt wire counter electrode, and a glassy carbon working electrode (CH Instruments Inc. Electrochemical Instrumentation, Austin, TX, USA). Buffered sample (2 mM peptide + 2 mM $CuCl_2$) was taken in 75 uL aliquots and diluted 2x with 25 mM MES, pH 5.6 + 100 mM KCl. The supporting electrolyte was 25 mM MES, pH 5.6 + 50 mM KCl. Cyclic voltammetry was conducted in the potential range of -0.500 to 0.600 V vs. Ag/AgCl at scan rates of 0.025, 0.050, 0.100, 0.250 and 0.500 (V/s). The analyte's open circuit potential was defined as the starting sweep potential, and all runs were cycled starting in the positive potential direction. Before each measurement, the electrolyte was degassed with N_2 for ~1 min. The working electrode was polished before use and in-between runs with an alumina slurry. A buffer measurement between each run at a scan rate of 0.100 V/s verified each experiment was performed with a clean working electrode with no detectable carryover signal/drift. Data was processed in AfterMath. To convert Ag/AgCl-referenced potentials to SHE-referenced reduction potentials at any given pH at 25 °C: $E_{(SHE)} = E_{Ag/AgCl} + (0.059 \text{ x pH}) + E^{o}_{Ag/AgCl}$, where pH = 5.6 and $E_{Ag/AgCl}$ = 0.228 V. The first cycle from each run was discarded.

Diffusion constants were calculated from the Randles-Sevcik equation modified for electrochemically quasi-reversible systems at room temperature: $i^{quasi} = 2.62\ X\ 10^{5} FAcn^{\frac{3}{2}}\sqrt{Dv}$, where i^{quasi} = forward voltammetric current (A), F = Faraday's Constant (96,485 C/mol), A = electrode area (0.071 cm^2), c = concentration (0.0008 M), n = number of electrons (1), v = scan rate, and D = diffusion coefficient (cm^2/s)[32, 48].

Circular Dichroism Spectroscopy (CD)

CD spectra were recorded using the Jasco-810 CD spectropolarimeter at room temperature. Spectra between 260 nm and 180 nm were collected with a 0.1 mm path length cell, with a step size of 0.2 mm and a speed of 50 nm/s. All spectra were recorded in triplicate and averaged. Ellipticity (mdeg) was converted to mean residue molar ellipticity (MRME, [θ], $deg \bullet cm^2 \bullet dmol^{-1}$) by $[\theta] = \theta/(10 \bullet n \bullet C \bullet l)$, where 'n' is the number of backbone amide bonds per peptide, 'C' is the molar concentration (mol/L) and '1' is the cell path in cm.

Fourier Transform Infrared Spectroscopy (FT-IR)

All FT-IR spectra were recorded using a Jasco FT-IR 4100 (Easton, MD, USA). Aliquots (10 μL) of peptide solution were fan-dried onto a Pike GaldiATR (Madison, WI, USA) diamond at room temperature and averaging 1,068 scans with 2 cm^{-1} resolution. Background spectra were subtracted from each sample.

Fluorimetry

H_2O_2 production was measured using a commercially available Amplex Red assay kit (Sigma) in stickered 96-well, black-walled, optical glass-bottom plates (Greiner Bio-one). Samples and standards were prepared as described by the kit's instructions with no procedural modifications. Samples were diluted 20x in buffer and reaction mixture prior to measurement. Cu(I)-mediated ROS production was initiated with freshly prepared 0.45 eq. sodium ascorbate (0.9 reducing eq.) prior to mixing with the kit reaction mixture. Sacrificial reductant was intentionally supplied as the limiting reagent as it triggers H_2O_2 production in the kit's master mix through the activity of the included horseradish peroxidase. All experiments were performed in a Synergy Mx plate reader (BioTek) with 300 μL sample volume maintained across all wells. The scan rate was set to 1 read/10 min with a 7 s shake period prior to every measurement.

Powder X-Ray Diffraction (pXRD)

Assembled K16A fibers and ribbons were collected by centrifugation using an Eppendorf centrifuge 5810 R (Mississauga, Ontario, CAN) at 4000 rpm held at 4 °C to prevent heating and melting the sample and to remove free monomer and small heterogeneities from the assembly mixture. The pelleted sample was decanted, resuspended in metal-free water, and re-pelleted 3x to remove buffer salts as well. The washed pellet was frozen and lyophilized to yield a dry powder for pXRD. The powder spectra were obtained using APEXII diffractometer with a Cu X-ray source, provided through Emory's X-Ray Crystallography Center.

Transmission Electron Microscopy (TEM)

10 µL peptide assembly aliquots were drop cast onto CF200-Cu Carbon Film 200 Mesh Copper grids (Electron Microscopy Sciences, Hatfield, PA). Peptide assemblies were settled on the grid surface for 1 minute. Excess solution was wicked away using a kimwipe. Immediately following, 10 µL of a 1.5% uranyl acetate (in water) stain was applied for 1 minute and similarly wicked way. Electron micrographs were imaged with a Hitachi HT-7700 Microscope at 80 kV at the Robert P. Apkarian Integrated Electron Microscopy Core.

Image measurements were performed using ImageJ, which were fit to Gaussian functions in Origin 2018b.

Atomic Force Microscopy

Samples were diluted 100-200x to ensure sample dispersion, 45 µL aliquots were drop cast onto silicon chip for 2 min (Ted Pella Inc., Redding, CA, USA). Excess solution was removed via micropipette.

Tapping mode analysis on a Veeco Dimension 5000 atomic force microscope with a full acoustic enclosure was employed using ultra-sharp non-contact silicon cantilevers with typical frequencies ranging from 150 kHz for the largest tip to 315 kHz for the smallest tip (NSC35/AIBS, MikroMasch, Watsonville, CA, USA). Samples were imaged simultaneously in topography and phase modes, with a filter of 0.2 Hz, a scan clock of 0.1667 ms, and a reference of at 70% of the maximum amplitude. The images were analyzed in Gwyddion.[49]

Electron Paramagentic Resonance (EPR)

EPR simulations of spectra obtained for the range of Cu(II)–assembly binding, at [Cu(II)]/[K16A] ratios of 0.1 – 0.6, indicate contributions from three dominant components. The [Cu(II)]/[K16A] = 0.1 spectrum cannot be simulated by using a single set (single Cu(II) species) of EPR simulation parameters (electron *g* and strain-broadening, Cu hyperfine, ^{14}N superhyperfine), because the amplitude of the simulated ^{14}N superhyperfine multiplet, associated with the requisite Cu(II) *g*- and hyperfine parameters, exceeds the experimental amplitude by >5-fold. This introduces a critical constraint on the model for the different Cu(II) site contributions. The overall Cu lineshape is preserved, and the ^{14}N superhyperfine amplitude attenuated, if a second Cu(II) site (Component 2) with enhanced strain-broadening is present, relative to the Cu(II) site (Component 1) with less strain-broadening, that expresses the ^{14}N superhyperfine features. At [Cu(II)]/[K16A] = 0.1, Components 1 and 2 are present in proportions of 80 and 20%, respectively, and there are no additional significant components.

Components 1 and 2 are present in the spectrum at [Cu(II)]/[K16A] = 0.2 at altered proportions of 13 and 72%. A small deviation of the sum of Components 1 and 2 from the observed spectrum in the g_{perp} region, that extends into the $g_{||}$ region, is accounted for by a Component 3 (15%), which is characterized by a broad derivative feature and absence of distinct Cu hyperfine features. The decline in ^{14}N superhyperfine amplitude at [Cu(II)]/[K16A] = 0.4 is accounted for by a relative decrease in the contribution of Component 2 (7%). Component 1 also decreases (53%) and is compensated by a rise in Component 3 (40%). At [Cu(II)]/[K16A] = 0.6, which approaches the saturation of Cu(II) binding sites, Components 1, 2, and 3 reach proportions of 6, 47 and 47%, respectively. These proportions appear to persist at [Cu(II)]/[K16A] ≥ 0.8, in the range where the dominant aqueous Cu(II) spectrum precludes quantification of bound Cu(II) line shape contributions.

Solid-State Nuclear Magnetic Resonance

HHQ[1-^{13}C]ALV[^{15}N]FFA-NH_2 (enriched K16A) assemblies were pelleted, decanted, and washed with metal-free water 3x at 4°C for 90 min using an Eppendorf centrifuge 5810 R (Mississauga, Ontario, CAN) at 4,000 to remove any unassembled monomer and buffer. The washed pellet was lyophilized to a powder. TEM confirmed assembly persistence following lyophilization. The NMR samples were packed into 4 mm solid-state NMR rotors and centered using boron nitride spacers. Rotational-Echo Double-Resonance (REDOR)[50-51] spectra were collected as described previously[52]. In dephasing the carbonyl carbon of HHQ[1-^{13}C]ALV[^{15}N]FFA-NH_2 nanoribbons, the distance of the H-bonded ^{15}N from the adjacent peptide was set to 4.93 Å (r_1) and the distance to the non-H-bonded ^{15}N was set to 6.0 Å (r_2). The angle between the two ^{13}C-^{15}N internuclear vectors was set to 114.7°. The experimental data were fit to a linear combination of 3-spin (one ^{13}C and two

^{15}N's) and ^{13}C{^{15}N}REDOR curve corresponding to the ^{13}C-^{15}N distances sufficient to fit the experimental data points using the Non-Linear Fit routine in Mathematica.

X-ray Absorption Spectroscopy (XAS)

XAS Spectra were collected at Argonne National Laboratory (ANL) on beamline 20-B in fluorescence excitation mode with a 1 x 1 mm X-ray beam 10% defocused at 9.5 KeV (harmonic cutoff = 13.2 KeV). An insertion device beamline was not utilized to minimize potential beam damage.

The data were collected at 72 K, which was maintained by a liquid nitrogen cryostat (< 10 mTorr) with a sample-to-edge distance of 25 mm and a detector-cryostat distance of < 45 mm. A 12-element Ge detector with 2 us peaking time and 0.55 s integration time was used.

All samples were pelleted and resuspended in buffer to 80% original volume to remove potential peptide monomer-Cu(II) complexes. Immediately before freezing, samples were diluted back to the original volume with glycerol and mixed thoroughly to prevent Bragg scattering by water ice crystallites. Reduced samples were prepared in a portable glovebag (Sigma) that was purged 5x with argon.

Samples were aliquoted into a 3D-printed sample holder supplied by the beamline. The sample holder had two sample chambers stacked vertically, each with a volume of 350 uL and an 18 x 5 mm window area. The window material consisted of kapton film that was secured via an aluminum frame and steel screws. The entire cuvette was covered with a piece of tin sheeting with slits cut in to expose the windows while preventing excitation of the adventitious copper detected in the screws.

To minimize beam damage, sample was aliquoted in both chambers in duplicate with twenty scan sites that alternated across both sample chambers. Each scan collected 467 data points over 13.42 min between 8,830 and 9,953 eV.

All spectra were calibrated to standard copper foil data[53] in Athena (Demeter)[54] and individually inspected for photodamage. Satisfactory replicate scans were aligned, deglitched, and merged.
XAS data was fit in a custom IgorPro routine[55-56].

Molecular Modeling and Molecular Dynamics (MD)

Peptide assembly models were generated using Maestro 11.4 (Schrodinger Suite).[57] K16A peptides were extended as antiparallel β sheets and arranged into a bilayered lattice of 8 β sheet chains consisting of 8 peptides each for a total of 128 peptides. Peptides were spaced according to the hydrogen-bonding and lamination distances reported by pXRD, and the peptide registry according to the ^{13}C{^{15}N} REDOR fit.

Unrestrained MD was performed on the peptide lattice using GROMACS v2018.3[58] in a centered cubic box of TIP4P[59] water with periodic boundary conditions and a 1.0 nm protein-box distance using the OPLS-AA[60] force field. Short-range Van Der Waals and electrostatics were cutoff at 1.0 nm each using the Verlet scheme[61]. The system was neutralized with Na^+ and Cl^-. The system was energy minimized for 1,000 steps using a steepest descent algorithm then equilibrated via 100 ps NVT and 100 ps NPT ensembles. Average temperature was kept at 300 K using a Berendsen thermostat[62] with a 1.0 ps time constant, and average pressure was kept at 1 bar using a Parrinello-Rahman barostat[63] with a 2.0 ps time constant. MD was performed until the aligned protein's RMSD converged at approximately 1.2 ns. Bond distances were constrained with the LINCS algorithm[64-65] with a 2-fs integration time step.

The final frame's coordinates of the apo-peptide lattice were simulated with a dummy copper (DCU) to estimate the coordination sphere geometry. The DCU was constructed from a centroid placed within the bilayer and between the 4th and 5th β sheets to minimize the effects of bulk solvent exposure and peripheral β sheet peeling. The DCU was repositioned into ligation proximity using Chimera. To minimize experimenter bias, only the Cα-Cβ and Cβ-Cγ bond torsions of the N-terminal HISE were adjusted. The DCU-containing models were simulated identically to the apo-lattice, until the RMSD of an aligned, water-excluded 4 Å radius of DCU visibly plateaued.

The exported coordinates and the OPLS-AA force field was modified to include the experimental parameters from XAFS and ESEEM and simulated for 2 ns. RMSD typically converged in > 1 ns.

MD trajectory analysis (trajectory RMSD, bond length measurements, *etc.*) was performed using VMD.[66] Trajectory visualization/rendering and model raytracing was performed using PyMOL.[67]

A .pdb of the final frame was used to simulate a pXRD pattern using CRYSOL (ATSAS suite).[68-69] Default simulation parameters were used except for the order of harmonics and the order of the Fibonacci grid, which were maximized. The simulated pattern was normalized in Origin 2018b.

Electron spin-echo envelope modulation (ESEEM) spectroscopy

ESEEM data were collected at 6 K on a home-built pulsed-EPR spectrometer[70] by using the three-pulse ($\pi/2$-τ-$\pi/2$-T-$\pi/2$-τ-echo) microwave pulse sequence with pulse-swapping.[71] The τ value was selected from a scan of the τ values, corresponding to the relation, $\tau = \frac{n}{\nu_{1_{\mathrm{H}}}}$, where n = 1, 2, 3, … and $\nu_{1_{\mathrm{H}}}$ is the free precession frequency of the ^{1}H nucleus at the prevailing external magnetic field. These τ values correspond to τ-suppression [72] of the free ^{1}H contribution to the ESEEM. The τ values of 160 ns (n = 2) and 310 ns (n = 4) were chosen to emphasize the low-frequency ^{14}N nuclear quadrupole features and their combination lines, and the ^{14}N double quantum line (υ_{dq}) and its corresponding combination feature ($2\upsilon_{\mathrm{dq}}$), respectively. ESEEM was cosine Fourier transformed to generate the ESEEM frequency spectra. Modulation in the dead time portion of the ESEEM waveform was reconstructed by inverse-Fourier transformation of prominent features in the initial Fourier transform.[73] All data processing was performed by using laboratory-written MATLAB (Mathworks, Natick, MA) programs running on local computers.

Electron spin-echo envelope modulation (ESEEM) simulations.

Numerical simulations of the ESEEM were performed by using the OPTESIM ESEEM simulation and analysis software suite.[74] Simulation of ESEEM that arises from the coupling of the remote ^{14}N of imidazole ligands to the unpaired electron spin on Cu(II) has been described in detail.[20] Briefly, the coupled electron–single ^{14}N system is parameterized by using the following eight adjustable parameters: A_{xx}, A_{yy}, A_{zz} (electron-^{14}N superhyperfine coupling constants), e^2qQ/h and η (^{14}N nuclear quadrupole coupling constant and asymmetry parameter), and α_Q, β_Q, γ_Q (Euler angles that relate the principal axes of the superhyperfine and nuclear quadrupole tensors). For simulation of the Cu(II)-bis-imidazole complexes, these eight parameters are assumed to be common to the two imidazole ^{14}N. For the bis-imidazole complex, α_A, β_A, and γ_A (Euler angles that relate the two ^{14}N superhyperfine dipolar tensor axes) are additional adjustable parameters. The simultaneous confidence region for each adjustable parameter, at a specific confidence level (here, 99%), was calculated, as described[74].

3.5 References

1. Rengifo, R. F.; Sementilli, A.; Kim, Y.; Liang, C.; Li, N. X. A.; Mehta, A. K.; Lynn, D. G., Liquid-Like Phases Preorder Peptides for Supramolecular Assembly. *ChemSystemsChem* **2020,** *2* (6), e2000007.
2. Anthony, N. R.; Mehta, A. K.; Lynn, D. G.; Berland, K. M., Mapping amyloid-β(16-22) nucleation pathways using fluorescence lifetime imaging microscopy. *Soft Matter* **2014,** *10* (23), 4162-4172.
3. Hsieh, M.-C.; Lynn, D. G.; Grover, M. A., Kinetic Model for Two-Step Nucleation of Peptide Assembly. *The Journal of Physical Chemistry B* **2017,** *121* (31), 7401-7411.
4. Bruni, S.; Cariati, F.; Daniele, P. G.; Prenesti, E., Speciation and structure of copper(II) complexes with histidine-containing peptides in aqueous medium: a combined potentiometric and spectroscopic study. *Spectrochim Acta A Mol Biomol Spectrosc* **2000,** *56* (4), 815-27.

5. Shearer, J.; Soh, P., The Copper(II) Adduct of the Unstructured Region of the Amyloidogenic Fragment Derived from the Human Prion Protein is Redox-Active at Physiological pH. *Inorganic Chemistry* **2007,** *46* (3), 710-719.
6. Gordon, C. K.; Luu, R.; Lynn, D., Capturing nested information from disordered peptide phases. *Peptide Science* **2021,** *113* (2), e24215.
7. Rha, A. K.; Das, D.; Taran, O.; Ke, Y.; Mehta, A. K.; Lynn, D. G., Electrostatic Complementarity Drives Amyloid/Nucleic Acid Co-Assembly. *Angewandte Chemie International Edition* **2020,** *59* (1), 358-363.
8. Rengifo, R. F.; Li, N. X.; Sementilli, A.; Lynn, D. G., Amyloid scaffolds as alternative chlorosomes. *Organic & Biomolecular Chemistry* **2017,** *15* (34), 7063-7071.
9. Sinz, A.; Jin, A. J.; Zschörnig, O., Evaluation of the metal binding properties of a histidine-rich fusogenic peptide by electrospray ionization Fourier transform ion cyclotron resonance mass spectrometry. *Journal of Mass Spectrometry* **2003,** *38* (11), 1150-1159.
10. Grossoehme, N. E.; Akilesh, S.; Guerinot, M. L.; Wilcox, D. E., Metal-Binding Thermodynamics of the Histidine-Rich Sequence from the Metal-Transport Protein IRT1 of Arabidopsis thaliana. *Inorganic Chemistry* **2006,** *45* (21), 8500-8508.
11. Barber-Zucker, S.; Shaanan, B.; Zarivach, R., Transition metal binding selectivity in proteins and its correlation with the phylogenomic classification of the cation diffusion facilitator protein family. *Scientific Reports* **2017,** *7* (1), 16381.
12. Curtain, C. C.; Ali, F. E.; Smith, D. G.; Bush, A. I.; Masters, C. L.; Barnham, K. J., Metal ions, pH, and cholesterol regulate the interactions of Alzheimer's disease amyloid-beta peptide with membrane lipid. *Journal of Biological Chemistry* **2003,** *278* (5), 2977-82.

13. Mantyh, P. W.; Ghilardi, J. R.; Rogers, S.; Demaster, E.; Allen, C. J.; Stimson, E. R.; Maggio, J. E., Aluminum, Iron, and Zinc Ions Promote Aggregation of Physiological Concentrations of b-Amyloid Peptide. *J. Neurochem.* **1993,** *61* (3), 1171-1174.
14. Parthasarathy, S.; Long, F.; Miller, Y.; Xiao, Y.; McElheny, D.; Thurber, K.; Ma, B.; Nussinov, R.; Ishii, Y., Molecular-level examination of Cu^{2+} binding structure for amyloid fibrils of 40-residue Alzheimer's b by solid-state NMR spectroscopy. *J Am Chem Soc* **2011,** *133* (10), 3390-400.
15. Bush, A. I., The metallobiology of Alzheimer's disease. *Trends in Neurosciences* **2003,** *26* (4), 207-214.
16. Kau, L. S.; Spira-Solomon, D. J.; Penner-Hahn, J. E.; Hodgson, K. O.; Solomon, E. I., X-ray absorption edge determination of the oxidation state and coordination number of copper. Application to the type 3 site in Rhus vernicifera laccase and its reaction with oxygen. *Journal of the American Chemical Society* **1987,** *109* (21), 6433-6442.
17. DuBois, J. L.; Mukherjee, P.; Stack, T. D. P.; Hedman, B.; Solomon, E. I.; Hodgson, K. O., A Systematic K-edge X-ray Absorption Spectroscopic Study of Cu(III) Sites. *Journal of the American Chemical Society* **2000,** *122* (24), 5775-5787.
18. Schweiger, A.; Jeschke, G., *Principles of pulse electron paramagnetic resoncance.* 2001.
19. Mims, W. B., Elimination of the dead-time artifact in electron spin-echo envelope spectra. *Journal of Magnetic Resonance (1969)* **1984,** *59* (2), 291-306.
20. Hernández-Guzmán, J.; Sun, L.; Mehta, A. K.; Dong, J.; Lynn, D. G.; Warncke, K., Copper(II)-bis-Histidine Coordination Structure in a Fibrillar Amyloid β-Peptide Fragment and Model Complexes Revealed by Electron Spin Echo Envelope Modulation Spectroscopy. *ChemBioChem* **2013,** *14* (14), 1762-1771.

21. Colaneri, M. J.; Peisach, J., An electron spin-echo envelope modulation study of copper(II)-doped single crystals of L-histidine hydrochloride monohydrate. *Journal of the American Chemical Society* **1992,** *114* (13), 5335-5341.
22. Colaneri, M. J.; Peisach, J., A single crystal EPR and ESEEM analysis of Cu(II)-doped bis(L-histidinato)cadmium dihydrate. *Journal of the American Chemical Society* **1995,** *117* (23), 6308-6315.
23. Sun, L.; Hernandez-Guzman, J.; Warncke, K., OPTESIM, a versatile toolbox for numerical simulation of electron spin echo envelope modulation (ESEEM) that features hybrid optimization and statistical assessment of parameters. *J Magn Reson* **2009,** *200* (1), 21-8.
24. Sarell, C. J.; Syme, C. D.; Rigby, S. E. J.; Viles, J. H., Copper(II) Binding to Amyloid-β Fibrils of Alzheimer's Disease Reveals a Picomolar Affinity: Stoichiometry and Coordination Geometry Are Independent of Aβ Oligomeric Form. *Biochemistry* **2009,** *48* (20), 4388-4402.
25. Cordes, M.; Giese, B., Electron transfer in peptides and proteins. *Chemical Society Reviews* **2009,** *38* (4), 892-901.
26. Moser, C. C.; Page, C. C.; Dutton, P. L., Darwin at the molecular scale: selection and variance in electron tunnelling proteins including cytochrome <i>c</i> oxidase. *Philosophical Transactions of the Royal Society B: Biological Sciences* **2006,** *361* (1472), 1295-1305.
27. Gray, H. B.; Winkler, J. R., Electron tunneling through proteins. *Q Rev Biophys* **2003,** *36* (3), 341-72.
28. Arregui, L.; Ayala, M.; Gómez-Gil, X.; Gutiérrez-Soto, G.; Hernández-Luna, C. E.; Herrera de los Santos, M.; Levin, L.; Rojo-Domínguez, A.; Romero-Martínez, D.;

Saparrat, M. C. N.; Trujillo-Roldán, M. A.; Valdez-Cruz, N. A., Laccases: structure, function, and potential application in water bioremediation. *Microbial Cell Factories* **2019,** *18* (1), 200.

29. Cristaldi, J. C.; Gómez, M. C.; González, P. J.; Ferroni, F. M.; Dalosto, S. D.; Rizzi, A. C.; Rivas, M. G.; Brondino, C. D., Study of the Cys-His bridge electron transfer pathway in a copper-containing nitrite reductase by site-directed mutagenesis, spectroscopic, and computational methods. *Biochim Biophys Acta Gen Subj* **2018,** *1862* (3), 752-760.
30. Roberts, G., *Encyclopedia of Biophysics*. Springer Berlin Heidelberg: 2013.
31. Zimbardi, A. L. R. L.; Camargo, P. F.; Carli, S.; Aquino Neto, S.; Meleiro, L. P.; Rosa, J. C.; De Andrade, A. R.; Jorge, J. A.; Furriel, R. P. M., A High Redox Potential Laccase from Pycnoporus sanguineus RP15: Potential Application for Dye Decolorization. *International Journal of Molecular Sciences* **2016,** *17* (5), 672.
32. Bard, A. J.; Faulkner, L. R., *Electrochemical methods: fundamentals and applications*. 2nd ed.; John Wiley & Sons, Inc.: Hoboken, NJ, 2000.
33. Ahrenholtz, S. R.; Epley, C. C.; Morris, A. J., Solvothermal Preparation of an Electrocatalytic Metalloporphyrin MOF Thin Film and its Redox Hopping Charge-Transfer Mechanism. *Journal of the American Chemical Society* **2014,** *136* (6), 2464-2472.
34. Celis-Salazar, P. J.; Cai, M.; Cucinell, C. A.; Ahrenholtz, S. R.; Epley, C. C.; Usov, P. M.; Morris, A. J., Independent Quantification of Electron and Ion Diffusion in Metallocene-Doped Metal–Organic Frameworks Thin Films. *Journal of the American Chemical Society* **2019,** *141* (30), 11947-11953.

35. Daum, P.; Lenhard, J. R.; Rolison, D.; Murray, R. W., Diffusional charge transport through ultrathin films of radiofrequency plasma polymerized vinylferrocene at low temperature. *Journal of the American Chemical Society* **1980,** *102* (14), 4649-4653.

36. White, H. S.; Leddy, J.; Bard, A. J., Polymer films on electrodes. 8. Investigation of charge-transport mechanisms in Nafion polymer modified electrodes. *Journal of the American Chemical Society* **1982,** *104* (18), 4811-4817.

37. Jiang, D.; Li, X.; Liu, L.; Yagnik, G. B.; Zhou, F., Reaction Rates and Mechanism of the Ascorbic Acid Oxidation by Molecular Oxygen Facilitated by Cu(II)-Containing Amyloid-β Complexes and Aggregates. *The Journal of Physical Chemistry B* **2010,** *114* (14), 4896-4903.

38. Jiang, D.; Men, L.; Wang, J.; Zhang, Y.; Chickenyen, S.; Wang, Y.; Zhou, F., Redox reactions of copper complexes formed with different beta-amyloid peptides and their neuropathological [correction of neuropathalogical] relevance. *Biochemistry* **2007,** *46* (32), 9270-82.

39. Reybier, K.; Ayala, S.; Alies, B.; Rodrigues, J. V.; Bustos Rodriguez, S.; La Penna, G.; Collin, F.; Gomes, C. M.; Hureau, C.; Faller, P., Free Superoxide is an Intermediate in the Production of H2O2 by Copper(I)-Aβ Peptide and O2. *Angew Chem Int Ed Engl* **2016,** *55* (3), 1085-9.

40. Cheignon, C.; Tomas, M.; Bonnefont-Rousselot, D.; Faller, P.; Hureau, C.; Collin, F., Oxidative stress and the amyloid beta peptide in Alzheimer's disease. *Redox Biol* **2018,** *14*, 450-464.

41. Cheignon, C.; Faller, P.; Testemale, D.; Hureau, C.; Collin, F., Metal-catalyzed oxidation of Aβ and the resulting reorganization of Cu binding sites promote ROS production. *Metallomics* **2016,** *8* (10), 1081-1089.

42. Guilloreau, L.; Combalbert, S.; Sournia-Saquet, A.; Mazarguil, H.; Faller, P., Redox chemistry of copper-amyloid-beta: the generation of hydroxyl radical in the presence of ascorbate is linked to redox-potentials and aggregation state. *Chembiochem* **2007,** *8* (11), 1317-25.
43. Omosun, T. O.; Hsieh, M.-C.; Childers, W. S.; Das, D.; Mehta, A. K.; Anthony, N. R.; Pan, T.; Grover, M. A.; Berland, K. M.; Lynn, D. G., Catalytic diversity in self-propagating peptide assemblies. *Nature Chemistry* **2017,** *9* (8), 805-809.
44. Rodger, A.; Marrington, R.; Roper, D.; Windsor, S., Circular Dichroism Spectroscopy for the Study of Protein-Ligand Interactions. In *Protein-Ligand Interactions: Methods and Applications*, Ulrich Nienhaus, G., Ed. Humana Press: Totowa, NJ, 2005; pp 343-363.
45. Johnson Jr., W. C., Circular Dichroism and Its Empirical Application to Biopolymers. In *Methods of Biochemical Analysis*, 1985; pp 61-163.
46. W C Johnson, J., Secondary Structure of Proteins Through Circular Dichroism Spectroscopy. *Annual Review of Biophysics and Biophysical Chemistry* **1988,** *17* (1), 145-166.
47. Micsonai, A.; Wien, F.; Kernya, L.; Lee, Y.-H.; Goto, Y.; Réfrégiers, M.; Kardos, J., Accurate secondary structure prediction and fold recognition for circular dichroism spectroscopy. *Proceedings of the National Academy of Sciences* **2015,** *112* (24), E3095-E3103.
48. Compton, R. G.; Banks, C. E., *Understanding Voltammetry (2nd Edition)*. World Scientific Publishing Company: 2010.
49. Nečas, D.; Klapetek, P., Gwyddion: an open-source software for SPM data analysis. **2012,** *10* (1), 181.

50. Gullion, T.; Schaefer, J., Rotational-Echo Double-Resonance NMR. *Journal of Magnetic Resonance* **1989,** *81* (1), 196-200.
51. Gullion, T., Introduction to rotational-echo, double-resonance NMR. *Concept Magnetic Res* **1998,** *10* (5), 277-289.
52. Li, S.; Mehta, A. K.; Sidorov, A. N.; Orlando, T. M.; Jiang, Z.; Anthony, N. R.; Lynn, D. G., Design of asymmetric peptide bilayer membranes. *Journal of the American Chemical Society* **2016,** *138* (10), 3579-3586.
53. Kraft, S.; Stümpel, J.; Becker, P.; Kuetgens, U., High resolution x-ray absorption spectroscopy with absolute energy calibration for the determination of absorption edge energies. *Review of Scientific Instruments* **1996,** *67* (3), 681-687.
54. ATHENA, ARTEMIS, HEPHAESTUS: data analysis for X-ray absorption spectroscopy using IFEFFIT. *Journal of Synchrotron Radiation* **2005,** *12* (4), 537-541.
55. *Scarrow, R. S.; Shearer, J. EXAFS123, v. 0.5; Trinity University: San Antonio, TX, 2019.*
56. Rehr, J. J.; Kas, J. J.; Vila, F. D.; Prange, M. P.; Jorissen, K., Parameter-free calculations of X-ray spectra with FEFF9. *Physical Chemistry Chemical Physics* **2010,** *12* (21), 5503-5513.
57. Schrödinger Release 2020-1: Maestro, Schrödinger, LLC, New York, NY, 2020.
58. Berendsen, H. J. C.; van der Spoel, D.; van Drunen, R., GROMACS: A message-passing parallel molecular dynamics implementation. *Computer Physics Communications* **1995,** *91* (1), 43-56.

59. Jorgensen, W. L.; Chandrasekhar, J.; Madura, J. D.; Impey, R. W.; Klein, M. L., Comparison of simple potential functions for simulating liquid water. *The Journal of Chemical Physics* **1983,** *79* (2), 926-935.
60. Jorgensen, W. L.; Maxwell, D. S.; Tirado-Rives, J., Development and testing of the OPLS all-atom force field on conformational energetics and properties of organic liquids. *Journal of the American Chemical Society* **1996,** *118* (45), 11225-11236.
61. Verlet, L., Computer" experiments" on classical fluids. I. Thermodynamical properties of Lennard-Jones molecules. *Physical review* **1967,** *159* (1), 98.
62. Berendsen, H. J. C.; Postma, J. P. M.; Gunsteren, W. F. v.; DiNola, A.; Haak, J. R., Molecular dynamics with coupling to an external bath. *The Journal of Chemical Physics* **1984,** *81* (8), 3684-3690.
63. Parrinello, M.; Rahman, A., Polymorphic transitions in single crystals: A new molecular dynamics method. *Journal of Applied Physics* **1981,** *52* (12), 7182-7190.
64. Hess, B.; Bekker, H.; Berendsen, H. J. C.; Fraaije, J. G. E. M., LINCS: A linear constraint solver for molecular simulations. *Journal of Computational Chemistry* **1997,** *18* (12), 1463-1472.
65. Hess, B., P-LINCS: A Parallel Linear Constraint Solver for Molecular Simulation. *Journal of Chemical Theory and Computation* **2008,** *4* (1), 116-122.
66. Braun, S.; Humphreys, C.; Fraser, E.; Brancale, A.; Bochtler, M.; Dale, T. C., Amyloid-associated nucleic acid hybridisation. *PLoS ONE* **2011,** *6* (5), e19125.
67. **The PyMOL Molecular Graphics Syste, Version 2.0**, Schrodinger, LLC.
68. Svergun, D.; Barberato, C.; Koch, M. H. J., CRYSOL - A program to evaluate x-ray solution scattering of biological macromolecules from atomic coordinates. *Journal of Applied Crystallography* **1995,** *28*, 768-773.

69. Franke, D.; Petoukhov, M. V.; Konarev, P. V.; Panjkovich, A.; Tuukkanen, A.; Mertens, H. D. T.; Kikhney, A. G.; Hajizadeh, N. R.; Franklin, J. M.; Jeffries, C. M.; Svergun, D. I., ATSAS 2.8: a comprehensive data analysis suite for small-angle scattering from macromolecular solutions. *Journal of Applied Crystallography* **2017,** *50* (4), 1212-1225.

70. Sun, L.; Savory, J. J.; Warncke, K., Design and implementation of an FPGA-based timing pulse programmer for pulsed-electron paramagnetic resonance applications. *Concepts in Magnetic Resonance B. Magnetic Resonance Engineering* **2013,** *43* (3), 100-109.

71. Fauth, J.-M.; Schweiger, A.; Braunschweiler, L.; Forrer, J.; Ernst, R. R., Elmination of unwanted echoes and reduction of dead time in three-pulse electron spin-echo spectroscopy. *Journal of Magnetic Resonance* **1986,** *66*, 74-85.

72. Peisach, J.; Mims, W. B.; Davis, J. L., Studies of the electron-nuclear coupling between Fe(III) and N-14 in cytochrome-P-450 and in a series of low-spin heme compounds. *Journal of Biological Chemistry* **1979,** *254* (24), 2379-2389.

73. Mims, W. B., Elimination of the dead-time artifact in electron spin-echo envelope spectra. *Journal of Magnetic Resonance* **1984,** *59*, 291-306.

74. Sun, L.; Hernandez-Guzman, J.; Warncke, K., OPTESIM, a versatile toolbox for numerical simulation of electron spin echo envelope modulation (ESEEM) that features hybrid optimization and statistical assessment of parameters. *Journal of Magnetic Resonance* **2009,** *200*, 21-28 (Cover Article).

Chapter 4.

New peptide-metal co-assemblies with lead(II)

4.1 Introduction

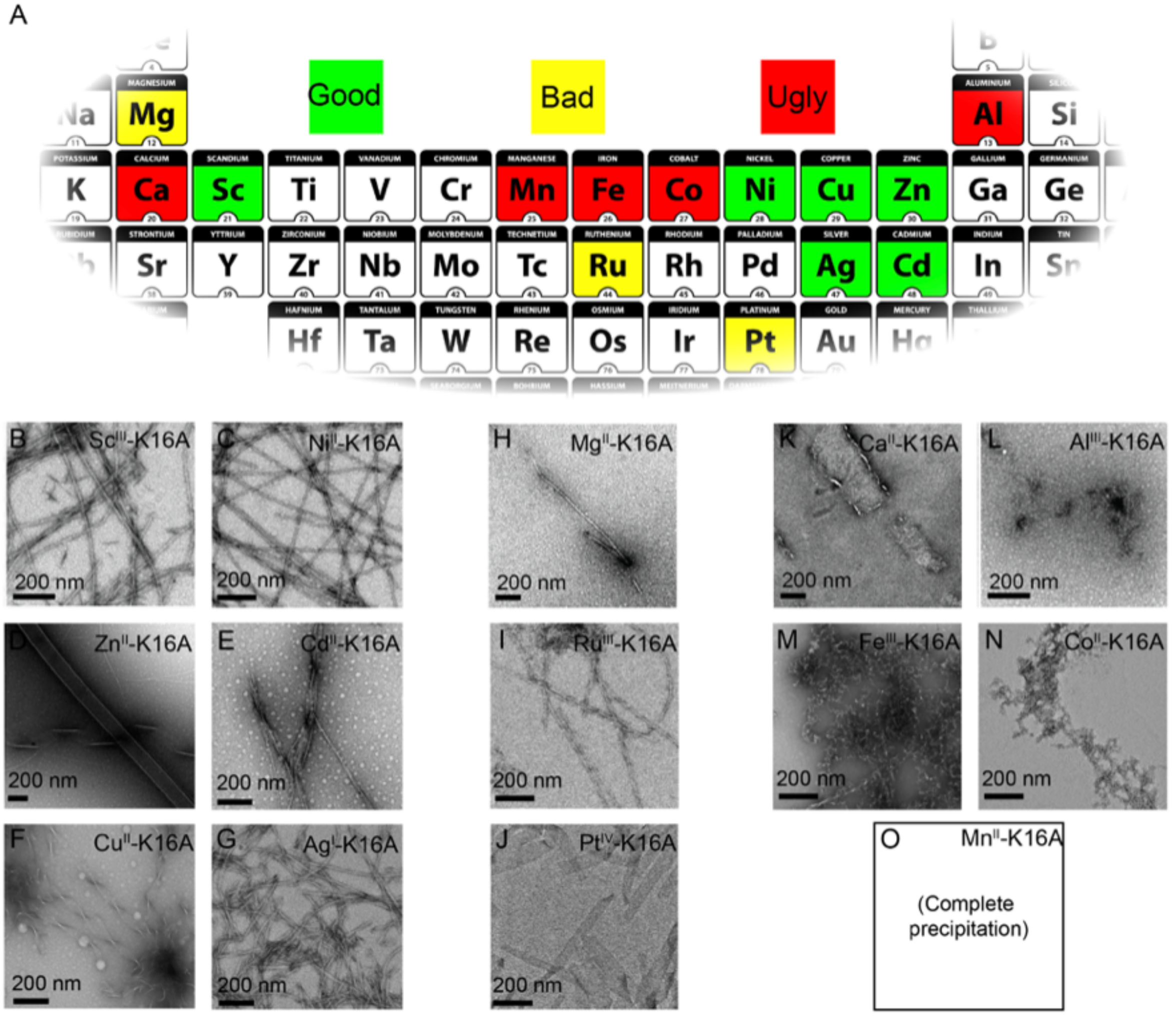

Figure 4-1. Periodic table-view screening of attempted metal-K16A assemblies to date. Assemblies prepared with green-labeled elements readily yield characterizable K16A assemblies by TEM. Elements labeled yellow produce mixtures of assembly and amorphous aggregate. Red elements form less structured associations with K16A. Representative TEMs of metal-K16A assemblies are shown in panels B-O. All assemblies were prepared as 1:1 co-assembly in 25 mM MES, pH 5.6. Chloride salts were used as the metal ion source, except for Al(III) and Ag(I), which were introduced as nitrate salts. The periodic table was adapted from freestock.ca.

In the previous chapter, the new peptide-metal co-assemblies and electron hopping between copper ions in the co-assemblies were reported. Closer coupling with semiconductivity of the metal complexes in the co-assemblies can be realized when the distance between the metal complexes is close. Perovskite crystals, which consist of three dimensional networks of corner-sharing octahedral complexes[1-2], can absorb light to generate potential or emit visible light when potential is applied[3-4], because of low band gaps of the coupled molecular orbitals of the complexes[4-5]. Pb(II) ions are generally used as cation part in halide perovskite which have a type of crystal structure as $APbX_3$ (A is a small cation and X is a halide) because of high photoluminescence and quantum yields. Organic-inorganic hybrid lead halide perovskites, that usually have methylammonium and formamidinium as the A cation, have been studied and applied for perovskite solar cells with high power conversion efficiencies and low cost production methods[6]. Other metal ions, such as Sn(II) or Ge(II), have been tried to replace toxic Pb(II), but they showed poor stabilities and optical performance[7].

Transition metals and its complexes with ligands are also utilized for catalysts for organic reactions[8-9], fluorescence imaging[10], and photosensitizers[11]. In previous research of Dr. Lynn's lab, peptide-metal co-assemblies with various transition metal ions were tried. H-HHQALVFFA-NH_2, K16A, was used for the surveys (Fig. 4-1). Among the assemblies with metals, ruthenium which is commonly used for photosensitizers was attempted for a co-assembly with K16A, but the morphology was heterogeneous and amorphous aggregate was dominant. Pb(II), used for active materials of photovoltaics as introduced above, have not tested yet. Because of the larger size of the lead ions compared to copper ions, distances between Pb(II) in peptide-metal co-assemblies can be shorter, which may result in better couplings of the complexes with distinct optical or redox chemistry. In this chapter, to investigate this idea, new peptide-Pb(II) co-assemblies and its applicable functions are tested.

4.2 Results and discussion

4.2.1 K16A-metal co-assemblies in DMF solvent systems

Because of solubilities of essential chemicals and precursors for organic-inorganic hybrid lead halide perovskites, dimethylformamide (DMF), N-methyl-2-pyrrolidon (NMP), or dimethyl sulfoxide (DMSO) were used as solvents[12-13]. Also using these organic solvents is much better to make fine films on cells of devices due to low surface tensions of the solvents. Therefore, peptide-metal co-assemblies with K16A and PbI2 in DMF was tried first. Because of the low polarity (higher hydrophobicity than water) of the solvent, slow rate of forming assembled structures was expected. So, higher concentrations of peptides, 4 mM, was prepared. Circular dichroism (CD) analysis is not available because of the DMF which absorb the amide's range since DMF has literally an amide bond. Time-dependent TEM images for K16A self-assembly in DMF show thin and short fibers at 6-week time point (Fig. 4-2). Compared to K16A self-assembly in aqueous solvent, the assembly in DMF has slow growing of the assembly, and even after 6 weeks, the nanofibers were not dominant on the TEM grids. Considering the higher concentration and the slow rate, the higher hydrophobicity of the solvent inhibits the hydrophobic interactions between peptide strands. However, when K16A forms co-assembly with PbI_2, it shows more assemblies (Fig. 4-3). It still presents short fibers but has thicker bundled morphologies. After 6 weeks, it formed longer bundled fibers. Based on the TEM images,

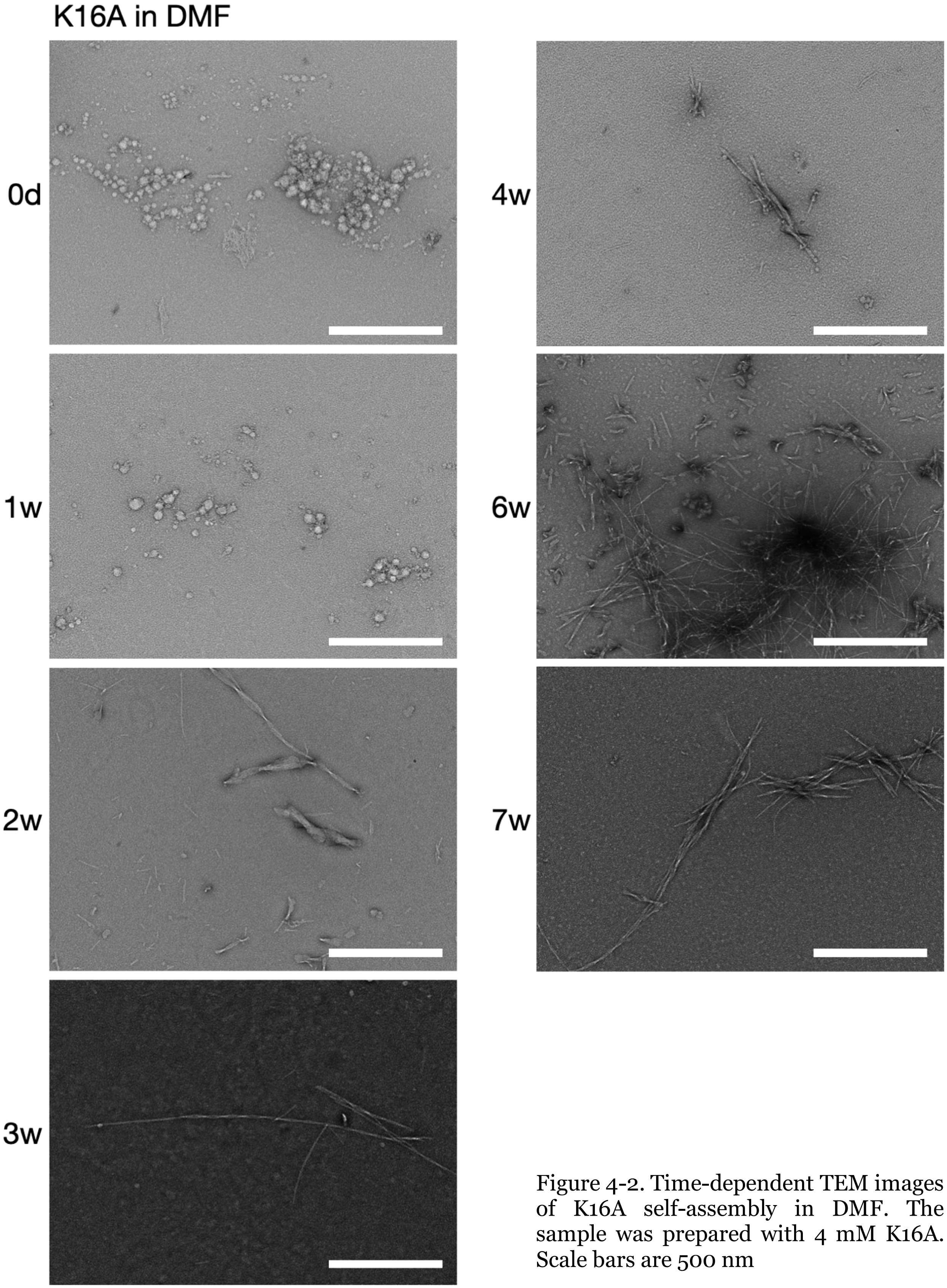

Figure 4-2. Time-dependent TEM images of K16A self-assembly in DMF. The sample was prepared with 4 mM K16A. Scale bars are 500 nm

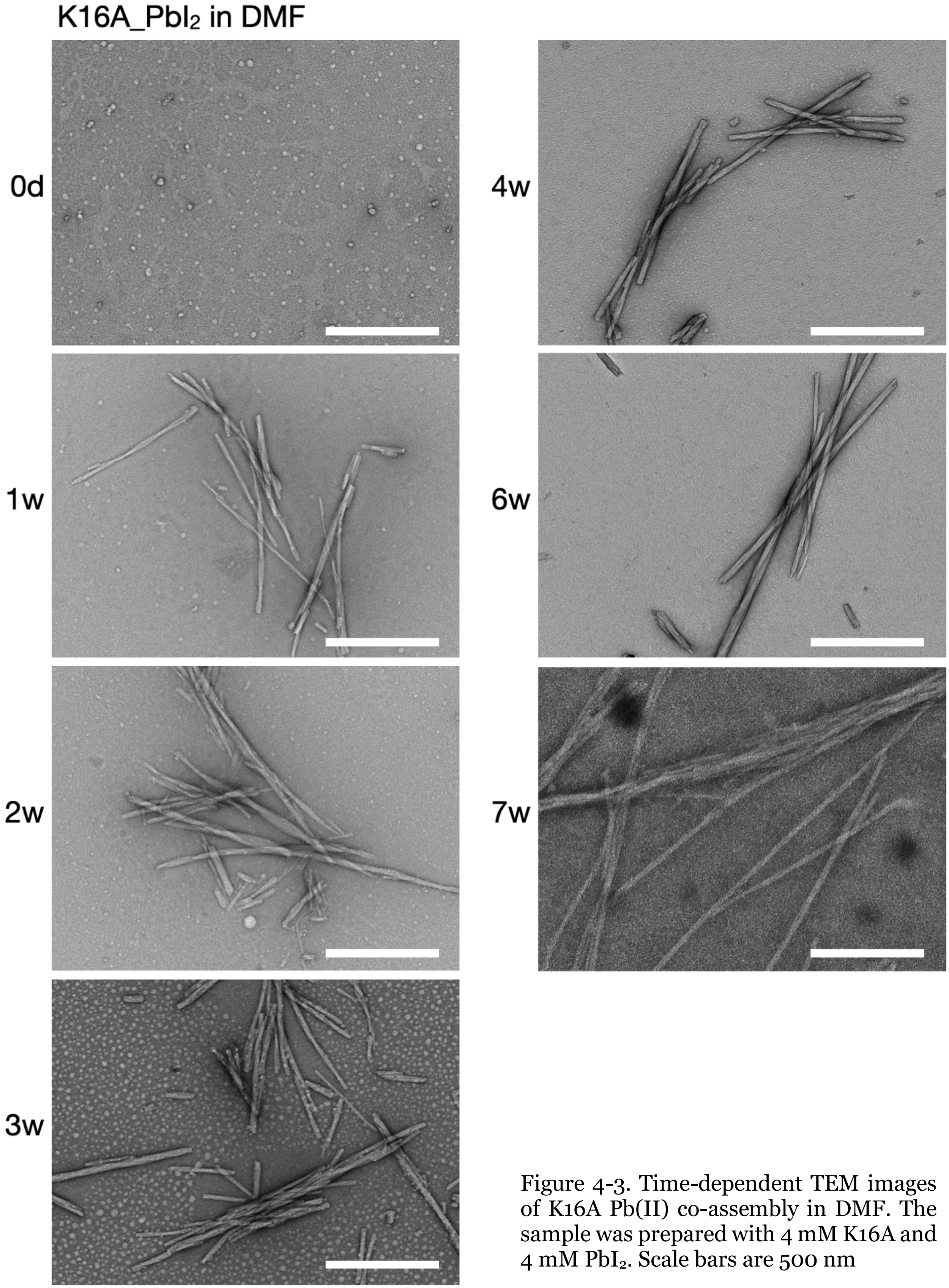

Figure 4-3. Time-dependent TEM images of K16A Pb(II) co-assembly in DMF. The sample was prepared with 4 mM K16A and 4 mM PbI_2. Scale bars are 500 nm

Pb(II) ions may incorporate between the thin K16A fibers, so the nanostructure prefer to have thick bundled forms rather than longer fibers. In order to increase polarity of solvent, 20% water in DMF was prepared as solvent. The highest limitation of ratio of water in DMF is 20% to dissolve PbI_2 in the solvent. The limitation of solubility was reported[14] and also confirmed by experiments. Excess of water more than 20% of water in DMF causes precipitation of PbI_2. Since the higher polarity of DMF with 20% of water, faster rate of forming assembly and more nano-morphologies were expected. Based on the TEM images (Fig. 4-2 and 4-4), the sample with 20% of water forms thicker bundled and longer fibers. Although it is difficult to differentiate with only the TEM images, the samples with and without 20% of water do not have dramatic different rate of forming assemblies. However, K16A-Pb(II) co-assembly in DMF with 20% of water forms much more bundled fibers (Fig. 4-5). Poor solubility of PbI_2 in water and higher polarity may accelerate hydrophobic interaction and metal-ligand interaction between Pb(II) and histidine.

IR spectra of the assemblies indicates the assemblies have beta sheet secondary structure. While three assemblies have maximum absorbances at around 1628nm, the red-shifted and strong amide-I band, at 1624 nm, of K16A-Pb(II) co-assembly in DMF with 20% of water implies that it has longer fibers which have longer range amide coupled by hydrogen bonds (Fig. 4-6). Moreover, the K16A-Pb(II) co-assembly in DMF with 20% of water shows distinct UV/Vis absorption at 350 nm (Fig. 4-7A). The samples for UV/Vis spectroscopy was diluted to 200 μM of K16A and 200 μM PbI_2 to reduce the absorption intensity under detection limits of the spectrometer. The co-assembly in DMF does not have difference from PbI2 in DMF, but the co-assembly in DMF with 20% of water shows additional absorption at 350 nm which PbI_2 in DMF with 20% of water solution does not have. The absorption can be from coupling of Pb(II) incorporated in the co-assemblies.

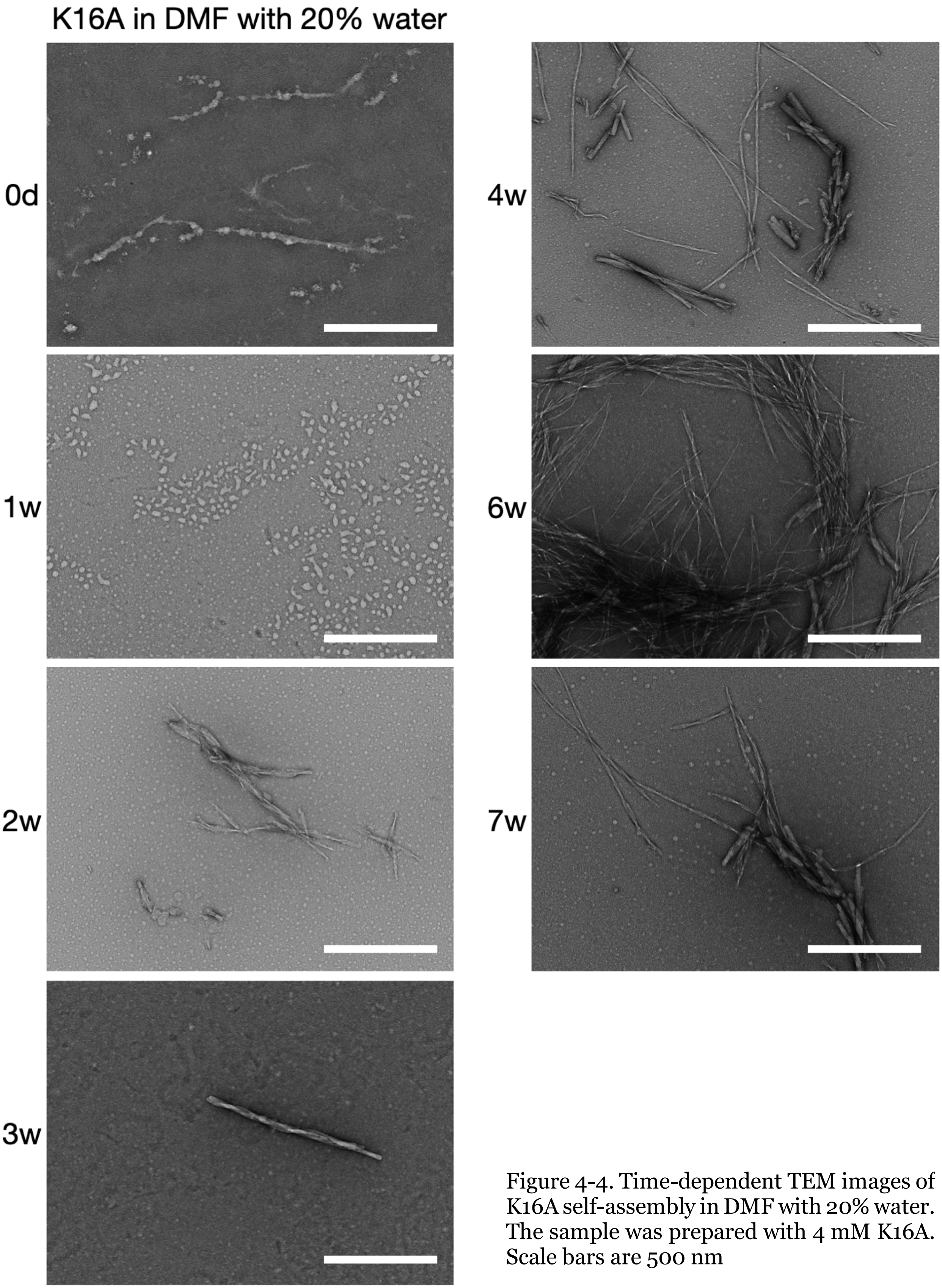

Figure 4-4. Time-dependent TEM images of K16A self-assembly in DMF with 20% water. The sample was prepared with 4 mM K16A. Scale bars are 500 nm

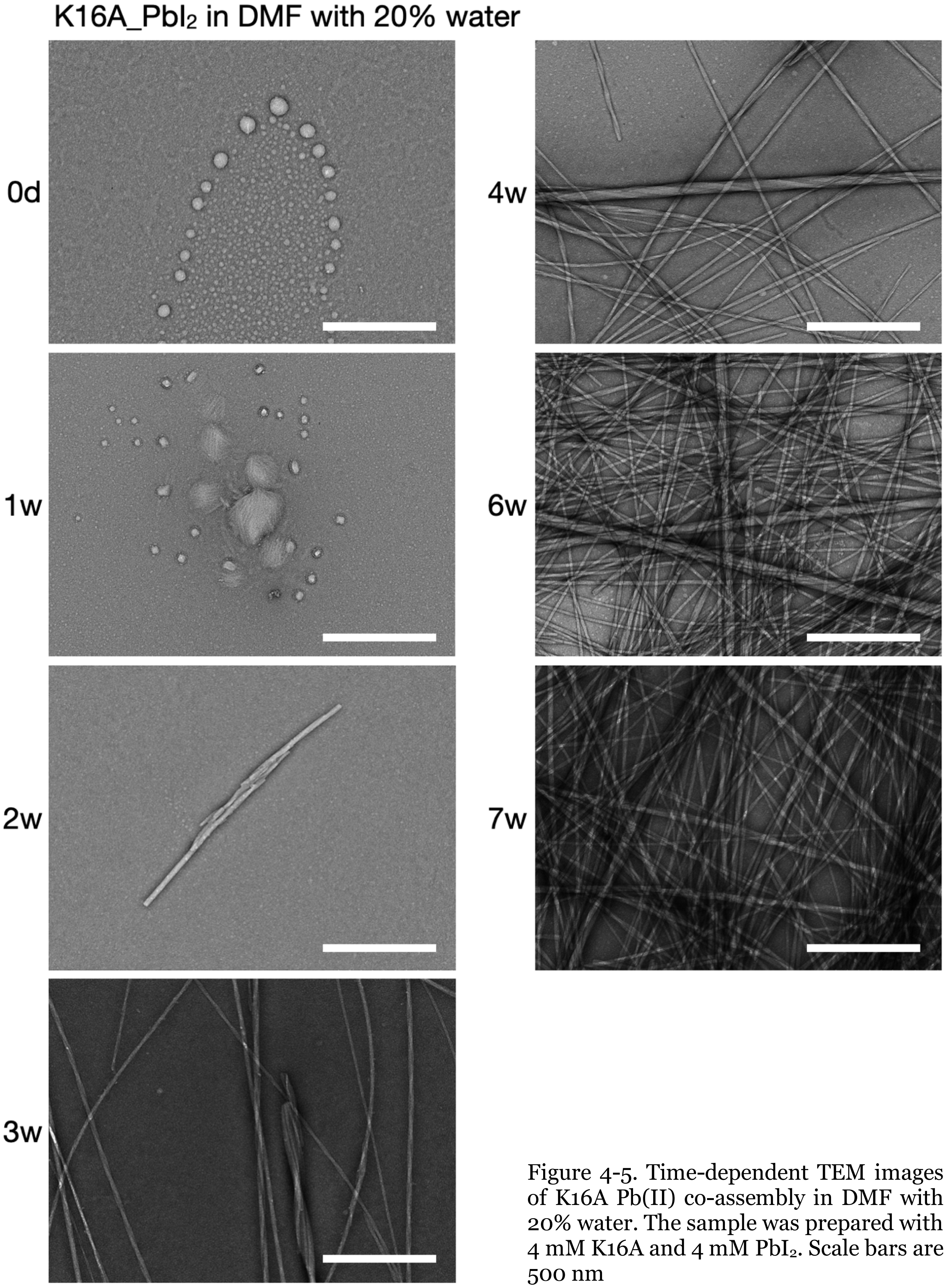

Figure 4-5. Time-dependent TEM images of K16A Pb(II) co-assembly in DMF with 20% water. The sample was prepared with 4 mM K16A and 4 mM PbI_2. Scale bars are 500 nm

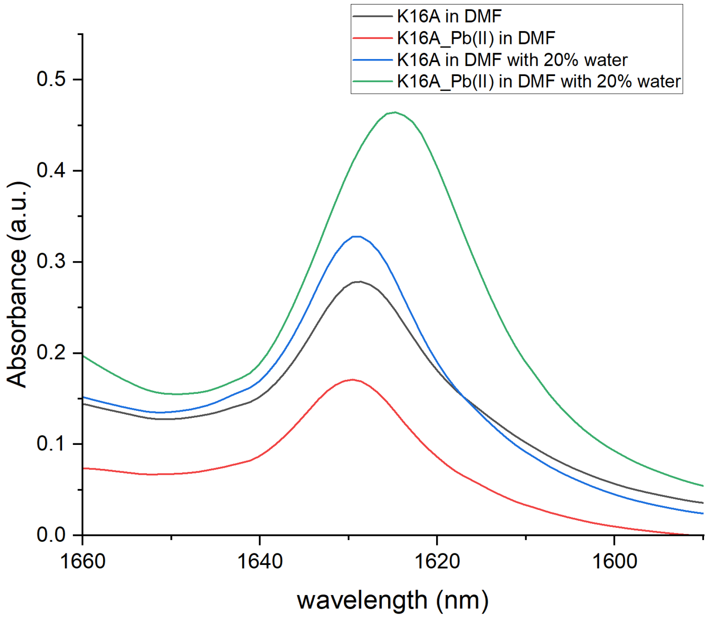

Figure 4-6. Amide-I band of K16A assembly series at 4-week time point in DMF solvent systems.

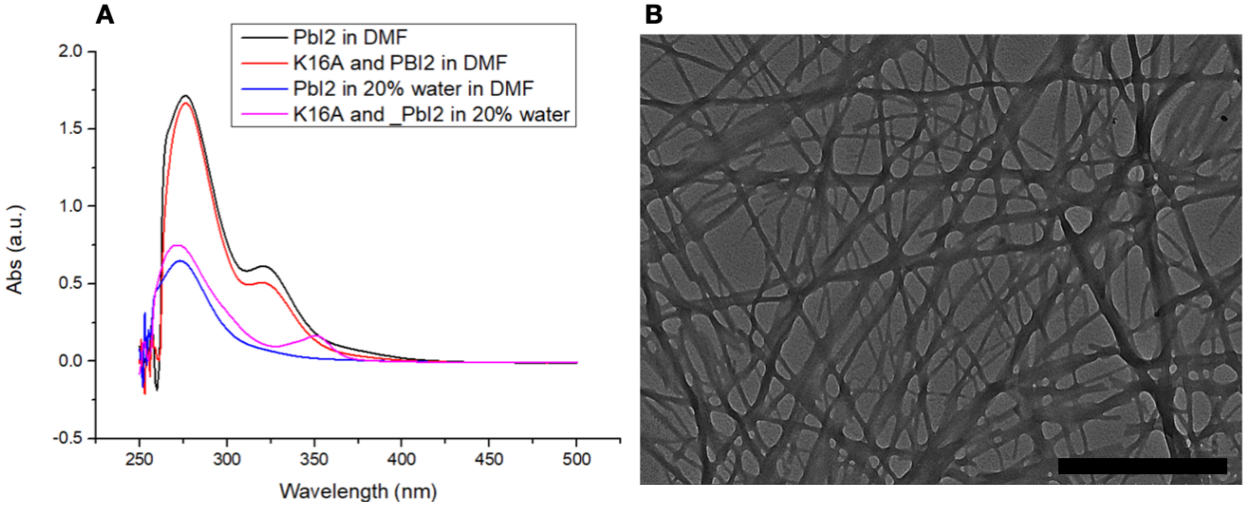

Figure 4-7. A) UV/Vis spectra of K16A_Pb(II) assembly series and PbI_2 in DMF solvent systems. B) a TEM image of K16A_Pb(II) in DMF with 20% of water without staining.

The TEM image in figure 4-7B without negative staining shows homogeneous and dense lead distribution in the fibers, which can support the coupled Pb(II)/or Pb(II) complex

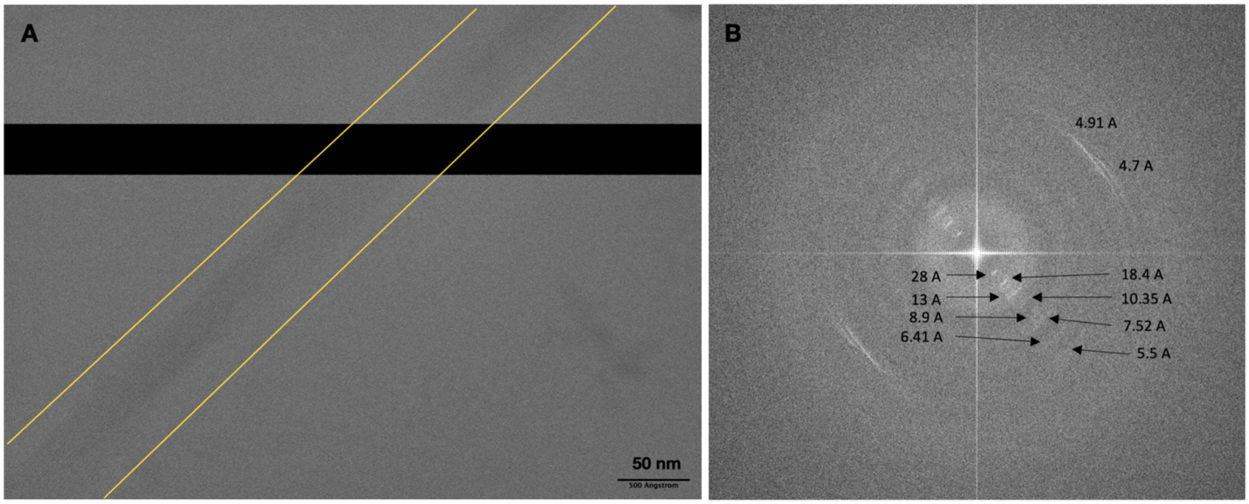

Figure 4-8. A) a Cryo-EM image of K16A_Pb(II) co-assembly in DMF with 20% of water. Another bundled fiber group are covered by the black box to clarify patterns' directions. B) FFT of the fibers in the yellow box in figure A. d-spacings of the patterns are indicated in the figure.

assumption. Fast-Fourier transformation (FFT) of a cryo-EM image which presents patterns indicate 4.91 Å and 4.7 Å in direction of the fiber propagation axis, and several spaces in the perpendicular to the propagation axis (Fig. 4-8B). 4.7 Å is typical d-spacing of between hydrogen bonded peptide strands of beta sheets. 4.91 Å is unknown d-spacing but it can be a distance between lead ions. 10.35 Å is indicating the d-spacing of lamination between beta sheets, and there are many d-spacings which may show gaps of bundled fibers. The FT-IR spectra (Fig. 4-7) and the FFT (Fig. 4-8) exhibit the cross-beta structure of the K16A-Pb(II) co-assemblies in DMF with 20% of water.

K16A and $PbCl_2$ co-assemblies were tested in the DMF solvent systems. The samples were also prepared with 4 mM peptide and 4 mM $PbCl_2$. Unlike PbI_2 co-assemblies, $PbCl_2$ assemblies barely shows nanostructures (Fig. 4-9). Although the sample in DMF/Water has more short fibers than the sample in DMF, compared to PbI_2 assemblies $PbCl_2$ shows less tendency to form nanostructures. This is probably because of the higher free energy barrier for the dissociation of chloride ions from the $PbCl_2$ than

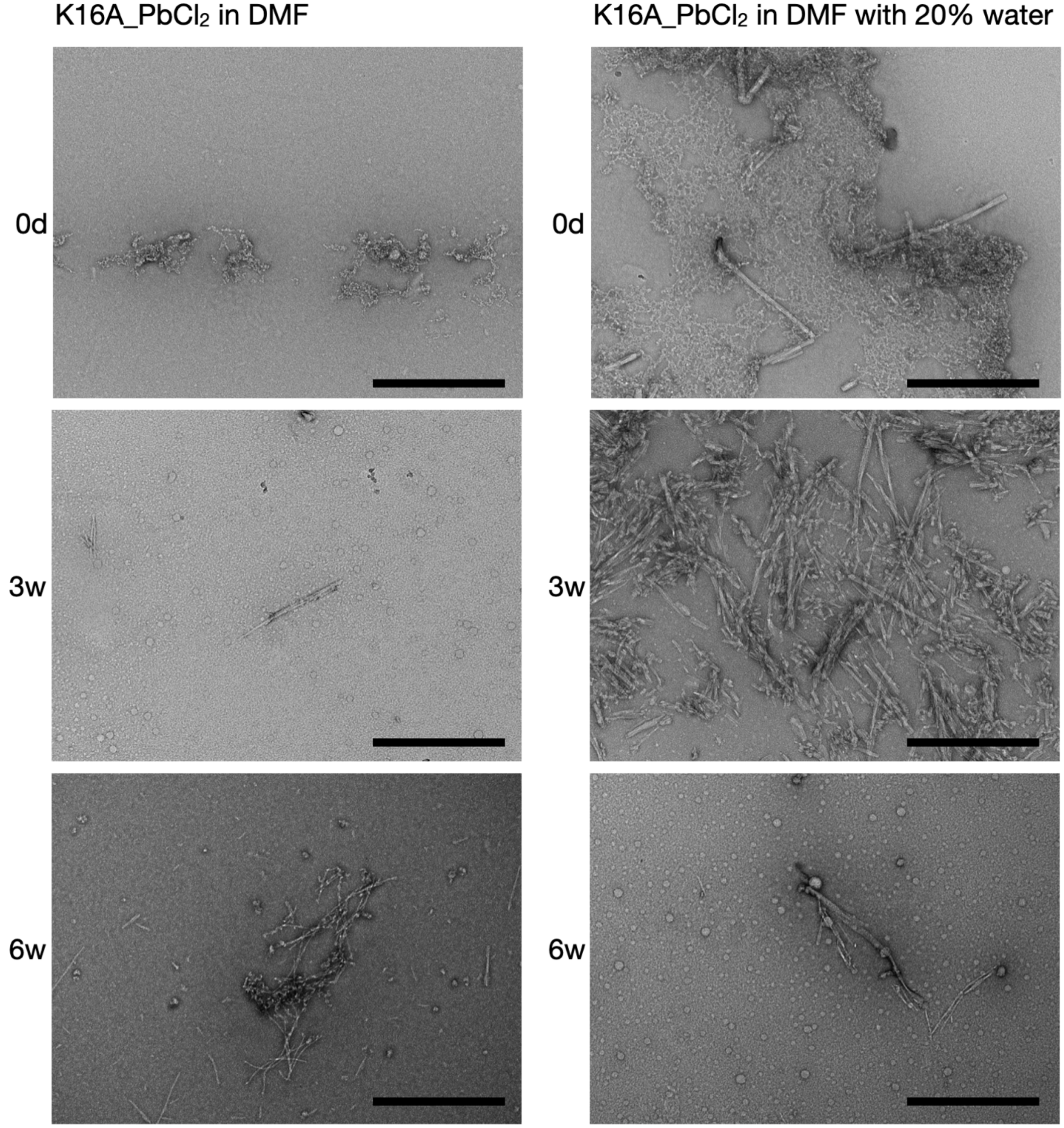

Figure 4-9. Time-dependent TEM images of K16A co-assemblies with $PbCl_2$ in DMF with 20% of water. The samples are prepared with 4 mM K16A and 4 mM $PbCl_2$. Scale bars are 500 nm.

that of iodide ions[15]. Pb(II) in $PbCl_2$ may prefer to stay as lead-halide precursor rather than associate with peptides. Other K16A co-assemblies with different metal compounds were also tested. To compare with K16A-Cu(II) co-assemblies in aqueous solvent, Cu(II)

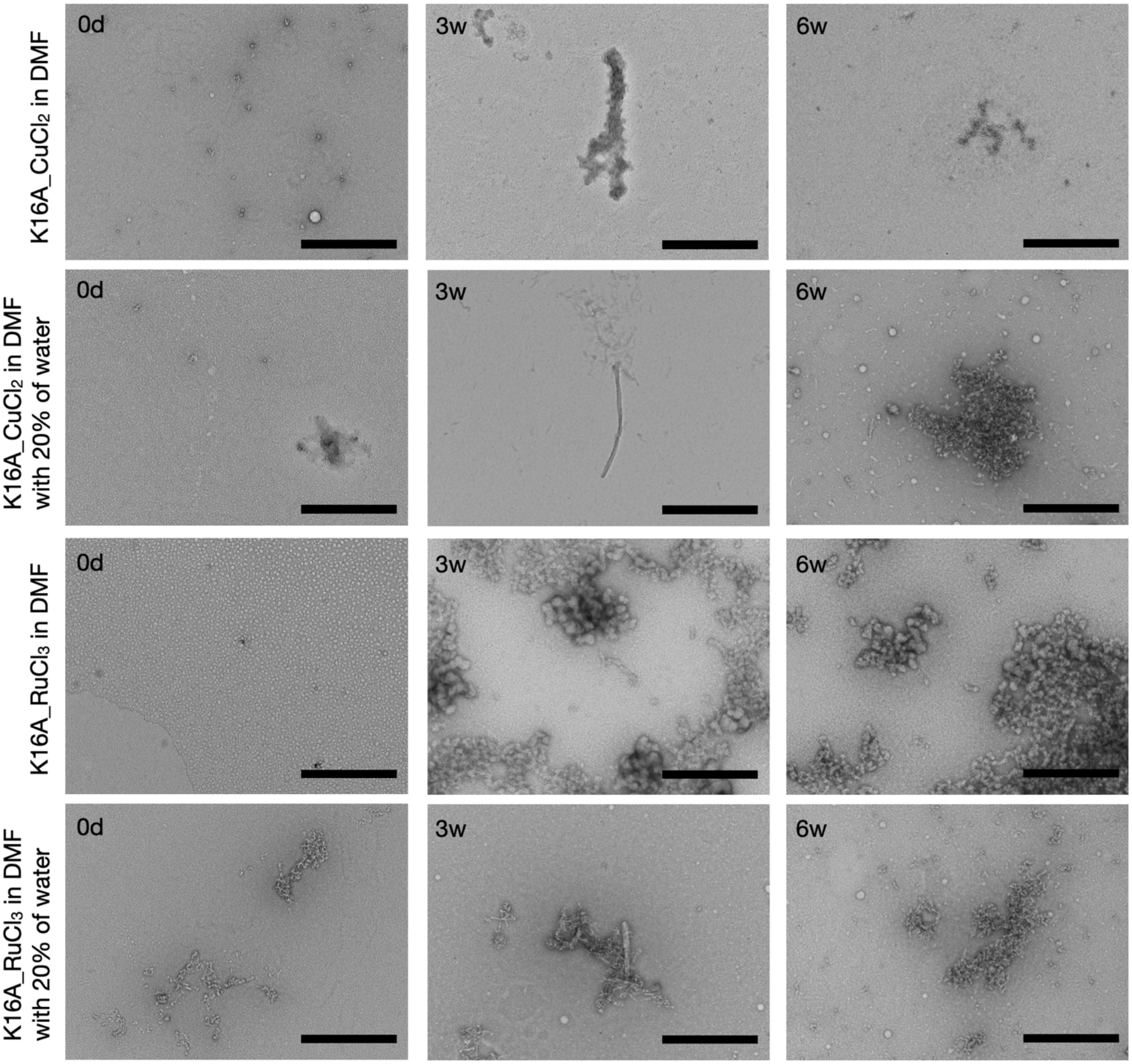

Figure 4-10. Time-dependent TEM images of K16A-metal co-assemblies with $CuCl_2$ (top two rows) and $RuCl_3$ (bottom two rows) in DMF solvent systems. The samples are prepared with 4 mM K16A peptide and 4 mM or metal compound. Scale bars are 500 nm.

co-assemblies was chosen. In addition, Ruthenium (III), which is used as dye/photo-sensitizer[16-17], is also tried to form well-ordered peptide-Ruthenium co-assemblies that can probably show distinct optical or photovoltaic properties. However, even though the samples show some assembled morphologies, very limited population of the ordered fibers are shown, and the most morphologies are amorphous aggregations (Fig. 4-10).

4.2.2 K16A-Pb(II) co-assemblies in aqueous solvent

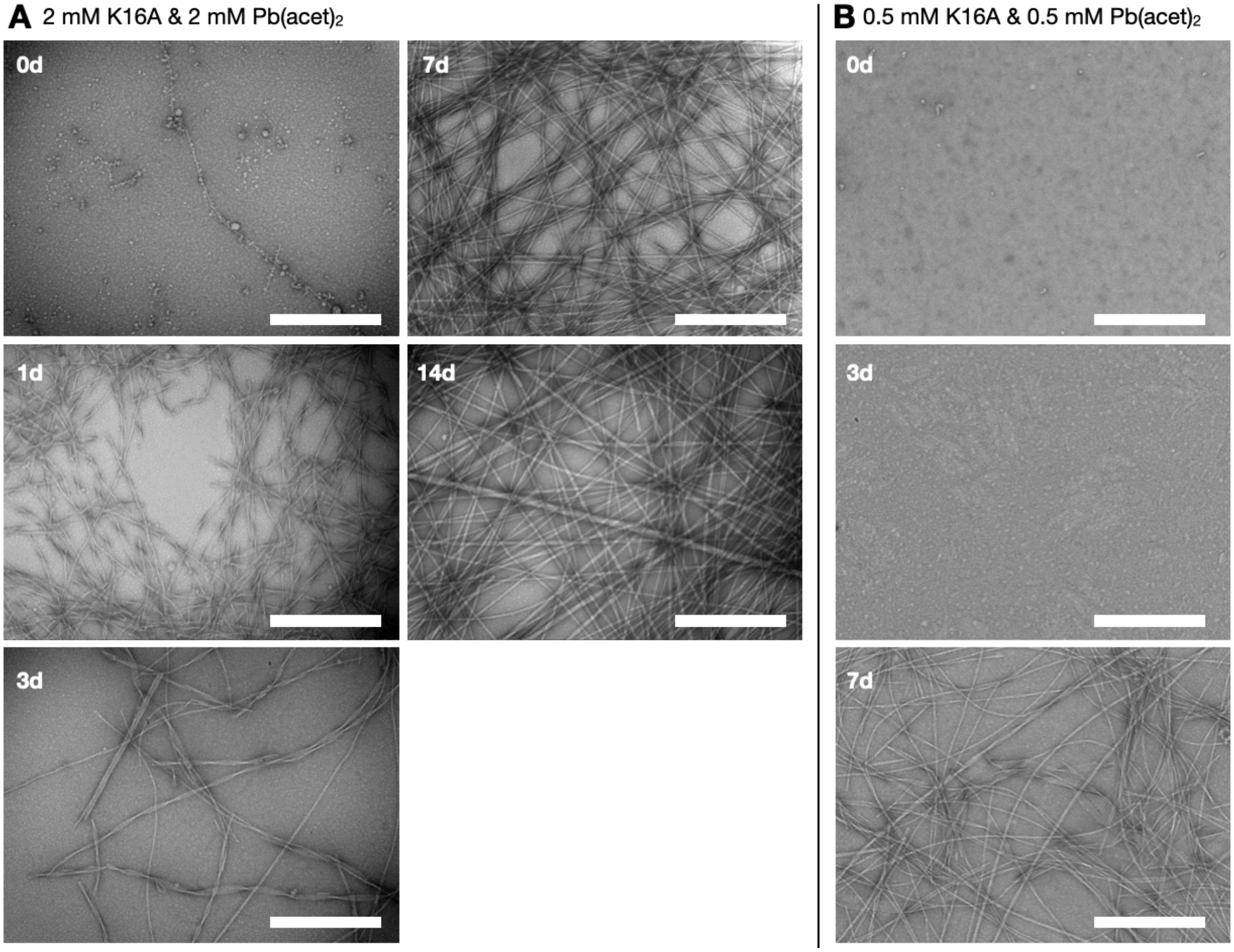

Figure 4-11. Time-dependent TEM images of 2 mM K16A and 2 mM Pb(acet)$_2$ assembly (A), and 0.5 mM K16A and 0.5 mM Pb(acet)$_2$ (B). Both assemblies were prepared with 25 mM MES (pH 5.6). scale bars are 500 nm.

In addition to the Pb(II) co-assemblies in DMF solvent, the aqueous solvent with 25 mM MES (pH 5.6), which conventionally used for K16A and K16A_Copper co-assemblies as explained in chapter 3, was applied to form the K16A_Pb(II) co-assemblies with lead(II) acetate (Pb(acet)$_2$) that is soluble in water. The co-assembly solution which consists of 2 mM K16A, 2 mM Pb(acet)$_2$, and 25 mM MES (pH 5.6) forms twisted

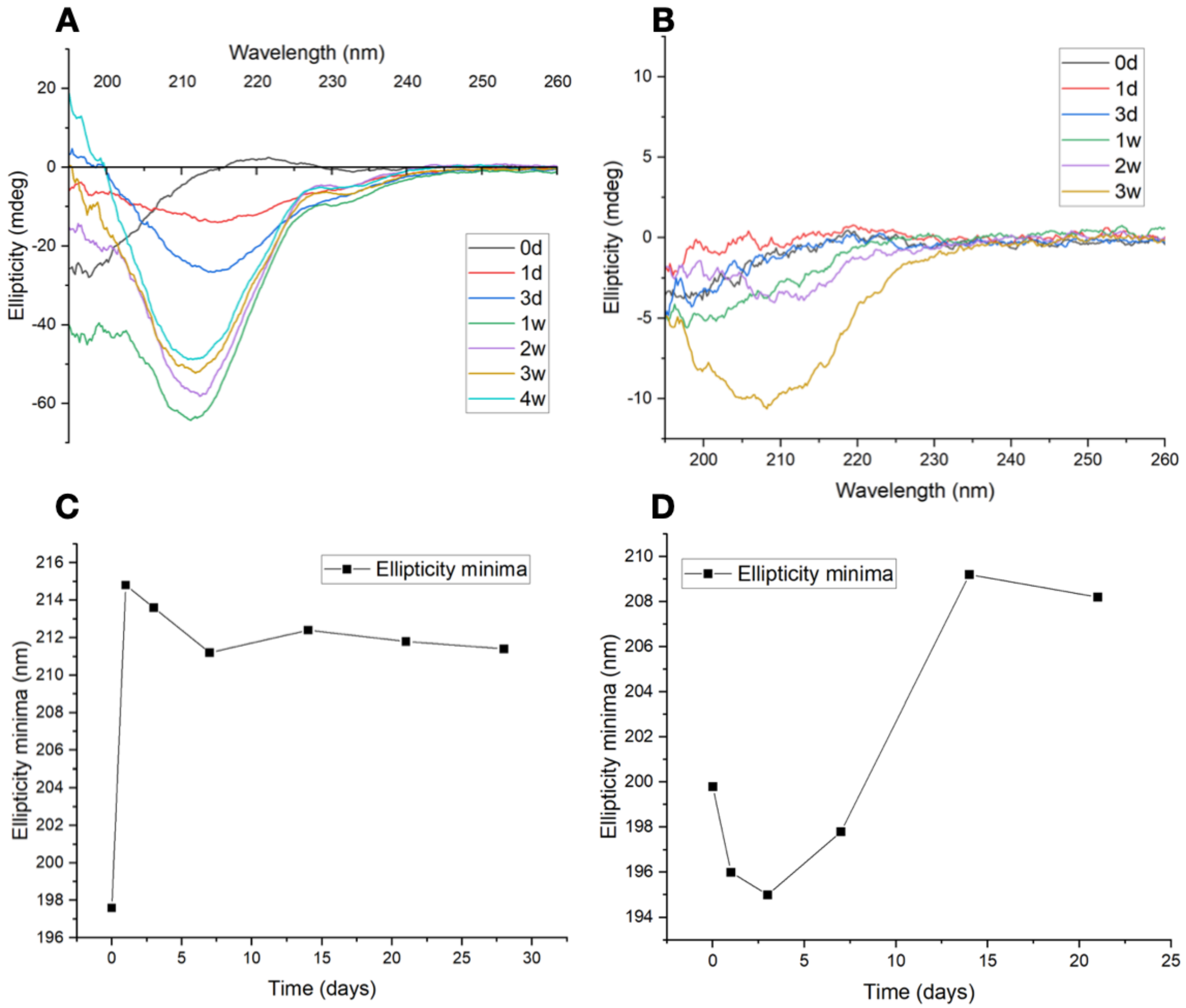

Figure 4-12. Time-dependent CD spectra of 2 mM K16A and 2 mM Pb(acet)$_2$ assembly (A), and 0.5 mM K16A and 0.5 mM Pb(acet)$_2$ (B). The location of x-axis is adjusted for clarity of spectra. Ellipticity minima as function of time (days) of 2 mM K16A and 2 mM Pb(acet)$_2$ assembly (C), and 0.5 mM K16A and 0.5 mM Pb(acet)$_2$ (D). Both assemblies were prepared with 25 mM MES (pH 5.6). scale bars are 500 nm.

nanoribbons, and eventually has nanofibers (Fig. 4-11). This morphological transition was not found in K16A-copper co-assemblies, and it is indicated in CD spectra (Fig. 4-12A and C). At the initial time point, the ellipticity minima implies random coils which is matched with the TEM image, and from 1-day time point CD spectra indicates beta-sheet secondary structure with minima at 215 nm. However, the minima blue-shifted to 212 nm

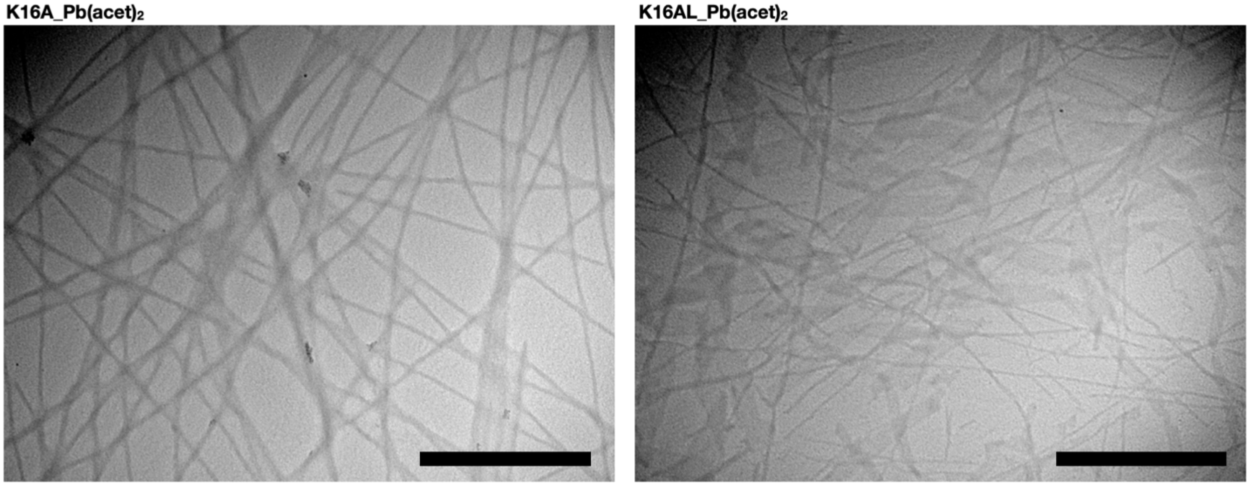

Figure 4-13. TEM images of K16A_Pb(II) (Left), and K16AL_Pb(II) co-assemblies in MES buffer (pH 5.6) without staining. The samples were prepared with 0.5 mM peptide and 0.5 mM lead(II) acetate. Scale bars are 500 nm.

after the 1-day time point. Moreover, the CD spectra shows no maxima at around 195 nm with relatively high "high tension (HT)" value. To reduce the HT and investigate if the absence of maxima was resulted from the high HT, an assembly sample was prepared with lower concentration of K16A and Pb(acet)$_2$ and tested. This low concentration sample does not show the transition from nanoribbons to nanofibers in TEM (Fig. 4-11B). Considering the noisy spectra due to the low concentration, the minima transition can be regarded as being red-shifting (Fig 4-12D). I rationalize that high concentration of the peptide and metal quickly process nucleation and propagation that has a kinetically favorable structure, and then form a thermodynamically stable structure, while the low concentration sample have slow liquid-solid transition which forms thermodynamically favorable structure, fibers in this case. In addition, despite of the lower concentrations and lower HT, the CD spectra of the 0.5 mM K16A and Pb(acet)$_2$ assembly does not present the maxima at around 195 nm (Fig. 4-11B). The left-circularly polarized light pi-pi* absorption (at near 195 nm) of beta-sheets can be canceled out by right-circularly

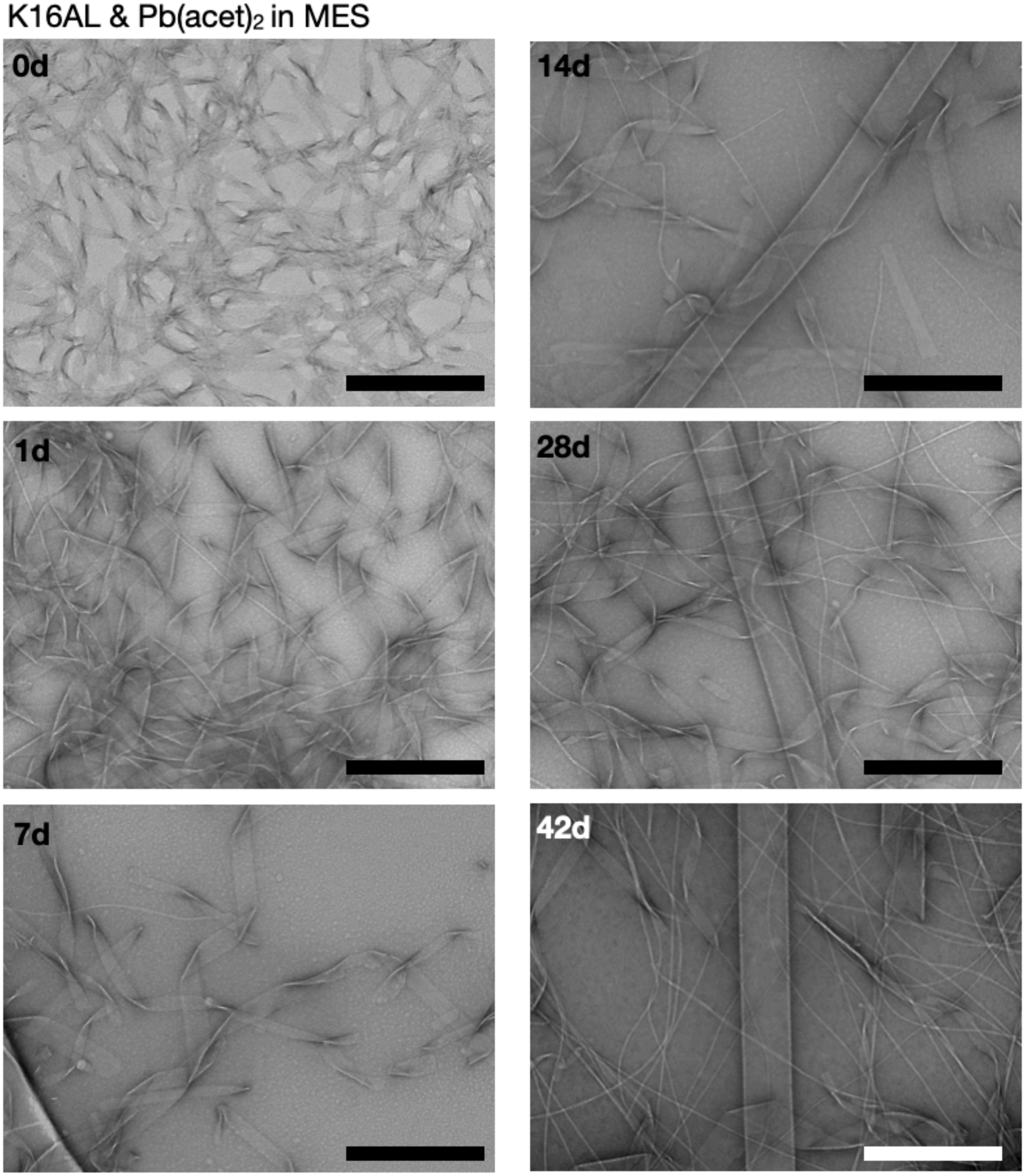

Figure 4-14. Time-dependent TEM images of 0.5 mM K16AL and 0.5 mM Pb(acet)$_2$ assembly. The assembly was prepared with 25 mM MES (pH 5.6). scale bars are 500 nm.

polarized light absorption of a new Pb(II) complex, which has homogeneously incorporated in the co-assembly (Fig. 4-13).

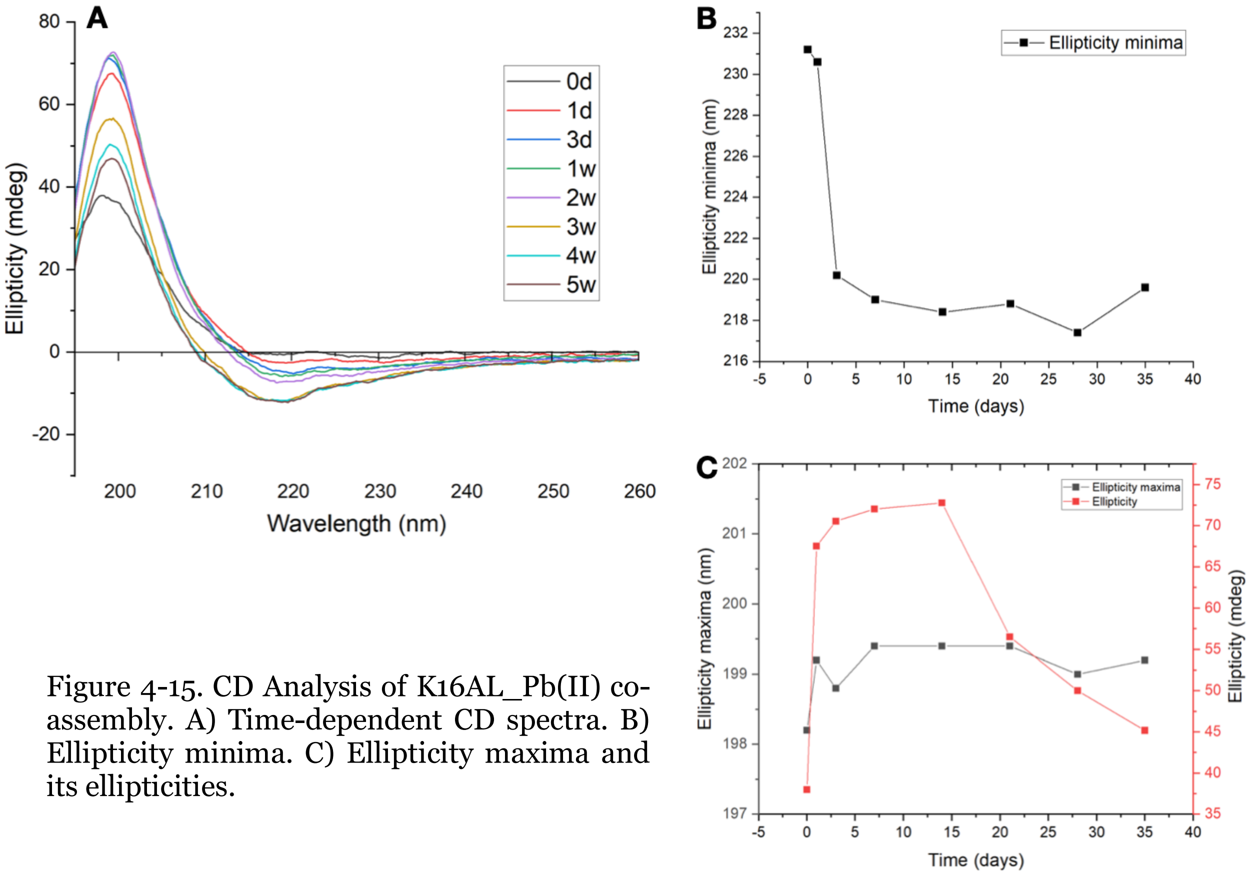

Figure 4-15. CD Analysis of K16AL_Pb(II) co-assembly. A) Time-dependent CD spectra. B) Ellipticity minima. C) Ellipticity maxima and its ellipticities.

K16AL, H-HHQALVFFAL-NH_2, peptide sequence was also tested. Based on the time-dependent TEM images, the change of morphological is similar with K16AL peptide self-assembly (Fig. 4-14 and 3-22). Twisted ribbons at the initial time point were converted to nanotubes and eventually the assemblies have tubes and many fibers. CD spectra also have same trend in Full CD spectra, ellipticity minima and maxima (Fig. 4-15, 3-25A, 3-26A, and 3-27A). Unlike K16AL and copper co-assemblies' cases that have clear morphological changes from K16AL self-assemblies, this K16AL-Pb(II) assembly does not show clear differences in both CD spectra and TEM images. Even the TEM image of K16AL_Pb(II) co-assembly without negative staining indicates the existence of lead ions in the co-assemblies (Fig. 4-13), further studies, such as electron paramagnetic resonance spectroscopy (EPR) analysis, to investigate if lead ions are incorporated in the assembly structures are needed. Some evidence about this phenomenon will be shown in the next section.

4.2.3 Isolating heavy metals using peptide-metal co-assemblies

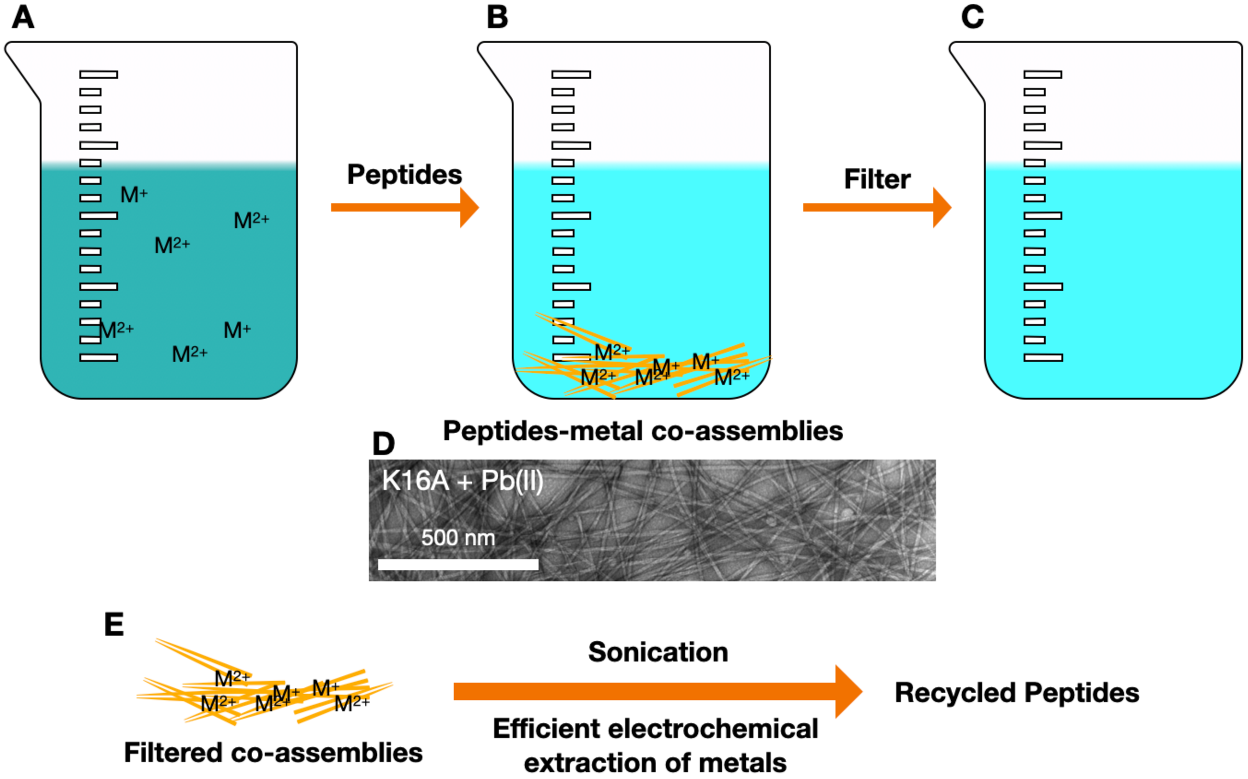

Figure 4-16. Schemes of isolating heavy metals from contaminated water by using metal-binding properties of peptide assemblies. A) Contaminated water with heavy metals. B) Pre-treated contaminated water with peptides which formed peptide-metal co-assemblies (yellow). C) Filtered clean water. D) A TEM image of peptide-metal co-assemblies (K16A_Pb(II) co-assembly in this case) showing the size of nanostructures. E) Steps of electrochemical extraction for the heavy metals collected with co-assemblies and recycling the peptide by sonication.

In this chapter and chapter 3, metal binding/collecting property of peptides forming co-assemblies was reported. The copper and lead ions that were shown for the co-assemblies are considered heavy metals resulting in soil/water contaminations which have significant impact on agricultural productivities[18]. Conventional ways to wash heavy metals require high energy consumption[19], high chemical agent consumption[20], or expensive filters[21]. Electrochemical treatments consume high energy to cover massive amount of contaminated water, and reverse osmosis requires expensive filters and high energy to pump contaminated water through filters. Using the peptide-metal co-assemblies can realize a new way to isolate heavy metals with low energy consumption, inexpensive filters, and low chemical consumption since the peptides can be recycled. To be specific, as described in figure 4-16A and B, widely spread heavy metal ions can be collected together by interaction with peptides forming peptide-metal co-assemblies. It is also a significant benefit. Since the peptide-metal co-assemblies have more than micrometer size, the water mixture of the co-assemblies can be easily filtered with lower energy and inexpensive filters or membranes (Fig. 4-16C and D). Then the collected peptide-metal co-assemblies can be treated by ultra-sonication to separate the co assemblies into individual peptide to reuse for another water cleaning. Remaining peptides in water cannot harm environments since peptides are biomaterials unlike other reagents such as ethylenediaminetetraacetic acid (EDTA). Because the metals were already collected in lower volume, it can be extracted by electrochemical treatments efficiently.

As a proof-of-concept of the scheme, experiments of measuring concentrations of copper and leas ions before after treatments were designed. The samples had 2 mM peptides (K16A or K16AL), and 2 mM metal ions (copper or lead). The treatments consist of centrifuging or filtering. To be specific, after the peptide-metal co-assemblies formed matured nanostructures, the samples were centrifuged, and the supernatant was taken and diluted to measure the concentrations of metals by inductively coupled plasma mass spectrometry (ICP-MS). Or the samples were filtered with a centrifuge tube filter by centrifuging, and the filtrate was measured for the concentration of metals by ICP-MS.

Peptide assembly	Measured metal	Isolate Method	ppb (µg/L)	% (removed)
K16A_Cu(II)	Cu	Control	492.450	-
K16A_Cu(II)	Cu	Centrifuged	328.421	-33.309
K16A_Cu(II)	Cu	Filtered	297.675	-39.552
K16A_Cu(I)	Cu	Control	351.656	-
K16A_Cu(I)	Cu	Centrifuged	77.320	-78.013
K16A_Cu(I)	Cu	Filtered	64.309	-81.713
K16A_Pb(II)	Pb	Control	265.134	-
K16A_Pb(II)	Pb	Centrifuged	238.412	-10.079
K16A_Pb(II)	Pb	Filtered	-	-
K16AL Cu(II)	Cu	Control	555.007	-
K16AL Cu(II)	Cu	Centrifuged	8.221	-98.519
K16AL Cu(II)	Cu	Filtered	0.714	-99.871
K16AL_Pb(II)	Pb	Control	294.439	-
K16AL_Pb(II)	Pb	Centrifuged	265.601	-9.794
K16AL_Pb(II)	Pb	Filtered	265.205	-9.929

Table 4-1. Concentrations of metals in peptide-metal co-assembly solutions before (control) and after treatments, measured by ICP-MS.

Copper co-assemblies shows better metal-binding properties than lead co-assemblies (Table 4-1). Although K16A-Cu(II) co-assembly shows less metal isolation than K16A-Cu(I) and K16AL-Cu(II) as expected since it shows very slow forming assemblies, Cu-co-assembly series present much higher metal isolations compared to Pb-co-assemblies. K16AL, which always shows fast assemblies, indicates the highest percentage of removed metals with copper. However, Pb-assemblies have lower metal bindings. As described above (Fig. 4-11 and 4-12), K16A-Pb(II) co-assembly shows relatively much faster rate of forming assemblies than K16A-Cu(II) co-assembly which takes more than two months, so incorporation of leads in propagation of the co-assemblies was expected as well as strong interactions in nucleation steps. However, according to the ICP-MS data, lead ions are barely incorporating in the co-assembly nanostructures, showing only ~10% of isolated metals. One possibility is that the fibers have lead ions, but it can be easily broken apart and release the metal ions due to the mechanical forces of centrifugation or filtration. The other possibility is incorporating of lead ions only in the nucleation step and after liquid-solid transition lead ions may not interact with peptides.

4.3 Conclusion

In order to develop the novel peptide-metal co-assemblies as functional materials, lead(II) ions and other metals were tested to form the co-assemblies in different solvent systems. To form the co-assemblies with a precursor, PbI_2, for active materials in perovskite solar cells and light emitting devices, DMF solvent systems were used because of PbI_2's solubility. Although forming the co-assemblies take relatively longer period than aqueous solvent, the co-assemblies in DMF solvent systems were successfully formed.

Adding of 20% of water into DMF accelerates the forming of co-assemblies. Ruthenium and copper ions were also tried, but these metal ions did not make fine nanostructures with K16A in DMF solvent systems. Although the distinct absorption, that probably indicates coupling of Pb(II) ions or Pb(II) complexes, was found from the K16A-Pb(II) co-assemblies in DMF solvent system, the absorption should have more red-shifted range that indicating low band-gap or HOMO-LUMO energy gap of the material to be applied for photovoltaics. However, this research can suggest a new way to engineer or design the peptide-metal co-assemblies for desired functions. Moreover, it also shows peptide self-assemblies and peptide-metal co-assemblies can be formed with non-typical solvents such as organic solvents.

Peptide-Pb(II) co-assemblies were also tested in aqueous solvent. K16A-Pb(II) co-assemblies in the aqueous solvent showed beta-sheet secondary CD spectra, but the left-circularly polarized light pi-pi* absorption (at near 195 nm) was not shown in the spectra. I assumed that the absorption was cancelled out by right-circularly polarized light absorption of a new Pb(II) complex in the co-assembly. K16AL peptide sequence was also used as the peptide part in peptide-metal co-assembly. However, it did not show morphological and spectroscopical differences from K16AL peptide self-assemblies.

ICP-MS analysis was used for the proof-of concept of peptide assemblies for isolation of heavy metals that contaminate water and have impact on environments such as agricultures and human health. The experiments prove that the peptides can be used for heavy metal isolations from contaminated water. Both K16A and K16AL peptides show metal binding properties and ability to isolate copper ions from solutions. However, even though lead ions present influences on the assembly kinetics and morphologies, lower efficiencies of isolating metals after the treatments were shown with both K16A and

K16AL. It can be caused from mechanically fragile nanofibers with lead ions, or weak interactions in the fiber propagation steps. This different metal binding property of peptide assemblies can be developed for selection of metals in contaminated water with multiple metals.

4.4 Future works

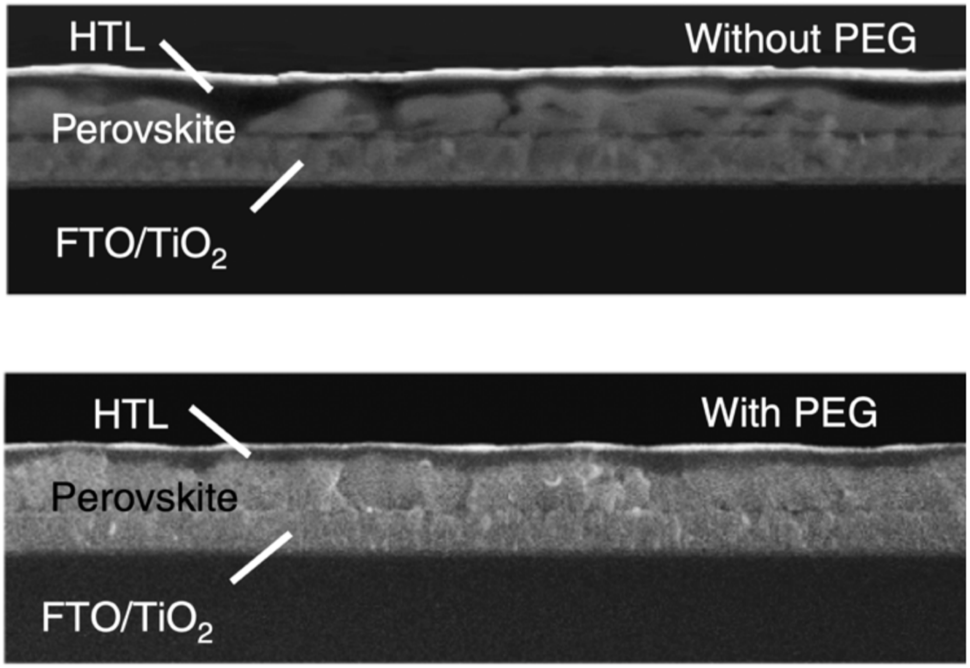

Figure 4-17 Cross-sectional SEM images of perovskite solar cells with or without PEG (Ref. 13)

Hybrid perovskites have attracted the attention of many due to their great photovoltaic performance and optoelectronic properties. The efforts spent on exploring hybrid perovskites did not go unnoticed, as the materials' efficiency in power conversion is over 20% of what it was 10 years ago[22]. Fabrications of perovskite have been developed using high temperature (>450 °C)[23-24], or high vacuum deposition[25], which makes the cells expensive. Although low-cost solution process has reduced the cost problems, there

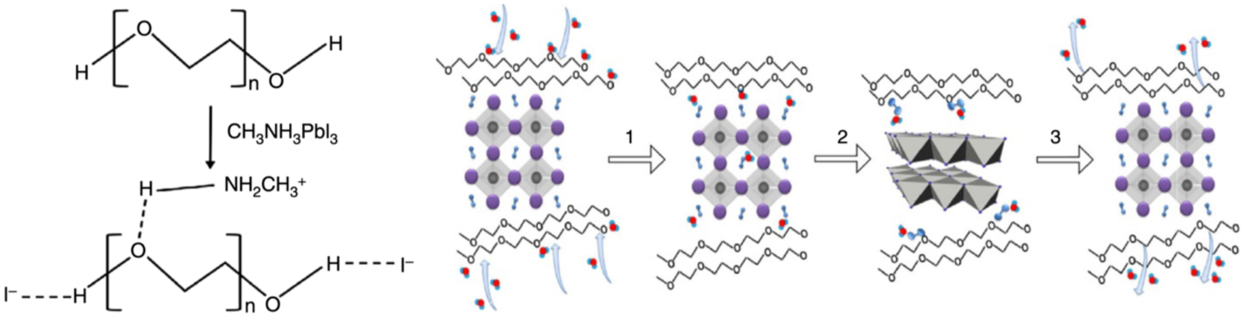

Figure 4-18. Schematic diagrams of hydrogen interaction between PEG and $MAPBI_3$, and self-healing mechanisms. (1) Water absorbs on perovskite; (2) Perovskite hydrolysis into PbI_2 and $MAI{\cdot}H_2O$ by water; (3). Restrained MAI by PEG react with nearby PbI_2 to form perovskite again after water evaporates. (Ref. 13)

are still issues, such as film quality and humidity resistance, that need to be resolved for improved performance and practical applications. Early reports with lab scale devices showed lifetime of only a few minute[26], and recently developed models show stabilities of weeks[23-24]. In order to commercialize perovskite solar cells (PSCs), lifetime over years should be achieved in outdoor operation[27].

Scientists are particularly focused in achieving homogeneous distribution of perovskite films on cells by using polymers[12-13, 28]. Giving templates to perovskite some polymers help increase nucleation and slow crystal growth of perovskite which impacts on better quality of film on cells[12, 28]. Others show that hydrogen bonding interactions between the polymers, such as polyethylene glycol (PEG) and perovskite components enhance the quality of perovskite films and power conversion efficiency with 14% (8% without PEG) (Fig. 4-17)[13]. Moreover, strong hydrogen bonding improves humidity resistance and shows self-healing behaviors against damages from water exposure, preventing evaporation of methylammonium iodide (MAI) (Fig 4-18). A conductive

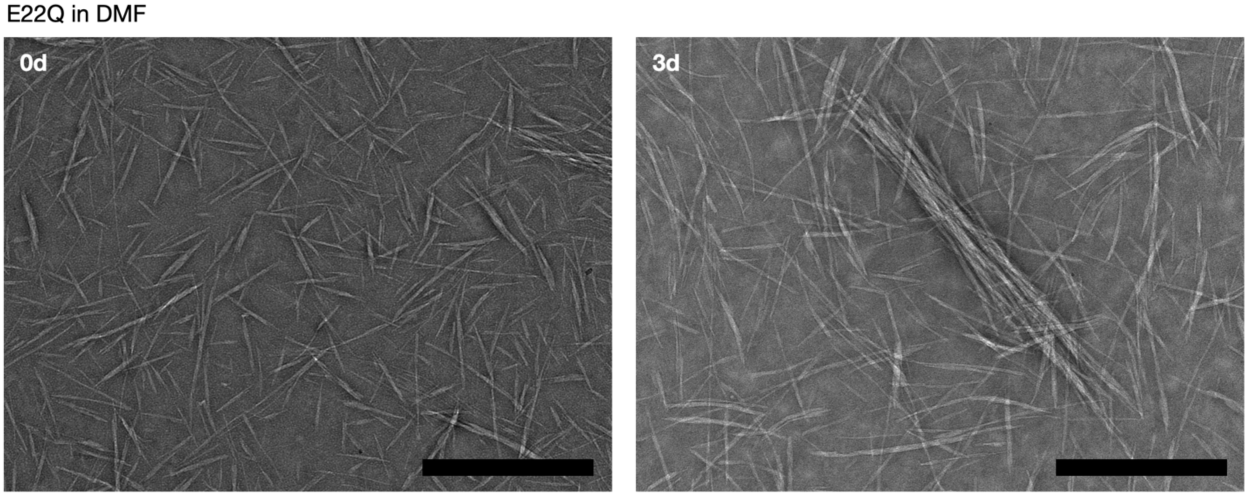

Figure 4-19. TEM images of E22L peptide self-assemblies in DMF at initial time point (left) and 3-day time point (right) scale bars are 500 nm. Peptide concentration is 2 mM.

polymer, including H-bonding acceptor units, poly[2-methoxy-5-(2-ethylhexyloxy)1,4-phenylenevinylene] (MEH-PPV), was blended with $MAPbI_3$ to gain homogenous film, reducing additional conductive layers such as PEDOT:PSS or $PC_{61}BM$[29].

Peptides can be additives in the active layers with perovskite because of the many of hydrogen bonding acceptors and donors which can interact with perovskite mateirals and even with other neighbor layers like FTO and Spiro (will be explain below). Considering the fact that generally used organic parts of cation of perovskite, methylammonium (MA) and formamidinium (FA), are exactly same as lysine and arginine amino acid residues, peptides or peptide self-assembly should provide templates for nucleation of crystal growth and hold the organic materials even if hydrolysis breaks perovskite crystals, enhancing self-healing properties. Indeed, the amide bonds of poly(N-vinyl-2-pyrrolidone) (PVP) with partial charges (-O-C=N+) shows an important impact on electron transfer process of photocatalytic hydrogen evolution systems using photosensitizers[30-31]. Like this, peptide bond including amide bonds should help electron or hole transfer in perovskite cells.

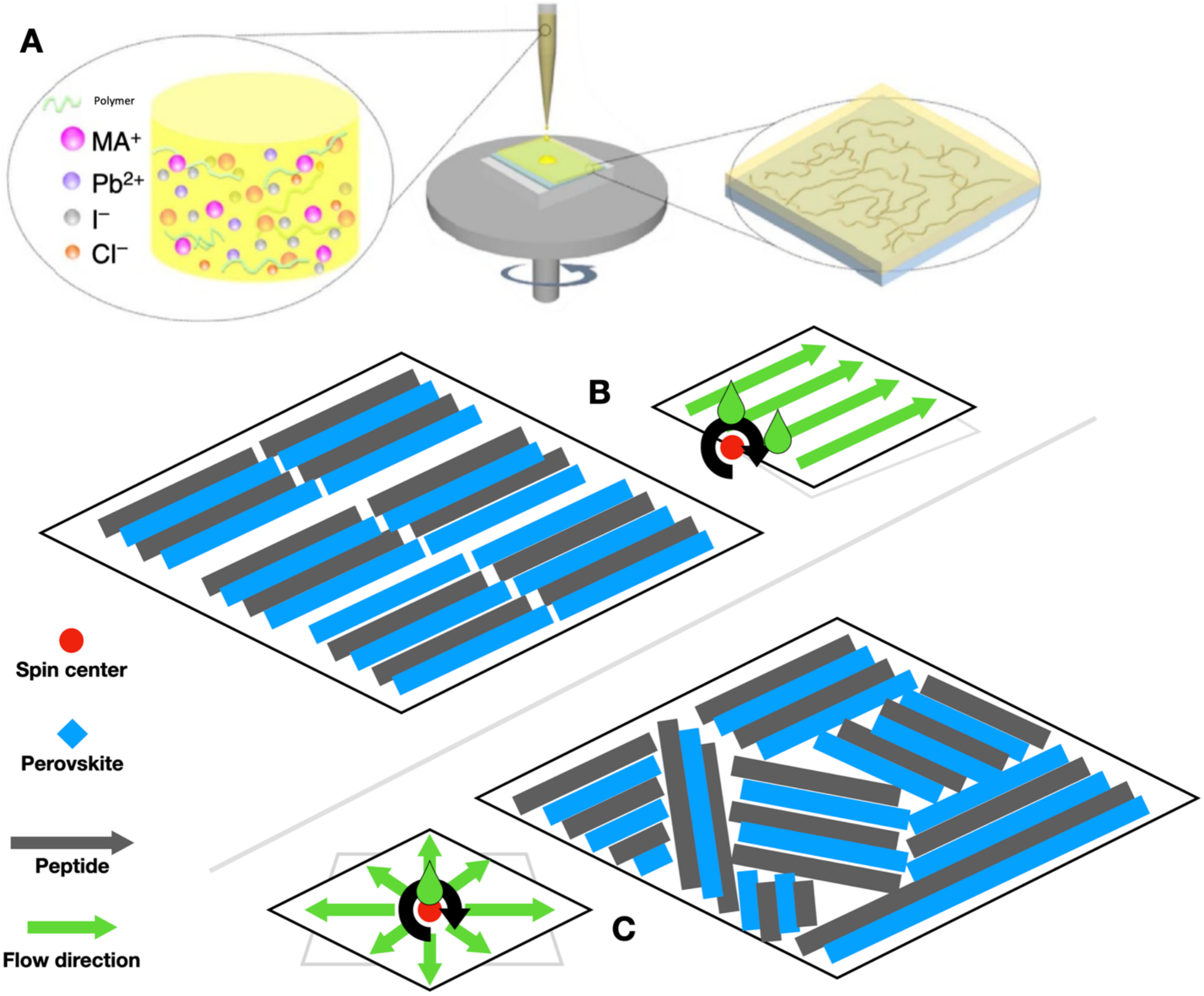

Figure 4-20. (A) a scheme of spin coating of a cell with polymers/peptides and perovskite precursors. Schemes of peptide assisted perovskite films with controlled alignments by different spin centers. Top) spin center positioned at one of the cell's edges, making well aligned perovskite crystals. Bottom) spin center positioned center of the cell, making disordered crystals.

Ac-KLVFFAQ-NH_2, E22Q, peptide sequence has been well studied and because of the lysine on N-terminal and glutamine on C-terminal, it can be one of the candidate peptides as the additives for perovskite active films. Unlike K16A peptide, E22Q shows significantly fast forming of assembly nanostructures (Fig. 4-19). Even at the initial time point it shows thin needle-like fibers. So, the fibers can be aligned depending on spin center when the E22Q and perovskite precursors are being coated (Fig. 4-20). When the cell is coated with a spin center at the edge of the cell, the alignment of peptide-perovskite crystals can be ordered. On the other hand, the alignment can be disordered when a spin center placed in the center of the cell. These difference orders of alignment can have an impact on power conversion efficiency because long terms of delocalization of excitons in the well aligned perovskite crystals can delay transfer of the excitons to other layers molecular orbitals.

The perovskite absorber layer with the proposed peptides can be prepared on the TiO_2 (40 nm thickness)-coated fluorine doped tin oxide (FTO) glass by spin coating followed by annealing at 105 °C for 70 min. 2,29,7,79-tetrakis-(N,N-di-pmethoxyphenylamine) 9,99-spirobifluorene (Spiro-OMeTAD) and gold will be applied as the hole transport layer and electrode, respectively. The proposed polymers or peptides will be added in the precursor solution of $PbCl_2/PbI_2$ and MAI (1:3 molar ratio). The molar ratio of the peptides to $MAPbI_3$ will be optimized with survey of 0.5:1, 1:1, 1.5:1, and 2:1. The film qualities from the survey will be tested by scanning election microscopy (SEM) (Fig. 4-17) and atomic force microscopy (AFM). Volumes of the solution and revolution per minute (RPM) will be used to make constant film thickness (~400nm). To test photovoltaic properties, thin-film UV/Vis spectroscopy will first be investigated to see if the polymer blending effects on intensity and wavelength range of the absorbance. For, the proposed conductive polymers, higher intensity and larger absorbance are expected because of the polymer's long conjugated pi system. J-V curves will show power conversion efficiency (PCE) and, the curves with different ratio will characterize what ratio has highest efficiency under simulated AM (Air mass) 1.5 illumination of 100 mW

cm^{-2}. With results of “stability and self-healing test”, the best ratio of maximum balanced PCE and stability will be determined.

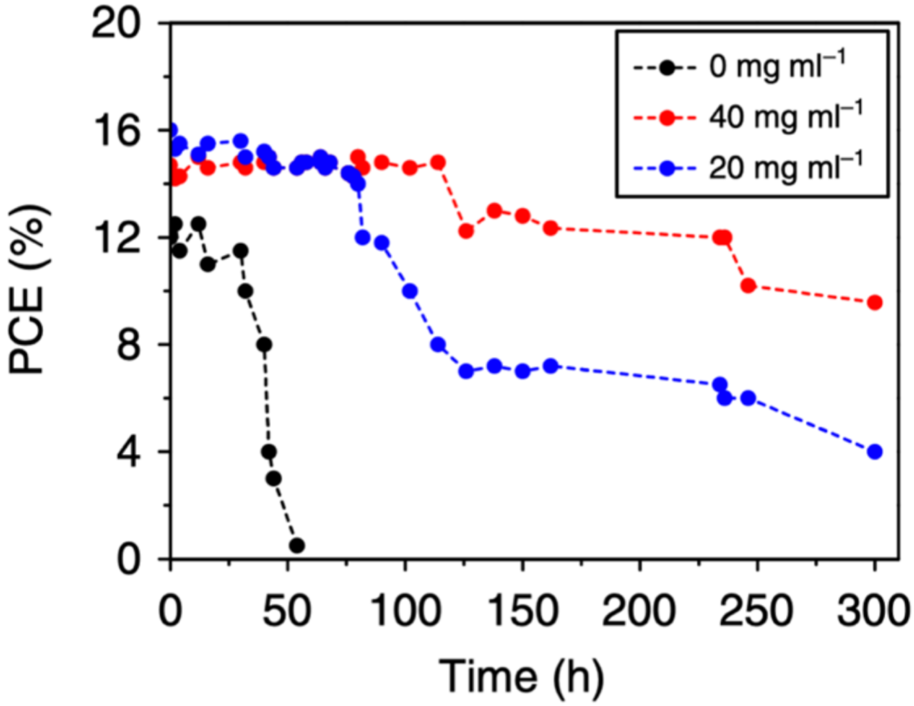

Figure 4-21. An example of the stability test with different ratios of additives in 70% relative humidity condition. (Ref. 13)

In general tests for stability of PSCs are insulated by plastics to avoid infiltration of any chemicals such as oxygen or humidity into active layers. However, to test the stability from humid and self-healing property, PSCs with the proposed peptides will not be covered. J-V curve of the PSCs with the peptides will be measured as a function of time in highly humid environment (relative humidity 70%) (Fig. 4-21). Like the measurements of PCE with different ratio, self-healing property will also be tested with the different ratios. Cells with higher peptides ratio probably have better stability in humid condition and better self-healing properties. However, depend on the result from the previous PCE tests without humidity, best ratio for performance and stability will be decided. Investigation of self-healing, optical properties, such as thin-film UV/Vis and PL, and J-

V curves, will involve how well the self-healing process recovers the original properties. Multiple exposures to the humid environment will be tested to show that these treatments can tolerate variable weather conditions. When the stabilities of PSCs including proposed peptides are verified, PSCs sealed with plastics will be investigated for commercial level tests.

As I rationalized, introducing of peptides or peptide assembly systems into perovskite solar cell's active layers can improve the film quality, enhance stabilities, and give self-healing properties. Moreover, beyond helping nucleation and growing perovskite crystals, using the peptide assembly nanostructures can control paracrystallinity of the layer. It can suggest a new method to control the delocalization of electron-hole pairs and improve power conversion efficiency of perovskite solar cells.

4.5 Materials and Methods

Synthesis and purification of peptides

Peptides were synthesized on a CEM Corporation microwave peptide synthesizer (Matthews, NC, USA) using standard Fmoc chemistry. The solid support for peptide synthesis was an Fmoc rink-amide resin (AnaSpec, Inc., Fremont, CA, USA) with a typical substitution range of 0.4-0.6 meq./g. Resin was pre-swollen in minimal dimethylformamide (DMF) for 15 min. Microwave assisted Fmoc deprotection was completed using 20% piperidine in DMF at 45-55°C for 180 sec followed by three DMF flushes. Each coupling step was performed using 0.1 M Fmoc-protected amino acid and activated with 0.1 M 2-(1H-Benzotriazole-1-yl)-1,1,3,3-tetramethyluronium hexafluorophosphate (HBTU) and 0.2 M N,N-diisopropylethylamine (DIEA) in DMF.

Microwave coupling temperatures were maintained within 75-82 °C for 300 s then rinsed with DMF 3x. Histidines were doubly coupled at 50 °C with 11 W power instead of 8 W. After cleavage with trifluoroacetic acid/thioanisole/EDT/anisole, 95/5/3/2 v/v/v/v, crude peptide was extracted 3x in -20 ^{o}C ether and vacuum desiccated.

Peptides were purified using a Waters HPLC with a XSELECT™ CSH™ Prep C18 column (Waters, Milford, MA, USA) with a reverse-phase gradient of H_2O/MeCN. All solvents contain 0.1% TFA. Gradient method was optimized to allow for a minimum of 10 min before sample peak elution and a minimum of 5 min after peak collection before column re-equilibration. Gradient ramp rate = 1%/min. Fraction quality was assessed by MALDI-TOF on an Applied Biosystem 4700 Proteomics analyzer with a 355 nm ND:Yag laser operating at 200 Hz (Foster City, CA, USA). The matrix used to facilitate analyte desorption was α-cyano-4-hydroxycinnamic. (HHQALVFFA-NH_2, 1068.228 ($M+H^+$). Confirmed product fractions were concentrated in vacuo before lyophilizing in a FreeZone Plus 12 Liter Cascade, Labconco, freeze dryer system (Kansas City, MO, USA). Lyophilized peptides were stored at room temperature inside a vacuum desiccator.

Peptide Assembly

peptide assemblies and buffers were prepared using ASTM Type II metal-free water (EMD Chemicals Inc., Gibbstown, NJ, USA) with 25 mM MES, pH 5.6.

<u>Peptide fibrils in aqueous solvent</u>: K16A/K16AL peptide was dissolved at 2x the desired concentration in metal-free water and vortexed for 5 sec. This 2x peptide stock was diluted to full volume with 50 mM MES buffer, pH 5.6, accompanying another vortex period.

Co-assembled metal-peptide nanoribbons in aqueous solvent: a 2x peptide stock was prepared as described previously, except with the 100 mM metal stock addition occurring directly after diluting to 1x with 50 mM MES, along with a third vortex period. Note, the volume of water used to prepare the 2x stock was reduced to accommodate the final addition of metal stock.

Peptide fibrils in DMF solvent system: K16A/K16AL peptide was dissolved at the desired concentration in DMF (or 20% water with DMF) and vortexed for 5 sec.

Co-assembled metal-peptide in aqueous solvent: peptide was dissolved in DMF (or 20% water with DMF) and vortexed for 5 sec. metal stock in DMF (or 20% water with DMF) was added and the final solution was vortexed for 5 sec.

Circular Dichroism Spectroscopy (CD)

CD spectra were recorded using the Jasco-810 CD spectropolarimeter at room temperature. Spectra between 260 nm and 180 nm were collected with a 0.1 mm path length cell, with a step size of 0.2 mm and a speed of 50 nm/s. All spectra were recorded in triplicate and averaged. Ellipticity (mdeg) was converted to mean residue molar ellipticity (MRME, [θ], $\text{deg}\bullet\text{cm}^2\bullet\text{dmol}^{-1}$) by $[\theta] = \theta/(10\bullet n\bullet C\bullet l)$, where ‘n’ is the number of backbone amide bonds per peptide, ‘C’ is the molar concentration (mol/L) and ‘1’ is the cell path in cm.

Fourier Transform Infrared Spectroscopy (FT-IR)

All FT-IR spectra were recorded using a Jasco FT-IR 4100 (Easton, MD, USA). Aliquots (6 μL) of peptide solution were fan-dried onto a Pike GaldiATR (Madison, WI, USA) diamond at room temperature and averaging 1,068 scans with 2 cm^{-1} resolution. Background spectra were subtracted from each sample.

Transmission Electron Microscopy (TEM)

10 μL peptide assembly aliquots (4 μL for samples in DMF solvent) were drop cast onto CF200-Cu Carbon Film 200 Mesh Copper grids (Electron Microscopy Sciences, Hatfield, PA). Peptide assemblies were settled on the grid surface for 1 minute. Excess solution was wicked away using a kimwipe. Immediately following, 10 μL of a 1.5% uranyl acetate (in water) stain (8 μL for samples in DMF solvent) was applied for 1 minute and similarly wicked way. Electron micrographs were imaged with a Hitachi HT-7700 Microscope at 80 kV at the Robert P. Apkarian Integrated Electron Microscopy Core.

Inductively-coupled plasma - mass spectroscopy (ICP-MS)

Peptide assembly solutions were treated by centrifuge (12k RPM for 20 min) or filter centrifuge (1k RPM for 2 min) with Corning® Costar® Spin-X® centrifuge tube filters (cellulose acetate membrane, pore size 0.22 μm, non-sterile) and the treated samples were diluted to desired concentrations within 1 ~ 1000 ppb (ug/L) range. The concentrations of metal in samples were calculated with calibration curve of standards, measured by Perkin Elmer NexION 2000 at the Mass Spectrometry Center at Emory University.

4.6 References

1. Grätzel, M., The light and shade of perovskite solar cells. *Nature Materials* **2014,** *13* (9), 838-842.
2. Infante, I.; Manna, L., Are There Good Alternatives to Lead Halide Perovskite Nanocrystals? *Nano Letters* **2021,** *21* (1), 6-9.
3. Wang, Q.; Wang, X.; Yang, Z.; Zhou, N.; Deng, Y.; Zhao, J.; Xiao, X.; Rudd, P.; Moran, A.; Yan, Y.; Huang, J., Efficient sky-blue perovskite light-emitting diodes via photoluminescence enhancement. *Nature Communications* **2019,** *10* (1), 5633.
4. Xing, J.; Zhao, Y.; Askerka, M.; Quan, L. N.; Gong, X.; Zhao, W.; Zhao, J.; Tan, H.; Long, G.; Gao, L.; Yang, Z.; Voznyy, O.; Tang, J.; Lu, Z.-H.; Xiong, Q.; Sargent, E. H., Color-stable highly luminescent sky-blue perovskite light-emitting diodes. *Nature Communications* **2018,** *9* (1), 3541.
5. Quan, L. N.; Zhao, Y.; García de Arquer, F. P.; Sabatini, R.; Walters, G.; Voznyy, O.; Comin, R.; Li, Y.; Fan, J. Z.; Tan, H.; Pan, J.; Yuan, M.; Bakr, O. M.; Lu, Z.; Kim, D. H.; Sargent, E. H., Tailoring the Energy Landscape in Quasi-2D Halide Perovskites Enables Efficient Green-Light Emission. *Nano Letters* **2017,** *17* (6), 3701-3709.
6. Chen, Q.; De Marco, N.; Yang, Y.; Song, T.-B.; Chen, C.-C.; Zhao, H.; Hong, Z.; Zhou, H.; Yang, Y., Under the spotlight: The organic–inorganic hybrid halide perovskite for optoelectronic applications. *Nano Today* **2015,** *10* (3), 355-396.
7. Jellicoe, T. C.; Richter, J. M.; Glass, H. F. J.; Tabachnyk, M.; Brady, R.; Dutton, S. E.; Rao, A.; Friend, R. H.; Credgington, D.; Greenham, N. C.; Böhm, M. L., Synthesis and Optical Properties of Lead-Free Cesium Tin Halide Perovskite Nanocrystals. *Journal of the American Chemical Society* **2016,** *138* (9), 2941-2944.

8. Sharland, J. C.; Wei, B.; Hardee, D. J.; Hodges, T. R.; Gong, W.; Voight, E. A.; Davies, H. M. L., Asymmetric synthesis of pharmaceutically relevant 1-aryl-2-heteroaryl- and 1,2-diheteroarylcyclopropane-1-carboxylates. *Chemical Science* **2021,** *12* (33), 11181-11190.
9. Liu, W.; Twilton, J.; Wei, B.; Lee, M.; Hopkins, M. N.; Bacsa, J.; Stahl, S. S.; Davies, H. M. L., Copper-Catalyzed Oxidation of Hydrazones to Diazo Compounds Using Oxygen as the Terminal Oxidant. *ACS Catalysis* **2021,** *11* (5), 2676-2683.
10. Dou, Y.-K.; Shang, Y.; He, X.-W.; Li, W.-Y.; Li, Y.-H.; Zhang, Y.-K., Preparation of a Ruthenium-Complex-Functionalized Two-Photon-Excited Red Fluorescence Silicon Nanoparticle Composite for Targeted Fluorescence Imaging and Photodynamic Therapy in Vitro. *ACS Applied Materials & Interfaces* **2019,** *11* (15), 13954-13963.
11. Luo, G.-F.; Biniuri, Y.; Chen, W.-H.; Neumann, E.; Fadeev, M.; Marjault, H.-B.; Bedi, A.; Gidron, O.; Nechushtai, R.; Stone, D.; Happe, T.; Willner, I., Artificial Photosynthesis with Electron Acceptor/Photosensitizer-Aptamer Conjugates. *Nano Letters* **2019,** *19* (9), 6621-6628.
12. Bi, D.; Yi, C.; Luo, J.; Décoppet, J.-D.; Zhang, F.; Zakeeruddin, Shaik M.; Li, X.; Hagfeldt, A.; Grätzel, M., Polymer-templated nucleation and crystal growth of perovskite films for solar cells with efficiency greater than 21%. *Nature Energy* **2016,** *1* (10), 16142.
13. Zhao, Y.; Wei, J.; Li, H.; Yan, Y.; Zhou, W.; Yu, D.; Zhao, Q., A polymer scaffold for self-healing perovskite solar cells. *Nature Communications* **2016,** *7* (1), 10228.
14. Liu, D.; Traverse, C. J.; Chen, P.; Elinski, M.; Yang, C.; Wang, L.; Young, M.; Lunt, R. R., Aqueous-Containing Precursor Solutions for Efficient Perovskite Solar Cells. *Adv Sci (Weinh)* **2018,** *5* (1), 1700484.

15. Kaiser, W.; Radicchi, E.; Mosconi, E.; Kachmar, A.; De Angelis, F., Iodide vs Chloride: The Impact of Different Lead Halides on the Solution Chemistry of Perovskite Precursors. *ACS Applied Energy Materials* **2021,** *4* (9), 9827-9835.
16. Willner, I.; Maidan, R.; Mandler, D.; Duerr, H.; Doerr, G.; Zengerle, K., Photosensitized reduction of carbon dioxide to methane and hydrogen evolution in the presence of ruthenium and osmium colloids: strategies to design selectivity of products distribution. *Journal of the American Chemical Society* **1987,** *109* (20), 6080-6086.
17. Tomar, N.; Agrawal, A.; Dhaka, V. S.; Surolia, P. K., Ruthenium complexes based dye sensitized solar cells: Fundamentals and research trends. *Solar Energy* **2020,** *207*, 59-76.
18. Xu, J.; Liu, C.; Hsu, P.-C.; Zhao, J.; Wu, T.; Tang, J.; Liu, K.; Cui, Y., Remediation of heavy metal contaminated soil by asymmetrical alternating current electrochemistry. *Nature Communications* **2019,** *10* (1), 2440.
19. Salt, D. E.; Blaylock, M.; Kumar, N. P. B. A.; Dushenkov, V.; Ensley, B. D.; Chet, I.; Raskin, I., Phytoremediation: A Novel Strategy for the Removal of Toxic Metals from the Environment Using Plants. *Bio/Technology* **1995,** *13* (5), 468-474.
20. Leštan, D.; Luo, C.-l.; Li, X.-d., The use of chelating agents in the remediation of metal-contaminated soils: A review. *Environmental Pollution* **2008,** *153* (1), 3-13.
21. Gajdošová, L.; Búgel, M.; Bakalár, T., Heavy metal removal using reverse osmosis. *Acta Montanistica Slovaca* **2009,** *14* (3), 250-253.
22. NREL Best Research-Cell Efficiency Chart. https://www.nrel.gov/pv/cell-efficiency.html.

23. Burschka, J.; Pellet, N.; Moon, S.-J.; Humphry-Baker, R.; Gao, P.; Nazeeruddin, M. K.; Grätzel, M., Sequential deposition as a route to high-performance perovskite-sensitized solar cells. *Nature* **2013,** *499* (7458), 316-319.
24. Lee, M. M.; Teuscher, J.; Miyasaka, T.; Murakami, T. N.; Snaith, H. J., Efficient Hybrid Solar Cells Based on Meso-Superstructured Organometal Halide Perovskites. *Science* **2012,** *338* (6107), 643-647.
25. Liu, M.; Johnston, M. B.; Snaith, H. J., Efficient planar heterojunction perovskite solar cells by vapour deposition. *Nature* **2013,** *501* (7467), 395-398.
26. Im, J. H.; Lee, C. R.; Lee, J. W.; Park, S. W.; Park, N. G., 6.5% efficient perovskite quantum-dot-sensitized solar cell. *Nanoscale* **2011,** *3* (10), 4088-93.
27. Urbina, A., The balance between efficiency, stability and environmental impacts in perovskite solar cells: a review. *Journal of Physics: Energy* **2020,** *2* (2), 022001.
28. Masi, S.; Rizzo, A.; Aiello, F.; Balzano, F.; Uccello-Barretta, G.; Listorti, A.; Gigli, G.; Colella, S., Multiscale morphology design of hybrid halide perovskites through a polymeric template. *Nanoscale* **2015,** *7* (45), 18956-18963.
29. Masi, S.; Colella, S.; Listorti, A.; Roiati, V.; Liscio, A.; Palermo, V.; Rizzo, A.; Gigli, G., Growing perovskite into polymers for easy-processable optoelectronic devices. *Scientific Reports* **2015,** *5* (1), 7725.
30. Kliegman, R. M. M. a. J. M., Conformational studies on N-methyl lactams. Use of solvent effects in N.M.R. *Tetrahedron Letters* **1966,** *7* (9), 891-896.
31. Lin, H.; Liu, D.; Long, J.; Zhang, Z.; Zhuang, H.; Zheng, Y.; Wang, X., Towards a comprehensive insight into efficient hydrogen production by self-assembled Ru(bpy)3^{2+}–polymer–Pt artificial photosystems. *Physical Chemistry Chemical Physics* **2015,** *17* (16), 10726-10736.